ČESKÉ VYSOKÉ UČENÍ TECHNICKÉ V PRAZE

Fakulta stavební
Experimentální centrum

Characterization of high-performance fibre-reinforced cementitious composites subjected to high deformation rates

Charakterizace vysokohodnotných vlákny vyztužených cementových kompozitů při vysokých rychlostech deformace

DISERTAČNÍ PRÁCE

Ing. Petr Konrád

Doktorský studijní program:	Fyzikální a materiálové inženýrství
Studijní obor:	Stavební inženýrství
Školitel:	doc. Ing. Bc. Radoslav Sovják, Ph.D.

Praha, 2021

Prohlašuji, že jsem předloženou disertační práci vypracoval samostatně a všechny použité literární zdroje jsou citovány.

Disertační práce vznikla v souvislosti s řešením projektu Výzkum, vývoj, testování a hodnocení prvků kritické infrastruktury, VI20172020061.

Praha, 13. ledna 2021 Ing. Petr Konrád

Poděkování

Chtěl bych v první řadě poděkovat doc. Ing. Bc. Radoslavu Sovjákovi, Ph.D. jednak za vedení mé disertační práce ale i celého doktorského studia, za cennou pomoc a podporu při návrhu zkušebního zařízení a experimentálního programu. Dále pak zaměstnancům Experimentálního centra, zejména za provedení experimentů pro kvazi-statické zatížení, pomoc s výrobou zkušebních těles a zkušebního zařízení. V neposlední řadě děkuji Ing. Lukáši Fialovi, Ph.D. za výpomoc s nedestruktivním měřením pomocí elektrické cívky a Ing. Janu Havelkovi, Ph.D. za 3D tisk nástavce cívky.

Abstrakt

V této práci jsou zkoumány vysokohodnotné vlákny vyztužené cementové kompozity vystavené rázovému zatížení. Hlavním cílem je návrh, sestavení a optimalizace zkušebního zařízení a postupu pro provedení rázové zkoušky. Výsledkem této zkoušky jsou hodnoty vzorkem disipované mechanické energie v závislosti na poškození (šířce trhliny). Hlavním přínosem tohoto postupu je eliminace tuhých podpor, které při dynamické zkoušce mohou mít negativní vliv na přesnost dosažených výsledků. Princip zkoušky se tak mění z klasického silového na plně energetický přístup vyhodnocení odezvy materiálu. Nově navržené měřicí zařízení pak výrazně urychluje a zpřesňuje vyhodnocení experimentů. Pro lepší porozumění chování zkoumaných materiálů byly provedeny i kvazi-statické ohybové a tlakové zkoušky. Zkoumány byly celkem čtyři značně odlišné cementové kompozity v kombinaci s dvěma druhy výztužných ocelových vláken. Výsledky odhalily odlišné chování všech materiálů při rázovém zatížení. Dále byly popsány jisté efekty související se zvýšenou rychlosti deformace, které se lišily pro různé materiály a vlákna.

Klíčová slova: HPFRC, vysokohodnotný beton, cementový kompozit, vlákna, disipovaná energie, rychlost deformace, rázové zatížení, rázové kyvadlo

Abstract

High-performance fibre-reinforced cementitious composites subjected to impact loading are examined in this work. The main goal is the design, assembly and optimisation of the experimental apparatus and procedure to carry out the impact testing. The results of this experiment are the values of the mechanical energy dissipated by the specimen and tied to its damage (crack width). The main aspect of this procedure is the elimination of rigid supports, which could negatively affect the obtained results. The principle of the experiment then changes from the classical force-based to completely energetic evaluation of the material performance. The newly designed measuring apparatus greatly improves the speed and precision of the subsequent analysis. To better understand the material performance, quasi-static bending and compressive tests were also conducted. Four different cementitious composites in combination with two fibre types were examined. The results showed that the materials perform differently under impact loading. Next, several strain-rate related effects were identified, which were different between the materials and fibre types.

Keywords: HPFRC, high-performance concrete, cementitious composite, fibres, dissipated energy, strain-rate, impact loading, impact pendulum

Contents

Chapter 1

Introduction

Concrete is a material that has been extensively used by many generations. Its main advantages are well known. Use of the so-called ordinary concrete, made of just binder, aggregate and water, has seen a decline in the past decades in favour of more modern concrete, which incorporates more constituents, thanks to scientific advances. This modern concrete usually benefits from decreased water to cement ratio thanks to now common usage of high range water reducers. Since the microstructure of the cured concrete is directly tied to certain characteristics such as strength and durability, additional admixtures are added into concrete mixes. These might include fine particles of glass powder, silica fume, slag or fly ash. Some of these admixtures act as very fine fillers, to fill otherwise empty spaces between relatively large grains of cement, or they might also undergo chemical reactions and create new hydration products to further strengthen the concrete matrix in terms of mechanical strengths but even durability. Manufacturers of concrete are now able to tailor their product exactly to the needs of their customers, provided that they have sufficient knowledge of the effects of the various concrete constituents.

One major drawback of concrete, in general, is its low ductility and quasi-brittle mode of failure. This means that cracks can form relatively easily on the surfaces of the elements, and if the element is not reinforced, the cracks will quickly propagate until the elements completely fail. This is of course partially solved by introducing steel rods as reinforcement. The overall performance of the concrete element experiencing tensile stresses increases drastically. But cracking of the material still occurs. The reinforcement just stops the damage from expanding. Through these cracks, the environment can further degrade the concrete and eventually the reinforcement. This is especially a problem for structures that are loaded dynamically, for example, bridge structures, roads, but even buildings near roads, tunnels, etc. This behaviour can be further controlled by the introduction of reinforcing fibres. These fibres are usually much smaller than the traditional steel reinforcement, which means that they can provide tensile reinforcement in the entire volume of the material. This can prevent the cracks from forming entirely, or prevent further increases in the cracks' width.

Since the introduction of reinforcing fibres increases the ductility of concrete, it changes its mode of failure. The material is now able to absorb and dissipate much higher amount of mechanical energy before failure. This suddenly makes the fibre reinforced concrete a suitable material for applications where this ability

is desired. This might include all situations where a high energy dynamic loading is to be expected, for example, various barriers, protective structures either in the military or civilian sectors, industrial floors etc. Creating a composite material using the aforementioned constituents and/or the fibre reinforcement, results in concrete with improved parameters, compared to the ordinary concrete. Such material can then be called a high-performance concrete.

1.1 Aim of the research

In order to successfully employ the fibre reinforced concrete in real-life situations, it is necessary to be able to test and quantify its behaviour by determining certain mechanical parameters. If the materials are going to be used to withstand a sudden high energy loading, then the manufacturer needs to know how is the material going to perform. There are several ways to evaluate fibre reinforced concrete for this type of loading, which is going to be the topic of Chapter 3. This thesis aims to design an apparatus and testing method for determining the material's ability to absorb and dissipate mechanical energy, which is also going to be tied to a certain damage parameter. This, among other aspects, should be a key difference compared to, for example, the Charpy's hammer. Using this experimental method, several cementitious materials will be tested and their performance will be analysed.

1.2 Thesis structure

At first, a general introduction is made regarding the main principles of a high-performance concrete and the fibre reinforcement. It is beyond the scope of this work to provide a complete state-of-the-art and only the basic aspects are explained. Next, existing experimental methods for evaluating concrete subjected to high strain-rate loading are examined and their negatives are analysed. In the following Chapter 4, the impact pendulum is thoroughly described together with the newly designed measuring tools and analysis methods. This is one of the two main parts of this work. The second part is the experimental campaign, which is described in Chapter 5. At the end, the experimental results are presented, analysed and conclusions are drawn, together with the final evaluation of the presented experimental methods.

Chapter 2

High-performance fibre-reinforced concrete

High-performance concrete is a material that received significant attention in the past decades from both academic and industrial communities. Nowadays, it is probably incorrect to start describing a high-performance concrete as a new or emerging material. It has been extensively studied and the basic principles are well known. Right at the start, it is important to keep in mind, that a high-performance concrete is a broad term for a wide range of cementitious materials. In general, concrete is a high-performance type if it performs better compared to an ordinary concrete or a normal strength concrete. That is a somewhat vague definition, which is also apparent from the term itself. High-performance concrete is usually also a high-strength concrete, although a high-strength concrete is not automatically a high-performance type. Other characteristics of the material need to show a significant improvement as well. Aïtcin [1] argues that simply concrete with a water-to-cement ratio lower than 0.40 is already a high-performance concrete. Ratio this low signifies that certain admixtures were used to allow it to be this low, which results in a material with significantly improved mechanical characteristics. In general, high-performance concrete is a concrete type with high strengths, good durability, high modulus of elasticity and it is usually self-compacting as well.

Reinforcing fibres are another component that can be added to concrete to improve its characteristics. Doing so results in a composite material, where both parts, the concrete matrix and the fibres, work together. It is said, that fibres are usually used to control the formation and propagation of cracks [2]. That is certainly true, although high-performance fibre-reinforced concretes can also exhibit larger strengths compared to their unreinforced counterparts. Fibres drastically improve ductility of the material. This means that even after cracking, the concrete element can still perform its function and continue to do so even when large deformations are present. It is, however, important to note, that reinforcing fibres do not replace the standard steel rod reinforcement, which still needs to be present to provide a significant bending moment resistance to a concrete element. Both reinforcement types can be used together to fulfil different functions. Fibres can also be made from polymers, glass, basalt, aramid, carbon or natural materials and perform different functions than just increase strength or control cracking behaviour.

It is beyond the scope of this chapter to provide a detailed explanation of principles regarding high-performance concretes. Nevertheless, the following text will provide a basic introduction to the nature of the fibre-matrix interaction as that is an important mechanism responsible for increasing the mechanical characteristics of the composite. For the topic of this thesis, it is also important to highlight the behaviour of concrete when subjected to high strain-rate loading.

2.1 Applications

Fibre-reinforced concrete has been successfully used in many civil engineering projects. The particular uses are related directly to the benefits that fibres in concrete present. Improved mechanical properties are advantageous for example for bridge decks and overlays. Since traffic is loading the structures dynamically, there is a concern that a significant amount of cracks could form. This could significantly affect the durability of the structure, as bridge decks are also subjected to chemicals and the environment. Using fibres can prevent cracks from forming or prevent their further widening [3]. Fibres can also allow the design of thinner bridge decks as fibres increase the punching resistance [4]. Similar benefits are utilized in hydraulic structures, where fibres limit the water penetration into concrete and surface abrasion [5]. Limited penetration of chemically aggressive water is a reason fibre-reinforced concrete is considered for waste-water or agricultural applications [6]. Industrial concrete floors reinforced with fibres have increased impact and abrasion resistance as well as durability [7]. Combining the fibre-reinforcement with a high-performance concrete matrix is also advantageous in most of these applications.

Pre-cast concrete industry also uses fibre-reinforced concretes to create various products. The material is used for the same reasons as outlined above. In general, pre-cast concrete elements can achieve higher quality. It is easier to control the mixing, casting and curing processes. Fibres are added for creating thin concrete slabs for cladding, lining or decorative purposes. They can be used to make railway slabs or sleepers, tunnel lining and pipes [8]. High-performance fibre-reinforced concrete can be used for pre-cast slabs for ballistic protection or barriers.

High ductility of fibre-reinforced concrete can significantly improve the performance of structures under seismic loading. Beams and columns can either be prefabricated of cast in-situ. Fibres can decrease the need for regular steel reinforcement, especially in joints, where the seismic load causes the most damage. Fewer reinforcing rods allow for easier construction and can lead to higher quality casting as the concrete can be more easily compacted [9].

Fibres are also used in sprayed concrete or shotcrete mixtures. This is also supported by the fact, that there are several standards governing the fibre-reinforced sprayed concrete (see Chapter 3.1). The motivation here is similar as before - higher ductility, strength and even reduction or complete elimination of regular steel reinforcement, which needs to be prepared in advance. A properly designed material with fibres can also lead to a lower rebound [10].

There are of course more possible uses of fibres in concrete, other than increasing ductility or control cracking. Notably, the polymer fibres are used for improved fire resistance of tunnel lining, where they prevent explosive spalling. Thanks to the polymer's relatively low melting point, the fibres can melt to create empty spaces that relieve increasing pressure during a fire. Interestingly, even though fibres are used this way already, this mechanism is still not yet sufficiently explained and it is the focus of continued research [11].

It can be seen from this brief introduction of selected applications that fibres are used in concrete design in various areas. A significant portion of the applications is related to high strain-rate loading. Research communities worldwide are continuing to investigate the possible uses of fibres for more applications, especially when combined with (ultra) high-performance concrete matrices.

2.2 Interfacial transition zone

2.2.1 Concrete matrix

The interfacial transition zone (ITZ) is an area in hardened concrete in close proximity to inclusions. These are the aggregate particles but also fibres or reinforcing bars. The strength parameters of the ITZ are directly tied to the overall mechanical parameters of the entire material, including the effectiveness of fibre reinforcement. The strength of the ITZ is determined by the matrix composition. In normal strength concrete, when high water to cement ratio needs to be used, the ITZ might be the weakest part of the composite. Because of a local wall-effect, water concentrates more around the inclusions, therefore locally increasing the water to cement ratio. This results in larger pores in the ITZ, thus creating an area with low relative strength compared to the rest of the matrix and the aggregate. An example of ITZ can be clearly seen in Figure 1. The smooth dark areas are the aggregate surrounded by the cement paste. It can be seen that the paste itself contains different grains, most notably the white unhydrated cement particles and the black pores [1, 12].

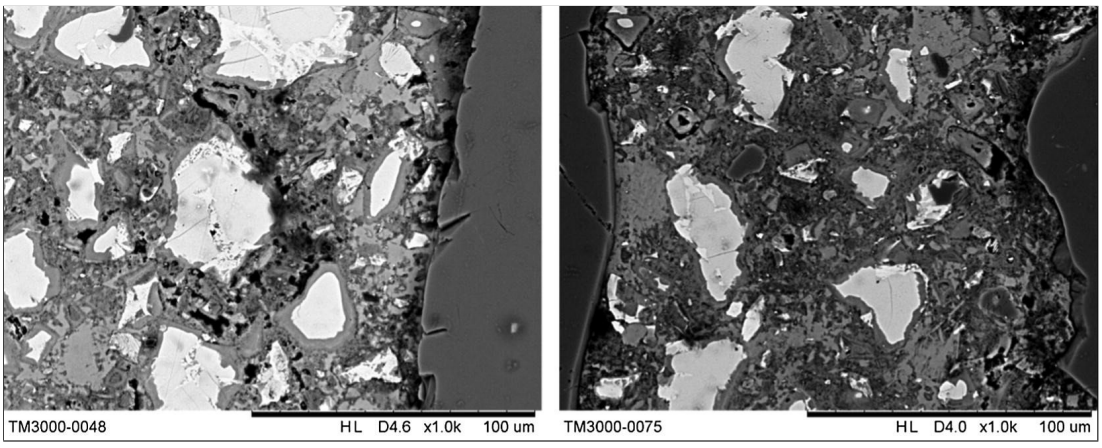

Figure 1: An example of the aggregate interfacial transition zone [12].

The ITZ can be made stronger using several methods. The first, that immediately presents itself, is to reduce the water to cement ratio. But for concrete using just cement and aggregate, that results in poor workability and the inability to achieve proper compaction. This behaviour can be improved by using water-reducing agents or high-range water reducers (HRWR). In the present, the HRWRs are commonly used even in normal strength concretes. This additive is responsible for breaking the cement particle clusters, that are forming because the individual particles possess an electrostatic charge. Breaking the clusters results in better workability of a fresh concrete without using additional water. This is of course a very simplified introduction to the principle of a HRWR as there are many more aspects related to its usability and how it reacts with concrete constituents [1].

When creating a high-strength or high-performance concrete, just applying an HRWR to strengthen the ITZ is not enough as the mixture needs to be further modified. This is done by using mineral admixtures. These admixtures can serve several purposes. One product of Portland cement hydration is portlandite ($Ca(OH)_2$), which doesn't contribute to the strength of the concrete and it can be dissolved in water, which causes durability issues. On the other hand, it is responsible for higher pH of concrete, which prevents further steel corrosion. Certain mineral admixtures can react with portlandite and create another calcium silicate hydrate (CSH) gels, which are the main product of cement hydration and are directly responsible for the material's strength. The most used mineral admixtures that can undergo these reactions are silica fume, fly ash, slag and glass powder [1, 13]. These materials can vary significantly in terms of chemical composition, reactivity and particle distribution and geometry. Especially the silica fume consists of extremely small spherical particles. It can fill spaces between much larger cement particles, provide better workability and also fill the ITZ. Other mineral admixtures work similarly in different particle size ranges. The ITZ can be significantly improved using mineral admixtures. It can be denser, therefore made much stronger. Figure 2 shows examples of a high-performance concrete matrix, where the aggregate ITZ is indistinguishable from the rest of the cement paste.

Using special curing regimes can also contribute to stronger ITZ and the rest of the matrix. The most common method found in literature is the heat curing [14–17]. It is applied for preparing an ultra-high performance concrete. Specimens are usually demoulded after 24 to 48 hours and immediately placed in a closed environment with a temperature of 90°C. They remain here for 2 to 3 days. Specimens are either cured in hot water or in steam. This process accelerates the chemical reactions and results in a higher density of the matrix including the ITZ.

2.2.2 Fibre anchoring

The ITZ also forms around fibres in a concrete matrix. The same principles as described above for the aggregate ITZ also apply in this case, including the methods of increasing the ITZ's strength. This means that improving the mechanical parameters of an unreinforced concrete matrix will also create a material where

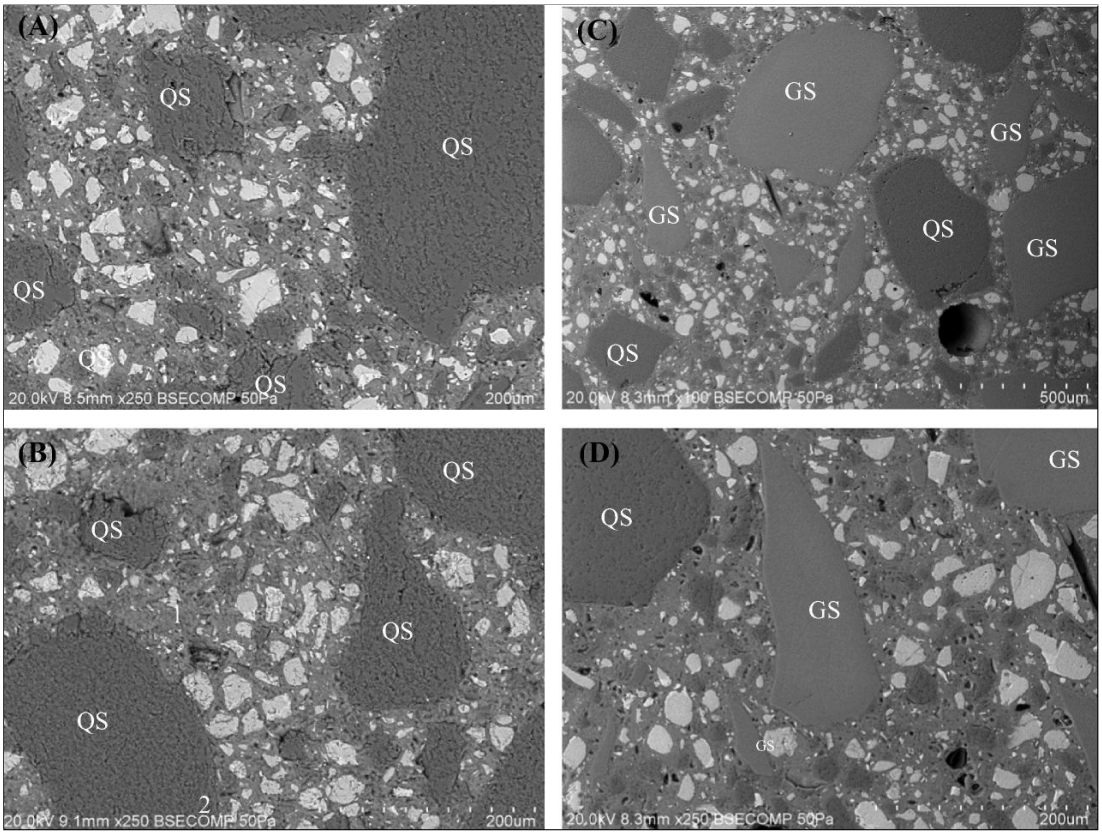

Figure 2: An example of the interfacial transition zone in high-performance concrete [18]. QS is quart sand, GS is glass sand.

fibres can be more effectively anchored. Figure 3 shows an example of a fibre ITZ. The fibre diameter is 0.2 mm. The unhydrated cement particles as well as pores can be observed here. Figure 4 shows the surfaces of multiple steel fibres. The surface of an unused fibre is clearly very smooth without defects. The surface of a fibre that has been pulled out of a cement paste shows cuts and grooves as it was scratched by the paste. There are traces of the paste on the surface of the fibre, but it is negligible. When silica fume was added to the mixture, it significantly improved the ITZ and even after the fibre was pulled out from the matrix, it clearly still has a layer of hydration products attached to its surface. This indicates, that the matrix around the fibre must have been significantly damaged in order to pull the fibre out, which required larger force. On the other hand, friction was the main anchoring principle in the case of a plain cement paste. This leads to a fact, that only relatively large steel fibres (with large surface area) can be effectively anchored in a normal strength concrete. These fibres are also modified by adding hooks on their ends, or they can be twisted to increase the needed pull-out forces. Using smaller fibres is beneficial as the resulting material can be more homogeneous thanks to a larger number of fibres. But small steel fibres can be effectively utilized only in (ultra) high-performance matrices. These fibres are usually straight, but modified geometry is also possible [18–20]. Examples of fibres can be seen in Figure 5. The following text will discuss fibre reinforcement further in terms of its mechanical interactions with the matrix during loading.

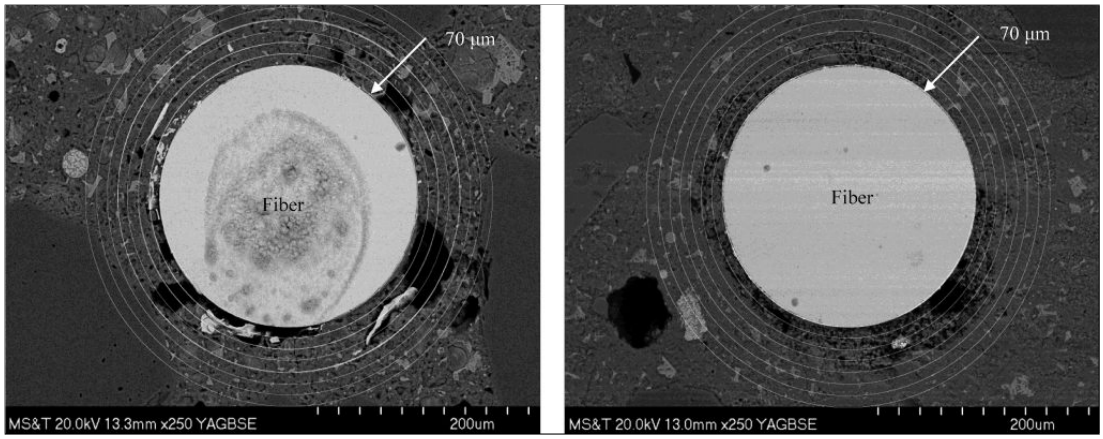

Figure 3: An example of the fibre interfacial transition zone [19].

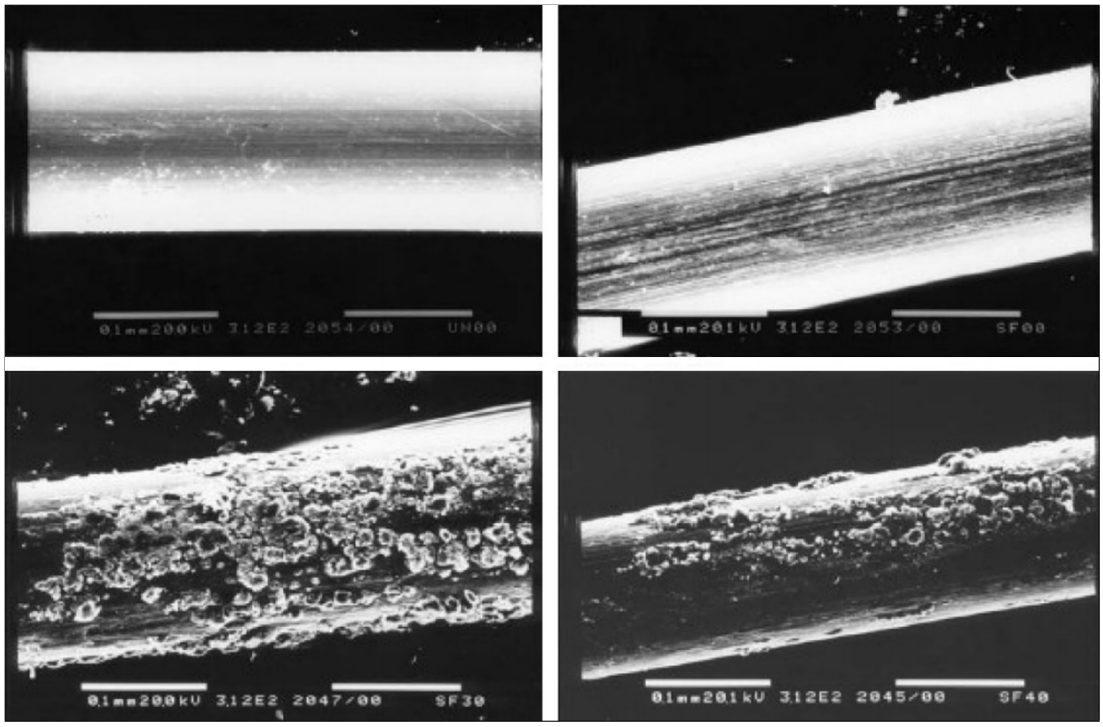

Figure 4: Steel fibre surfaces. Top left - unused fibre. Top right - fibre pulled from an ordinary concrete matrix. Bottom images - fibres pulled from a matrix with silica fume [20].

2.3 Fibre-matrix interaction

This analysis is focused on steel fibres or other fibre materials, which are primarily chosen for significantly increasing strengths and energy dissipation capacity of hardened concrete. For example, polymer fibres would behave differently, but those kinds of fibres would not be primarily added for the same purposes. A hardened fibre-reinforced concrete undergoes multiple stages regarding the fibre-matrix interactions when load is gradually applied. The first stage is when the load is relatively small, no cracking occurred yet and fibres are still bonded to the matrix. This situation is illustrated in Figure 6. The lines indicate elastic deformation of the matrix, which is partially constrained by the stiffer fibre. Interfacial shear

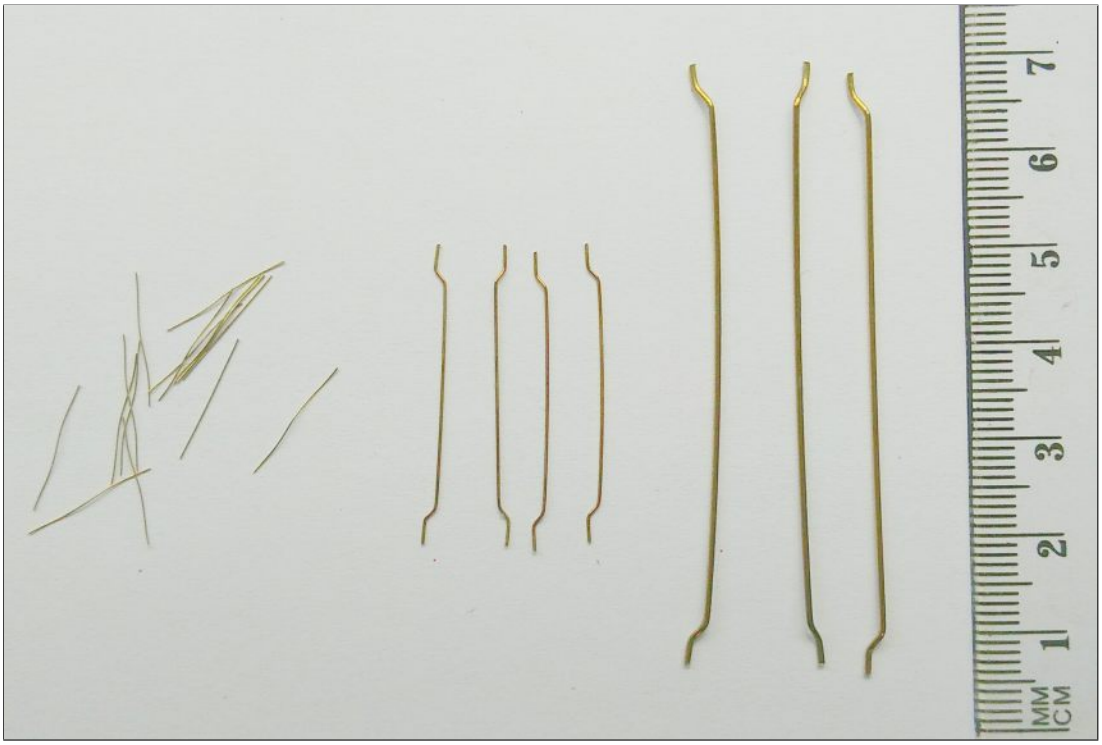

Figure 5: Examples of steel fibres. Straight micro-fibres and hook-ended macro-fibres with zinc coating.

stress develops in the ITZ, with a maximum at the fibre's ends. With an increase in load, several situations might occur. The bond could completely fail or the fibre could break before the matrix. These outcomes are highly improbable when ordinary fibres are used in a concrete matrix. Prior to the matrix cracking, the interface would either remain in an elastic state or partial debonding might occur at the fibre's ends. This debonding would activate a frictional slip mechanism, which means that the fibre would be starting to slip in the matrix, but shear stresses would still develop at the interface due to friction [10]. This stage before the tensile crack initiation is arguably of little interest as reinforcing fibres are usually added to improve the post-cracking behaviour. However, in some cases, the modulus of rupture (appearance of the first tensile crack) of the concrete element could be noticeably higher compared to unreinforced case [21]. It is clearly desirable to design the composite, so that the elastic bond is maintained as long as possible, at least up to the modulus of rupture.

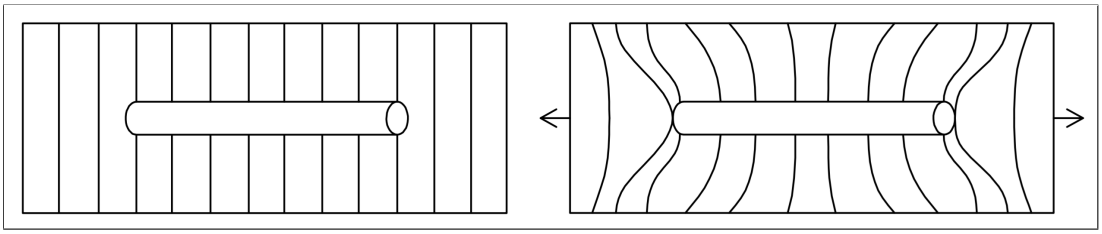

Figure 6: Elastic bond behaviour of a fibre embedded in a concrete matrix [10].

The fibres are going to drastically change the composite behaviour after the initiation of the first tensile crack. At this point, an unreinforced concrete would fail. Fibres start to bridge the cracks, keep them from widening and keep the concrete element from breaking apart. Figure 7 shows possible fibre behaviour during matrix cracking. When the fibre-matrix bond is strong and relatively weaker fibre material is employed, the fibre might break before being pulled out from the matrix. This situation would result in lower ductility of the composite. Depending on the specific point of fibre failure, the crack-bridging effect would not be applied and the overall composite would not reach its full energy-dissipating potential. This behaviour is not desirable. The second case shows a fibre being pulled from the matrix. This is the ideal behaviour (when aiming for energy dissipation capacity and ductility), especially when the tensile stress developed in the fibre is close to its tensile strength, which implies a sufficiently strong matrix. The whole element exhibits good ductility. Frictional slip is the main principle of energy dissipation. Prior to this, the fibre would undergo elastic deformation, as it is still firmly bonded to the matrix. That is shown in the third case. The fourth case shows another non-ideal behaviour when a complete de-bonding occurs and fibre loses contact with the matrix, which won't activate the frictional slip principle. This complete de-bonding is initiated from the crack surface and propagates further along the interfacial area. The last two cases show fibres at the tip of the crack, where they would usually be in the elastic phase, although the surrounding matrix is starting to develop tensile damage [10, 22].

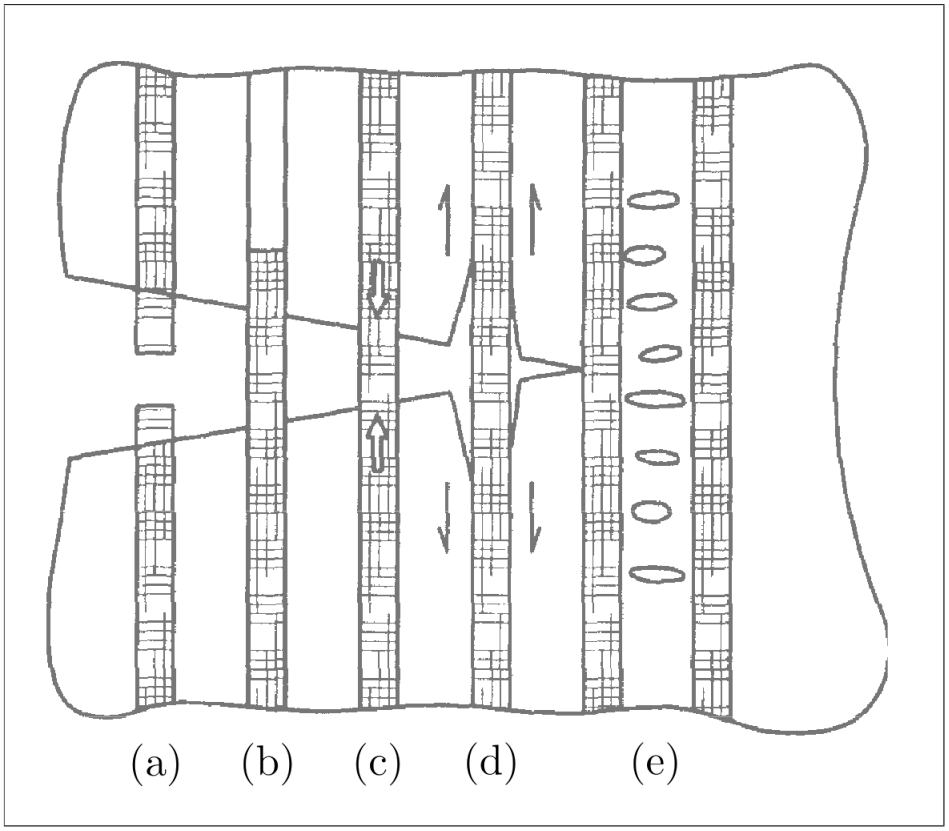

Figure 7: Fibre behaviour after concrete cracking - (a) fibre tensile failure (b) fibre pull-out (c) elastic bridging (d) gradual bond failure without friction (e) matrix cracking [22].

Using fibre pull-out experiments, it is possible to further analyse the fibre-matrix interaction. Figure 8 shows a typical force-slip (-displacement) diagram of a pull-out experiment of a straight fibre. Numbers 1 to 3 on the diagram show important points and regions that correspond to the schematic on the right. Small pull-out load results in elastic deformation of the fibre and a linear diagram curve. The curve becomes non-linear when de-bonding starts to appear at the fibre-matrix interface. This is indicated by the purple outline. It can be seen that it starts from the element surface, where the interfacial stresses are the highest, and continues along the fibre length. The de-bonded part is where the fibre starts to slip. A peak pull-out load is achieved at a point right before de-bonding occurs along the whole length of the fibre. Frictional slip mechanism is now fully activated in place of the elastic bond. Three possible situations might occur when the displacement is increased. In an ideal situation, the frictional slip will be linear until the fibre leaves the matrix, which is rather non-realistic. The matrix is likely to degrade along the interface, hairline cracks will form or the fibre surface will be damaged which results in lower friction and slip softening will be observed. Another possibility is the slip hardening, which could be expected if the damage developed along the interface results in increased friction [10, 23].

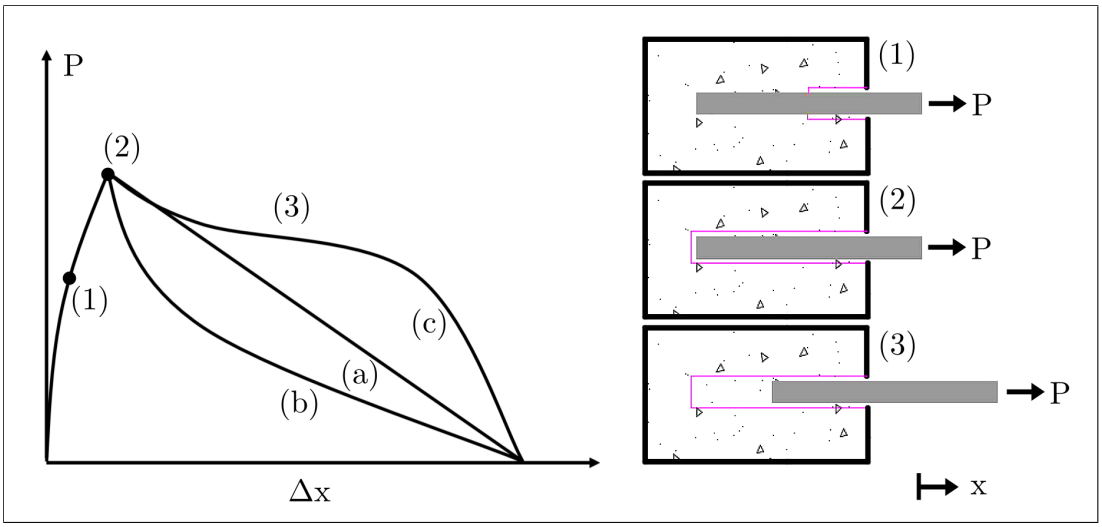

Figure 8: An example of a force-slip diagram of a fibre pull-out - (1) partial friction bond activation (2) complete fail of elastic bond (3) frictional fibre pull-out (a) ideal frictional slip (b) slip softening (c) slip hardening. After [10, 23].

Figure 9 shows possible failures of the fibre-matrix interface. Bond failure would be expected in normal strength concrete, while the matrix failure in close proximity of the fibre can be expected with certain high-performance matrices. This was also presented in Figure 4 as the hydration products are present on the pulled-out fibre surface. If de-bonding occurred at the fibre surface, the frictional slip could be expected to approach the ideal frictional slip as seen in Figure 8. However, lower peak pull-out forces will be observed. Matrix failure situation, on the other hand, should exhibit a higher peak pull-out force. The frictional bond would be between two rough faces of a damaged matrix which would experience further damage with increasing fibre slip. The bond would then decay faster and exhibit slip softening [23].

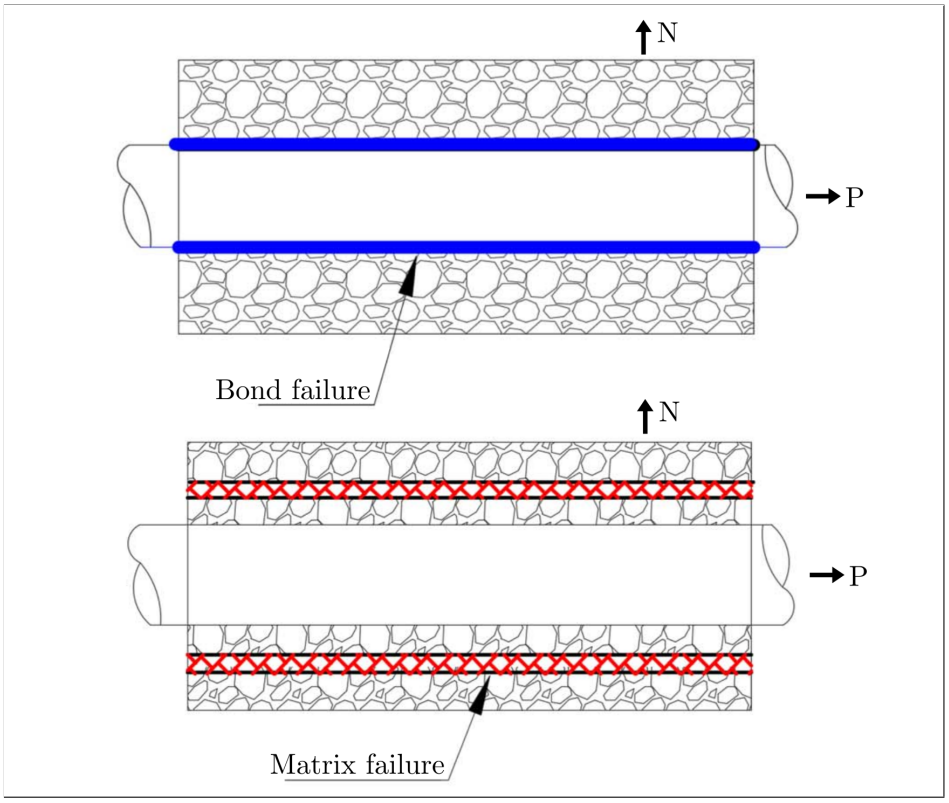

Figure 9: Possible modes of interfacial failures [23].

Friction at the fibre-matrix interface can only develop if the matrix pushes against the fibre. This creates normal stresses (compression) at the interface, which are directly responsible for the frictional forces during fibre pull-out. The normal stresses develop mainly due to the volume changes of the matrix. Shrinkage of the cement paste during curing is one example. The normal stresses can also be caused by external loading of the whole concrete element. Concrete matrices designed for low shrinkage, or even no shrinkage as a result of expanding admixtures, are not suitable for efficient fibre reinforcement.

During fibre pull-out, tensile strains develop in the fibre that are much larger than in the surrounding matrix. Due to the fibre's Poisson's ratio, the diameter of the fibre will decrease, thus lead to decreased normal stresses or even introduce tension at the interface. Further loading the fibre may also lead to its plastic deformation, which further decreases its diameter. This effect is dependent on the ratios between the elastic moduli of the fibre material and the matrix. In unloaded concrete element, a steel fibre will not be compressed by the matrix as much as a polymer fibre would be. The normal stress would then be much larger, which would lead to higher frictional forces as well for steel fibres. In an extreme scenario, when the normal stresses are low, the fibre-matrix elastic bond can fail in tension instead of shear. The frictional slip mechanism would not be activated in this case and the fibre would be pulled-out with negligible force. If the fibre material cannot withstand the normal stresses, it can fail longitudinally, but this situation is unlikely and would be preceded by very poor composite design [17, 23].

Since in fibre-reinforced composite fibres are oriented randomly, research has also focused on the pullout behaviour of inclined fibres. The pullout forces now introduce additional stresses in the concrete matrix perpendicular to the pullout direction. As seen in Figure 10, this can damage the matrix near its surface. The part of the matrix that is damaged this way cannot provide any anchoring for the fibre, therefore, this behaviour is undesirable. If the matrix spalling does not occur, it means it is strong enough to withstand the additional stresses. Inclined fibre will be more difficult to pull out, as larger frictional forces will be present on the matrix-fibre interface. Larger stresses also develop in the fibre itself, since the fibre needs to bend, depending on the angle. If the fibre is stiff (carbon, certain steel), then the stresses could be too large and the fibre might break before the complete pullout. Stiffer fibre also makes the matrix spalling more likely. Soft fibres (polymers) would usually bend easily, therefore their effectiveness with increased inclination could be much more significant. All of this greatly depends on the matrix composition. In any case, the ideal behaviour is achieved when a complete pullout of the fibre is accomplished without matrix spalling or fibre breaking [10, 24, 25]. This is an important fact that needs to be respected during the material design phase if an efficient material is to be created. The matrix needs to be able to fully utilize the potential of the fibres and vice versa. On a side note, this is a good example which shows that a fibre-reinforced concrete truly is a composite material. It combines the characteristics of each component and results in a material with greatly improved performance.

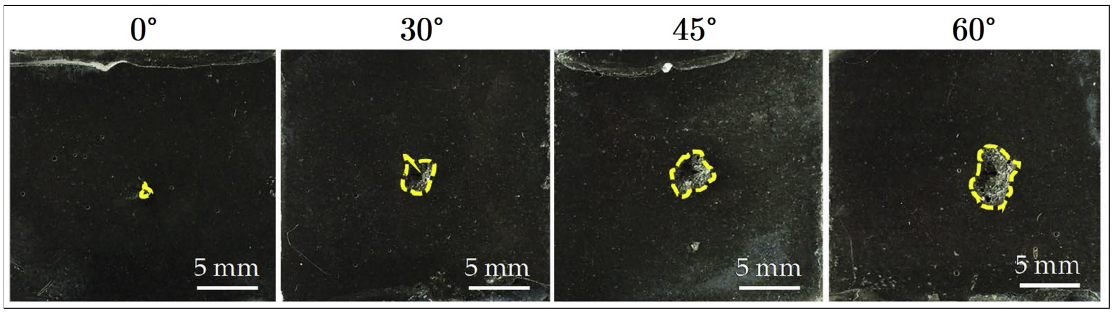

Figure 10: Matrix spalling with increasing fibre inclination [25].

2.4 High strain rate loading

2.4.1 Introduction

Loading a material results in its deformation - strain. As load changes, so does strain, therefore we can define the strain-rate as a time rate at which strain changes. Strain-rate's unit is an inverse time (s^{-1}). Figure 11 shows a logarithmic axis with values of strain-rate and loading situations, that usually invoke these values in the loaded materials. The area of interest of this thesis lies approximately around 10^0 s^{-1}. This is a region of a low-velocity impact which might be caused, for example, by a car crash, debris impact or other situations. It can be seen, that high strain-rate loading is usually caused by sudden and unexpected events.

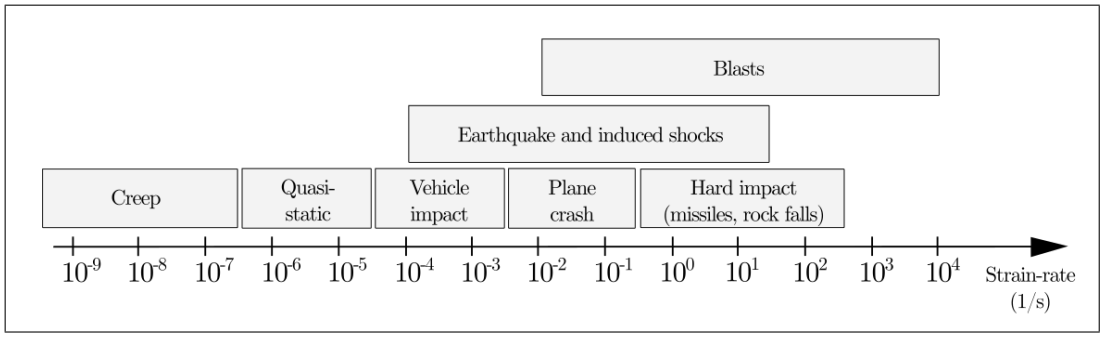

Figure 11: Strain-rates and related loading situations. After [26].

When concrete is subjected to this kind of fast loading, it behaves differently compared to the standard quasi-static loading. One way of quantifying this difference is by using the dimensionless dynamic increase factor (DIF) value. It is calculated by dividing the value of a material characteristic measured at a certain higher strain-rate by a value of the same characteristic measured at a quasi-static strain-rate. Examples of DIF values for compressive and tensile strengths for various strain-rates can be seen in Figure 12. It can be seen, that especially tensile strength of concrete can be significantly different at intermediate strain-rates. However, it is important to understand, that one experimental method cannot be applied over several orders of strain-rates. In other words, a standard quasi-static hydraulic press cannot be used for impact loading rates, impact loading apparatus cannot be used for blast loading rates etc. Considering strain-rate as the only variable of the DIF is, therefore, not correct as there are more variables either tied to the specific material behaviour (cracking behaviour, stress wave propagation) or the testing method (loading, measuring methods). Although this is probably just a problem of interpretation. The author believes the usage of DIF is correct, although it must be emphasized, that it is a comparison of not just the material characteristic, but also other parameters, as mentioned earlier. This will be discussed further in chapter 3.3 where experimental methods for high strain-rate testing will be introduced.

2.4.2 Concrete matrix

There are several factors that contribute to the behaviour of concrete under high strain-rate loading. Min et al. [28] conducted a series of splitting tensile strength experiments at strain-rates ranging from 10^{-7} s^{-1} to 10^{-4} s^{-1} using one concrete type. They measured DIF values up to 1.5. Tested specimens were further examined, especially their fracture patterns and failure surfaces. It was clear, that specimens tested at higher strain-rates showed smoother failure surfaces as the crack propagated even through stronger aggregate grains (Figure 13). The authors attribute this behaviour to the release of strain energy. When the load is applied relatively slowly, the strain energy is irreversibly dissipated when the material starts forming stable micro-cracks near existing cracks (the result of shrinkage or other effects not related to the loading). When the material is subjected to higher strain-rate, these micro-cracks do not form. The energy is released all at

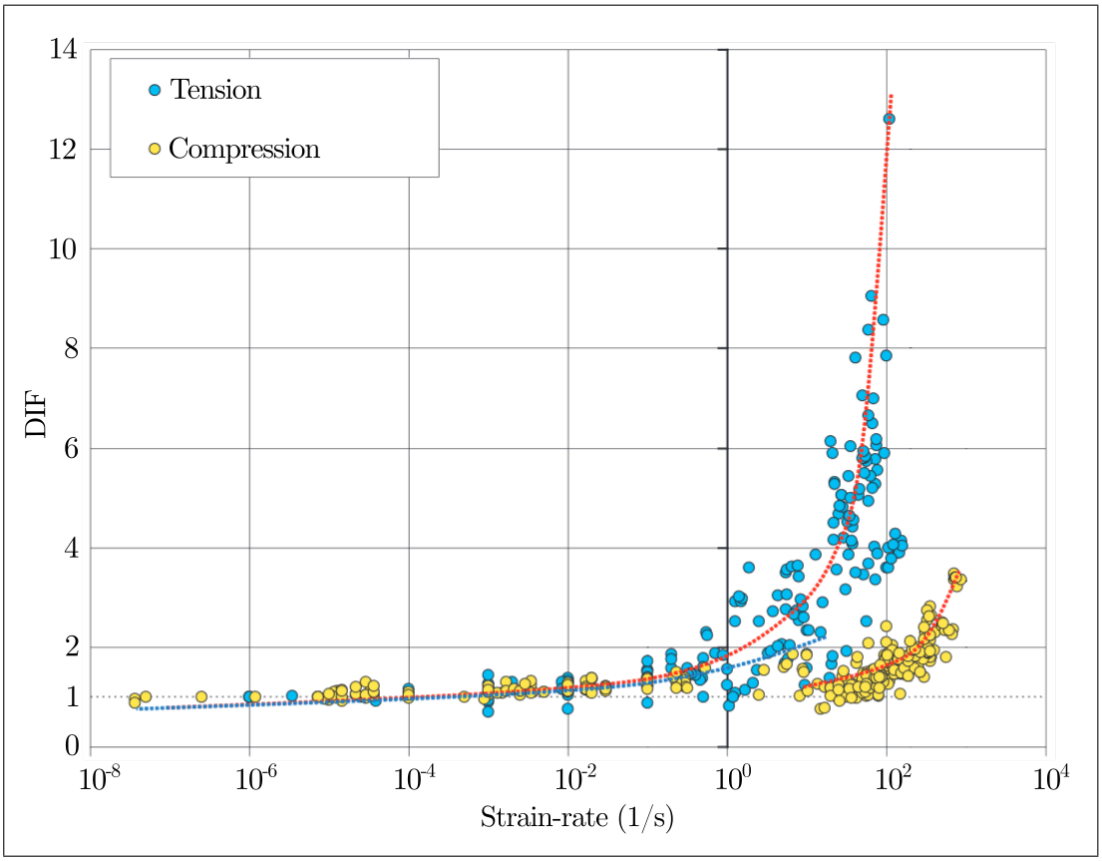

Figure 12: Examples of DIF values for various strain-rates. After [27].

once when the maximum stress is achieved. The amount of energy is then sufficient to cause damage even to stronger parts of the matrix, such as the aggregate grains. This then leads to the main crack propagating on a relatively straight path and the resulting failure surface is smoother. Strength of the concrete is measured higher at higher strain-rates as a result of this cracking behaviour. In this particular study, relatively low strain-rate values were used, which allowed the researchers to use one experimental method (a standard hydraulic press).

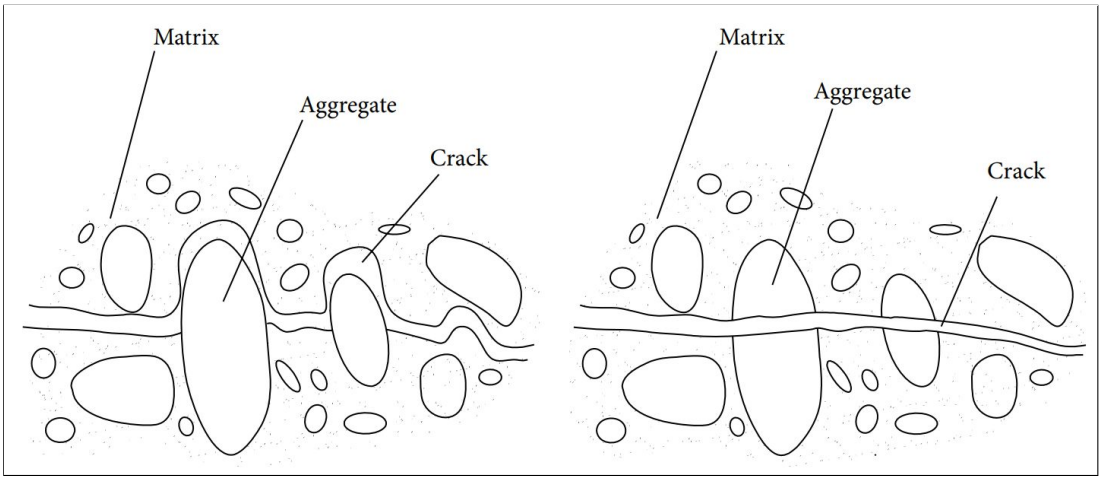

Figure 13: Crack propagation at quasi-static (left) and elevated (right) strain-rates [28].

When testing materials subjected to high-strain rate loading, the effect of inertial forces and finite stress wave propagation velocity must be considered. This is, in some cases, not related to the material itself, but to the concrete specimen size, geometry and other physical effects tied to the nature of high-strain rate loading. Nevertheless, these effects could significantly affect measurements and might lead to an incorrect conclusion regarding the material's behaviour. On the other hand, if a concrete element is subjected to high strain-rate loading, its response would be an inseparable sum of the material reaction as well as other physical effects. But it is clear, that for research purposes, we must strive to understand these effects separately to be able to design materials and estimate their behaviour with sufficient knowledge. In the following text, the other physical effects, not necessarily specific only to concrete, will be introduced.

Effects of inertial forces were thoroughly explained by studies conducted by Ožbolt, Sharma et al. [29], Ožbolt, Sharma and Reinhardt [30] and Bede et al. [31]. They especially focused on the inertial forces that are generated by the quasi-brittle nature of concrete, which starts to develop damage before complete failure of the material. This behaviour activates additional [1] inertial forces that can be significant for high strain-rates. They used a simple finite element model to illustrate this effect. The model is an object made by a cohesive and an elastic elements connected in series. The free end of the cohesive element is fixed and forms the support, while the opposite end (free end of the elastic element) is loaded by prescribed constant motion. A rate-sensitive microplane material model was employed. The cohesive element represents a volume of a concrete specimen that develops damage. This would be the interfacial transition zone, which is the area that essentially governs the strength of the material. Figure 14 shows the relationship between the measured loading force and reaction force in time for various strain-rates. For the low strain-rate, it can be seen that both the reaction and loading forces are almost identical. However, when strain-rate is much higher, the loading force drastically differs from the measured reaction force.

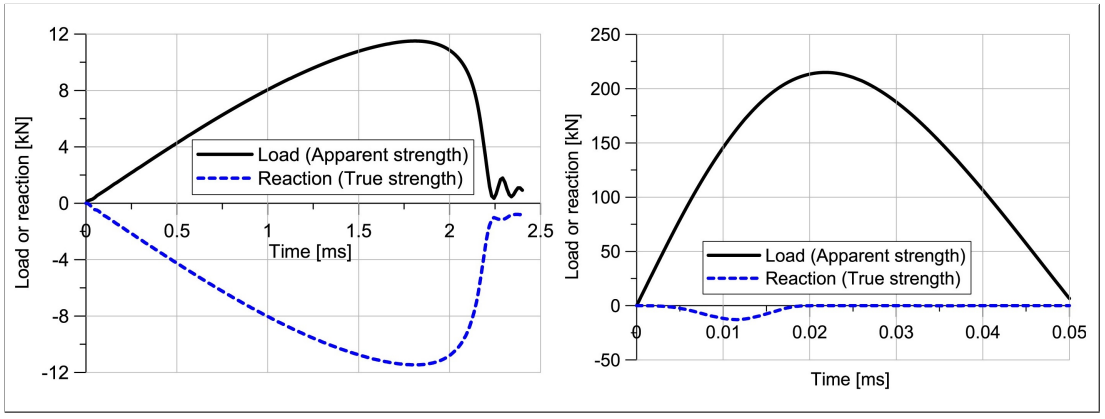

Figure 14: Force-time diagram of a simulated tensile loading test for 0.2 s^{-1} (left) and 200 s^{-1} (right) [30].

[1] The word 'additional' emphasises, that these inertial forces are activated on top of the macro-behaviour of the accelerating volume of concrete. Inertial forces are activated as a result of the acceleration of mass, as per the definition of the second law of motion. This is of course independent of material. But the effect described here is typical only to quasi-brittle materials.

In the first case, the load is applied much slower compared to the stress wave propagation velocity. The support can immediately react to the applied force, i.e. a static equilibrium is formed throughout the test, even when the cohesive element develops damage. On the other hand, when the load is applied much faster, the stress wave reaches the cohesive element, which starts to soften before the reaction forces start to rise. The interface between the cohesive and elastic elements start to accelerate as a result of the softening of the cohesive element. This activates a significant inertial force, that counteracts the loading force. The stress in the elastic element is, therefore, much larger than in the cohesive element. But the cohesive element is, in this case, representing the actual quasi-static concrete behaviour, which means that the reaction force represents the true strength of the material. But more often than not, the loading force is the force that is interpreted as the true strength, which it clearly is not. The authors argue, that for very high strain-rates and various testing methods, the results should be reviewed and interpreted more carefully. The effects of inertial forces should be eliminated, either by the testing method principle or by the subsequent results analysis. The problematic area can be seen back in Figure 12, where the tension DIF values exhibit a steep rise, which is probably due to the inertial effects. It is clear, that this damage-related inertial forces phenomenon is dependent on the size and shape of the material. It is also significantly higher for normal-strength concretes, where the damage zones are larger, i.e. the volume of the ITZ is larger.

Another explanation of the increasing strengths is the Stefan effect. When a viscous layer (water) is present between two objects, then separating these two objects requires higher force with higher separating velocity. This force can be expressed as

$$F = \frac{3\pi r^4 \eta v}{2h^3} \tag{1}$$

for two circular plates with a diameter r moving from each other with velocity v, separated by a layer with thickness h and viscosity η. It can be seen, that the force will significantly increase with a thinner interlayer. Higher viscosity, separating velocity and plate size will increase the force as well. This effect is, therefore, responsible for increased forces when pores and capillaries filled with moisture are present on a failure surface. Vegt and Weerheijm [32] investigated the moisture content effect on tensile strength of concrete at various strain-rates. DIF value for a strain-rate in the order of 10^1 s^{-1} was determined to be 8.4 in the case of the water-saturated specimen. The dried specimen exhibited significantly lower DIF of 2.8. For the same strain-rates, they also analysed the fracture energy of concrete and measured a DIF value of 5.4 for a dry specimen. This is already significantly higher fracture energy compared to a quasi-static case. But for a saturated specimens, they measured DIF of 15.9. However, for lower strain rates in the order of 10^0 s^{-1} the saturated specimens exhibited tensile strength and fracture energy closer to the dried specimens. It should be noted, that saturated specimens showed worse quasi-static performance. In other words, the DIF values were larger for saturated specimens, but partially because the base quasi-static value was lower. This shows that simply looking at the DIF values is incorrect, as the absolute mechanical parameters are also important.

2.4.3 Fibre behaviour

Similarly to fibre-matrix interactions, the fibre behaviour during high strain-rate loading can be examined by the pull-out experiments. Table 1 summarizes selected pullout experiments data available in literature. It shows which fibre type was used regarding the shape and diameter, displacement loading rate, dynamic increase factors (peak load and dissipated energy) and compressive strength of the concrete matrix used. Based on the compressive strength it can be seen that (ultra) high-performance concrete matrices were evaluated. All presented studies show that both the peak loads and energy needed to pull a single fibre out of the matrix are strain-rate dependent. However, the actual DIF values vary greatly between the studies. This can be attributed to the significant differences between the experimental procedures. Practically all experimental parameters, including the concrete composition, loading rates, measuring apparatus or specimen geometries, are different between the studies. Comparability of results is, therefore, difficult. This is a similar problem which is discussed throughout this thesis - lack of standardization in regards to high strain-rate testing and the possible influence of the testing/measuring system. This means that the experimental data could be partially influenced not just by the material variations, which should be the only variable.

It is also interesting, that certain observations or conclusions that were made for one study might not apply for a different study. This might be, again, contributed to material composition or the testing procedure. For example, Abu-Lebdeh et al. [37] concluded that pullout of straight fibres exhibits strain-rate insensitivity, which is in disagreement with data presented in Table 1. Especially data provided by Tai et al. [35] show the highest strain-rate sensitivity for straight fibres. Kim et al. [38] reported that hook-end fibres exhibit strain-rate insensitivity which is, yet again, in contradiction to other studies. An important observation was made by Park et al. [34]. They used a shrinkage reducing agent in one of their matrices. As was explained earlier, shrinkage of concrete plays an important role in creating an internal pressure that contributes to better anchoring of fibres. This principle was confirmed, as not only the quasi-static peak load was lower, but also the DIF values were lower for this matrix. These results might also indicate, that the strain-rate sensitivity of a (straight) fibre pullout is raised by the strength of the matrix. Tai et al. [35] suggested that this might indeed be true, as a denser, ultra high-performance concrete exhibits the creation of more cracks along the fibre-matrix interface during fibre pullout. And, as was explained earlier, the crack formation behaviour in concrete is one of the causes of strain-rate sensitivity.

All of the presented results so far were obtained from pullout experiments of fibres aligned with the pullout direction. Experimental data also exist for inclined fibres and higher strain-rates. Although, inconsistent conclusions are present here as well. Results comparison is again difficult as the testing parameters differ, as outlined above. For example, Yoo and Kim [25] reported that non-straight fibres, when inclined, achieved significantly lower DIF values during high-strain rate loading compared to straight fibres. The absolute values of peak forces and

Table 1: Summary of selected literature results for fibre pullout experiments.

Source	**Fibre type** ⌀(mm)	**Load rate** (mm min^{-1})	**DIF** Peak load	Energy	**Comp. str.** (MPa)
Cao et al. [33]	Hooked (0.375)	50	1.03	1.17	156.0
		500	1.12	1.28	
		1000	1.22	1.46	
Park et al. [34]	Straight (0.3)	10	1.50	1.43	200.0
		100	2.38	2.10	
	Straight (0.3)	10	1.63	1.74	188.9[a]
		100	1.52	2.03	
Tai et al. [35]	Straight (0.2)	1080	1.25	1.26	184.9
		10800	1.74	1.89	
		108000	2.11	2.04	
	Straight (0.4)	1080	1.13	1.20	
		10800	1.21	1.27	
		108000	1.47	1.34	
	Hooked (0.38)	1080	1.01	1.22	
		10800	1.32	1.27	
		108000	1.55	1.64	
	Twisted (0.5)	1080	1.21	1.38	
		10800	1.53	1.36	
		108000	2.02	1.36	
Xu et al. [36]	Straight (0.2)	150	1.10	1.10	194.0
		1500	1.19	1.03	
	Hooked (0.38)	150	1.07	0.95	
		1500	1.01	0.95	
	Half-Hooked (0.38)	150	1.18	1.26	
		1500	1.28	1.24	
	Twisted (0.3)	1500	1.14	1.43	
Yoo et al. [24]	Straight (0.3)	20760	1.38	1.72	128.1
		29238	1.79	1.80	
		21720	1.58	2.29	151.1[b]
		51834	1.97	2.89	
		22986	1.97	2.06	140.6[c]
		45348	2.55	2.40	
Yoo and Kim [25]	Straight (0.2)	18954	2.02	2.25	>150
		30666	2.86	2.40	
	Hooked (0.375)	25542	1.50	0.25[d]	
		55626	1.49	0.28[d]	
	Half-Hooked (0.375)	22806	1.99	2.00	
		54462	2.60	2.34	
	Twisted (0.3)	18930	2.00	1.41	
		56202	2.40	2.03	

[a] shrinkage reducing agent
[b] expanding agent 4%
[c] expanding agent 8%
[d] fibre broke before complete pullout

total absorbed energies were also lower for all inclined non-straight fibres during high strain-rate loading. This was partially caused by the fibres (or matrices) breaking before the complete pullout. Only for a 60° inclination the straight fibres showed worse performance for all loading rates. Xu et al. [36] tested hooked-end inclined fibres and reported a significant increase in DIF values compared to straight fibres. The problem of fibre or matrix failure with inclined fibres is present in other studies as well [24, 34, 35]. A general conclusion is that a high strain-rate loading is only going to increase the stresses in the fibre and the matrix. If the fibre anchoring is strong or made even stronger because of the fibre geometry then a premature failure is more likely. Comparing DIF or other values from different studies between aligned fibres (when a complete pullout was achieved) and inclined fibres (when a premature failure occurred) is possible, although inconclusive. The authors themselves also acknowledge the fact that in a concrete element, where multiple fibres are being pulled-out during crack-bridging, an individual fibre would most probably behave differently compared to a controlled experiment of a single fibre pullout.

2.5 Mechanical characteristics

2.5.1 Previous research

Figure 15 shows the load-deflection diagrams (four-point bending of beams, quasi-static) for a high-performance concrete reinforced with various amounts of straight steel fibres. These results were obtained in a previous research [21, 39] using a material designated as DM later in Chapter 5.1. The left graph shows the detail of the lower deflection values. Here we can observe the elastic and strain hardening regions and the peak force. For the lowest two percentages, the amount of fibre reinforcement is insufficient to raise the peak force, which is still governed mostly by the concrete matrix. In those cases, the behaviour is elastic until a brittle failure occurs and a sudden drop in force is measured [2]. Until this point, the fibres have a limited effect on the performance of the composite regardless of fibre dosage. Insufficient fibre reinforcement leads to unstable crack propagation, which is accompanied by a sudden release of a significant amount of mechanical energy. A specialised testing apparatus needs to be employed so that this energy release does not cause a sudden rise in deflection, which is apparent here for the lowest percentages. Smaller unstable drops in force are also present for higher percentages. This might indicate a non-homogeneous fibre dispersion or other material defects. The highest fibre dosage eliminates these issues. The strain-hardening region is negligible for the 0.125 % and the sudden drop is immediately followed by a strain-softening phase. Together with rising percentages, more tensile cracks form that are bridged by the fibres. This leads to a pronounced strain-hardening phase, especially for the two highest fibre percentages. The point of peak load is usually

[2] This point is also the point of failure for an unreinforced (ultra) high-performance concrete, which behaves similarly to other brittle materials. Certain mixtures, as well as normal strength concretes, exhibit a quasi-brittle behaviour in flexure. In compression, concrete usually exhibits more pronounced quasi-brittle behaviour.

a point when the crack formation stops and the main crack starts propagating next, which is the strain-softening phase. Strain-softening ends between 20 mm to 25 mm of deflection for all fibre percentages because it is mostly determined by the fibre length (13 mm in this case) which was constant.

An interesting observation can be made regarding fibre reinforcement efficiency. It can be seen, that the longest strain hardening phase is not achieved for the highest percentage, but for the 1 %. Also, the peak force does not drastically increase between the 1 % and 2 % as it does between the 0.5 % and 1 %. This indicates a certain fibre saturation region, which is most probably matrix specific. This particular mixture already showed poor workability for the 2 % volume of fibres, although researchers have reported using much higher percentages with different mixtures. In this particular case, the 1 % fibre volume seems like an ideal amount for maximum increase in mechanical properties in regards to the economy of the mixture (steel fibres are the most expensive constituent).

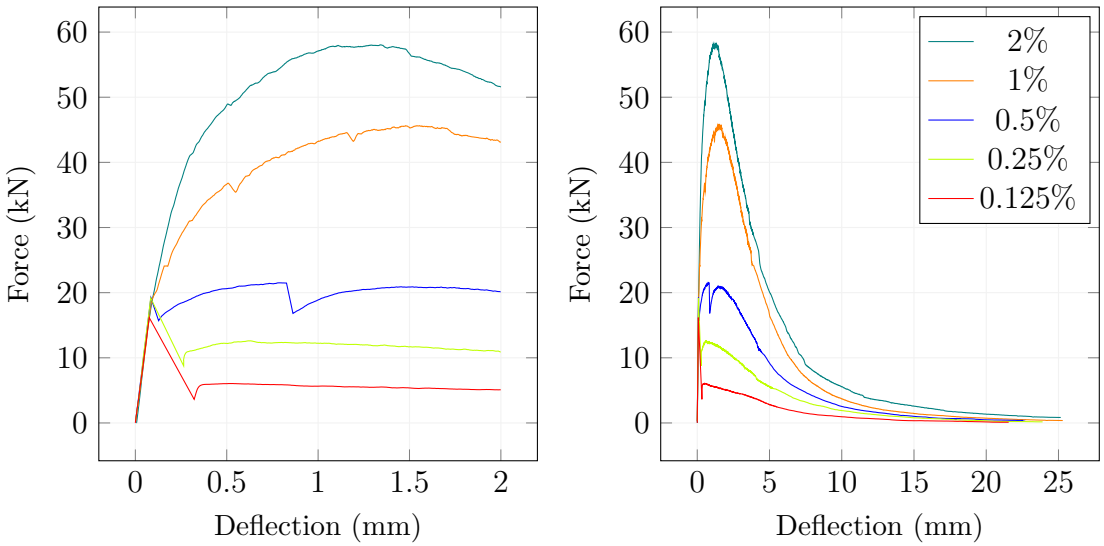

Figure 15: Typical load-deflection diagrams of a four-point bending tests on a high-performance fibre-reinforced concrete [21].

Figure 16 shows the mechanical energy absorbed during the four-point bending experiments from the previous Figure. This graph shows that the post-peak performance is crucial in terms of energy dissipation. Approximately 50 % of mechanical energy was absorbed around 4 mm of deflection, which was already well into the strain-softening region for all fibre percentages. Compared to an unreinforced material, even the smallest percentages drastically improve the energy dissipating capacity. The peak forces for all percentages were achieved at relatively small deflection values. Energy absorbed up to this point was small compared to the total absorbed mechanical energy. This proves the importance of the post-peak performance of a fibre-reinforced concrete in regards to energy dissipation. In practical applications of various energy-absorbing elements, the ultimate strength of the material is not so important. In static conditions, the material should be loaded in the elastic region anyway, i.e. utilizing only the strength of the matrix. During an extreme loading event, such as crash, explosion or earthquake, the energy needs to be absorbed by the crack formation and prop-

agation. Ideally, after the load energy has been dissipated, the element should still be able to perform its static function. If we assume that the element is statically loaded around 50% of its elastic phase, then similar forces are achieved well into the strain-softening region, after the majority of energy has been dissipated. Therefore, it should be possible to design elements with enough energy absorbing capacity to safely contain the effects of extreme unexpected loading conditions. It is expected, that the element would be replaced after such an event, as the deformations are irreversible.

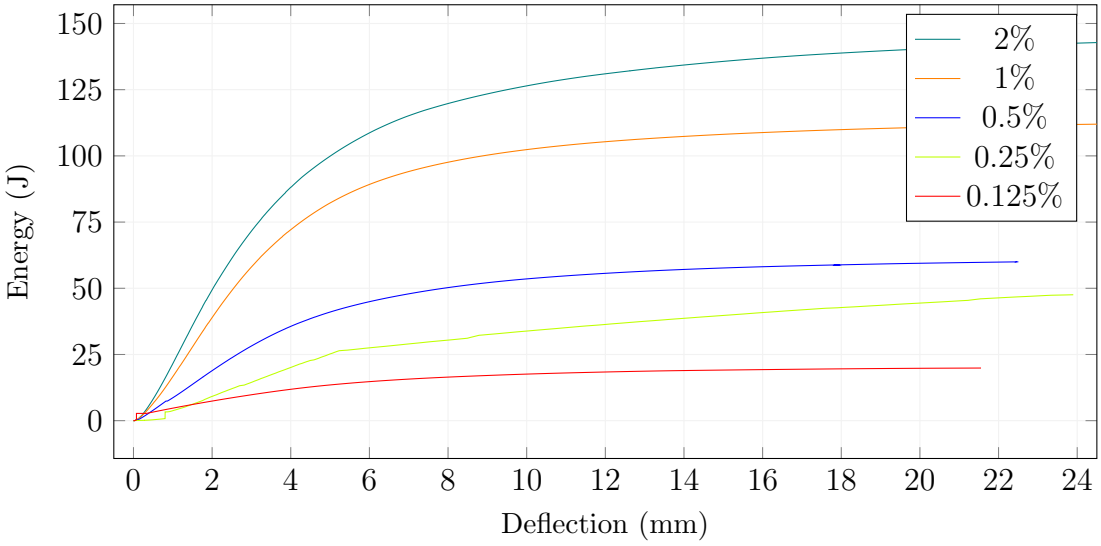

Figure 16: Energy absorbed during four-point bending experiments [21].

Figure 17 compares the results obtained in [21, 39] for quasi-static and impact experiments. The quasi-static results are the same as presented in Figure 15. Even though this direct comparison is not accurate, as different experimental methods must have been used, it clearly illustrates the differences between the loading rates. Lower fibre volumes showed negligible differences between loading rates, unlike the higher percentages. The higher spread of results for the impact loading especially at higher percentages was caused by a much more varied damage pattern between the specimens. The number of developed cracks significantly varied and the main tensile cracks propagated at various distances from the middle of the span. That is partially a reason why research in this thesis uses notched specimens.

2.5.2 Literature overview

Mechanical parameters of high-performance concretes have been extensively studied in the past decades, so a plethora of experimental results are available in the literature. In this subsection, only a brief summary of mechanical characteristics relevant to this thesis is presented. Since a broad range of mixture designs can be classified as high-performance concretes, it is difficult to make accurate summaries regarding the fibre reinforcement and its benefits. In general, fibre reinforcement introduces significant strain-hardening and strain-softening behaviour after the initial elastic phase. Ductility, tensile and flexural strengths increase dramatically. An example of flexural strengths increases is in Figure 18. An almost

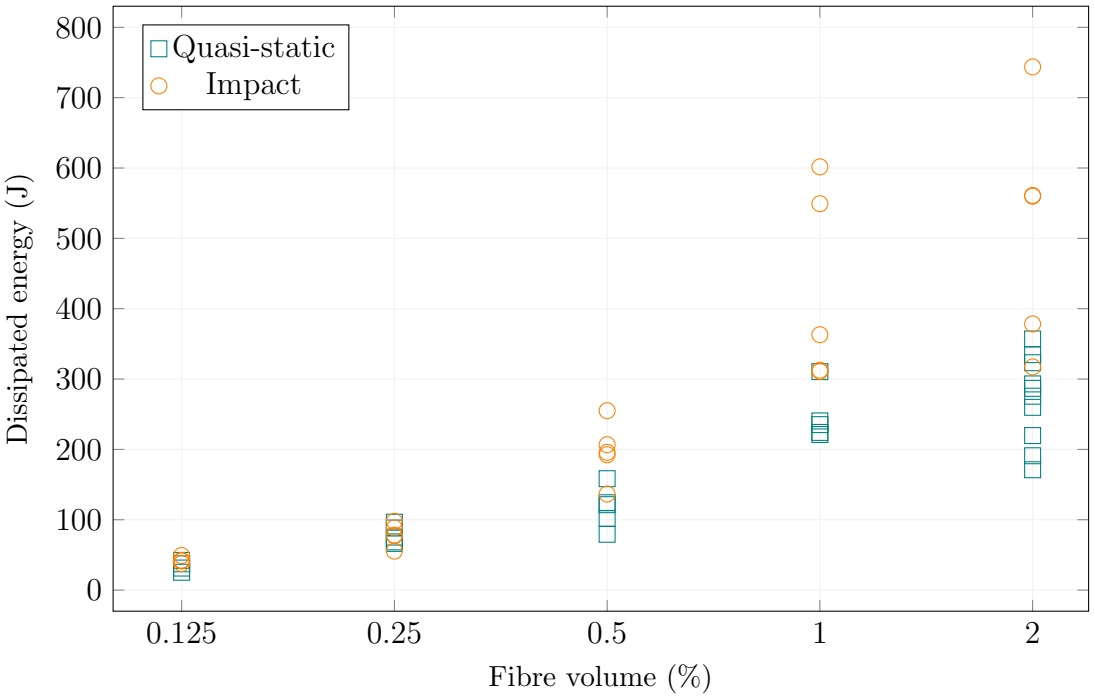

Figure 17: Comparison of energy absorption between the quasi-static and impact loading for various fibre volume contents [21].

linear increase can be observed here, which is only possible thanks to a matrix optimised for very high fibre content. However, just like with the results presented from the previous research, the optimal fibre content is not the maximum value, but probably the 3 % volume. Compressive strengths are only slightly affected by the fibre content. Depending on the matrix, certain volumes of fibres might lead to a small decrease in compressive strengths as the compressive strengths are mostly influenced by the material homogeneity [17].

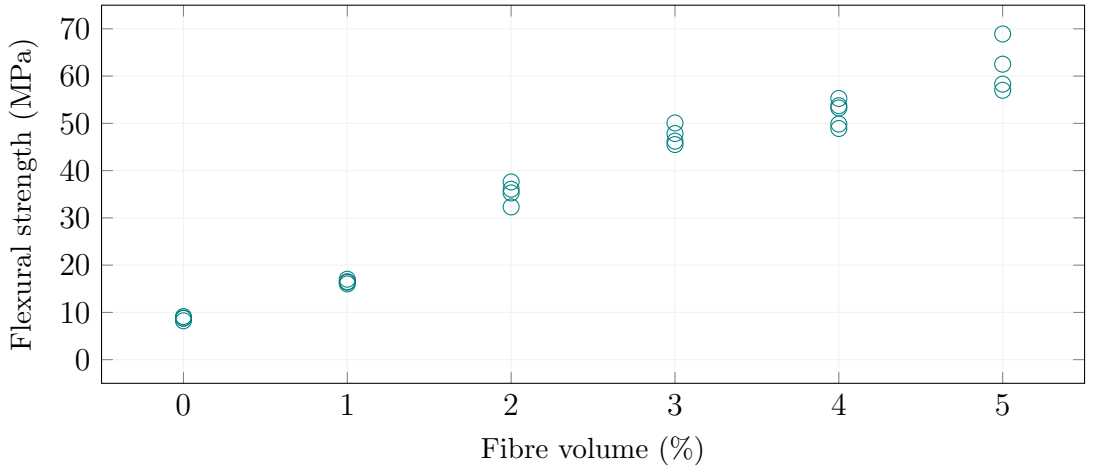

Figure 18: An example of flexural strengths with increasing fibre content [17].

Fibre dispersion and orientation play a crucial role in the overall performance of a fibre-reinforced concrete element. Figure 19 shows how the flow of the fresh material influences the orientation of fibres. In this particular case, it is a situation in a beam-like mould where the material was poured in one place from which it freely flowed to the rest of the mould volume. Fibres tend to orient parallel with the flow. The flow velocity is highest in the centre, which is where the forces that act on the fibres are also the highest. Towards the sides, the fibres are also oriented, but mostly due to the wall-effect, as most fibres are more likely to be parallel rather than perpendicular to the wall. Zhou and Uchida [40] studied the effect of fibre orientation. They made large slabs from which they cut several small beams that they tested for flexural strengths. Some beams were cut parallel and some perpendicular to the flow. Beams with preferred orientation showed as much as ten times the flexural strength. Clearly, the effect of material flow can only apply for materials that achieve certain high flowability of the fresh mixture. In the author's own experience, some concrete mixtures, especially with high fibre content, show almost no flowability and need to be vibrated for optimal compaction. In those cases, the fibre orientation and dispersion is mostly random.

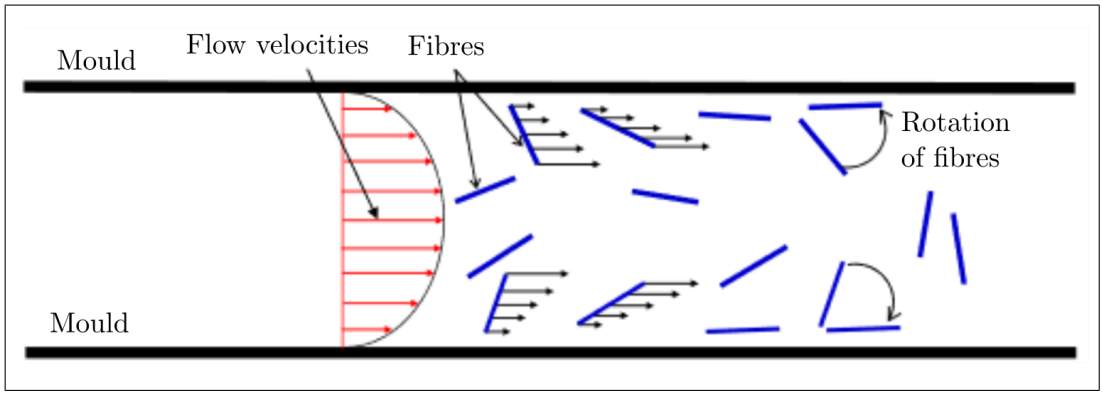

Figure 19: Fibres orientation due to the fresh concrete flow [41].

Chapter 3

Testing of fibre reinforced concrete

The testing procedures related to normal strength concretes are well known, agreed upon and mostly standardized. High-performance and fibre-reinforced concretes could behave similarly when subjected to certain standardized testing procedures. However, when investigating the tensile and flexural characteristic, they usually exhibit significantly different behaviour, which calls for a modification of the usual experimental methods. Also, there needs to be completely new testing procedures for a fibre-reinforced concrete to fully understand its potential. Since high-performance fibre-reinforced concretes are not new materials, several testing standards exist.

One of the biggest improvement that a (high performance) fibre reinforced concrete offers over an unreinforced and normal strength concrete is its ability to absorb and dissipate mechanical energy. This creates a need to test this ability and also examine it when the load is applied at various rates, apart from the quasi-static one. The previous chapter already introduced the behaviour specific to concrete that is responsible for changes in mechanical characteristics depending on the strain-rates. But the actual effects of strain-rate on the overall material performance depend on so many factors that general conclusions often inaccurate. Making these conclusions is made even more difficult, as no standardization currently exists for high strain-rate testing of concrete. This means that several different methods are used, each with their own possible problems.

This chapter is going to focus on various testing methods to determine characteristic relevant to a fibre reinforced concrete. The following text is intended to provide a summary of selected European standards, briefly introduce them and mention some of their worldwide counterparts. To the best of the author's knowledge, these standards are active at the time of writing this thesis. Next, selected novel experimental methods for determining various parameters of fibre-reinforced concretes will be introduced. This includes parameters of the fibre reinforcement, such as fibre orientation and dispersion. The main focus of this chapter is going be on high strain-rate loading, as that is the main topic of the subsequent experimental part of this thesis. Several experimental principles currently used worldwide are going to be described together with their possible shortcomings.

3.1 Standards

There exist several standards defining the basic specifications of fibre-reinforced concretes. These standards focus not only on testing of hardened concrete but also on, for example, specification of the fibres, manufacturing and fresh concrete properties. The general goal of standards is to provide a guideline on how to approach certain processes so that they are carried out the same way between different manufacturers or laboratories. That is the necessary step to ensure the comparability of acquired data. For the purposes of this thesis, highlighting certain aspects defined by the standards can also serve as a summary of areas related to fibre-reinforced concretes that are important to note for subsequent research. In other words, certain standards could be viewed as a summary of the most important aspects related to a given subject, either as a result of scientific advances or industrial experience.

3.1.1 Specifications and manufacturing

The European standard EN 14889-1 (Fibres for concrete - Part 1: Steel fibres - Definitions, specifications and conformity) [42] defines parameters related to steel fibres. Manufacturers of steel fibres are required by this standard to declare fibre characteristics such as manufacturing principle, geometry and strength. Manufacturers should also provide information on how their fibres affect concrete in terms of the workability of the fresh mixture and of course the strength of hardened concrete. It is safe to assume, that one type of steel fibres will affect these concrete properties differently for different mixtures. That is why a related standard EN 14845-1 (Test methods for fibres in concrete - Part 1: Reference concretes) [43] defines reference mixtures that are used to evaluate the fibre effects. This standard does not provide a specific mixture design in terms of precise constituent contents, but it defines parameters that either the fresh mixture of the hardened concrete needs to meet. This relatively vague definition is most probably necessary because strictly defined input materials might not be available everywhere.

3.1.2 Fresh concrete

Parameters of the fresh fibre-reinforced concrete are defined by a Czech preliminary standard ČSN P 73 2451 (Fibre-reinforced concrete - testing of fresh fibre-reinforced concrete) [44]. It is important to note, that the standard specifically states that it should not be used to evaluate fresh self-compacting high-performance concretes. A standard for those kinds of concretes, to the best of the author's knowledge, does not exist in the Czech Republic. This standard is intended to expand the family of European standards EN 12350 (Testing fresh concrete). In general, it prohibits the use of certain methods common to unreinforced concretes and specifies modifications of existing methods. Properties of fresh concrete that are usually tested are slump or slump-flow, compaction, air content or bulk density.

Another parameter that can be determined using fresh concrete is fibre content. This type of measurement is usually conducted as part of quality control in a large-volume production, to confirm correct fibre dosage. Standard EN 14721 (Test method for metallic fibre concrete - Measuring the fibre content in fresh and hardened concrete) [45] describes a method, during which an exact volume of fresh fibre concrete is prepared and weighted. Fibres are extracted from this volume by washing away the fresh concrete matrix. The remaining fibres are dried and weighted to calculate the fibre content. This is called the wash-out method. It is also specified by other standards, such as the Australian RC 377.01 [46] or the Japanese JSCE-F 554 [47]. This method is also defined for hardened concrete, where the fibre extraction is of course more difficult.

3.1.3 Hardened concrete

Testing hardened concrete is probably the most important part of the whole testing process, as it gives us the mechanical parameters used to design concrete elements and structures. Since fibres in concrete greatly improve its tensile behaviour, the standards focus more on this area of testing. The Czech preliminary standard ČSN P 73 2452 (Fibre-reinforced concrete - Testing of hardened fibre-reinforced concrete) [48] expands the family of standards EN 12390 (Testing of hardened concrete) to include methods for fibre-reinforced concretes. Determining the compressive strength is the same as for concrete without fibres, but the flexural testing is significantly different. The specimen is a prism 700 mm × 150 mm × 150 mm, which is relatively large. A four-point bending setup is used with the load applied in one-thirds of a 600 mm span. Typical behaviour of a fibre-reinforced concrete is the ability to withstand loading forces even after the concrete matrix cracked. The testing machine must be stiff enough to not be affected by a possible sudden drop in the specimen's stiffness after the crack formation. The standard then described the necessary output data, for example, various points in the load-displacement diagram and subsequent calculations. The standard does not directly mention it, but it is clearly not intended for high-performance fibre-reinforced concrete. The specimen size would be unnecessarily large for smaller fibres and also the expected post-cracking behaviour mentioned in the standard is typical for relatively ordinary concrete matrices reinforced with large steel fibres.

A similar setup for a flexural strength test is described by the EN 14488-3 (Testing sprayed concrete - Flexural strength (first peak, ultimate and residual) of fibre reinforced beam specimens)[49]. It also considers a four-point bending experiment, however, the specimen size is 75 mm × 125 mm × 500 mm and it must be cut out from a large slab of sprayed fibre-reinforced concrete. The span between supports is 450 mm.

The Japanese standard JSCE-G 552 [50] also describes a four-point bending experiment, but it allows different sizes of the specimens. If the fibre length is higher than 40 mm, then the specimen width and depth must be 150 mm, if the fibre length is lower than 40 mm, the specimen can be smaller with a cross-section of 100 mm × 100 mm. The span between supports is 3 times the width. The same

two specimen geometries are stated by the American standard ASTM C1609 [51]. These standards better reflect the possible fibre sizes. Deflection is measured by displacement gauges placed on a steel fixture in the middle of the specimen's height. This applies to all the mentioned standards. An example of a four-point bending setup is in Figure 20

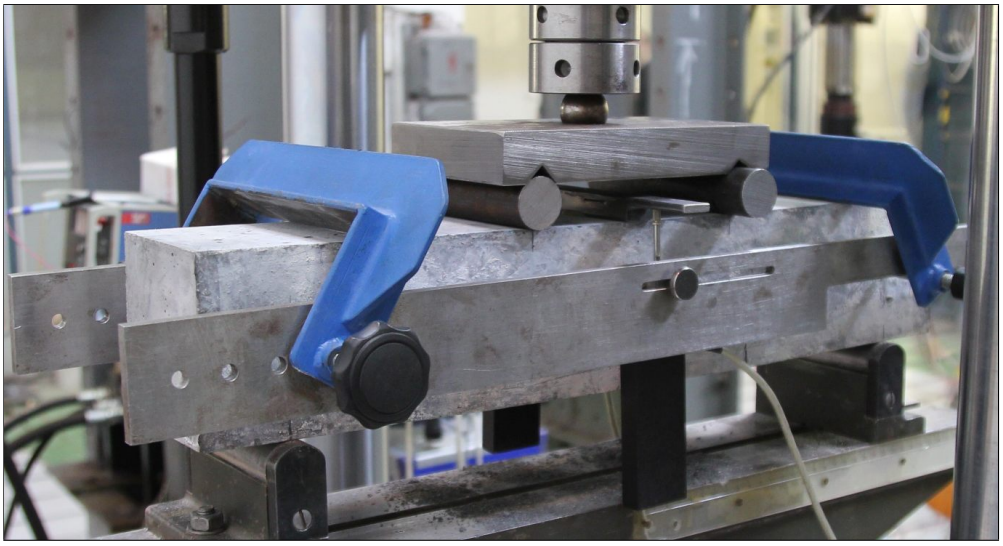

Figure 20: A typical four-point bending setup [21].

A different approach is outlined in the European standard EN 14651 (Test method for metallic fibered concrete - Measuring the flexural tensile strength (limit of proportionality, residual strength)) [52]. It describes a three-point bending setup using notched specimens. The specimens are the same size as described earlier for the ČSN P 73 2452, but the span between supports is 500 mm. The standard recommends measuring the crack-mouth opening displacement (CMOD) of the notch, but it also allows a displacement measurement, which can then be calculated to obtain the CMOD. A limit of proportionality (LOP) is obtained from the experiment, which is the equivalent of flexural strength, but it needs to be calculated using the true height of the specimen, i.e. height minus the notch.

It is worth noting, that this standard probably also expects testing of a relatively ordinary type of concrete reinforced with long steel fibres and not a high-performance concrete with small fibres. The standard describes the LOP as the maximum stress achieved but only to a CMOD of 0.05 mm. If the maximum load occurred after this CMOD value, then the stress is calculated based on the loading force at CMOD equal to 0.05 mm regardless of the actual maximum force. For an ultra-high performance fibre-reinforced concrete, the LOP value would therefore be meaningless, as the maximum force is usually achieved well after the first cracks appeared on the specimen. Similar problems can be seen for the previous standards as well. It can be seen, that the standards strive to analyse the material by providing ideally a single value, that can be used for designing purposes. It is the author's belief that this approach is not applicable to many types of modern concretes, as their behaviour is significantly different compared to normal strength concrete, even those reinforced by long steel fibres.

The American Concrete Institute issued a report 544.2R-89 [53], where they describe an impact resistance testing method, which uses a cylindrical specimen, which is being loaded by a repeated impact to its centre. Figure 21 shows the configuration of this experiment. The steel ball transfers the impact force from a drop-weight (not shown) into the specimen, so that the diameter of the ball is kept constant between different drop-weight machines. The specimen is simply resting on a rigid support. No physical quantities are measured during the experiment, only the number of blows. This can be used to roughly compare different materials for their ability to withstand the impact load.

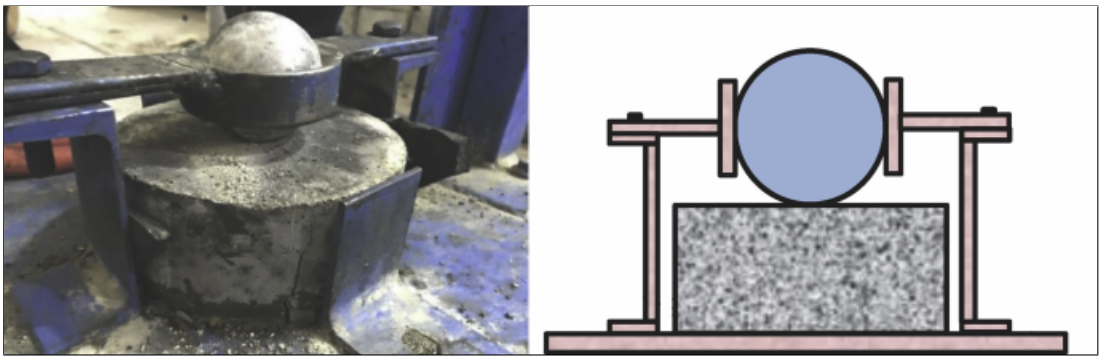

Figure 21: A setup of the impact resistance experiment [54].

3.2 Non-destructive and semi-destructive test methods

As was explained in Chapter 2, the fibre content, orientation and distribution of the individual fibres plays a crucial role in determining the final mechanical parameters. If enough past experience is available with a particular fibre reinforced concrete, then it is possible to estimate the behaviour of the concrete element based on the knowledge of the actual fibre parameters. Using a non-destructive method is convenient, as the test can be conducted quickly without damaging the tested element. This is useful in regular quality control of for example pre-cast products or as a diagnostic tool. But non-destructive methods can, in general, suffer from poor correlation between the measured physical quantity and the material's mechanical parameters. Care must be taken to have a sufficient amount of data (usually acquired from destructive testing) to statistically prove, that there is a consistent correlation. Semi-destructive methods can offer better correlation, but the drawbacks are apparent - the tested element is damaged. For maximum precision, a destructive method needs to be employed, which gives us the mechanical parameter directly. A destructive method is, for example, the impact pendulum measurement, which is at the core of this thesis. At the end of the impact pendulum experiments, there is a destroyed specimen and the experimental data. But for fibre reinforced concretes, there could be several non-destructive and semi-destructive test methods to estimate these results (with varying degrees of precision) beforehand.

3.2.1 Magnetic properties

One possible non-destructive approach to evaluate the quality of fibre reinforcement is magnetic probing. This principle only applies to steel fibres or theoretically to any fibre that will react to a magnetic field. There are several configurations available. One method is, without much detail, introduced in an older Japanese standard JSCE SF7 [55]. It shows a transformer-like apparatus, which has a primary and a secondary coil on a hollow circular core. An alternating current is applied to the primary coil and depending on various parameters, including the quality of the core, a current develops on the secondary coil. This secondary current changes, when a cylindrical fibre reinforced concrete specimen is put inside the core. The permeability of the concrete matrix (hardened or fresh) is negligible compared to the metal fibres, so only the fibres will be responsible for any change in the secondary current. The standard introduces this method to evaluate only the fibre content in the specimen. The specimen can be either a fresh concrete in a plastic container or a hardened specimen, for example, a core specimen. The measured current cannot be used to calculate the fibre parameters, but it can be compared to other results obtained from destructive testing.

A similar non-destructive method was proposed by Torrents et al. [56]. They created several single coils with various parameters, such as the uniformity of windings and the number of windings of copper wire. The coil was wrapped around a rectangular base, which allowed the insertion of a concrete cube 150 mm in size inside the coil. They conducted an inductance measurement of the coil first without the specimen to obtain the base inductance. Then they inserted the specimen and conducted measurements along all 3 axes of the specimen. Since they used the same cube for these 3 measurements, the total amount of fibres inside the specimen was constant. Therefore, the variations in inductance after the specimen was turned must have been the result of the fibre orientation. If a fibre is positioned parallel in the direction of the applied field it will alter the inductance of the coil. Perpendicular orientation results in much lower inductance change. Using this method, the authors could estimate the amount of fibres with an accuracy better than 5 kg/m^3 and determine in which axis did the fibres align more preferably. It is clear, that the fibre material and geometry plays an important role. Data obtained and calibrated for one type of fibre cannot be used for a different type. But this limitation is typical for most non-destructive methods.

3.2.2 Image analysis

Image analysis can be considered a semi-destructive method. It is intended to evaluate the fibre parameters such as orientation and dispersion in one plane of a specimen. This plane needs to be prepared by cutting a concrete specimen, for example, a core specimen or laboratory specimen. A camera picture of this plane is then taken, while the camera is perpendicular to the cut plane. Lighting needs to be applied so that the cut fibres are reflecting this light into the camera, which makes them brighter than the rest of the concrete matrix. A brightness threshold is applied to the image, to make the brightest areas appear white and

the rest of the area black. Examples of such images can be seen in Figure 22. A special algorithm is then applied, which identifies a white area and fits an ellipsoid to its circumference. These ellipsoids will have different ratios of their axes based on the fibre orientation. If the ellipsoid is a circle, then the fibre is exactly perpendicular to the analysed plane. Since the centres of these ellipsoids are also known, the fibre distribution can be analysed [57]. This method can be easily applied for specimens that have been already destroyed in tensile or flexural strength experiments. The image analysis principle is relatively simple and easy to conduct if the computer algorithm is available. A major disadvantage is that only a single plane is analysed.

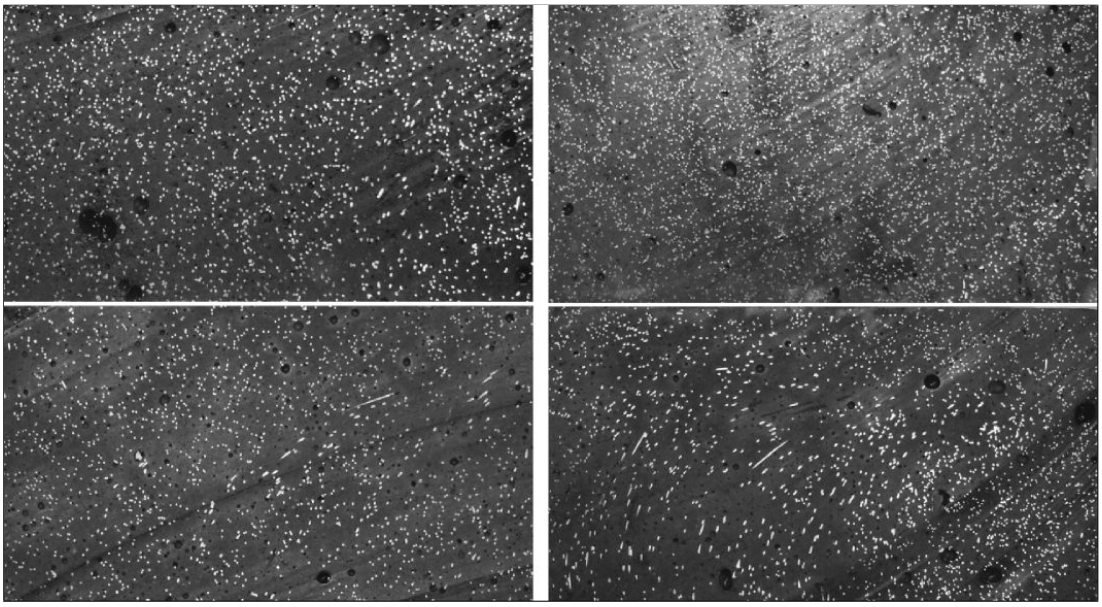

Figure 22: An example of cut planes to be analysed by the image analysis principle [57].

3.2.3 X-ray scanning

Using the image analysis, it was possible to evaluate the fibre orientation and dispersion in one plane, that needed to be physically cut. More cuts are theoretically possible to prepare, but there is a certain minimal possible thickness of the slices before they break. Additional cutting is also very time-consuming and results in the complete destruction of the specimen.

Using a computerized tomography (CT) scanning, we can obtain a high number of X-ray plane images. One image corresponds to one virtual cut of the material. The distances between these cuts can be very small. Vicente et al. [58] obtained a slice thickness of only 30 µm. An example of an X-ray image can be seen in Figure 23. Specimens there were cut from a cube specimen subjected to a compressive strength test. Dark and bright areas in the images correspond to materials with lower and higher ability to block the X-rays, respectively. This way, we can clearly identify cracks (air), concrete matrix and steel fibres. Special computer software can combine all the images and create a 3D image. Subsequent

analysis can filter out particular colours of the 3D image and leave only voxels (3D image points - the equivalent of a pixel in the 2D image) corresponding to the fibres. Coordinates of these voxels can be exported and analysed, to assign them to the individual fibres based on the voxel proximities. An example result of this analysis is in Figure 24. A final step is a calculation of fibre orientation and dispersion [58, 59].

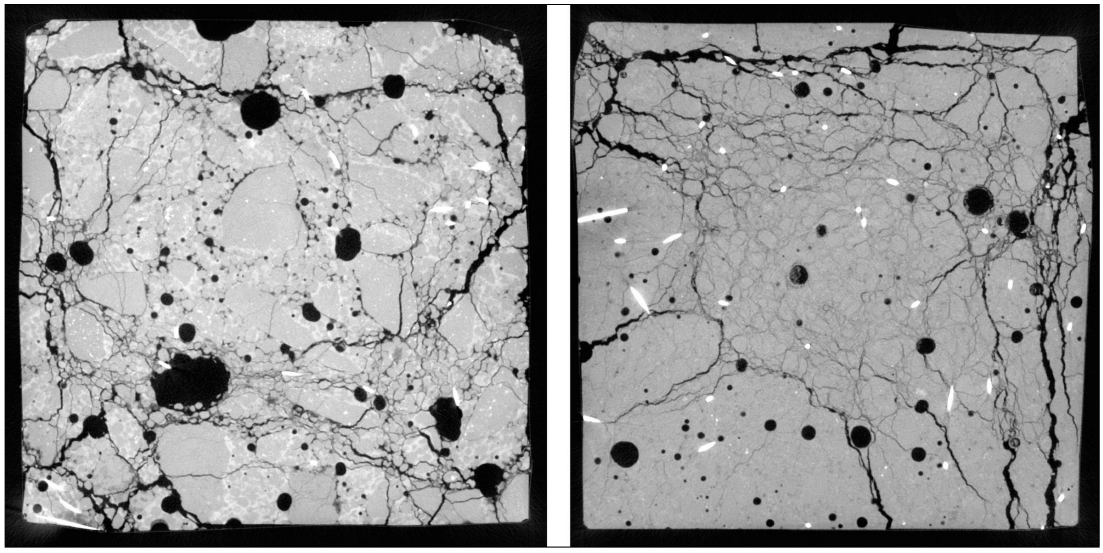

Figure 23: An example of a X-ray image of a damaged fibre-reinforced concrete specimen [58].

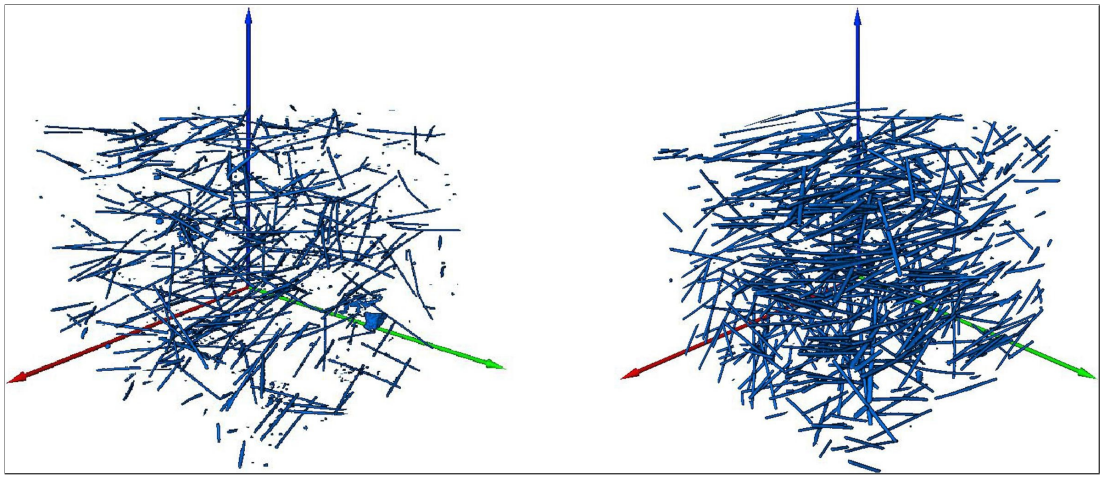

Figure 24: An example of a fibre distribution and orientation analysis [59].

CT scanning using X-ray imaging provides a complete analysis of a given volume of fibre-reinforced concrete. Although, there are several disadvantages of this measuring principle. Size of the specimen is limited, a CT industrial scanner is expensive and the fibre position analysis can be time-consuming. A major advantage of this principle is the non-destructive nature of the measurement, although due to the limited specimen size, it usually needs to be cut from a bigger element or structure (core sampling). A single image analysis, as described in the previous subsection, requires cheaper equipment and can be conducted faster. The fact that only a single plane can be analysed might be sufficient in certain situations.

3.2.4 Natural frequency analysis

Reinforcing fibres have significantly different elastic properties compared to the rest of the concrete matrix. Since the resulting material is a composite, its overall elastic properties should be influenced by all its constituents. Leung and Balendran [60] conducted research to study the effects of fibre reinforcement (among other variables) on the mechanical resonant frequency of concrete specimens. They used a vibration inducing device to introduce vibration of a specific frequency to the specimen and another device to measure the specimen's response. A higher resonant frequency would imply a higher elastic modulus of a material, i.e. the material is stiffer. The authors of this research used polypropylene fibres. Specimens with these fibres exhibited clearly lower resonant frequency compared to the unreinforced specimen. The authors attributed this to the lower density of polypropylene. Although it should be noted, that the frequency differences were not large.

3.3 High strain-rate testing

3.3.1 Drop-weight methods

Probably the most common principle for conducting high strain-rate experiments is the drop-weight method. It is a very simple principle which needs only a relatively simple testing machine and allows many possible configurations. This, on the other hand, makes the drop-weight method probably the least suitable for direct comparison of results between different laboratories, as every testing apparatus is different, sometimes significantly so. Figure 25 shows selected examples of experimental devices using the vertical drop-weight principle. The two pictures on the left show structures specifically constructed to be the drop-testing machines. These usually include straight guiding rails to which the weight is attached. The specimen is located at the very bottom, to allow for a variety of heights to be used. On the other hand, the picture on the right shows a drop-weight impact experiment conducted using only a frame which holds the specimen, while the weight is held by a crane. In this case, a square slab is the specimen, unlike the previous examples, that are configured for beam specimens.

Regarding the weight itself, several problems can be immediately identified. Depending on the structure's design, the weight can experience certain energy losses when being guided by the rails on its way down. This could be a problem if only the initial height is given as the only information regarding the loading conditions. When the weight finally makes contact with the specimen, it usually rebounds, but strikes the specimen a second time and then rests on it, which could distort the measurements. This problem is eliminated with the design of an impact pendulum, where weights are moving towards the specimen from one side.

In most cases, researches want to constrain the specimen's rebound after the impact. This is because the measured forces, accelerations or strains would show

Figure 25: Examples of drop-weight devices, from the left [61–63].

all the additional impacts between the specimen and the supports. As can be seen in all examples in Figure 26, this constraint is done using several different methods. A plate specimen can be fixed into a steel frame or directly bolted to a supporting frame. Beam specimens can also be bolted to the supports using various steel elements, or they can be held over the support using additional steel cylinder, either using springs or bolts. While this approach eliminates the rebound, it presents new variables. In the case of a frame along the circumference of a plate specimen, it becomes a completely new system which has significantly different dynamic behaviour. Measuring, for example, oscillations from accelerometers placed on the specimen, would yield significantly distorted results. Similar problems should be expected for force measurements as well. In the case of the constraints to the beam specimens, it is not clear how exactly does the constraint behave during the experiment. If a bolted connection is used, it is safe to assume that the strength with which the bolts were tightened plays a role. This is partially eliminated by the spring connection approach, as the spring strength is constant. But even then, the spring, as well as the bolts, dissipate a certain amount of energy which is difficult, if not impossible, to analyse.

Measuring forces is yet another problem with the drop-weight principle. Force sensors are usually placed either as supports, as part of the weight or both, but most studies are conducted using only one force sensor position. The sensors that

form supports can only measure the residual reactionary force, which is the impact force without the inertial forces of the specimen. This can be beneficial to eliminate the inertial element. Sensors in the weights, on the other hand, cannot measure forces without including the inertial forces. It is also possible to measure forces using accelerometers and multiplying the measured accelerations with mass. But the mass value is difficult to precisely identify, as not all of the object's mass is undergoing the measured acceleration at a given time point due to the stress wave propagation and oscillations. Displacements or strains are also measured by some researchers. Displacement can either be obtained using standard contact sensors, optical contactless devices or high-speed cameras. When analysing the results, it is important to understand that measurements cannot be paired just like with the quasi-static experiments. For example, presenting a load-displacement diagram is incorrect, as forces and displacements must have been measured at different positions, therefore they are time-offset due to the stress-wave propagation velocity.

The configuration of a drop-weight experiment can be almost the same as a quasi-static bending experiment when beam specimens are used. This similarity can be seen as very positive because a direct comparison of impact and quasi-static results might be possible. But the nature of the dynamic behaviour of not only the specimen, but the overall testing apparatus makes the impact testing significantly different, so the strain-rate would not be the only variable between the experiments. Overall, drop-weight testing can be made very simple and could probably serve as a basic evaluation of material performance under impact loading. However, comparing the results obtained using different machines is very problematic as is a detailed investigation of the material behaviour.

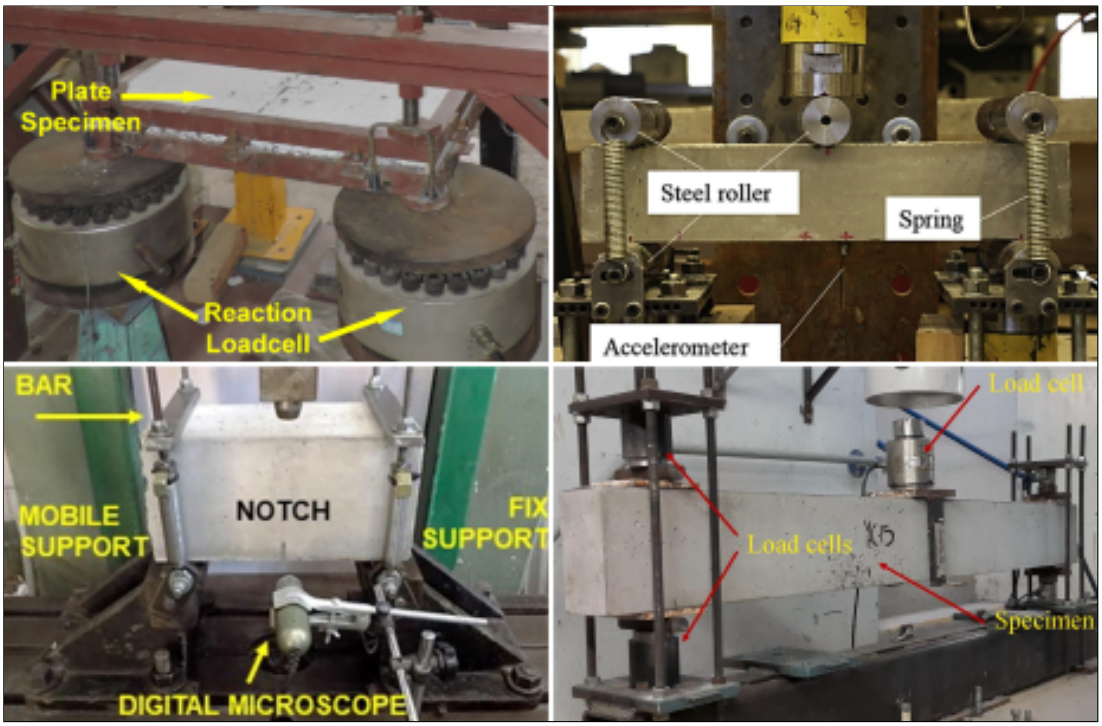

Figure 26: A typical four-point bending setup. From the top-left corner [64–67].

3.3.2 Split-Hopkinson bar

The split-Hopkinson bar is a family of experimental devices intended to analyse the dynamic behaviour of materials. Three main configurations exist for inducing compression, tension of torsion loading. The basic principle of operation can be described using a simplified schematic in Figure 27. On one end of the device, there is usually a tank containing pressurized air, which can be quickly released to propel a striker or a projectile. This projectile comes in contact with a long steel bar commonly referred to as the incident bar or the input bar. A stress wave starts propagating through this bar and finally reaches the specimen, which is a cylinder with a similar diameter as the bar (in case of concrete). At the specimen-bar interface, the stress wave is split into a wave that continues into the specimen and the reflected wave that starts moving backwards through the incident bar. The stress wave in the specimen causes certain plastic deformation and continues to the output bar, sometimes called the transmitter bar. The residual energy of the output bar is dissipated by a shock absorber at the end of the device, depending on the design. The lengths of the bars are much longer than their diameters. This minimizes the negative effects of the stress waves reflecting from the surface of the bars, which ensures a one-dimensional stress wave propagation [68–70].

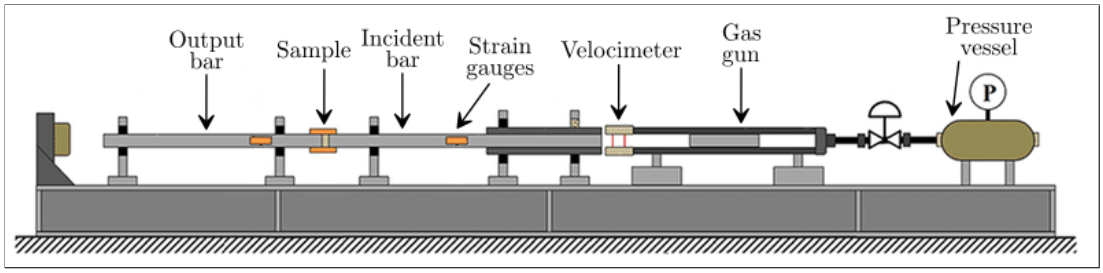

Figure 27: A typical split-Hopkinson bar schematic [68].

If compression loading is needed, then the specimen is simply put between the bars. The stress wave propagating through the specimen is counteracted by the inertial forces and loads the specimen with uniaxial compression. Biaxial configuration is also possible. The device then has two pairs of perpendicular bars and loading devices, which now need to be precisely synchronised to load the specimen in both directions at the same time [71]. For uniaxial tension loading, a modification is necessary. It is possible to use a specimen with a smaller diameter than the bars with a hollow tube over it. The specimen is then either glued or screwed to both of the bars. When the stress wave reaches the specimen, it bypasses it through the tube, which prevents compression loading of the specimen, but the reflected waves load the specimen in tension. This approach is suited for metallic specimens [72], but for concrete, a more common approach to tensile loading is to reverse the direction of the applied pulse to the incident bar. This is usually done by using an incident bar with a collar on its end. The striker is a tube with the incident bar inside of it, striking the collar in the direction away from the specimen [73]. The specimen also needs to be glued to the bars. Examples of a split-Hopkinson tension bar schematics can be seen in Figure 28, where the modified striker and incident bar are apparent. An example of a vertical split-Hopkinson tension bar with a drop-weight striker is in Figure 29.

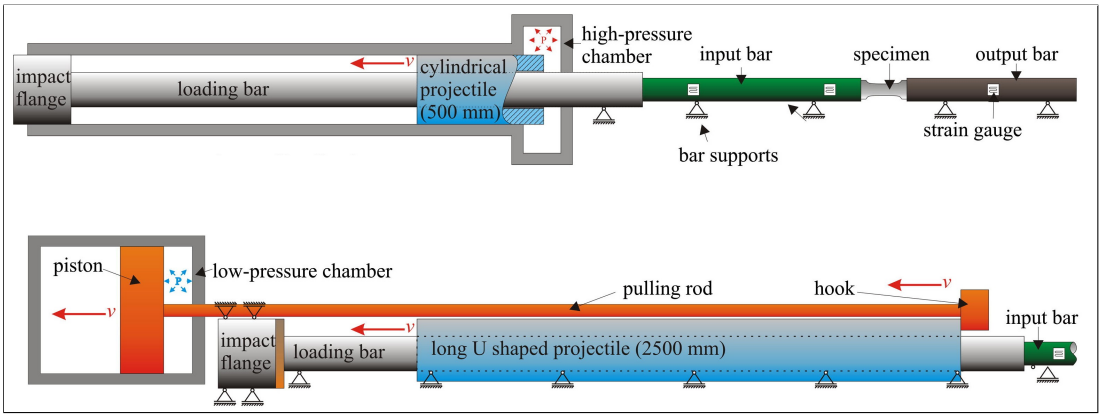

Figure 28: Examples of a split-Hopkinson tension bars [73].

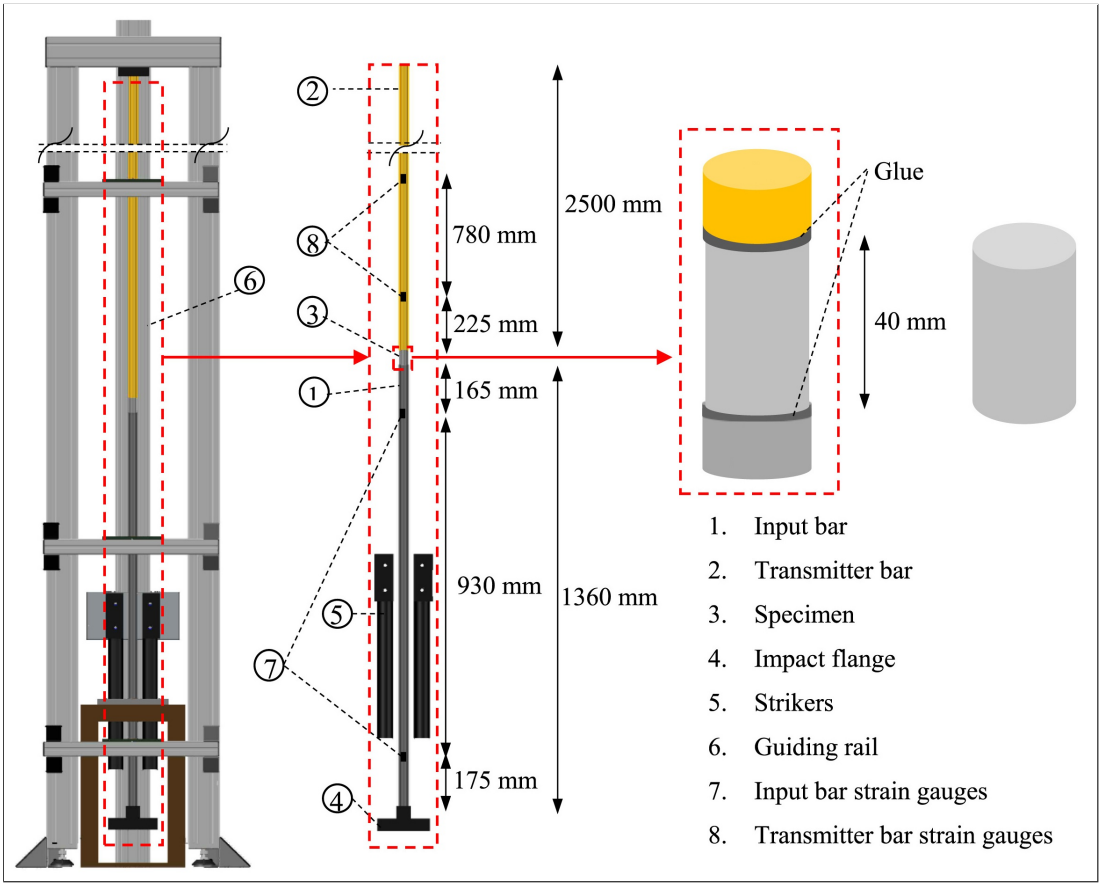

Figure 29: A drop-weight split-Hopkinson tension bar [74].

Strain is measured on both the incident and the output bars. This is usually done by attaching strain gauges to their surfaces, but contactless optical methods can also be used. Displacement of the ends of the specimen in contact with the bars can be calculated from the strain measurements. Similarly, forces acting on both ends of the specimen can also be calculated, since the cross-section of the bars is known. The stress wave propagation velocity through the metal bars must be known as well, or directly measured by using strain gauges at various positions on the bars. The measured data is sufficient to calculate the stress, strain and strain-rate of the specimen. One example of a stress-time diagram for

a compression testing on a split-Hopkinson pressure bar can be seen in Figure 30. The input pulse is clearly visible, although it shows unwanted oscillations. The length of this pulse is a function of the physical length of the striker. A long striker will act on the incident bar longer after initial contact. The amplitude of the pulse is dependent on the kinetic energy of the striker. After the pulse reaches the specimen, a stress equilibrium needs to be achieved in the specimen before the crack initiation, otherwise the stress and strain calculations are invalid. For certain geometry of the specimen, a specific pulse length and rise time of the loading wave needs to be established. This is done using pulse-shapers in the form of very thin slices of various soft metals placed between the bars and the specimen. Several rebounds of the loading wave between the ends of the specimen are necessary to establish the equilibrium. Ideally, the specimen would be as small as possible. However, fibre-reinforced concrete specimen need to be rather large, depending on the fibre size and the manufacturing principle of the specimen, to create a representative volume. In Figure 30, we can observe the reflected wave on the incident bar. The measurement of the reflected wave determines the maximum time interval of the experiment. The incident bar strain-gauge measurements are valid only to the point when the reflected wave reaches the start of the incident bar, reflects yet again and reaches the strain-gauge. This point is also apparent in the presented diagram at around 275 µs. The experiment must be designed so that the material will achieve complete failure in this time period [74, 75].

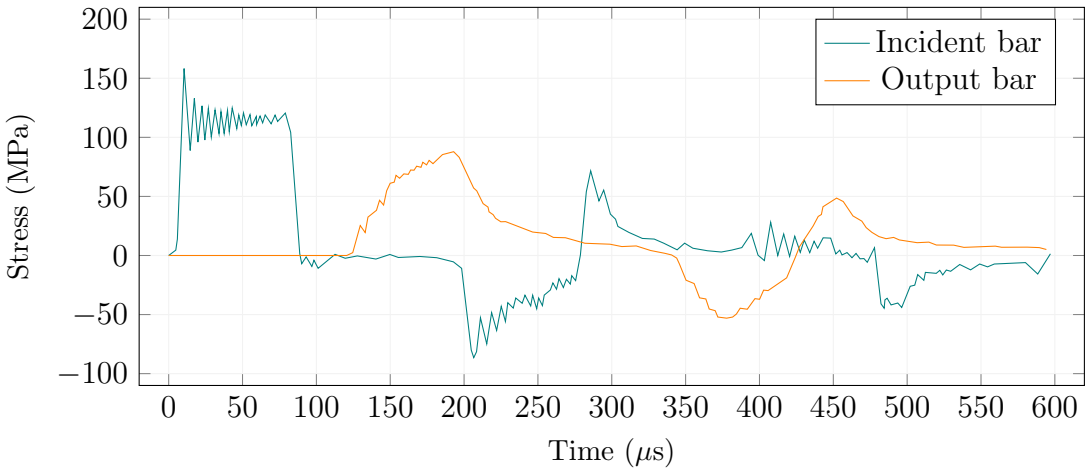

Figure 30: An example of data acquired during a split-Hopkinson pressure (compression) bar experiment [68].

It is clear, that many factors play key roles in successful split-Hopkinson bar experiments and significant variations between the devices are possible. This, again, raises a question, whether a direct comparison of results between different laboratories is possible. The assumption of stress-equilibrium is particularly problematic. Especially for a material such as concrete, which shows significant inhomogeneity, especially when reinforced with fibres. The micro-mechanics of concrete, the pre-crack damage formation, inertial forces and various other aspects prevent a uniform distribution of stress. The specimen size is also a major concern when testing concrete, such that a representative volume of fibre-reinforced concrete is only achievable with large experimental devices. Small cylindrical specimens would show a large influence of wall-effect on fibre orientation. Only a

core specimen would be possible. The calculated strain-rate during loading is also only a rough estimate, as it will not be achieved throughout the specimen, nor will it remain the same during the entire loading phase. Nevertheless, the split-Hopkinson bar devices are suitable for a more scientific approach to investigating material parameters, but the experiments are difficult to conduct correctly and the possibility of results comparison in unclear [75–77].

3.3.3 Projectile impact

Projectile impact testing is another method of evaluating fibre-reinforced concrete's performance when subjected to high strain-rate loading. Unlike the previously introduced experiments, this type of testing is usually not done to obtain specific material characteristic, but rather to see whether the material can or cannot withstand the loading or how much damage was caused. The studied material is expected to be used for various anti-ballistic elements. Figure 31 shows an example of various projectiles. A type of projectile depends on the method of acceleration. Military weapons and ammunition can be used. In that case, comparability of results is relatively good, as the projectiles are standardized [78]. In laboratory testing, the accelerator is usually compressed air. Projectiles, in that case, can significantly vary, including the materials they are made from. Shapes of the fronts of the projectiles can range from completely flat to very sharp conical [79, 80].

Figure 31: Examples of projectiles used in concrete impact experiments. From the left [78–81].

Measurements during the experiment usually only include measuring the projectile's velocity before the impact or if it penetrated then after the impact as well. A high-speed camera can be used for that purpose as well as to monitor the specimen's damage development, either on the front or the back face. A specially designed projectile can also include an acceleration sensor, which can be used to obtain the deceleration after the impact and to calculate velocity or force. This data is especially useful for numerical simulations. The impacted specimen can be

extensively analysed after the impact by measuring the number of cracks, depth of penetration, crater volume or circumference etc. The specimen is usually a slab or a cylinder with dimensions depending on the calibre of the projectile. Steel frames or tubes are used to hold the specimen or create deformation constraints [81–83].

3.3.4 Full-scale testing

Full-scale experiments are another form of testing. Various impact, crash or blast tests can be executed using a full-scale structural elements (panels, barriers) and loading elements (cars, planes). Examples of such experiments can be seen in Figure 32. Similarly to the projectile impacts, this kind of testing is usually done only to evaluate the behaviour of the elements or if they can or cannot withstand the load, stop the vehicle etc. Analysis of material parameters is usually not done. Full-scale testing is, in most cases, the next step in designing specific structural elements, i.e. the material has already been optimised using laboratory testing. Data is often acquired using accelerometers, high-speed cameras or displacement sensors. Numerical simulations can be created based on this data to further confirm the numerical models [84–87].

Figure 32: Examples of full-scale experiments. From the top-left plane-crash [84] car-barrier testing [85] blast loading of a concrete panel [86].

Full-scale experiments are usually very costly. But on the other hand, they form a necessary step before introducing a final product to the market, for example, a car barrier. Comparison of results between different experiments is problematic because of the large amount of variables. Since the experiments are usually set up depending on the current needs, the technical parameters of the experiments are rarely the same. Data acquired during the tests can be used to roughly estimate the behaviour of the overall element, but especially for blast loading, significant inertial forces and other negative effects are present.

3.3.5 Other methods

A different testing method was devised by Tran and Kim [88]. Their device is called the Strain energy frame impact machine (SEFIM) and can be seen in Figure 33. It is, in many aspects, similar to the split-Hopkinson bar. Instead of a striker, which would impact an incident bar, a hydraulic jack is used to load the energy frame. At a certain stress level, a coupler between the jack and the frame breaks, which releases the stored elastic energy of the frame. The opposite side of the frame is connected to a grip, which holds one end of a dog-bone concrete specimen, which is loaded by the released energy. The other end of the specimen is connected to a transmitter bar, which is held by fixed support. Strain-gauges are attached to the transmitter bar and are used to calculate stress, based on the knowledge of the cross-section of the bar and its modulus of elasticity. A high-speed camera is used to monitor the specimen and using image analysis, displacement of various points on the specimen can be calculated. Combining these two measurements, a stress-strain diagram can be plotted. A major advantage of this design is the possibility of using larger specimens, compared to the split-Hopkinson bar. A disadvantage is the complexity of the machine and the negative aspects related to this. For example, the authors use two strain-gauges on opposite sides of the incident bar. The measurements between the gauges are significantly different. This indicates that the experiment is not a truly uniaxial loading and the stress equilibrium was not established. Therefore, the measured data is not representing actual material behaviour.

Last but not least, Yu et al. [89] used an impact pendulum device. The basic principle is similar to a drop-weight method introduced earlier but the specimen is held by steel ropes instead of fixed support. Also, the weight follows a circular trajectory and strikes the specimen from the side, instead of from the top. The same pendulum principle as well as the specimen support design is used with the impact pendulum used in this thesis, therefore the detailed functioning will be described later. The authors of this device used steel tubes to construct the apparatus. The striker is also a steel tube with various weights attached to its front. The specimen is a relatively large slab, with the impact point being in its centre. The device is in Figure 34. The measuring is done using a high-speed camera. The subsequent video analysis is done to obtain velocities of both the striker and the specimen. This is possible thanks to the white board with a uniform grid behind the structure that can be used to measure positions of the objects. This approach is, by default, burdened by certain inaccuracies. Based on pictures provided by

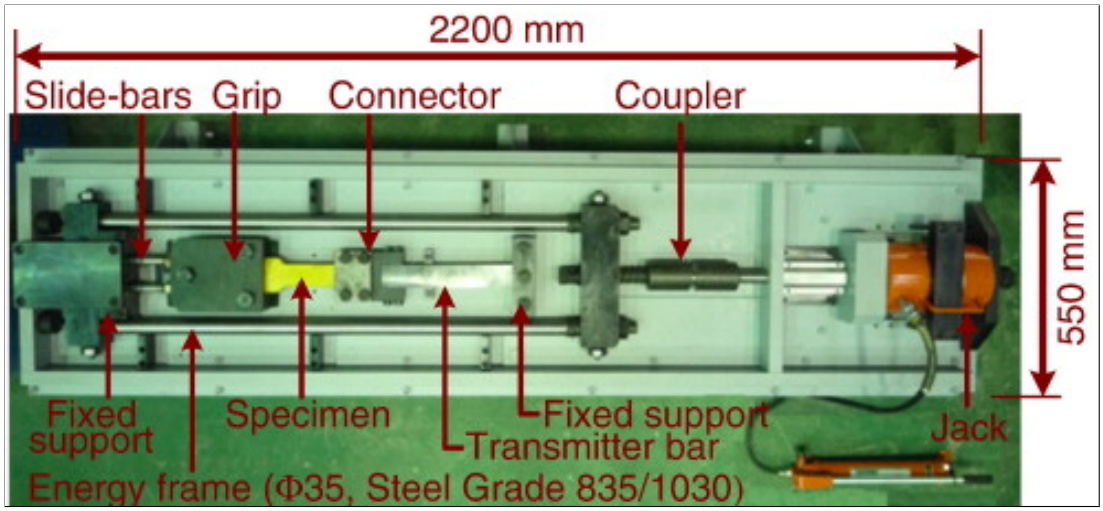

Figure 33: The Strain energy frame impact machine [88].

the authors, the high-speed camera was making relatively low FPS videos, as the moving objects are blurry. The authors do not provide detailed information regarding the measurement accuracy nor other significant details regarding the device. However, the authors rightly pointed out the need of an impact testing approach that will eliminate possible energy-dissipating elements, such as the specimen supports.

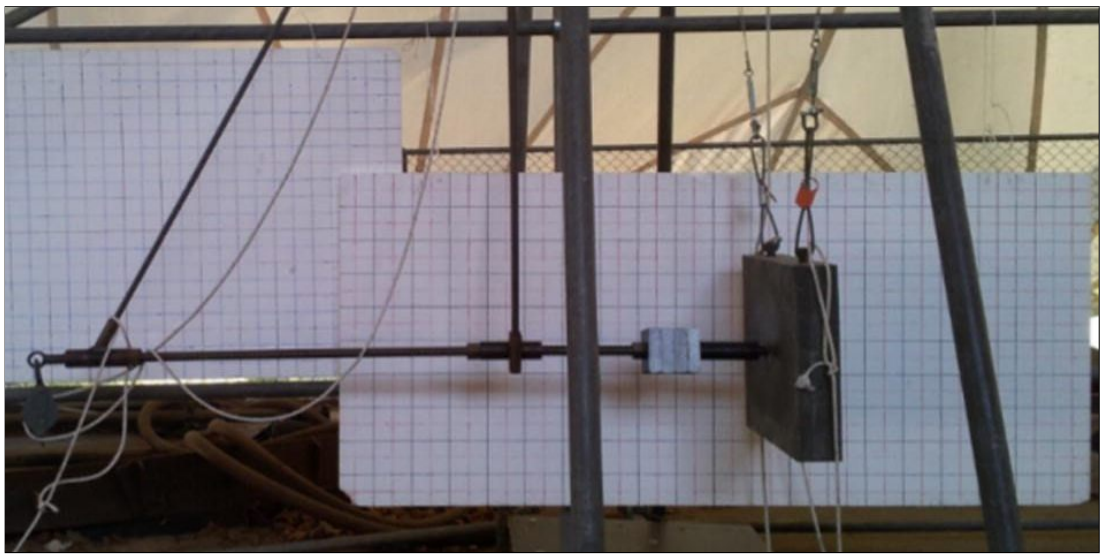

Figure 34: The impact pendulum with suspended specimen [89].

Chapter 4

Impact pendulum

In the last chapter, several experimental principles were introduced. Those principles and methods are used in various parts of the world and they allowed and continuously allow researchers to test and evaluate material's performance using various strain rates. It is clear that those principles and their experimental applications vary greatly. But even laboratory equipment using the same principle (for investigating the same mechanical property) can have a significantly different design, as there are no standards or common practices available yet. The measurements obtained in different laboratories can therefore be affected by different factors, or certain factors can have more significance with certain experimental setups. It is then logical to assume that the comparison of results might be difficult.

If we were to design an ideal experimental method for testing materials at higher strain rates then we need to respect a couple of factors. The most important ones are the effect of inertial forces and finite stress wave velocities. During the standard quasi-static testing, inertial forces are usually too small to be of any concern. The testing machine is stiff enough so that its deformation doesn't alter the measured results. Loading forces are applied slowly. When analysing the results obtained from quasi-static testing, we can use the simple force equilibrium equations to calculate, for example, the reaction forces, bending moments and stresses. These calculations assume instantaneous changes in reactions anywhere in the system based on the changing actions. This assumption is of course not correct even for very low strain-rates. This is due to the finite propagation velocity of mechanical stresses, but the errors obtained when applying this assumption are negligible in this case. Faster changes in the applied loading forces are going to make these errors more severe. Dynamic equilibrium equations need to be used to include the inertial forces to the overall force equilibrium. But since the inertial forces rapidly change, it is difficult, if not impossible, to calculate bending moments and stresses at higher strain rates. And, as was explained in chapter 2.4, if the reaction forces are measured, they might show values that do not correspond to the actual material parameters. The experimental apparatus itself might also start distorting the results, as stress waves will propagate through its structure as well as through the specimen. This could trigger unwanted eigenmode oscillations with significant amplitudes. The stress wave could also propagate unevenly through the specimen or the measuring apparatus, which is a concern with the split-Hopkinson bar experiments.

In this part of this thesis, an experimental method for determining the material's ability to absorb and dissipate mechanical energy is going to be introduced and thoroughly described. The aim of the design of this method is to identify any factors that could potentially affect the experimental results. These factors are then either completely eliminated by appropriate design choices, or sufficiently described. The machine used to conduct the impact experiments is called the impact pendulum. The following text is first going to describe the apparatus itself and highlight its main features. Next, the measuring principle will be introduced which is followed by the description of the practical measurement procedures.

4.1 Basic overview

The entire impact pendulum's schematic can be seen in Figure 35. In Figure 36 there is a photograph of the entire apparatus. The main principle of an impact pendulum is that the load is applied horizontally using an impactor that can move on a circular trajectory. The impactor can be seen in Figure 35 in various possible positions (pulled up to a certain height and resting at the lowest point). It is suspended on four steel ropes, that are attached to the impactor using connectors with spherical plain bearings (Figure 37). On the opposite side, these ropes are connected to two steel rods, that are attached to the supporting structure using ball bearings (Figure 38). This design keeps the impactor in a horizontal position at all times. The main body of the impactor is made of a solid block of ordinary construction steel. Small steel cylinders are welded on the sides for attaching the connectors. Towards the front, there are small steel blocks welded to the main body. These blocks have threaded holes for screwing in accelerometers.

The nose, which comes in contact with a specimen, is a detachable cylinder made from hardened steel. The cylinder's surface measures an average hardness of 55 HRC (Rockwell C), which roughly corresponds to a strength of 2000 MPa. The front of the impactor can be seen in Figure 39. Dimensions of the impactor are 775 mm $\times$ 120 mm $\times$ 50 mm. Lifting the impactor up is done using an electric winch located in the upper left corner of the schematic in Figure 35. The winch is connected to the impactor with an electromagnetic lock, which allows for an easy and quick release. The structure of the impact pendulum is made stiff enough to provide sufficient support to the impactor as it moves towards the specimen. On the right side of the schematic, there is a steel table that forms a support for various equipment used to either hold the tested specimen or conduct the actual measurements. In this case, there are the two measuring frames, to conduct position tracking of the specimen, and a smaller optical gate for the impactor. The comb-like attachment on the side of the impactor works together with this optical gate. All measuring equipment is going to be described later in more detail. The whole structure of the impact pendulum is firmly attached to the concrete floor.

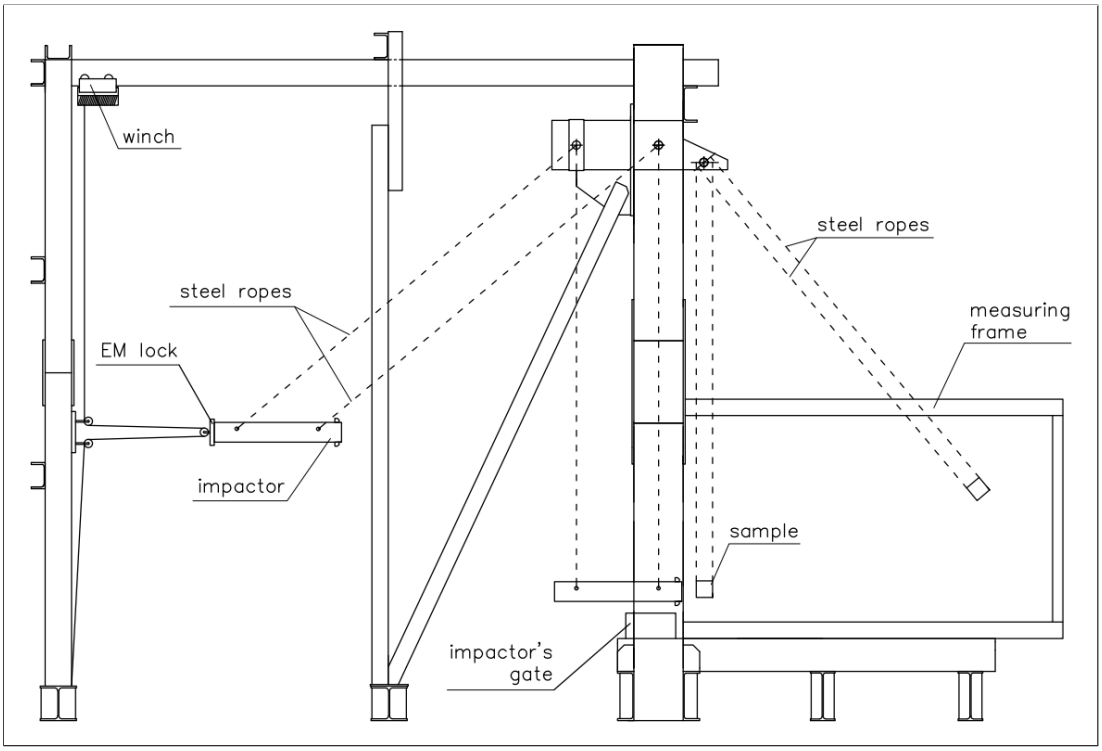

Figure 35: Schematic of the impact pendulum.

Figure 36: The complete impact pendulum.

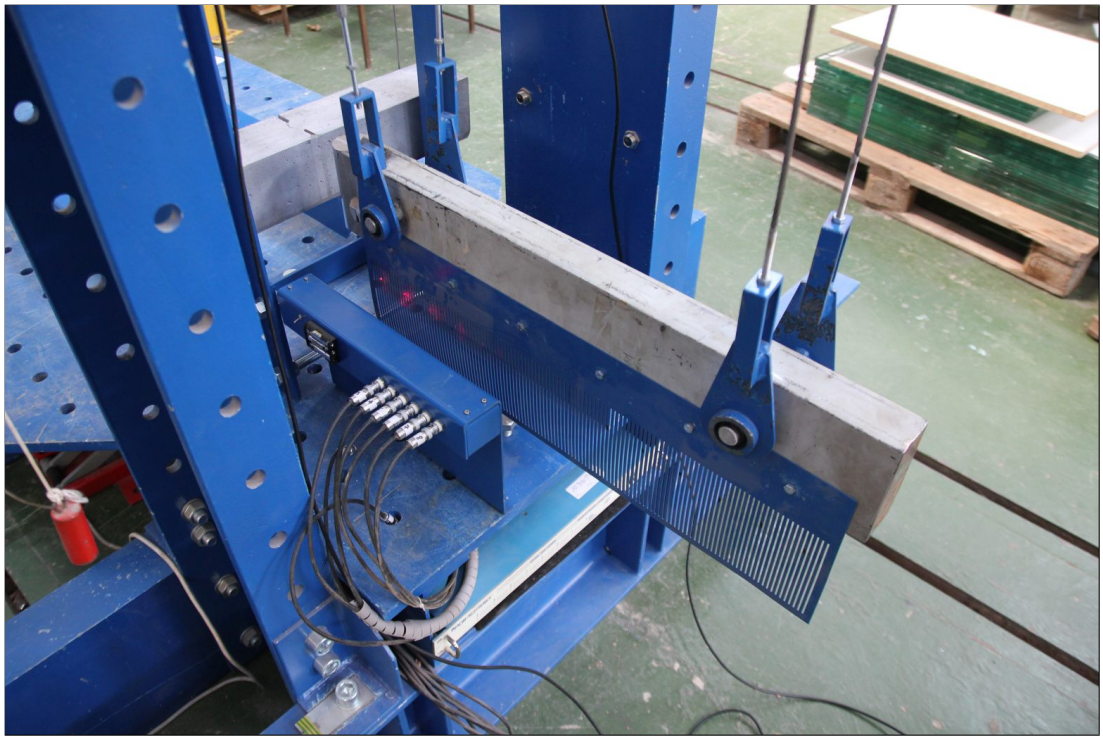

Figure 37: The steel impactor.

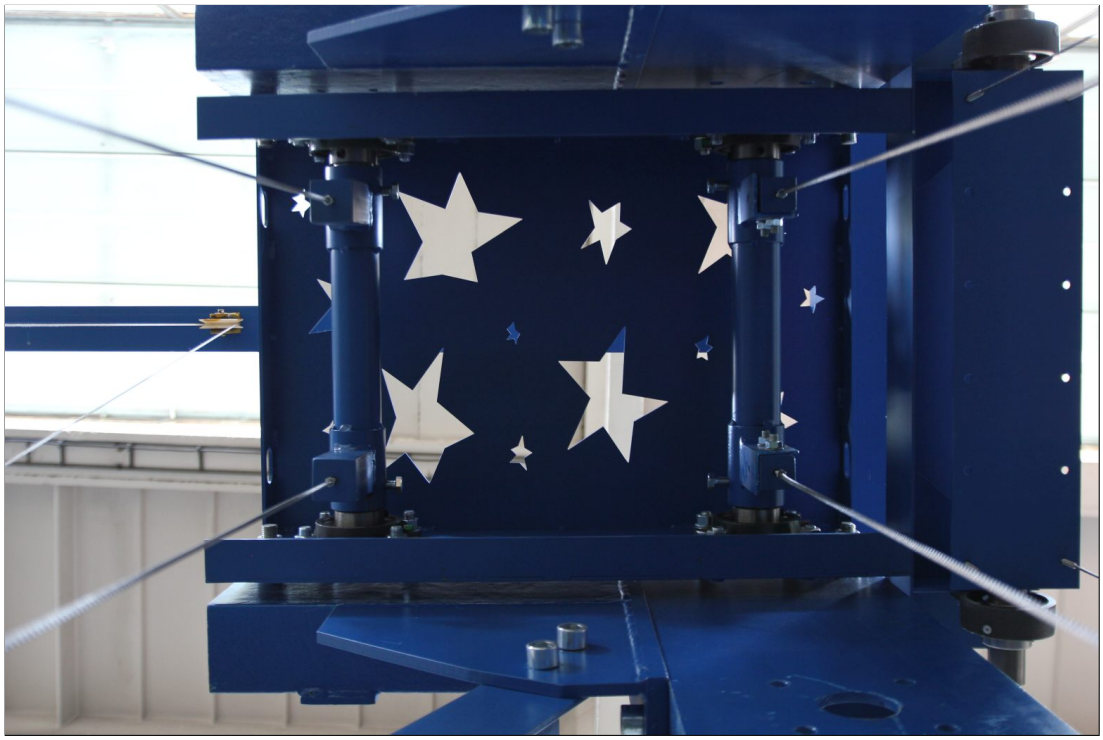

Figure 38: Connections between the structure and the steel ropes.

Figure 39: The detachable hardened nose of the impactor.

The most important characteristic of this particular setup is that the specimen is not held by a rigid support. It is suspended on steel ropes, similarly to the impactor. By eliminating the fixed supports, we are also eliminating any possible energy losses caused by them during high strain-rate loading. This changes the entire characteristic of the experiment from a classic force-deflection based measurements to a completely energetic approach. This removes a major variable in the whole testing process, which is, in the author's opinion, the biggest problem with the aforementioned experimental principles used in literature. To keep the suspension as simple as possible (to not introduce any additional weight to the specimen and therefore additional inertial forces), there are no objects to connect the specimen to the ropes. The specimen is simply resting in loops formed by the ropes. This method was also used in similar impact testing of glass plates, where it was proven that the suspension has no effect on the behaviour of the plate [90]. As can be seen in Figure 40 the specimen is positioned inside the measuring frames, so that its supporting ropes are outside of the frames. The measuring frames are made so that the movement of both objects is not obstructed before and after the impact. The steel ropes are both connected to a mechanism, which can freely rotate in two ball bearings attached to the pendulum's structure (Figure 41).

The measuring frame is designed for a specific size of a specimen. However, the entire impact pendulum was made to accommodate several other experimental setups, with or without the measuring frame. The rotating mechanism allows the steel ropes to be attached with different spans. The rotation can also be disabled. The line loading impactor can be easily switched for a point and area loading impactors. The measuring frames can be disconnected from the structure and removed. Overall, the impact pendulum is a highly modular testing apparatus.

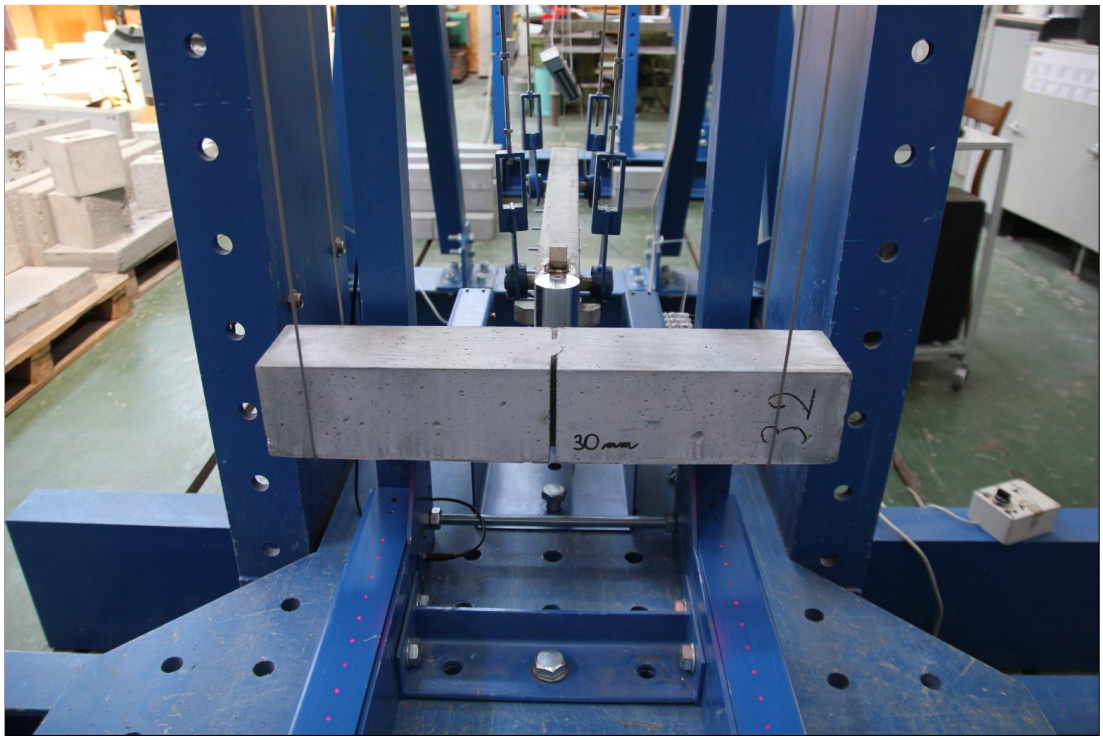

Figure 40: The suspended concrete specimen.

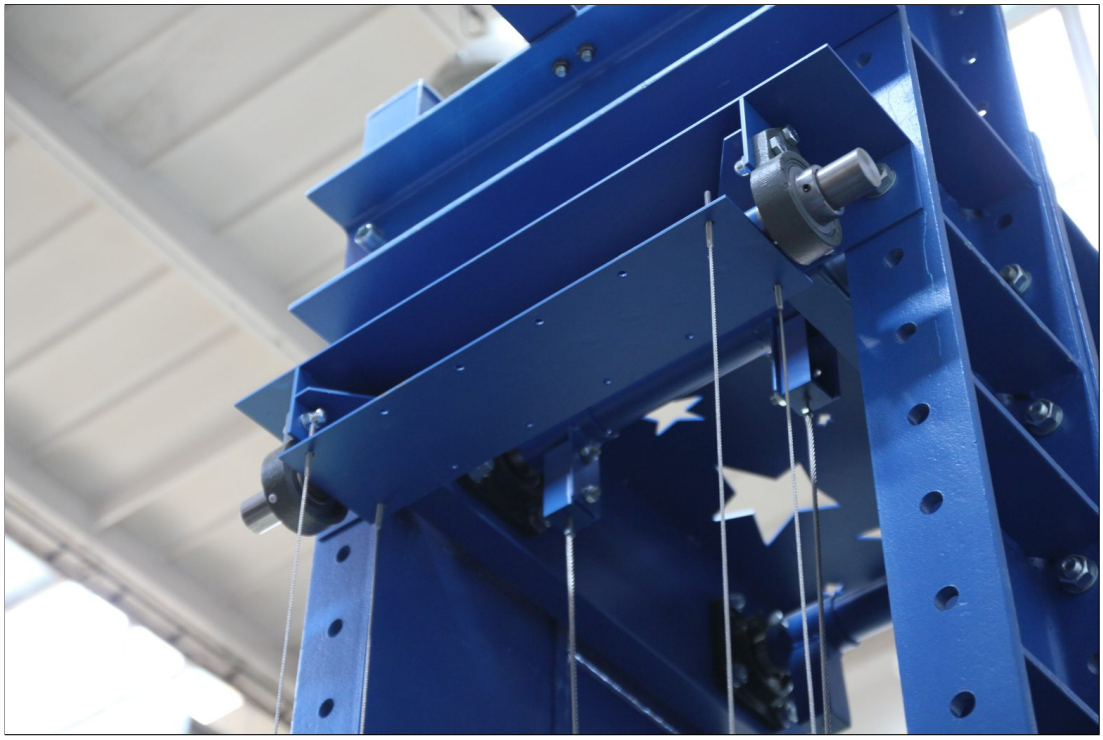

Figure 41: The mechanism that allows rotation of the specimen suspension.

4.2 Measuring principle

As stated above, the experimental setup is designed for a complete energetic approach and to evaluate the material's ability to absorb and dissipate mechanical energy. We will start with the energy input into the whole experiment at the beginning of it. That is done by lifting the impactor to a certain height, therefore increasing its potential energy which is easily calculated from

$$E_{pot} = MgH \tag{2}$$

where M is the mass of the impactor, g is the gravitational acceleration and H is the height. Right at the start, it is important to understand, that we are dealing with a physical pendulum, i.e. the pendulum system is not an infinitely small object suspended on a massless cord. The mass M is therefore the total mass of all objects of the pendulum system and height H is the vertical change of the centre of mass of the whole system. The experiment starts by releasing the electromagnetic lock so that the impactor can start moving on its trajectory towards the specimen. As the impactor moves closer to its resting position, its potential energy decreases and its kinetic energy increases, but the total mechanical energy stays the same. In this explanation, we will not consider any energy loses, but those will be addressed later. Just before the impact, the impactor is in the lowest position of its trajectory and its potential energy is therefore fully transformed into kinetic energy

$$E_{kin} = \frac{1}{2} J\omega^2 \tag{3}$$

where J is the moment of inertia[3] and ω is the angular velocity. This change between potential and kinetic energies allows us to also calculate the velocity v of the impactor at the point of zero potential energy, i.e. just before the impact

$$v = \sqrt{2g\frac{R^2 MH}{J}} \tag{4}$$

where R is the distance between the centre of rotation of the pendulum and the point where we want to evaluate the horizontal velocity v. A less accurate velocity calculation can be made by substituting the fraction with only the initial height of the impactor. This will disregard the rest of the pendulum system, but since the impactor is the heaviest component of it, the approximation is fairly close to the actual value.

At this point, the impactor collides with the specimen. Some part of the initial mechanical energy of the impactor must now transfer to the specimen. Since the force is applied relatively fast, significant inertial forces will be formed in the specimen to counteract the loading force. This results in stresses inside the specimen that are high enough to cause irreversible damage to the specimen. In order to create this damage, a portion of the mechanical energy transferred to the specimen from the impactor needs to be spent. That is the dissipated energy

[3]Not to be confused with the second area moment or area moment of inertia, which is usually denoted with I (m^4) and only describes the geometry of a cross-section. The moment of inertia J ($\mathrm{kg\,m}^2$) or the mass moment of inertia reflects the mass distribution.

that we want to determine from the experiment. But there are also residual energies in both the impactor and the specimen since both objects will be moving after the impact. This means that in order to calculate the dissipated energy, three separate mechanical energies need to be calculated beforehand. It is the impactor's energy at the start of the experiment ($E_{I.pre}$), impactor's energy after the impact ($E_{I.post}$) and the specimen's energy after the impact ($E_{S.post}$). A simple energy balance equation

$$E_{Ai} = E_{I.pre} - E_{I.post} - E_{S.post} \tag{5}$$

can be used to calculate the dissipated energy (E_{Ai}) after one impact. The residual energies can be calculated just like the initial impactor's energy using equations 2 or 3 even for the specimen, as it also is a pendulum system, just with different parameters. This principle can only be used for impacts after which the specimen remains in one piece (it didn't fail yet). Since this experiment aims to obtain the overall dissipated energy until failure, the specimen must be impacted multiple times. The overall dissipated energy is then calculated as

$$E_A = \sum_{i=1}^{n} E_{Ai} \tag{6}$$

where n is the number of last impact but one, i.e. excluding the last impact after which the specimen completely failed. This introduces a minimal inaccuracy of the results, as will be later explained.

For future calculations, the parameters of both pendulum systems (the impactor and the specimen) need to be analysed. Simplified schematics of the systems can be seen in Figures 42 and 43. The parts of the system are rotating rods in the ball bearing housings (1), cable connectors on these rods (2), cables (3), cable connectors on the impactor (4), the impactor itself (5) and the attachments (6) (counted as two, since the attachment and its counterweight are the same weight with roughly the same centre of mass height). For the specimen, it is again a rotating rod (1), connector plate (2), cables (3), specimen (4) and part of the cable underneath the specimen (5). The schematics are not drawn to scale, they only illustrate the components. The corresponding Tables 2 and 3 show the masses of these components, their centres of mass relative to the centres of the rods (centres of rotation), number of these components in the system, their moments of inertia and the parallel axis theorem (Steiner's theorem) component. For the subsequent calculations, the total masses, centres of mass and moments of inertia are shown. It can be seen, that the components of the total moments of inertia due to rotation are negligible. The most important are the parallel axis theorem components of the heaviest objects - the specimen and the impactor. This means, that using the ideal mathematical pendulum model, with the weight concentrated in a small point on a massless cord, would not be that inaccurate. But since all the subsequent calculations will be done automatically using a PC, there is no reason to not use more accurate, yet complicated, models. The specimen's weight will change with a different specimen, therefore the resulting specimen pendulum system parameters need to be a function of this weight in the calculations, which is again, not a problem with the use of a PC analysis.

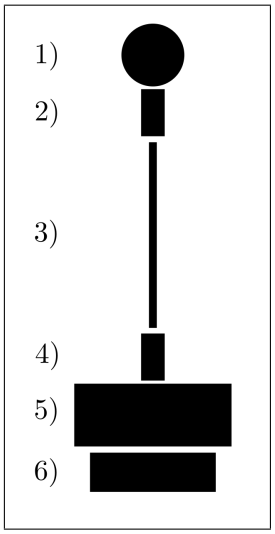

Figure 42: Impactor moving parts.

Part	m_i (kg)	c_i (m)	No.	$J_{rot,i}$ ($kg\,m^2$)	$J_{par,i}$ ($kg\,m^2$)
1	7.707	0	2	0.003	0
2	0.401	0.075	4	0.001	0.009
3	0.273	1.280	4	0.603	1.789
4	0.295	2.670	4	0.002	8.412
5	36.50	2.685	1	0[a]	263.137
6	1.002	2.740	2	0[a]	15.050
M = 57.794 kg					
C = 1.872 m					
J = 289.007 $kg\,m^2$					

[a] Parts not rotating

Table 2: Impactor pendulum analysis.

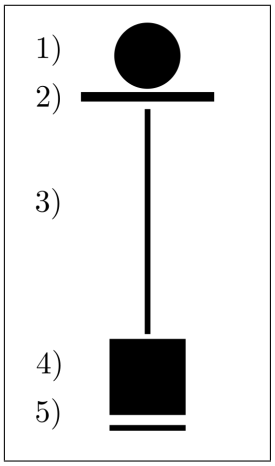

Figure 43: Specimen moving parts.

Part	m_i (kg)	c_i (m)	No.	$J_{rot,i}$ ($kg\,m^2$)	$J_{par,i}$ ($kg\,m^2$)
1	7.694	0	1	0.002	0
2	2.462	0.022	1	0.004	0.001
3	0.109	1.285	4	0.242	0.720
4	12.885	2.525	1	0.021	82.150
5	0.004	2.575	2	0[a]	0.056
M = 23.486 kg					
C = 1.412 m					
J = 83.196 $kg\,m^2$					

[a] Negligible, rounded to zero

Table 3: Specimen pendulum analysis.

4.3 Measurements

Balance equation 5, together with equations 2 and 3, shows us exactly which variables need to be measured in order to calculate the equation's terms. Different measuring techniques can yield either the velocities for calculating kinetic energies or heights for calculating potential energies. Certain methods can combine both approaches and allow the calculation of both. At the start of the experiment, the impactor is lifted to a certain height. This height can be simply measured and the impactor's mechanical energy before the impact can be calculated from its potential energy. Another way to calculate its mechanical energy is to measure its velocity right before the impact. Measuring velocities, in general, is a measurement of a position difference in a time interval. To achieve maximum accuracy, this time interval should be infinitely small. After the impact, the mechanical energies of both objects can be calculated as kinetic energies again, but now based

on velocities obtained right after the impact. Since both objects will continue moving after the impact, they will inevitably reach the highest point on their circular trajectories, where the velocities will be zero. At this point, measuring the heights of the objects will allow us to calculate the objects' mechanical energies from the potential energy equation. But unlike the height measurement of the impactor before the impact, when it was stationary, both objects are free to move this time. This means than the height measurement needs to be conducted at exactly the right moment when the velocities reach zero and the height is truly maximal. Tracking methods are also possible when the objects are tracked in real-time, which allows the fitting of a theoretical pendulum curve on the measured data. This is the method that can result in both the kinetic or potential energies.

It is clear, that obtaining the velocities and the heights as explained above, might prove difficult in some cases. The following text will discuss practical difficulties associated with these measurements, what kind of inaccuracies might be present and describe the measuring techniques chosen for the impact pendulum.

4.3.1 Measuring velocities

For the kinetic energy approach, velocities need to be measured right before and after the impact. For a single velocity measurement, it is necessary to know the positions of an object in at least two points in time. The difference between those two points should ideally be infinitely small. During the initial testing of this measuring principle on the impact pendulum, a high-speed camera was used to track the motion of the impactor and the specimen. Several key factors were identified when using this type of measuring technique. The first practical problem is to make sure the same physical point on an object is tracked in different time points. This is usually done by fixing a special marker on the object - a fiducial. But the image quality is almost always going to be insufficient to obtain a correct velocity value from position measurements from just two time points, so more measurements are done and the resulting partial velocities are averaged[4]. An example of measuring the velocity of an ideal pendulum can be seen in Figure 44. It shows a calculated horizontal velocity just before it reaches the lowest point of its trajectory (at 0.824 s - a quarter of a period). The initial heigh was set to be 0.5 m with a cord length of 2.7 m, which are approximately realistic parameters of a typical experiment. The high-speed camera would be positioned above the object facing straight down. The lime line is the actual velocity. Let's assume that we used a frame rate of 900 FPS and chose to obtain four partial velocities before the impact. This means that five position measurements are needed, which is indicated by the orange markers, which are connected by the orange lines. We can see that the orange lines almost perfectly cover the lime line because it's

[4]Let's assume that an object with a constant velocity is tracked with a high-speed camera. Frame N (one position measurement) is used to calculate two partial velocities. The first partial velocity from frames N-1;N and the second partial velocity from frames N;N+1. In other words, partial velocity calculations are tied to the previous partial velocity value, therefore an average between these partial velocities should result in an accurate overall velocity measurement. More accurate with a higher number of partial velocities obtained. But only when the object has negligible acceleration.

barely visible, so the partial velocities would be more precise. Lowering the frame rate to 300 FPS but still using the same number of measurements is indicated by the purple dots and lines. This time, the lines are further off the lime line. This means that the partial velocities are not that precise and more importantly, the measurements start further away from the moment of impact. However, the individual position measurements would be more precise for the lower frame rate, since the camera would be able to capture each frame with a higher resolution. Also, when determining a velocity value from a relatively large position difference, even moderate absolute distance errors in the actual position measurements might not result in a significant error in the resulting velocity.

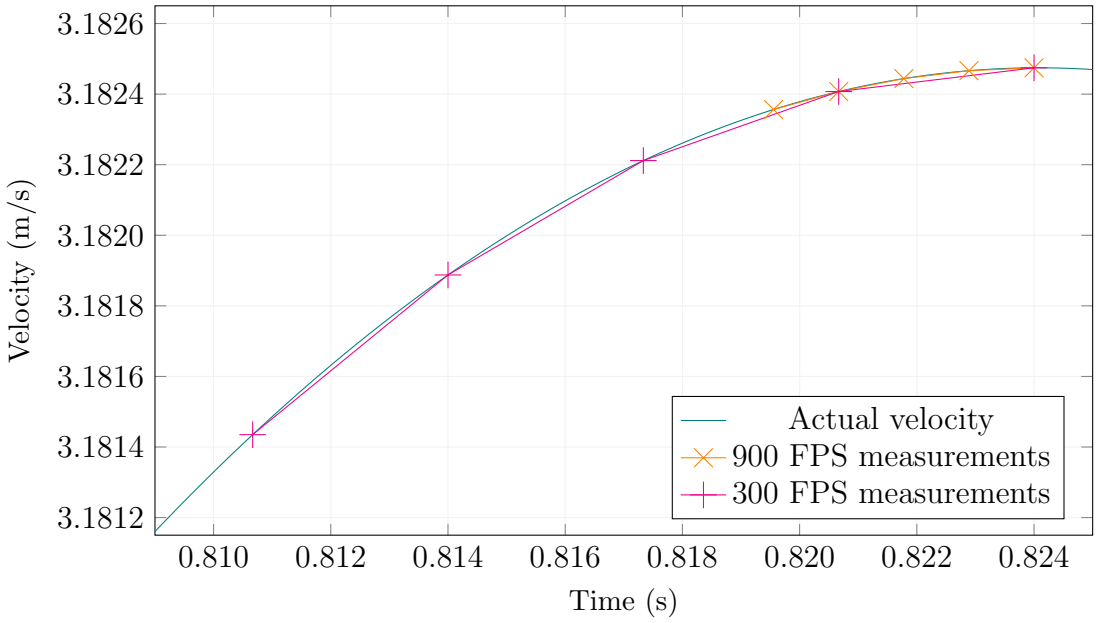

Figure 44: Example of measuring velocities of a non-linear motion.

The impactor is going to accelerate up to the moment of impact. This means that the partial velocities measured between the captured frames further before the impact are lower than the true impact velocity. Measuring velocities well before the impact also introduces some distortion of the position measurement due to the curved trajectory. The object is going to be closer to the camera at first and farther at each consecutive frame. The solution to these problems is finding an ideal balance between the frame rate and resolution, so that position measurements are conducted on fewer frames closer to the moment of impact. In other words, a balance between the frame rate and the resolution must be found to allow us to conduct measurements as close to the moment of impact as possible while maintaining a certain level of precision. Having sufficiently long suspension of the impactor pendulum (radius of its trajectory) is going to help mitigate these problems. It can be seen from Figure 44, that the velocity change is small in this time interval before the impact. But in this case, when velocities would be used for kinetic energy calculations, the errors would become larger as the velocity is squared. However, in some situation, this inaccuracy could be acceptable, especially for higher velocities.

A different situation occurs for the after-impact velocities. In this case, it is also necessary to conduct the measurements as close to the moment of impact as possible because of the reasons explained above. The only difference here is that the objects are decelerating after the impact, instead of accelerating. But there are a couple of factors that make the velocity measurements more difficult. First is the duration of contact between the objects. Theoretically, the contact between the impactor and the specimen would happen in an infinitely small time interval. But in a real experiment, the contact lasts for a certain time. During this time, the mechanical energy is transferred to the specimen. It was observed, that there might even be multiple contacts between the objects due to the mechanical oscillations. In any case, it is clear that the after-impact velocity measurements need to start after the contact ends. This factor alone introduces a certain error to the residual kinetic energies of both objects, although the contact period is still very short.

The second factor is the mechanical oscillations of both objects. When the impactor first comes in contact with the specimen, it makes the mass of the specimen around the impact point accelerate, while the rest of its volume is still motionless. This results in different velocities in different parts of the objects, as the entire mass of the objects adjusts to the conducted impact. When tracking one particular point on an object, it appears that the point is alternating between lower and higher velocities - it oscillates. This of course makes it difficult to measure the true velocity that can be used to calculate the kinetic energies. One approach, which was used in previous studies, was to only use the measured partial velocities after the oscillations settled down. Filtering out the oscillations is usually not possible due to their fast decay. This introduced an error because the after-impact velocities were not measured right after the impact, but some short time later.

A third factor, related more to the measurement of the specimen, is the rotation. Figure 45 illustrates this problem. The exact position of the centre of mass of the specimen is assumed to be in its geometrical centre. The impactor is set to strike the specimen in its centre as well. But due to some minor variations in homogeneity of the specimen, the actual centre of mass could be slightly off-centre. This means that a minor rotation of the specimen might be present. However, since the high-speed camera would measure the velocity of a point on the top surface, the rotation would seemingly increase or decrease the horizontal velocity of that point. The measured velocity would then be incorrect. Using a second high-speed camera from a different angle would help with this problem. But the overall issue with the high-speed camera approach is an already high time consumption of the video analysis. Therefore, a different approach must have been chosen for determining the mechanical energies after the impact. Although it is safe to assume, that factors described for the high-speed camera approach will be, to some degree, present in different velocity measuring principles as well.

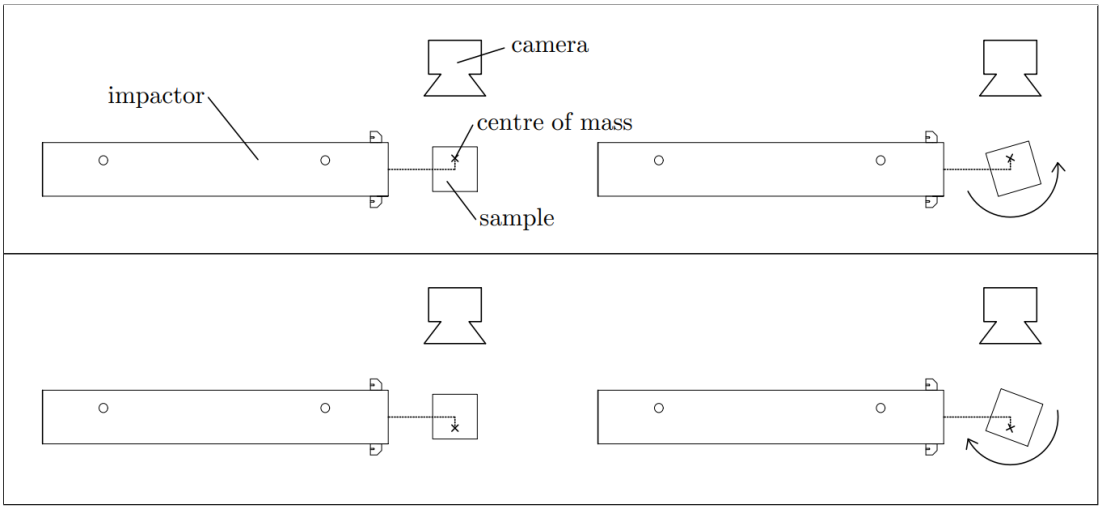

Figure 45: The possible rotation of the specimen after the impact because of an uncertain position of its center of mass.

4.3.2 Position tracking - impactor

The high-speed camera captures a relatively large area. But the impactor follows mostly the same trajectory during each individual impact experiments. This means that it could be beneficial to design a simpler way of measuring only a certain fixed point or points on the impactor. There are many ways, apart from the high-speed camera approach, to track the impactor's position. Clearly, the measuring principle needs to be a contactless approach, as we don't want to introduce any unnecessary mechanical energy losses. An optical method was finally chosen. Figure 46 shows special optical gates device. It is a steel U-shaped element, that has the electronic parts inside the boxes on both sides. On one side, there are laser modules. These modules contain everything necessary to produce a sufficiently narrow laser beam when an external power supply is provided. The beams are aimed directly at photodiodes positioned on the opposite side of the steel element. There are 6 pairs of laser modules and photodiodes in total. One pair is called an optical gate. Only a single pair is necessary for the measurements, but more pairs were added to provide more data that could be averaged or to try different methods of tracking. Figure 47 shows the photodiode circuitry. The circuitry is powered by 3 AAA batteries to provide an interference-free constant-level signal. This signal is brought to the photodiodes, which pass it forward to separate signal outputs when the corresponding photodiode is illuminated by the laser beam. The signal is completely blocked when the laser beam is interrupted. The ambient light has no meaningful effect on the circuitry. The signal from each photodiode is captured separately using a PC oscilloscope card.

The impactor itself is equipped with a special comb-like steel attachment that can be seen attached to the impactor in Figure 48. It is made from a 1 mm thick steel plate and all the holes are laser-cut for maximum accuracy. The widths of the holes and spacings between them were limited by manufacturing limitations (thinner holes resulted in thermal warping during cutting). This attachment is intended to break the laser beams as the attachment moves through the optical

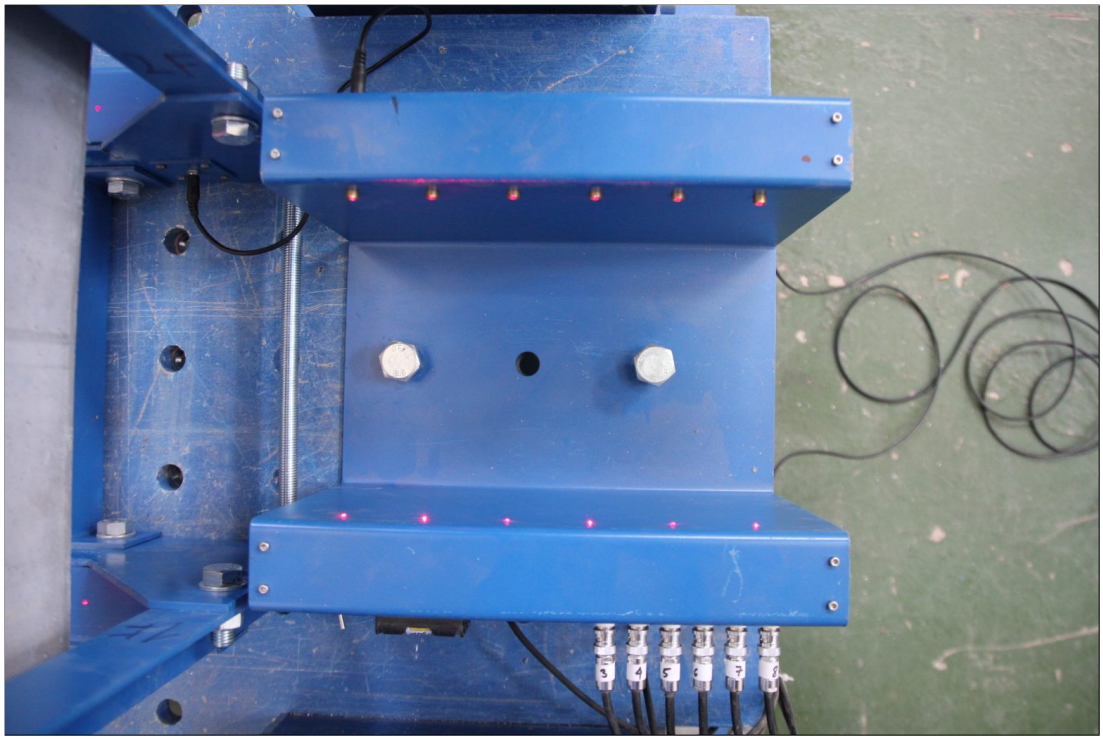

Figure 46: The six optical gates in a separate custom steel housing for the impactor tracking measurements.

gates. A relatively high number of holes was chosen to test several possible measuring methods, but as will be explained later, one possible tracking method can work with only a single laser-interrupting element. There is a counterweight on the opposite side of the impactor to not cause a horizontal offset of the impactor's centre of mass. The attachments are bolted to the impactor. How exactly is the optical gate used and what data can we obtain from it is going to be further explained in chapter 4.4.

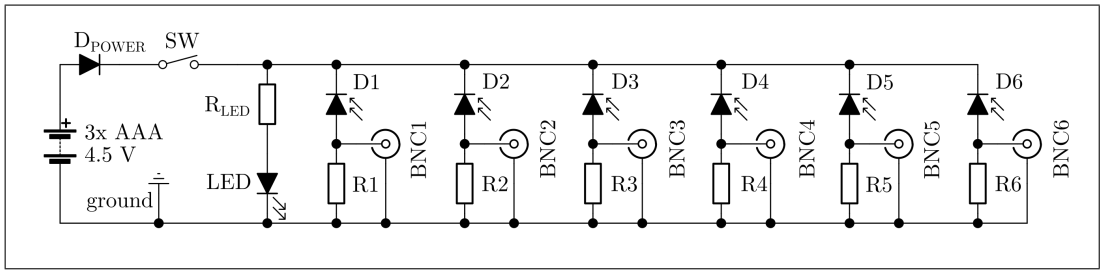

Figure 47: Schematic of the impactor's gate photodiode circuit. D_{power} is a reverse voltage protection of the power supply. Switch SW is a power switch. An LED indicates a power-on state. R_{LED} (10k Ω) is a current limiting resistor for the LED. D1-D6 are the photodiodes. R1-R6 (10k Ω) are the photodiodes' load resistors. BNC1-BNC6 are the output cable connectors.

Figure 48: The impactor's attachment for interacting with the optical gate.

4.3.3 Position tracking - specimen

As explained earlier for the velocity measurements, it is more difficult to conduct measurements of the specimen due to various reasons (mostly the specimen rotations). Using the same approach as for the impactor, i.e. attaching some sort of adapter and tracking it using a relatively small optical gate, is not going to return precise measurements. It would also introduce an unnecessary foreign object to the specimen. It was clear, that the specimen will have to be tracked during its entire trajectory. Figure 49 shows the measuring frame which was built for this purpose. It is again a steel structure, but unlike for the impactor, it is built around the entire expected trajectory of the specimen. It uses the optical gates principle using pairs of laser modules and photodiodes. There are 50 pairs on one half of the entire structure, so 100 pairs in total. The laser modules are positioned on the bottom beams facing up. The photodiodes and their circuitry are inside the top beams, so the ambient light does not cause much interference. The 40 pairs closest to the specimen's resting position are 3 cm apart, the rest of the pairs are 5 cm apart. The smaller initial spacing is intended for low energy impacts, where the specimen would not move through a sufficient number of laser beams (for precision purposes) if the spacing was larger.

Thick protective covers, with small holes just for the laser beams, cover the bottom part of the frame so the failing specimen won't damage the laser modules. The bottom steel beams are connected together and bolted to the impact pendulum's structure to provide a rigid base for the columns. The front two columns are also bolted to the structure and the back two columns are connected together using an X-shaped reinforcing element. The top beams are electrically isolated

from the rest of the structure using plastic washers. This eliminates any possible electrical grounding issues that might introduce noise into the signal. As can be seen from Figure 49, the frame is made to not interfere with the specimen's movement. The impactor can also move freely into the frame area. The top beams would eventually block the specimen's movement, but the height of the frame is designed to allow the specimen (undamaged, without a notch) to be impacted by the impactor released from a height of 50 cm. The entire frame structure can be quickly detached and moved away from the impact pendulum to change the experimental setup.

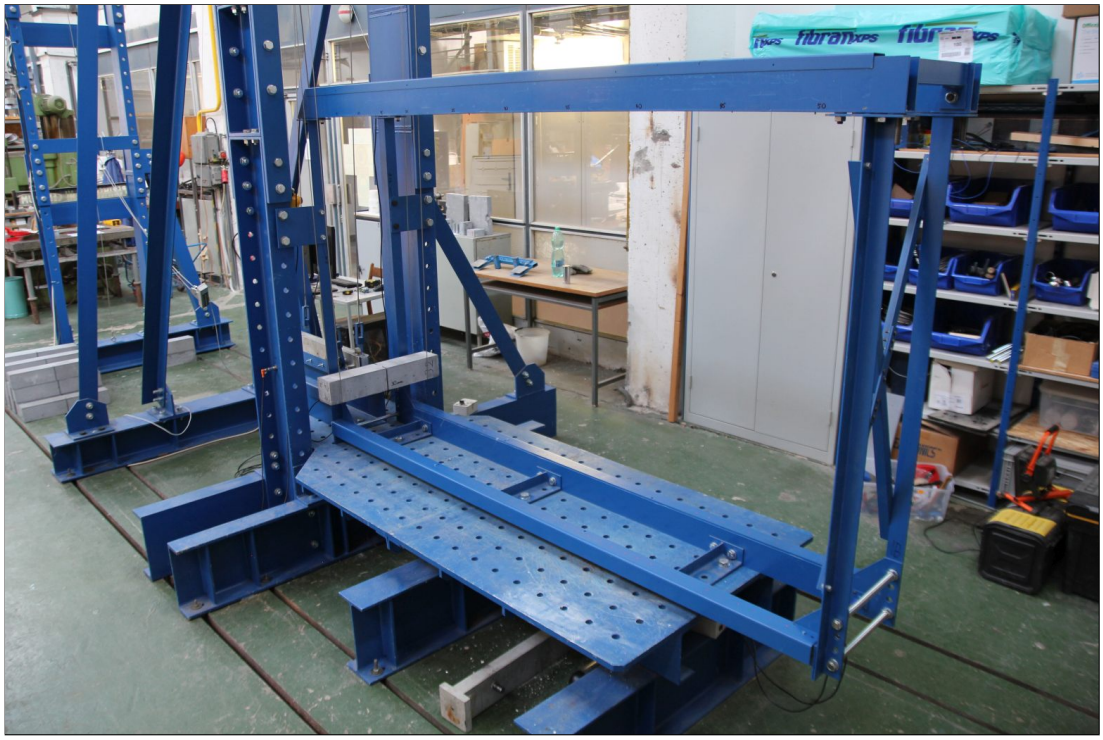

Figure 49: The measuring frame intended to track the position of the specimen.

The top U-shaped beams house the photodiodes circuitry. For easier installation, the insides are placed on a removable 10 mm thick steel strips that are bolted to the beams. Both the beams and these strips have holes with the same spacing as the bottom beam with the laser modules. These holes are much larger diameter than the diameter of the laser beams. Plastic optical lenses are glued on top of the steel strips. A small piece of a pre-made circuit board serves as a basis for the photodiode and its connections. The boards, with the photodiode facing down, are glued to the top of the lenses. The lenses serve as a reverse collimator, that ensures the laser beams always aim directly into the photodiode, even if the frame structure experiences mechanical oscillations. This oscillation would also show in the measured signal and it would affect the accuracy or even the possibility of a successful analysis. The main circuit board is vertically attached to the middle of the strip and connected with all the photodiodes. A steel cover is used to close the top of the beams to complete the electromagnetic shielding and protect the electronics from dust. The inside of the top beams can be seen in Figure 50.

The circuit schematic is shown in Figure 51. It uses an operational amplifier (OA) configured as a summing amplifier, which takes the output of each photodiode module and sums it into one (inverted) output signal. The amplifier is powered using 9 V batteries (the OA requires positive and negative power supply voltages) and the signal is provided using a single AA battery. The schematic only shows 3 photodiode modules but one circuit connects 50 modules in total and sums the signal out of all of them. When a photodiode Da1 is illuminated, it practically shorts the voltage between Ra1 and Db1 (using the first module as an example) to the ground and no signal passes through Db1. When the laser beam is interrupted, the photodiode has almost no effect on the module, therefore the signal passes through Db1 and Rb1 into the summing amplifier. The signal amplitude from one module is approximately 0.4 V to 0.7 V, depending on a voltage drop across D_{power} and Db1. This means that the resulting signal going to the BNC output connector changes by this voltage every time a laser beam is interrupted or illuminated again after being interrupted. Just like with the impactor's optical gate, a detailed usage of the measuring frame is going to be part of Chapter 4.4.

Figure 50: The photodiode circuitry in the top beam of the measuring frame.

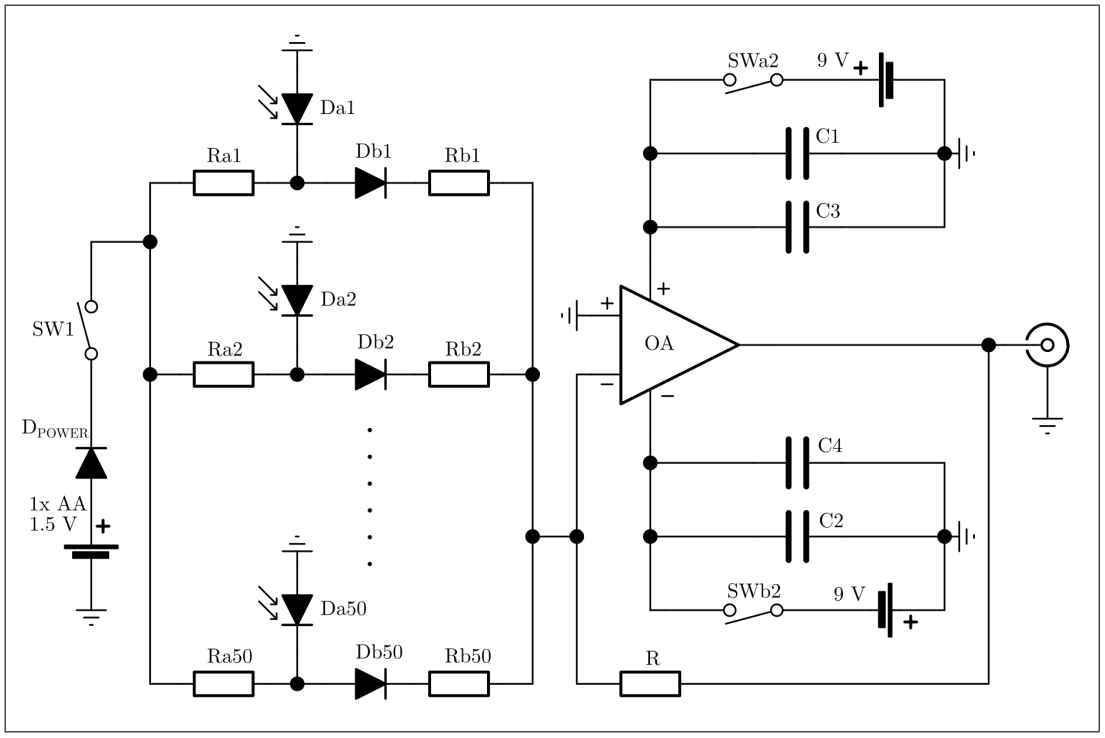

Figure 51: Schematic of the measuring frame photodiode circuitry. D_{power} is a reverse voltage protection of the AA battery. Switch SW1 is a signal switch. Ra1-Ra50 (1k Ω) isolate the signal voltage between the photodiode modules. Da1-Da50 are the photodiodes. Db1-Db50 are diodes that only allow positive voltages further into the circuit. Rb1-Rb50 (10k Ω) are the summing amplifier input resistors. R (10k Ω) determines a unity gain of the summing amplifier. OA is an operational amplifier NE5532. C1-C2 (100 µF) are a large electrolytic filter capacitors. C3-C4 (100 nF) are a small ceramic filter capacitors. SW2 (two pole) switches on the power to the operational amplifier. BNC is the output cable connector. Only 3 photodiode modules shown out of 50.

4.4 Processing the measured data

One of the main goals of the measuring principle design was to acquire data that could be automatically analysed using a computer. A script was written in MATLAB version R2019b that requires the unprocessed raw data and outputs the final mechanical energy dissipated by the specimen after one impact. This considerably lowers the time consumption of the analysis compared to manual analysis of the high-speed camera footage. Also, the accuracy of the results is higher as the entire analysis process is kept constant and since it is done by a computer, the complexity of it does not matter. The complete computer script will be explained in detail in the following text. Since the positions of the impactor and the specimen are tracked using different means, the script is also divided in two basic parts.

4.4.1 Optical gates - impactor

An example of acquired raw data from one of the photodiode - laser module pair from the impactor's optical gate can be seen in Figure 52. There are 2 voltage levels. The higher (base) level is 4.5 V which is a state when the corresponding photodiode is fully illuminated by the laser beam and therefore allows the signal through to the output. The low level of 0 V is the situation when the laser beam is interrupted by the impactor's attachment. This example is taken from the photodiode furthest away from the specimen, so it was the first to start acquiring data. The slight ripple at the end of the graph is caused by the other photodiodes' measurements but it can be seen that it is negligible. This is caused by the shared voltage source as the batteries' voltage slightly decreases when the load is suddenly applied by the other optical gates. The impact occurred at approximately 0.57 s after the start of data acquisition. It can be easily distinguished by the sudden change in frequency between the signal level changes, which was caused by the impactor's sudden deceleration. Since this is the photodiode furthest away from the specimen, it has the highest amount of signal level changes before the moment of impact. The data was acquired at a frequency of 500 kHz.

The changes in signal levels did not occur instantly, because the laser beam is not infinitely narrow, but has a conical shape with a diameter (on the photodiode) of approximately 3 mm, which is also the diameter of the photodiode casing. The laser beam is therefore interrupted gradually, although the light intensity required to cause the photodiode to fully block the signal is probably not the full beam intensity. The rise and fall times are in the order of 10^{-4} s. The photodiode itself has a response time in the order of 10^{-8} s (depending on the reverse voltage and the load resistance) so its response can be considered instantaneous for these purposes. The signal seen in Figure 52 corresponds to the forward movement of the impactor, but after it finishes the swing in this direction, it will go through the optical gates again in the backwards direction. The complete signal (not shown here) will therefore have two symmetrical parts with a clear gap between them. But only for a case when the swing forward was long enough to move the entire impactor through the optical gate. The backward motion will be important for the analysis explained later.

Since the changes in signal levels occur gradually, it is necessary to choose a certain criterion to treat each laser beam interruptions the same way. The moment of interruption and subsequent illumination is chosen as the closest measured points in the signal to a 2.25 V level (middle point between high and low levels). This is done by subtracting 2.25 V from the raw data and applying the *abs* function to invert the negative values into positive. The signal is then multiplied by a negative 1 so that positive peaks of the signal correspond to the time points that we want to extract. This extraction is done using the *findpeaks* function, which is limited to find peaks only around the 0 V level and fixed minimal distance apart to prevent the identification of unwanted peaks.

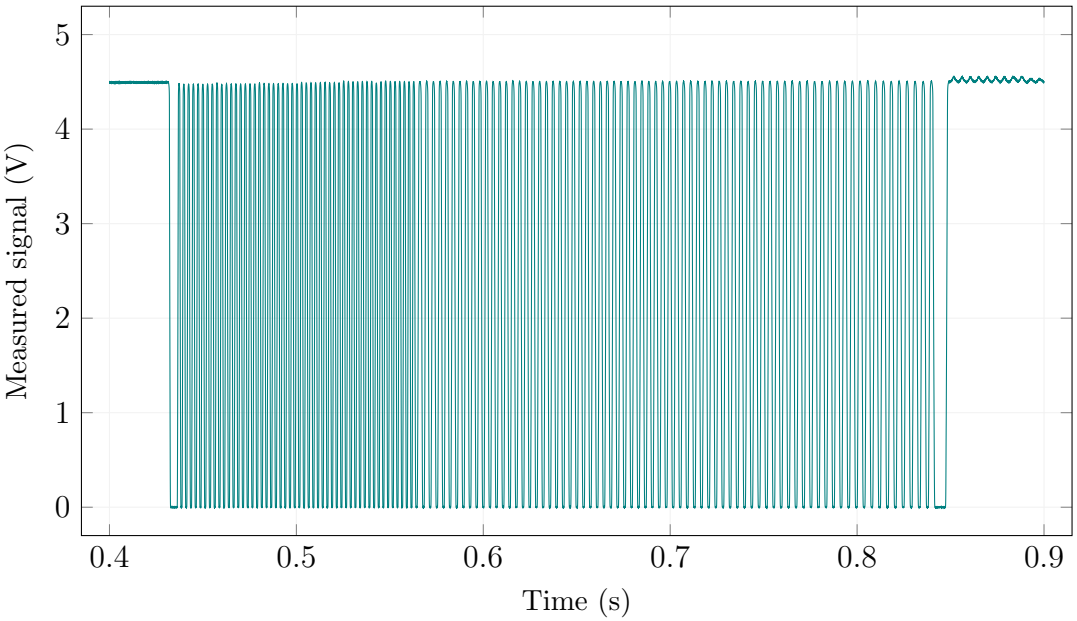

Figure 52: An example of the impactor's optical gate raw output (one photodiode).

The design of the comb-like attachment assumed using the velocity measurements approach and subsequent kinetic energy calculation. Therefore, the number of holes in the attachment is rather high to provide many laser beam interruptions for more accurate velocity measurements. But for the reasons explained earlier, the velocity measurements are by default prone to certain errors. Measuring the velocity of the impactor before it strikes the specimen can still be done, although a simpler way of calculating its initial mechanical energy is by using the potential energy approach. That requires only the measurement of the initial heigh of the impactor relative to its resting position. This measurement should not be used directly, but to calculate the centroid of the whole impactor pendulum system for maximum accuracy. There is of course a certain amount of energy lost during the impactor's movement, so the velocity measurement before the impact should, theoretically, be more precise. However, a high-speed camera measurement in the previous testing of the impact pendulum showed, that the energy losses are negligible. Ultimately, both approaches can be used simultaneously to confirm correct measurements and signalise an error in either the experiment or the data analysis.

Since we now know the exact time points when the attachment interrupted the laser beams, we need to pair this data with the geometry of the attachment. There are 250 time points stored in a column vector. This vector needs to be differentiated using the *diff* function to obtain the time differences between two consecutive time points. This reduces the number of values of the vector to 249. Another vector with the same number of values needs to be created. This vector stores the widths of the steel strips and holes of the attachment. Dividing the width vector values with the time differences vector values results in a vector of partial velocity values. Figure 53 shows these values in a graph. The moment of impact is now clearly visible. From this graph, the duration of the impact (the energy exchange) can be roughly estimated, as the velocity drop is not immediate.

It is also worth noticing the irregular velocity values right after the impact, which is most probably due to the impactor's oscillations. This only shows that averaging the partial velocity values right after the impact will most probably not result in an accurate kinetic energy calculation. But the velocities before the impact are mostly constant. Averaging, for example, 10 partial velocities before the impact can be successfully used for calculating the impactor's initial mechanical energy.

In the script, the identification of the moment of impact is done using the *diff* function again, as it will show a clear peak (which is identified using the *findpeaks* function) when the velocity drop occurred. The partial velocities vector can then be split at this time point. A fixed number of values are deleted either from the end or the beginning, for the before-impact vector and after-impact vector, respectively. This removes the values corresponding to the time interval when the impactor was still in contact with the specimen. This process is repeated for all of the photodiode measurements.

After-impact velocity is obtained similarly, but from averaging 10 to 20 partial velocities. Averaging a lower number would be possible, but probably for values after the oscillations stopped. Just like the impactor, the attachment stays horizontally oriented, but it follows a circular trajectory. This means that further away from the zero pendulum angle, the attachment's velocity vector will start having an increasing vertical component. This will seemingly lengthen the distances between the holes from the perspective of the optical gates. It could be possible to introduce a correction for this effect, but since the measurements are taken very close to the zero angle and the radius of the pendulum is much longer than the attachment's length, it is not necessary. However, the effect should be understood and only the partial velocities as close as possible to the moment of impact should be used. In Figure 53 it can be seen that the velocity starts noticeably decreasing approximately 0.05 s after the impact, which is caused by both the aforementioned effect and the natural slowing down of the impactor as it gains height.

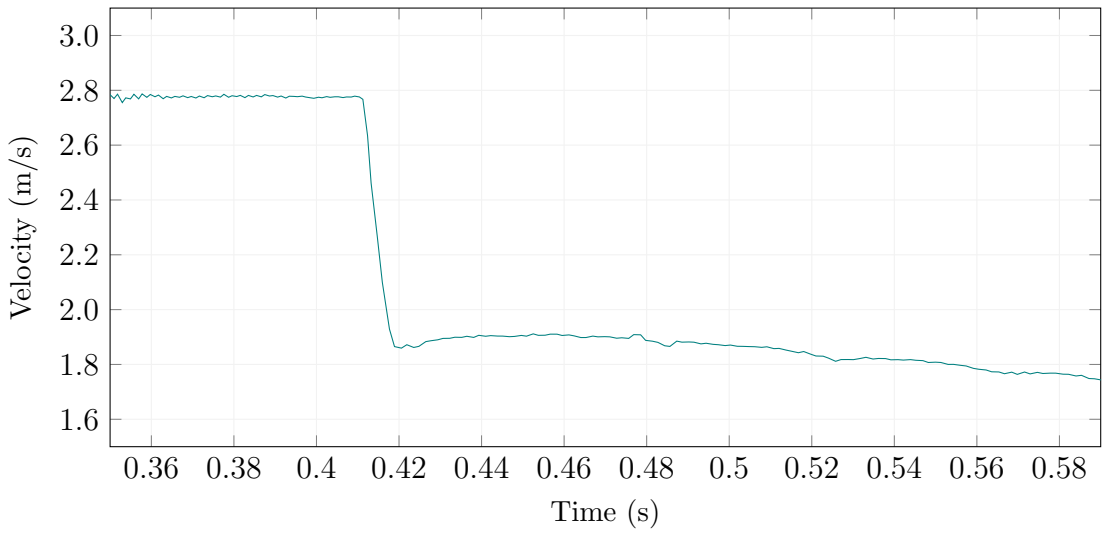

Figure 53: Typical calculated partial velocities of the impactor.

The velocity of the impactor after the impact can be determined also in another way. The exact geometries of the impactor, its attachment and its relative position to the optical gates are known. We can choose a point on the attachment, for example, its back edge. The position of this point relative to each optical gate can be determined. For each optical gate, the impactor pendulum angle (angular displacement) can be calculated for a situation when this point is exactly in the corresponding gate during its movement. Six different pendulum angular displacements θ are therefore defined using the equation

$$\theta_i = \arcsin \frac{l_i}{L} \tag{7}$$

where l_i is the horizontal distance between the chosen point on the attachment and one of the optical gates and L is the length of the pendulum's cord. In this case, that is the bearing-to-bearing distance of the cords, since both the pendulum and the attachment are staying horizontally oriented. Figure 54 illustrates this calculation for the edge of the attachment and the first optical gate.

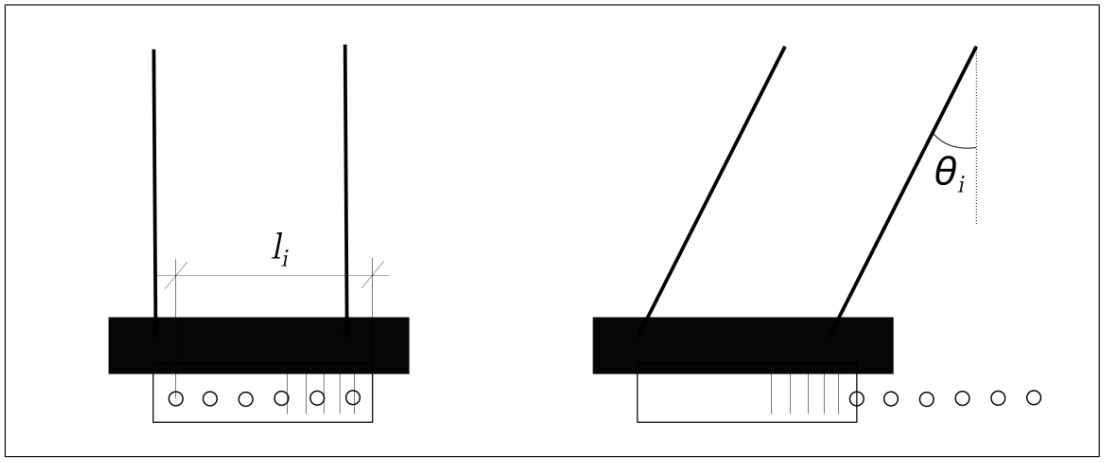

Figure 54: Schematic of the pendulum angle calculation based on the attachment's position relative to the optical gates.

When the impactor strikes the specimen, it will reach the maximum point of its trajectory and it will start moving backwards, which means that it must pass the optical gates again. Two time points are therefore obtained for the chosen point for each optical gate. Identifying these time points is done using the same peak-finding principle as described above. The back edge of the attachment was chosen intentionally because it will show in the measured signal as the last voltage change for the forward motion and the first voltage change for the backward motion. A time interval between these two points can be calculated. Dividing this time interval by two then logically gives us the time point when the impactor reached the maximum height (and zero velocity) on its trajectory. This time interval is calculated for each optical gate. Clearly, the backwards movement must be slower, as a certain amount of mechanical energy was dissipated by the swinging pendulum. If more than one optical gate measurements are available, a quick comparison between the forward and backward velocity can be made. Based on experimental data, the velocity decrease is no more than 0.5 %, which means that movement energy losses are almost negligible and the maximum height on the trajectory truly did occur at the middle of the obtained time intervals.

We can pair the calculated angular displacements with the corresponding halves of the time intervals and plot them, which can be seen in Figure 55. This means that at the time zero, there is the maximum height of the trajectory, which is unknown. But since the parameters of the pendulum, and at least two X coordinates and one Y coordinate are known (the time zero and at least one optical gate measurement), we can obtain a theoretical curve of the pendulum's motion. An equation of a physical pendulum motion is

$$J\frac{d^2\theta}{dt^2} + MgC\sin\theta = 0 \tag{8}$$

where J is the moment of inertia of the whole pendulum system about the pivot point, θ is the angular displacement, M is the mass of the entire system and C is the distance between the centre of mass of the system and the pivot point. In literature, a simplified pendulum equation can be found. But this is the general form without the small-angle assumption. Not only are large angles expected here, but higher accuracy is needed.

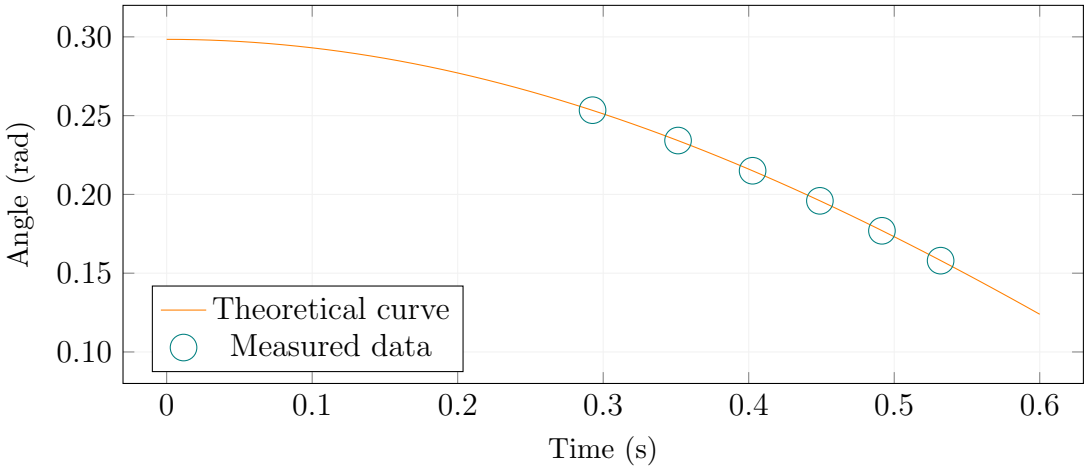

Figure 55: A fit of the theoretical curve on the measured positions of one point on the impactor's attachment.

The differential equation can be solved in MATLAB using the *ODE45* solver. The initial conditions for the solution are going to be the angular displacement and the angular velocity, which is unknown and zero, respectively. This calls for an iterative solution. A reasonable value of the angular displacement is chosen for the initial iteration cycle (0.5, for example). The differential equation is solved and points on the theoretical curve with the same X coordinates as the experimental data are identified (using the *deval* function on the differential equation solution). Y coordinates of these points are averaged as well as the Y coordinates of the experimental data. If the relative difference between these two averages is larger than 0.01 % then the iteration continues to find a better initial angular displacement. The angular displacement value for the next cycle is estimated using a simple linear rule. We want to calculate the coefficients a and b of a linear equation

$$P = \theta a + b \tag{9}$$

We can use the angular displacements θ and the relative differences P to write a

system of two linear equations with two unknowns

$$\begin{aligned} P_{old} &= \theta_{old} a + b \\ P_{new} &= \theta_{new} a + b \end{aligned} \tag{10}$$

where the *old* index represents values calculated for the previous iteration cycle and the *new* index for the current cycle. If the iteration just started, then the *old* values are from the solution of the differential equation where the angular displacement value was chosen and the *new* values are for the initial iteration cycle, where the chosen angular displacement was raised or lowered by a fixed value. A simple larger-or-lower check of the difference between the averages of Y values determines whether the angular displacement needs to be raised or lowered for the initial cycle.

After solving this system of equations, we can use Equation 9 to calculate the angular displacement for the next step. We simply make P equal to zero, as that is the desired difference between the ideal curve and the experimental data as described above. This linear rule is of course not precise, as the actual relationship between the angular displacement and the subsequent relative difference is not linear, but nevertheless, when used as an estimate, it makes the iteration process converge very well. The conditions are usually satisfied after just 5 cycles. The fitted ideal curve can be seen in Figure 55. Even though all six measured points are shown there, only one is necessary for a successful calculation. It can be seen, that the fit is almost perfect. This is because the physical pendulum equation was used and moment of inertia, mass and centre of mass position were determined, accurately describing the pendulum system. In a way, this is also a check that negligible mechanical energy is dissipated by the motion of the pendulum and that the pendulum's parameters were determined correctly, otherwise the fit would not be as good.

The next step is to obtain the final value for the initial angular displacement θ_{final} (used in the last iteration cycle) and use it to calculate the vertical height of the pendulum and its potential energy using equation

$$E_{I.post} = Mg(C - C\cos\theta_{final}) \tag{11}$$

where M and C are the same as for Equation 8. Kinetic energy can also be calculated from the theoretical curve, but unnecessarily complicated calculation must be made to obtain the velocity at the point of zero angular displacement. However, the velocity can be calculated the other way around from the kinetic energy, since it is equal to the potential energy from Equation 11. This velocity can be used to compare it with the velocity obtained from the previously explained approach of the attachment tracking. Based on experimental data, the velocity and the mechanical energy obtained using this second approach is consistently slightly higher compared to the first approach. This is correct, as the first approach truly must provide lower velocities because of the inability to measure velocities immediately after the impact because of the oscillations. The second approach is, therefore, more precise, burdened only by the energy loses during the pendulum swings between the forward and backward measurements. But, as explained above, this effect is negligible. Similarly to the before-impact impactor energy, two approaches can be used simultaneously to prevent errors.

4.4.2 Measuring frames - specimen

Processing the measuring frames data is more difficult compared to the impactor's optical gates measurements. Since there are 50 photodiodes' signals being summed into a single output signal, a more complicated signal processing needs to be used. An example of raw data from one half of the measuring frame is represented by the green signal in Figure 56. Similarly to the impactor's optical gate, each sudden drop in the signal level corresponds to a laser beam being interrupted. Each sudden rise is a moment when a laser beam could illuminate the photodiode again. The exact time points when these sudden changes happened need to be extracted. The signal is first smoothed using a Savitzky-Golay filter (*sgolayfilt* function with order 1 and frame length 101[5]), which removes the high-frequency digital noise which is the result of an analogue to digital signal conversion in the PC oscilloscope card. More high-frequency noise is also introduced by all the resistors in the measuring circuit. Electrical resistance introduces certain thermal noise with increasing resistance and temperature. Since the circuit sums the signal from 50 modules, this noise must be taken into account. That is the reason why the resistor values must be kept to a minimum while maintaining a certain degree of module separation and signal battery load. The noise has an acceptable amplitude but its high frequency creates very steep gradients. Its presence would prevent us from analysing the signal further.

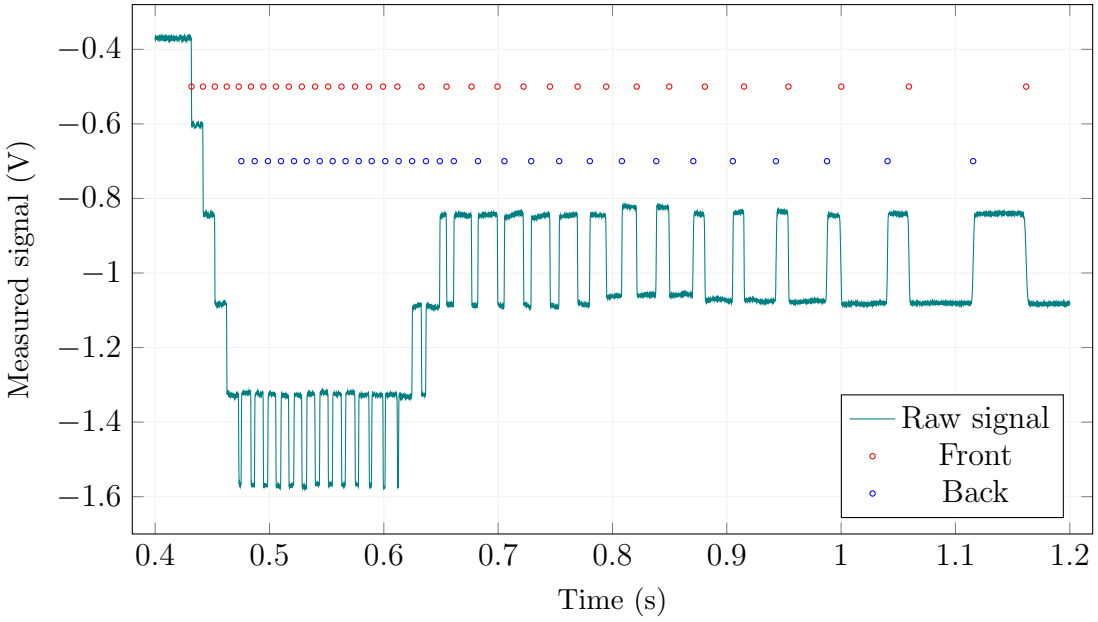

Figure 56: A typical position tracking raw signal with automatically identified specimen positions.

[5]The frame length is, simply put, the number of values considered by the filter in the vicinity of the currently evaluated point. i.e. it is the level of smoothening. It must always be an odd number. This frame length value might seem rather high. This is due to the high data acquisition rate of 500 kHz which is, in this case, unnecessary. In general, the acquisition rate and the degree of filtering should be balanced to have the lowest number of measured points (to speed up the analysis process) while retaining a certain level of data precision and signal-to-noise ratio.

Since we are looking for instances in the signal where it rapidly changes, the *gradient* function is applied to return a one-dimensional numerical gradient of the original signal. The result of this phase can be seen in Figure 57. Next, peaks that are present here are identified using the *findpeaks* function, which is set to only find a single highest peak in approximately a 0.01 s interval, otherwise some smaller peaks or duplicates would be mistakenly identified as well. A minimum height of the peaks is set to a level just above the noise, which stays constant in all of the experiments (for given acquisition rate and filtering). The positive peaks represent a subsequent illumination of the photodiode, so these are labelled *back*, because it is the last point on the specimen that still blocked a laser beam. The negative peaks then represent the *front* of the specimen or the first point on the specimen that interrupted a laser beam. These negative peaks are identified using the same *findpeaks* function, but on an inverted data set. All of the identified peaks are shown back in Figure 56 as the red and the blue points. It can be seen, that the positions of these points do correspond with the changes in the raw signal. This graph is displayed to the user during the analysis process, to check for errors.

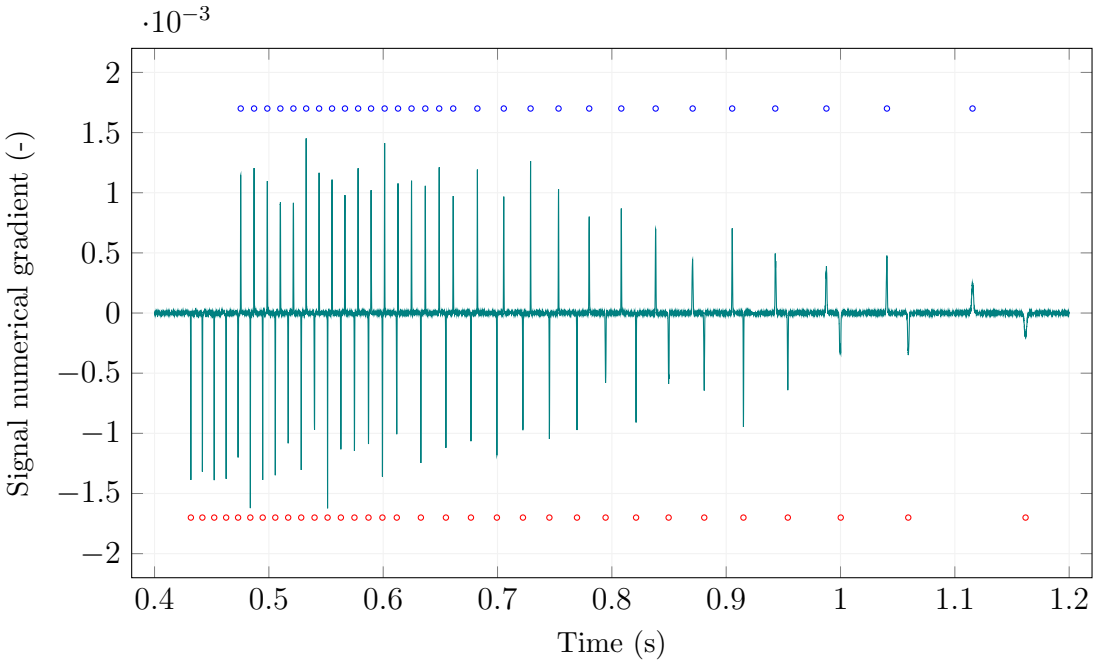

Figure 57: A numerical gradient of the raw signal used to identify the specimen positions.

All the peaks in the gradient data set are points, where there is an inflexion point in the raw signal. It can be safe to assume, that this inflexion point physically occurs at the same illumination level for each photodiode. Applying the same technique for each photodiode measurement should then give us precise time intervals between the laser beam interruptions, which is the desired result. Note that in figure 57 the peaks are lower on the right side of the graph. This is because the specimen is inevitably coming to a stop, therefore the laser beams (that have a certain diameter) are also interrupted at a decreasing rate, so the change in the photodiode illumination is also slower, resulting in a smoother change in the signal and lower gradient. The data is cut so that only the forward motion

measurements are considered. When the specimen starts moving backwards, after it reached its maximum position, it would flip the imaginary back and front of the specimen and unnecessarily complicate the following steps. The point where the specimen stopped moving is clearly visible because at this point there is the largest time interval between any changes in the raw signal.

The time data now needs to be paired with the geometry of the measuring frames. Before each experiment starts, it is necessary to measure the actual position of the specimen relative to the measuring frames and therefore the laser beams. The horizontal positions of the laser beams are known. But for the following calculations, we need to know the angular displacement θ of the specimen, so each laser beam position also needs to be converted to angular displacement using the formula

$$\theta_{beam} = \arcsin \frac{X_{beam}}{L} \tag{12}$$

where L is the length of the steel ropes and X_{beam} is a horizontal distance between a laser beam and the specimen. This calculation is done twice for each laser beam. First, the X_{beam} is calculated to the front of the specimen and second time the X_{beam} is calculated to the back of the specimen. This results in two vectors that store the corresponding angular displacements relative to both the front and the back of the specimen in its resting position. The script then reads the size of the time vectors, where the previously calculated time data is stored and cuts the angular displacement vectors so they are the same length. This results in two pairs of vectors for front and back measurements. There will always be more values in the front time vector, as the last interrupted laser beams were not cleared again in the forward motion of the specimen. Plotting the paired data shows us the movement of the front and the back of the specimen, which can be seen in Figure 58 as red and blue dots and lines, respectively.

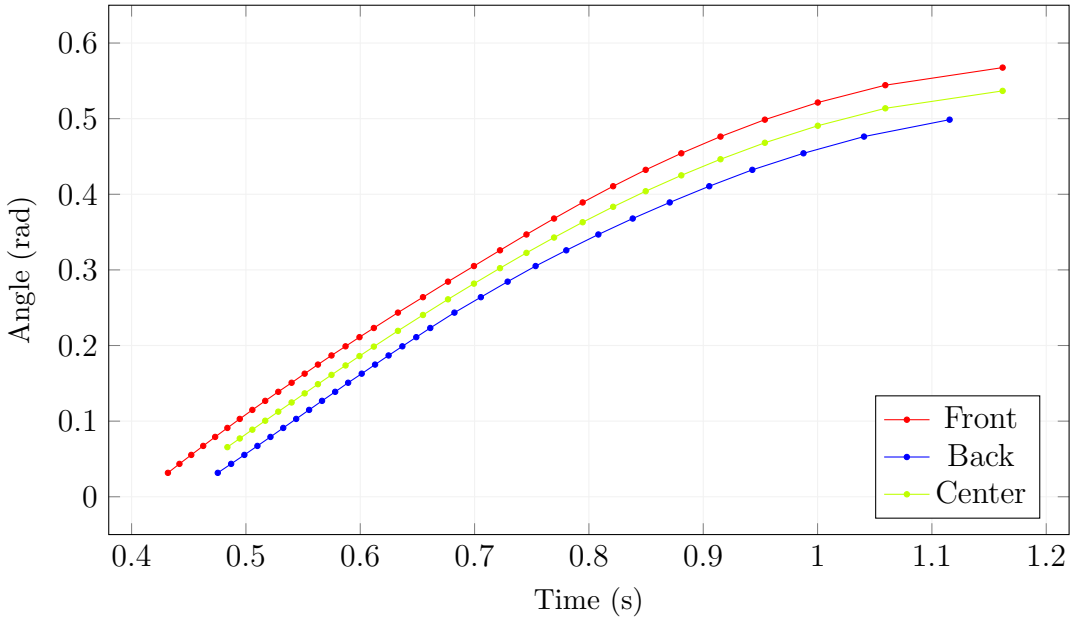

Figure 58: The signal points paired with the laser beam positions and a calculated centroid position.

The blue (back) dots are used to calculate a fit curve using the *fourier3* fit type. This allows us to evaluate Y coordinates of the fit curve for the same X coordinates of the red (front) dots. In the next step, the vertical distances between the corresponding Y values are averaged, which gives us the exact angular displacement between the measured data sets. This is the angular displacement corresponding to the centroid of the cross-section of the specimen that moved through the laser plane. In the graph in Figure 58, it is represented by the green dots and lines. This graph also serves as the final check of the correctness of pairing the measured data with the geometry of the measuring frames. Smooth curves like these must be obtained. Uneven changes in the curves signalise an error in the extraction of the time points from the raw signal. The user then must either remove certain photodiodes from the analysis (the script failed to recognize it) or remove a mistakenly identified peak (does not correspond to a photodiode). It should be noted, that with enough practice, this manual correction can be performed quickly and it does not worsen the accuracy of the results. The occurrence of these errors is minimised by acquiring a clearer signal, which is the reason for several technical measures explained throughout this text, including minimising the noise, increasing the frames' rigidity and using the optical lenses.

The theoretical pendulum motion curve is going to be fitted on the experimental data. A physical pendulum equation is going to be used, which is the same as for the second approach for determining the impactor's after-impact energy as explained above (Equation 8 with new values for the specimen pendulum system). The centroids' position tracking should have enough points, especially towards the maximum point of the actual trajectory, so that the theoretical pendulum's motion curve can be fitted to the experimental data. The differential equation 8 will be solved in MATLAB using the *ODE45* solver. But this time, the initial conditions for the solution are going to be the angular displacement of the first point of the centroids' tracking and the angular velocity which is unknown at this point. An iterative approach must be used. A reasonable value of the angular velocity is chosen for the initial iteration cycle. The differential equation is solved and points on the theoretical curve with the same X coordinates as the experimental data are identified (using the *deval* function on the differential equation solution). Y coordinates of the last 5 of these points are averaged and the Y coordinates of the last 5 points of the processed experimental data are averaged as well. If the relative difference between these two averages is larger than 0.01 % then the iteration continues to find a better initial angular velocity. The angular velocity value for the next cycle is estimated using a simple linear rule, exactly as previously explained for the impactor. This iteration is also completed after 4 to 5 cycles. The fitted ideal curve can be seen in Figure 59 represented by the green line over the orange points representing the calculated centroid positions.

In this example, it can be seen that the fit is also very good. Similarly to the impactor, this proves the correctness of the pendulum system parameters, otherwise the shape would not follow the measured data. During the impactor analysis, it was possible to simply take the iterated initial condition for the angular displacement and directly use it for the energy calculation. In this case, the iterated angular velocity is the angular velocity at the start of the curve, but that is not the time point of the impact. Therefore, this value is meaningless

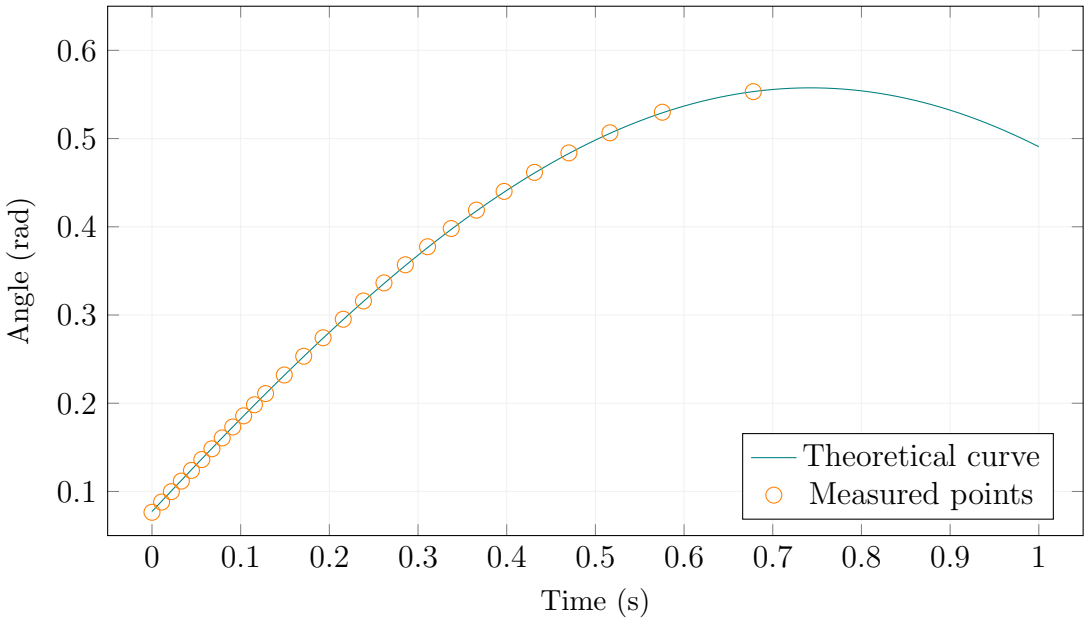

Figure 59: Final fit of the theoretical pendulum curve on the measured data.

and only serves for the iteration. The maximum point of the trajectory must be identified, which is done using a simple *while* loop in the script. It takes the value on the curve corresponding to the last measured point and evaluates the curve going forward with small steps. The loop stops when the next Y coordinate is lower than the previous one (the curve starts going down - the maximum has been reached). Differentiating the curve would have also been possible, but this numerical approach is simpler.

At this point in the analysis process, we have the maximum angular displacements of the centroids of the specimen's cross-sections moving through the laser planes on both measuring frames. Converting these angular displacements θ back into heights H (relative to the resting position) is easily done using equation

$$H = L - L\cos\theta \tag{13}$$

where L is the distance between the centroids and the pivot point of the pendulum. These two centroid heights need to be calculated into the height of the centre of mass of the specimen. If we assume a perfect prismatic shape of the specimen, then a simple average between the two values will suffice. However, the specimen will begin to deform due to the developing damage. Since the specimens have a notch, the crack will propagate more or less from the notch towards the impact point. i.e. through the middle of the specimen. This means, that two halves of the specimen are going to form with a certain angle between them. Averaging the centroids' positions will be less precise with increasing damage. This situation is illustrated in Figure 60 A (top view of the specimen). Only one half of the specimen is shown, the opposite half would be symmetrically oriented on the left side. This is an exaggerated example if the specimen was very heavily damaged. Angle α represents one half of the angle between the halves of the specimen. $CMOD$ is the crack-mouth opening displacement (measured after the impact - will be later explained). C_{SH} is the centre of mass of one half of the specimen,

while the C_S is the overall centre of mass. C_{FH} is the centroid position in the laser planes, which are 360 mm apart so 180 mm from the middle of the specimen. C_F would be the incorrectly calculated position of the overall centre of mass, based only on the centroids' positions. L_S is the length of one half of the specimen and W_S is its width. Points A and B and distances a and b serve only for the subsequent derivation.

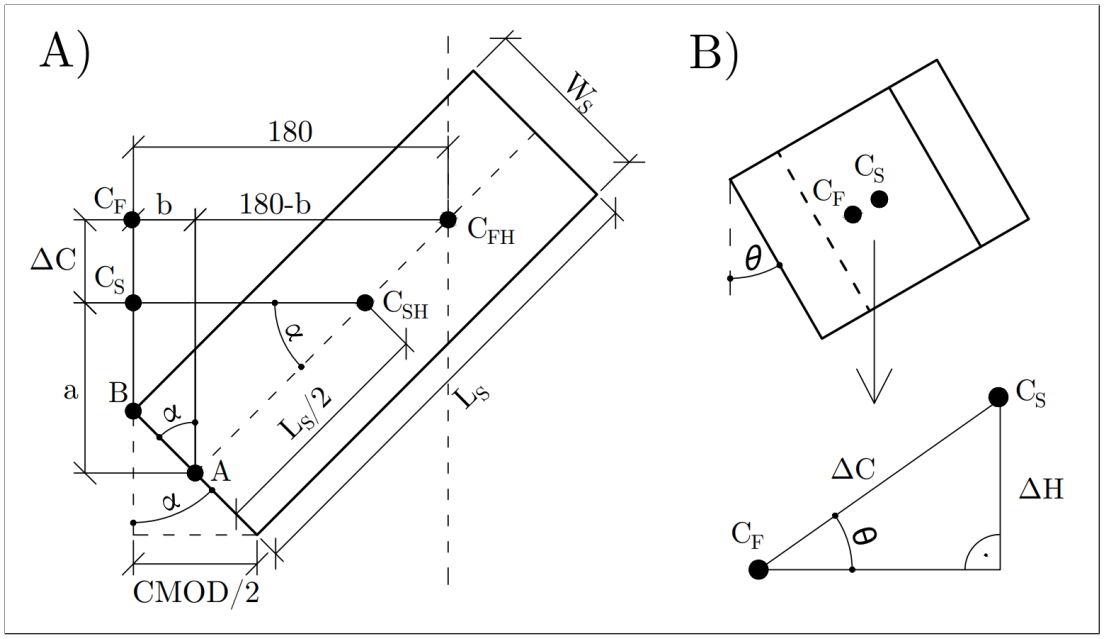

Figure 60: Schematic illustrating the specimen's centre of mass correction because of the damage-induced geometry change.

The correction of the position ΔC needs to be calculated. Using several similar triangle principles and considering the point A as the reference point, a surprisingly complex equation can be derived

$$\Delta C = \frac{90\ CMOD}{\sqrt{W_S^2 - (\frac{CMOD}{2})^2}} - \frac{CMOD^2}{8\sqrt{W_S^2 - (\frac{CMOD}{2})^2}} - \frac{L_S\ CMOD}{2\ W_S} \tag{14}$$

It should be noted, that because of the size of the specimen and the distance between the frames, the correction ΔC will always move the actual centre of mass forward, but a longer specimen could make the correction negative. Since the specimen will not only open like this, but also rotate along its length, the actual centre of mass will move higher. This is illustrated in Figure 60 B (side view of the damaged specimen). ΔC needs to be calculated into a vertical height correction and added to the previously acquired height H using equation

$$H_{final} = H + \Delta C \sin\theta \tag{15}$$

where θ is the angular displacement corresponding to the maximum point on the trajectory. Again, the height correction could be negative, if the specimen was longer or the measuring frames were closer.

This calculation introduced several simplifications. For example, the middle of the specimen is perfectly centred between the frames, the specimen will rotate with the same angle as is the pendulum's angular displacement and the effect of the specimen's horizontal rotation is not considered. Also, the θ in Equation 15 is slightly smaller, as it is the value corresponding to the uncorrected centre of mass. A correct value would need to be established iteratively. All of these effects were studied by modelling the specimen in AutoCAD and measuring the actual corrections for unrealistically exaggerated pendulum swings and specimen damage. It was observed, that all of these effects are negligible and even the above described calculation introduces only a minimal correction. It must be understood, that heavily damaged specimens will not swing high on the impact pendulum, therefore the *sin* function in Equation 15 will make the correction even smaller. Nevertheless, the correction is applied in the script for completeness. The final potential energy of the specimen is calculated as

$$E_{S.post} = Mg(C - C\ \frac{L - H_{final}}{L}) \tag{16}$$

where M is the mass of the whole pendulum system, C is the distance between the centre of mass of the system and the pivot point and L is distance between the pivot point and the centre of mass of the specimen only.

Chapter 5

Experimental program

The topic of this chapter is going to be the materials used for the experiments, manufacturing of specimens and introduction of the specific experimental processes (apart from the description of the impact pendulum, which was in detail described in Chapter 4). The impact pendulum experiments are only one part of the overall process of evaluating the composite materials. Quasi-static as well as suitable non-destructive experiments can further help to understand the material behaviour and to complement the high strain-rate results. As mentioned at the beginning of this thesis, a broad range of materials needs to be used. Using a wide selection of materials and therefore a relatively high number of specimens will serve two main purposes. The first one is the evaluation of the impact pendulum and the experimental principle from both the technical point of view as well as its suitability for material testing. This might reveal some possible problems and lead to further optimization of the process. The second purpose is gathering the actual experimental data regarding the materials' ability to absorb and dissipate mechanical energy.

5.1 Materials

Materials selected for this study are based on the literature overview as well as first-hand experience related to the author's previous work at the CTU. At first, the idea was to select materials based on several factors. The complete material composition should be available in literature together with the manufacturing process information. Also, since the impact pendulum is a new device, these materials should have already been subjected to different high strain-rate experimentation methods for possible comparison. Last but not least, the materials should be reproducible in the local conditions.

The literature overview revealed, however, that these factors are not met in the vast majority of cases. In some cases, authors do not provide the material design information at all. The largest number of scientific articles then provide rather limited information regarding their materials. Most often, the aggregate sizes are not provided or the admixtures are not specified. Unfortunately, this problem was predominant in articles dealing with ultra high-performance concretes and high strain-rate loading. One possible explanation might be, that the authors simply do not wish to disclose their mixture designs.

The ability to recreate materials in our local conditions is also limited. Cement types differ in different parts of the world. Aggregate sizes locally available are usually in the powers of 2 (4 mm, 8 mm, 16 mm etc.), but certain mixture designs require non-standard (to us) sizes. The admixtures, especially the silica fume, have different sources and might differ in their chemical compositions. The specific type or commercial designation of superplasticizer or high-range water-reducers are almost never mentioned in the articles. But, it is safe to assume that the same brands would not be locally available anyway. Water dosage is also problematic. Factors that influence the correct water dosage could be related to the high-range water-reducer, but also to the type of aggregate, its porosity or its level of humidity before mixing. None of these factors were addressed in the researched literature sources.

All of this leads to the final choice of approach to the material selection for this thesis. The majority of testing is going to be focused on materials that were already used in the Experimental Centre. The main variable with these materials will be the fibre content and types of fibres. From the literature, two different materials were chosen, because they satisfied the above-mentioned factors the best. However, their final composition was changed to fit the local manufacturing limitations. This means, that a subsequent comparison of results between the original source article and this thesis is meaningless. The mixture variants and their compositions are in Table 4. The constituents are given relative to the cement content. Table 5 shows the fibre volume contents and fibre types used with these mixtures. The following text will provide a further description of the mixtures including the fibre reinforcement and other details.

Table 4: Mixtures summary.

Constituents	**Mixtures**			
	HSC	**DM**	**L**	**R**
Cement 42.5 R	1.00	1.00	1.00	1.00
Silica fume		0.10	0.10	0.39
Silica flour		0.25		0.28
Ground limestone			0.07	
Aggregate (mm)				
0.1/0.6				0.70
0.1/1.2		1.60		
0/4	3.05		0.67	
4/8	1.95		1.18	
HRWR[a]	0.01	0.01	0.013	0.02
Anti-foaming agent		0.001		
Water	0.46	0.1[b]	0.30	0.38
Water/binder ratio	0.46		0.27	0.27

[a] high-range water reducers
[b] relative to the dry mixture's weight

Table 5: Fibre volumetric contents.

Mixture	Fibre type S	Fibre type H	Mixture	Fibre type S	Fibre type H
HSC		0.50	DM	1.00	
		0.63		1.50	
		1.00		2.00	
L		0.50			1.50
		1.00		0.50	1.00
		1.50		1.00	0.50
R	2.00				
	3.00				
	4.00				

S - Straight 13 mm × 0.14 mm
H - Hook-end 30 mm × 0.38 mm (DRAMIX 3D)

5.1.1 High strength concrete - HSC

A relatively ordinary fibre-reinforced concrete mixture (designated HSC - high strength concrete) was chosen to compare its performance with the rest of the high-performance concrete types. The mixture design was previously used by other researches at the Experimental Centre to study the effects of high-velocity impact [91, 92]. The unreinforced mixture achieved approximately 60 MPa compressive strength. As expected, this type of concrete exhibited significantly worse projectile impact resistance compared to high-performance concretes. It was reinforced using a 0.63 % fibre volume content.

For this study, the same fibre content was chosen as well as 0.5 % and 1.0 % for better comparability with other types. The mixture contains 350 $\mathrm{kg\,m^{-3}}$ of cement which is a value close to a commonly used modern concrete. This amount of cement combined with the absence of other special admixtures and high water to cement ratio only justifies the use of longer hook-ended fibres. The maximum aggregate size is only 8 mm, which is more suited for including reinforcing fibres. The high-range water reducer was the Sika ViscoCrete -20 HE.

5.1.2 High performance concrete - DM

High-performance concrete designated DM (dry mixture), is a concrete mixture developed, extensively tested and used in the Experimental Centre. This material was developed by doc. Karel Kolář [93]. It is a special type of concrete which uses mostly readily available materials. It is supplied to the laboratory in the form of a dry mixture, which contains every constituent except water and fibres. This makes it easy to use for specimen preparation. The fresh mixture offers great workability, but it sharply decreases as reinforcing fibres are added.

The compressive strengths measured in [21] were, on average, 120 MPa. A large number of other experimental data are available regarding the flexural and tensile strengths or projectile impact resistance for various fibre volumes [39, 83, 87]. The cement and silica fume content are rather low compared to other (ultra) high-performance designs found in the literature. This makes this material more commercially viable.

Since silica fume and relatively fine aggregate sizes are used, the use of small-diameter steel fibres is justified with this mixture. However, to better understand the effects or different fibre geometries, the larger hook-end fibres were also used. This serves for better comparability between mixtures DM and L. But especially the combined effect of two types of fibres is examined. This could combine the positive effects that the fibre types offer. The shorter fibres should provide better homogeneity of the mixture, as there is a larger number of fibres for a given volume. The larger fibres then offer better pull-out performance thanks to their length and hooked end. It was also observed, that the larger fibres do not affect the workability of the fresh mixture as much as the shorter fibres.

5.1.3 High performance concrete - L

Another mixture design was taken from a study conducted by Luccioni et al. [94]. It is a high-performance fibre-reinforced concrete with an average compressive strength of 114 MPa. It is a mixture design, that still uses the ordinary aggregate sizes used in the previously described HSC mixture. The major difference, however, is much higher cement content of 730 $\mathrm{kg\,m^{-3}}$ in combination with silica fume and ground limestone. These admixtures contribute to higher strengths, improved workability and allow for more efficient fibre anchoring. The water to binder ratio is also much lower. Luccioni et al. studied the resistance of this concrete against blast loading as well as quasi-static bending tests of slabs. They reinforced the material with hook-ended fibres 60 mm long in 0.5 % and 1.0 % volume contents.

For the research in this thesis, 30 mm fibres were used as longer fibres would exhibit significant preferential orientation in 100 mm wide moulds. Apart from these two fibre contents, a 1.5 % fibre content specimens were also manufactured. Although workability with this high amount of fibres was poor, vibrating the fresh mixture in moulds resulted in very good compaction. However, fibres started to form bundles and could not be completely dispersed. The fibres also seemed to start segregating from the fresh matrix.

The authors did not provide the specific type of high-range water reducer, therefore, the material was first tested with local types. In the end, the Stachement 2483 was used, as it provided the best workability. The authors stated, that their water to binder ratio was 0.24. This value was impossible to maintain with the local materials and conditions. This mixture forms a transition between the mixtures HSC and DM, as it uses coarse aggregate and larger fibres, but on the other hand similar cement and silica fume contents as the DM.

5.1.4 Ultra high-performance concrete - R

The second mixture taken from the literature is an ultra high-performance concrete matrix developed and presented by Ranade et al. [95]. The compressive strength of this material exceeds 150 MPa. It utilizes very fine aggregates only up to 0.6 mm (compared to the 1.2 mm in DM). It also has the highest cement content of 907 $\mathrm{kg\,m^{-3}}$ which is higher than the weight of the aggregate. Silica fume content is also very high at 353 $\mathrm{kg\,m^{-3}}$. The authors state, that they used a water to cement ratio of only 0.15 but the minimum locally achievable water to binder ratio was 0.27 with 2 % of the Sika ViscoCrete -20 HE (relative to cement content).

In the source study, the authors did not use steel fibres, but polyethylene. Nevertheless, this material was chosen for this thesis because of the high amount of binders, the usage of the same 0.1 to 0.6 mm silica aggregate which is locally available and also because no special curing regimes were used. Thanks to this aggregate size and the amount of silica fume, the mixture was an ideal candidate for very high fibre dosages. In the end, 4 % fibre volume content specimens were manufactured. Small trial specimens were possible to manually mix even with 6 %. However, the 4 % content proved to be the maximum amount for the large-volume mixing process in the available mixer.

The unreinforced fresh mixture surprisingly did not exhibit good flowability. The fresh mixture had a honey-like thick consistency. But unlike the DM, the workability and flowability did not drastically decrease with the addition of fibres and the placement into the moulds was still rather easy. However, when vibration was applied, the mixture did not show the same thixotropic behaviour as other mixtures, probably due to the very high amount of fibres. This material fills the role of a very high-strength composite above the mixture DM.

5.2 Specimens

All the specimens manufactured for the experimental program were beams 100 mm × 100 mm × 550 mm. The materials were mixed in a 70 l pan mixer. Water was added together with the high-range water-reducer. Fibres were slowly sprinkled into the mixture during mixing. Care was taken to place the fresh mixture only into the centre of the moulds. The material was free to flow to the rest of the volume either on its own or using vibration and manual compaction. It was important to use the same filling method for all specimens, as it limited the influence of the placement method on the orientation of fibres. Nevertheless, the varying orientation cannot be completely eliminated. The specimens were demoulded after 24 h and placed in a closed environment with high relative humidity for at least 28 days. For each mixture and fibre percentage or type, 9 specimens were made - 135 in total. Part of the specimens can be seen in Figure 61. Note the different colours of the specimens, which is indicative of the silica fume content.

Figure 61: A part of the manufactured specimens.

A notch was cut into the centre of all specimens after the curing period ended. The notch was 30 mm deep, as recommended by the standard JCI-S-001-2003 (Method of test for fracture energy of concrete by use of notched beam) [96]. For the impact pendulum testing, the notched specimens were chosen based on the previous research [21]. It was discovered, that under impact loading, specimens from the same sample developed significantly different damage patterns. Certain specimens, usually with higher percentages of fibres, cracked in various places around the centre span with the main crack propagating sometimes significantly far away from the centre. This was a variable, that made the comparison of the results problematic. A notch should unify the damage patterns. Notched specimens were used for the quasi-static testing as well. Without the notch, a standard four-point bending experiments would have to be used. However, the three-point setup resembles the impact pendulum experiment more, which should also improve the comparability.

5.3 Non-destructive testing

5.3.1 Electromagnetic coil measurement

Non-destructive principles were used to examine the possibility of tying the resulting mechanical parameters of the materials to a certain value that can be determined before the test. Since the parameters are going to be largely influenced by the dispersion and orientation of the metallic fibres, the electromagnetic coil measurement method was chosen. Every coil made of an electrically conductive wire is going to have certain electrical properties based on the wire material, its diameter, number of turns, shape and size of the coil and most importantly on the core material. The core is the space inside of the coil. Placing a metallic material, that would react to the magnetic field, inside the core will significantly change

the coil's behaviour in an electric circuit. Materials that exhibit no or negligible reaction to the magnetic field, such as air or concrete, will have a negligible effect on the coil's performance.

Figure 62 shows the setup for the electromagnetic coil measurements. The coil itself is wound on a custom 3D-printed rectangular frame. Its cross-section is 110 mm × 110 mm. The coil is made from copper wire 0.8 mm in diameter using 21 turns. An LCR meter Gwinstek LCR 6300 was used for the measurements and it was set to measure the coil's Q-factor. This parameter is dependent on all the variables of the circuit and the coil including all of the above-mentioned characteristic and also the voltage frequency that the meter generates for the measurements. The meter's maximum frequency is 300 kHz, so three different frequencies were used for the Q-factor measurements - 100 kHz, 200 kHz and 300 kHz. The measurements were conducted on the notched specimens.

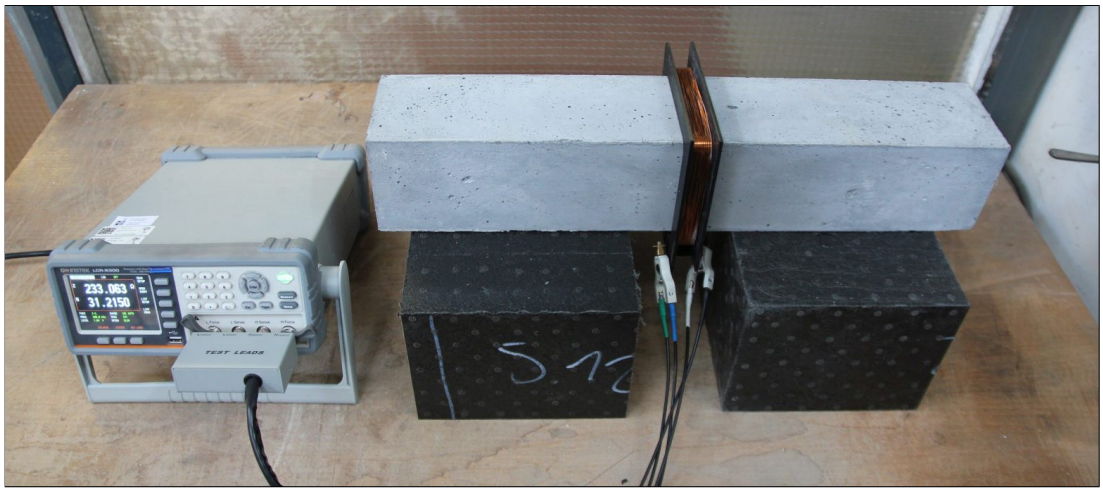

Figure 62: Measurements of the Q-factor of an electromagnetic coil on a fibre-reinforced specimen.

5.3.2 Natural frequency measurement

Another non-destructive method employed was the natural frequency measurement. The test had a very simple setup, which included only a single accelerometer placed on the back of the specimen. The concrete beam was placed in the impact pendulum and very lightly impacted by the impactor. The natural frequency was clearly apparent in the acquired accelerometer signal. Since only the frequency was being examined, only an arbitrary initial displacement was required without the need for specialised displacement-inducing tools or hammers. The measurements were also conducted on the notched specimens, which meant that the accelerometer was slightly offset from the centre. Figure 63 shows the setup for this experiment. The accelerometers were not used further in the impact pendulum testing, as they would introduce unnecessary weight to the specimen, especially with the cable connection.

Figure 63: An accelerometer measuring the mechanical oscillation of a specimen.

5.4 Quasi-static testing

The quasi-static testing was conducted using a three-point bending experiments. Figure 64 shows the setup. The span between supports was 500 mm and the load was applied in the centre of the beam, directly above the notch. Potentiometer displacement sensors were used to measure the displacement of the top surface. They were connected to a special fixture on both sides of the specimen. This fixture is attached to points in the centre of the specimen's height directly above the supports. On one side, it can slide on this attachment to accommodate the changing geometry of the specimen as the experiment progresses. The load is applied through an overlapping steel piece, which forms the reference surface for the potentiometers. The final displacement value was an average of the two measurements.

For later comparisons, the crack mouth opening displacement (CMOD, the width at the tip of the notch) values are needed. The CMOD values were not measured, as a specialised clip-gauge was not available. The CMOD was calculated from the measured displacement instead. Theoretically, the displacement of the top surface and the CMOD have a linear relationship expressed as

$$CMOD = \frac{2\delta H}{\sqrt{\delta^2 + (\frac{L}{2})^2}} \tag{17}$$

where δ is the displacement, L is the span and H is the height of the specimen. However, this relationship doesn't consider the actual technical solution of the displacement measurement. Since the potentiometers are attached to the fixture, there is a slight vertical movement. This problem can be solved graphically.

Figure 64: The three-point bending experiment for the quasi-static testing.

The experimental setup was drawn in AutoCAD for several different phases of the experiment, as the specimen became more and more damaged. Both the displacements (between the top surface and the fixture) and CMOD values were measured. Finally, an equation could have been calculated which would fit the values best. This equation is

$$CMOD = -0.0003085\delta^2 + 0.7999\delta \tag{18}$$

As can be seen, the quadratic element's coefficient is small, therefore the relationship is still almost linear. The experiment is carried out to a CMOD value of approximately 20 mm. The force is recorded using a transducer in the loading piston. The total dissipated mechanical energy was calculated as the area under the load-displacement curve. The experiment was displacement-controlled at the rate of 0.3 $\mathrm{mm\,min^{-1}}$. Data was acquired at a rate of 10 Hz.

All of the tested specimens, from both the quasi-static and impact pendulum testing, were kept for additional quasi-static compressive testing. The broken halves of the specimens were placed into the press so that their ends would be loaded in a 100 mm × 100 mm area. This last test was done mostly to see whether the materials showed similar compressive strengths as reported in the literature sources.

5.5 Impact testing process and analysis

At the start of the impact pendulum testing, the specimens are weighed and the width of the notch is measured using a digital calliper. In the impact pendulum, the specimen is loaded by approximately ten consecutive impacts. After each impact, the width of the notch is measured again. The data from the impact pendulum's measuring frames allow us to calculate the complete energy-dissipating capacity. However, analysing the whole loading process, not just the overall energy value, is also possible by combining this data with the measurements of the

widths. These are the CMOD values that serve as a damage-related parameter. A dissipated energy-CMOD diagram can then be created. Typical example of such a diagram is in Figure 65. The points represent the actual measurements, while the added lines just connect them to better visualize the shape.

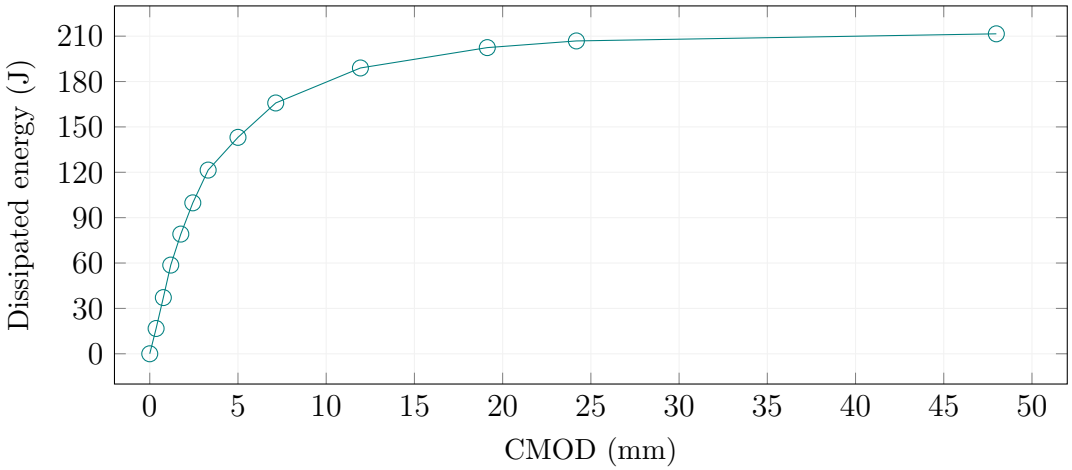

Figure 65: Example of a dissipated energy - CMOD diagram of one specimen tested on the impact pendulum.

It was mentioned, that the measuring frame tracking principle cannot be used for the last impact when the specimen finally breaks into two pieces. The energy dissipated during that last impact cannot be measured. But it can be seen in Figure 65 that this last impact would be responsible for an almost negligible increase in energy, as the graph flattens towards the end. In this particular case, if the CMOD of approximately 20 mm was reached, the experiment would have already been successful, as the specimen's energy-dissipating capacity is largely depleted by that point. The initial impactor's height is modified during the experiment so that the largest CMOD values are reached before the specimen's complete failure. It requires certain experience with the testing process, but it can also be estimated from the CMOD values. If a specimen experiences a much larger increase in CMOD compared to the previous impact, the initial height should be reduced.

The number of consecutive impacts was chosen arbitrarily to have sufficient points to construct this diagram, but also to limit the time-consumption of the experiment. Choosing the right initial heights was done based on previous experience with the materials and the impact pendulum, but also based on the behaviour of the first specimen from one sample. Each specimen was tested using different initial heights based on its behaviour throughout the experiment to approximately maintain the total number of impacts. It should be noted, that a different testing approach was also considered. That method would have involved only a single impact, usually with relatively high energy, after which the specimen would have been subjected to quasi-static testing to determine its residual bending capacity. This approach was eventually not implemented, as the author believes the dissipated energy-CMOD diagrams obtained from the presented approach are more valuable. Splitting the available specimens between different testing methods would result in an insufficient number of specimens tested by either method.

Another analysis procedure that can be done with the obtained data is the creation of an approximate load-CMOD diagrams. This is especially useful, as a comparison with the quasi-static results can be made. The obtained points from Figure 65 can be used to create an ideal curve using the *fit* function in MATLAB using a cubic interpolating spline. This model ensures that the resulting curve passes through the measured points, unlike other fit types. The load curve is then a derivative (gradient) of the dissipated energy curve. This process is rather unusual as in a quasi-static experiment, it is done the other way around as the experiments yield a load-deflection curve first. Since the load curve must always start at zero force, the energy curve must then have a zero gradient at the start. By default, this is not true for the fit curve made from the impact pendulum's experimental data.

A made-up point needs to be added to the experimental data in the second position. It needs to have zero energy value and an arbitrarily chosen very small CMOD value (for example, 1 µm). This ensures that the cubic spline passes this point, therefore between these two points, it will have zero gradient. It also forces the cubic spline to have a short convex region at the start followed by a concave shape on the rest of the graph. Figure 66 shows the fitted curve with the correct shape. The very small convex region is visible at the start. The calculated derivative (the load curve) is in the same graph plotted to the right Y-axis. Note that the shape of the load curve is correctly reversed. The inflexion points' CMOD coordinates must be the same on both curves. These approximate load-CMOD curves will be discussed further using the final results of the experimental part of this thesis. A comparison with the quasi-static load-CMOD diagrams will also be made.

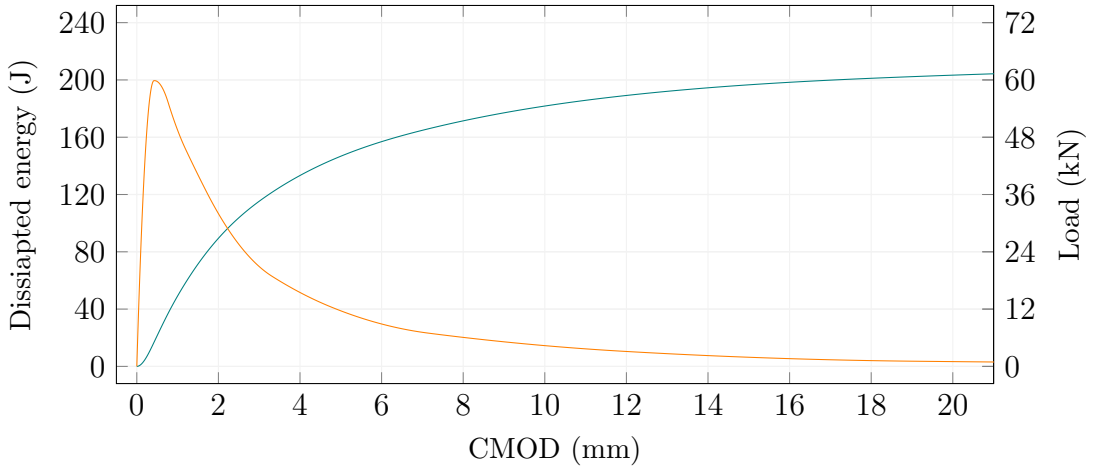

Figure 66: Example of fitted dissipated energy (green) curve and calculated load curve (orange).

Chapter 6

Experimental results

In the previous chapter, the experiments were described mostly in the chronological order of the actual testing program. The results, on the other hand, are presented in this chapter in a more logical manner. First, the basic quasi-static concrete mechanical characteristic - the compressive strength - is discussed followed by the bending tests. The impact testing results are presented afterwards. The non-destructive measurements are examined last because they need to be tied to the other experimental results. The final part of this chapter is going to be the comparison of the quasi-static and impact testing results.

6.1 Quasi-static testing

6.1.1 Compressive tests

The compressive strength tests' results are in Figure 67 and Table 6. The compressive strengths shown here serve just to confirm the assumptions regarding the material's basic performance. If the material achieves expected compressive strength, it is likely that the comparability of results for other testing methods should be more accurate. Since the compressive testing was conducted on the already tested beam halves, only fibre-reinforced materials were tested.

Mixture HSC achieved higher compressive strength than was expected. However, the source study measured the strength using cylinders and not cubes. Mixture L, on the other hand, showed lower strengths compared to the reported results of 121 MPa, 114 MPa and 113 MPa for 0.0 %, 0.5 % and 1.0 % fibre volume, respectively. The trend observed in this work is reversed. The strength increased with an increased volume of fibres. As mentioned earlier, the locally achievable water to binder ratio was higher and the fibre geometry was different. The difference in resulting compressive strengths is, therefore, acceptable. Overall, mixture DM showed lower compressive strength compared to previous experience with this material. Roughly up to 140 MPa strengths were expected. Nevertheless, similar strengths were measured for all of the fibre volumes and geometries. The trend of increasing strengths with increased volume was clearly present for the straight fibres. In the previous work [21], the compressive strengths showed an increase between 0 % to 0.25 % fibre content, then decrease to 1 % and increase again

to 2 %, which is in agreement with the presented results. Specimens with the hook-ended fibres and combinations with straight fibres showed slightly different strengths, but the differences were small.

The original source for mixture R only mentioned that the material should exhibit higher than 150 MPa compressive strength. It is not clear whether that is for unreinforced specimens or not. The 2 % fibre volume specimens showed very similar strengths compared to the DM 2 %. The increasing trend was present even here, but with much higher intensity. The 150 MPa threshold was broken by the 3% fibre volume specimens, while the 4% specimens approached the 190 MPa level. Similarly to mixture L, the locally achievable water to binder ratio was higher and different fibres were used. Unlike mixture L, precise compressive strength values for the original mixture were unknown. The standard deviations for most of the resulting compressive strengths were rather low. Only the mixture R showed an elevated spread of the results. This might indicate certain issues with the inhomogeneity of the mixture itself. Since the compressive strength was clearly significantly affected by the fibre content, the fibre orientation and dispersion inhomogeneity was part of this issue as well. Overall, the compressive strengths were acceptable for all mixtures.

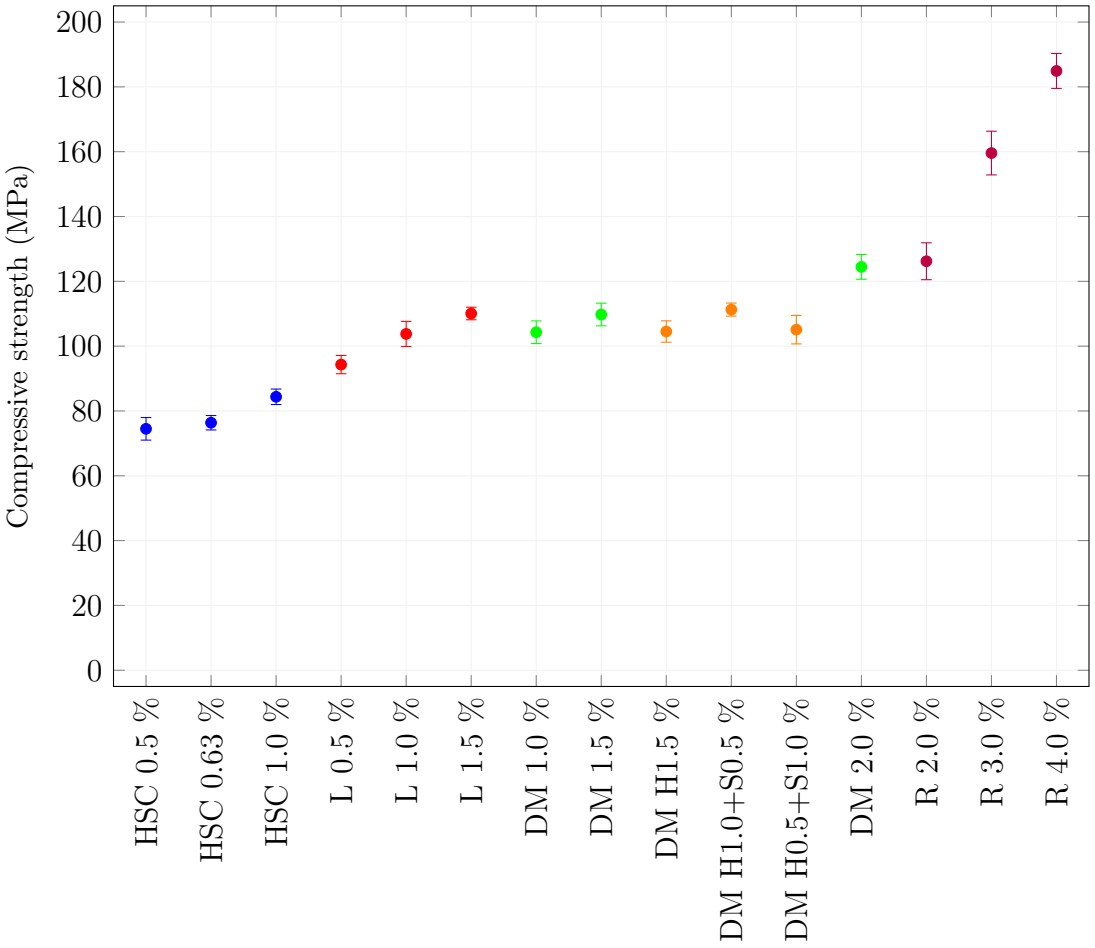

Figure 67: Summary of all compressive strengths of every sample used in the experimental campaign.

Table 6: Compressive strengths. Values in brackets are the standard deviations.

Mixture	Fibres (%)	Compressive strength (MPa)	
HSC	H 0.5	**74.5**	(3.5)
	H 0.63	**76.4**	(2.2)
	H 1.0	**84.4**	(2.4)
L	H 0.5	**94.3**	(2.8)
	H 1.0	**103.8**	(3.9)
	H 1.5	**110.1**	(1.9)
DM	S 1.0	**104.3**	(3.5)
	S 1.5	**109.8**	(3.5)
	H 1.5	**104.5**	(3.3)
	H 1.0 + S 0.5	**111.3**	(2.0)
	H 0.5 + S 1.0	**105.1**	(4.4)
	S 2.0	**124.5**	(3.8)
R	S 2.0	**126.2**	(5.7)
	S 3.0	**159.6**	(6.7)
	S 4.0	**184.9**	(5.4)

6.1.2 Bending experiments

The three-point bending experiments' results are summarised in Figure 68 and Table 7. The complete load - CMOD and dissipated energy - CMOD diagrams are shown in Appendix A and the end of the thesis. Overall, the quasi-static testing revealed the basic behaviour of each material mixtures and fibre volumes. Starting from mixture HSC, we can observe that the fibre saturation point probably lies before the 1 % fibre volume. The peak load was comparable to the 0.63 % specimens, but the force decayed more rapidly, which lead to lower dissipated energies. As mentioned earlier, this was expected based on the appearance of the fresh mixture, where fibres already seemed to not be able to disperse well.

The mixture L was better optimised for the use of reinforcing fibres due to the higher cement content and admixture use but most importantly lower amount of the largest aggregate. The mixture showed a clear, almost linear, ascending trend for both the dissipated energies as well as peak loads. Even though the 1.5 % fresh mixture was the most difficult to process and the fibres started to show worse dispersion, this was not evident from the results. The saturation point was most probably higher than 1.5 % fibre volume for mixture L.

Mixture DM was combined with both the straight and hook-ended fibres. Surprisingly, the hook-ended fibres lead to a drastic increase in both the dissipated energy and peak load for the same 1.5 % fibre content. When the volume of hook-ended fibres was partially substituted by straight fibres, the peak load was negligibly affected, while the dissipated energy clearly dropped. This was probably

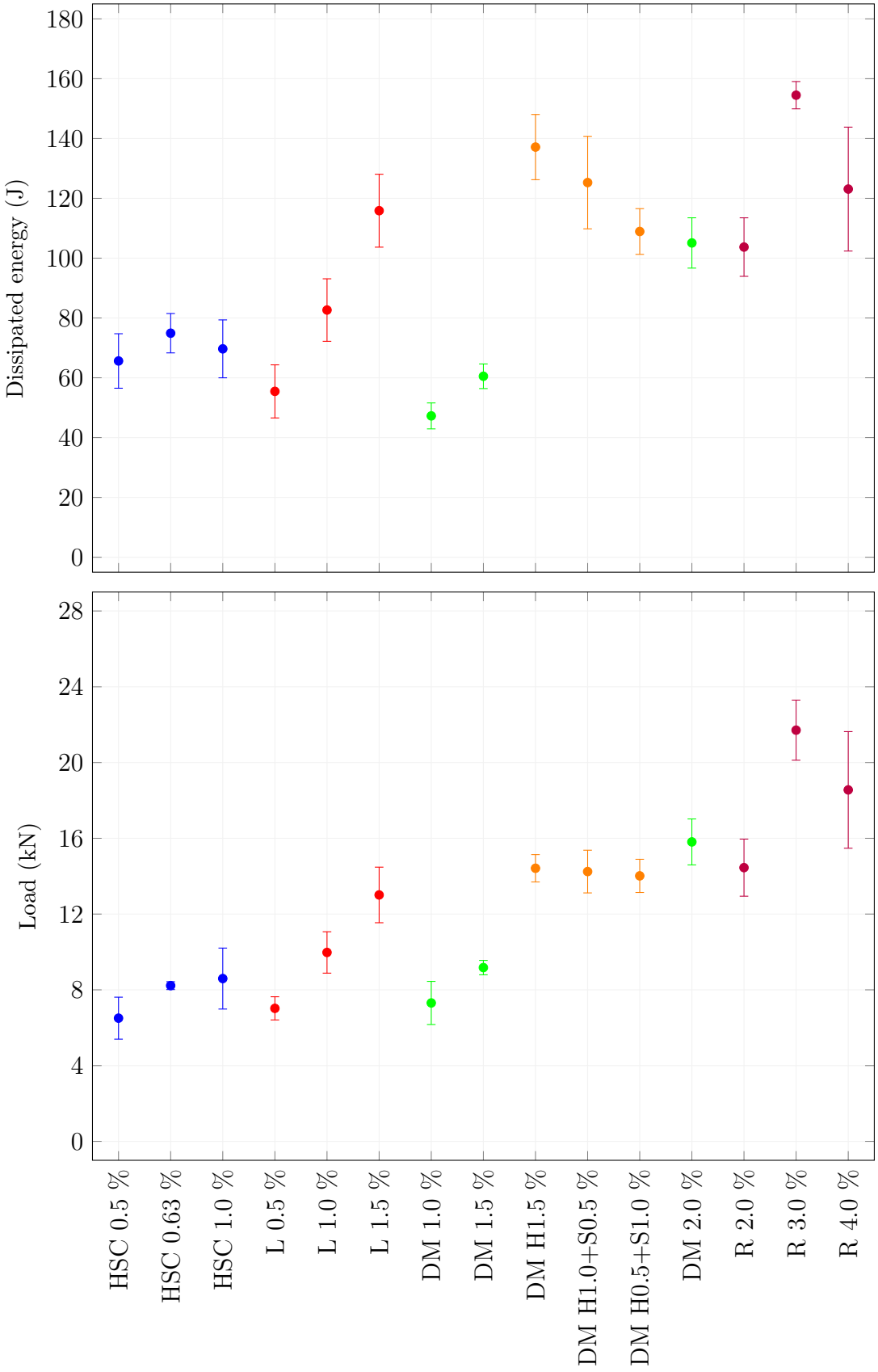

Figure 68: The dissipated energies (up to 20 mm CMOD) and peak loads for the quasi-static bending experiments.

Table 7: Dissipated energies and peak loads for the quasi-static bending experiments. Numbers in brackets are the standard deviations.

Mixture	Fibres (%)	Dissipated energy (J)		Peak load (kN)	
HSC	H 0.5	**65.6**	(9.1)	**6.5**	(1.1)
	H 0.63	**74.9**	(6.6)	**8.2**	(0.2)
	H 1.0	**69.7**	(9.7)	**8.6**	(1.6)
L	H 0.5	**55.5**	(8.9)	**7.0**	(0.6)
	H 1.0	**82.7**	(10.4)	**10.0**	(1.1)
	H 1.5	**115.9**	(12.2)	**13.0**	(1.5)
DM	S 1.0	**47.3**	(4.3)	**7.3**	(1.1)
	S 1.5	**60.5**	(4.1)	**9.2**	(0.4)
	H 1.5	**137.1**	(10.9)	**14.4**	(0.7)
	H 1.0 + S 0.5	**125.3**	(15.5)	**14.2**	(1.1)
	H 0.5 + S 1.0	**108.9**	(7.6)	**14.0**	(0.9)
	S 2.0	**105.1**	(8.4)	**15.8**	(1.2)
R	S 2.0	**103.7**	(9.8)	**14.5**	(1.5)
	S 3.0	**154.5**	(4.6)	**21.7**	(1.6)
	S 4.0	**123.1**	(20.7)	**18.6**	(3.1)

due to the length of the fibres. The peak load, as seen in Figures A.5 and A.7, was achieved before reaching 2 mm CMOD. At this CMOD value, most of the fibres of both geometries were still bridging the crack, therefore, they contributed to the peak load. But as the crack widened, the shorter fibres no longer played any role, which lead to a faster force decay and lower dissipated energy. This can be also seen when comparing the hybrid specimens to the 2 % straight fibre content. The 2 % specimens achieved higher peak force, but lower dissipated energy. For the straight fibres, the increase in both quantities is almost linear.

The straight fibres were used for the mixture R as well. For the 2 % fibre volume, the results were comparable between the mixtures R and DM, although the peak load was slightly lower. The highest values were observed for the 3 % specimens. Similarly to the mixture HSC, the mixture R probably had a fibre-saturation point between the two highest percentages of fibres tested, as the 4 % specimens showed worse performance compared to the 3 %. This last percentage, however, showed a significant spread of the results, which might indicate certain problems with inhomogeneity of this sample. But it might also indicate fibre over-saturation. The saturation point was probably closer to the lower 3 % content, unlike the mixture HSC, which didn't show that significant drop for its 1 % content. Testing the mixture R with, for example, 2.5 % fibre volume would reveal whether there is a linear trend up to the 3 % content or even the 3 % is close to or at saturation point.

From the bending experiments' point of view, the mixture L performed the best taking into consideration the composition of the material (its cost). Its energy-dissipating capacity was better than the mixtures DM and R for even 0.5 % higher fibre content. Although, the peak load was slightly lower. As expected, the mixture DM showed the best spread of the results for the straight fibres, as there could have been more of them for a given volume due to their smaller size, so achieving better homogeneity was easier. Especially the energy dissipation for the hook-ended fibres showed a worse spread of the results, partially due to the lower fibre count, but probably also due to the damage to the matrix. During the pullout of a hook-end fibre, there was an increased risk of premature matrix failure. If that happened, the fibre lost all bond to the matrix which lead to a faster decay of force during the experiment. The specimens' failure and crack patterns will be discussed further in later sections.

6.2 Impact testing

The results of the impact pendulum experiments are summarised in Figure 69 and Table 8. For better comparability, two dissipated energy values are shown, one for the 20 mm CMOD (calculated from the fitted curve as explained in the previous Chapter) and the total until failure. The peak loads are from the calculated load - CMOD diagrams. The complete dissipated energy - CMOD and load - CMOD diagrams are shown in Appendix B. The dissipated energy - CMOD diagrams are drawn with the points representing the actual measurements, with the lines being the ideal calculated curves.

The mixture HSC showed a roughly increasing linear trend for the dissipated energy values with increasing fibre content. The calculated peak loads, however, were similar between the 0.63 % and 1 % samples. Interestingly, specimens of mixture L with 0.5 % of fibres achieved relatively poor results, but the increasing trend with increasing fibre volumes was more significant. Samples of mixture DM with straight fibres performed as expected, also showing a linear trend. The most surprising results were achieved with the same mixture but using 1.5 % of hook-ended fibres. The dissipated energy was, on average, 2.2 times higher compared to the same volume for straight fibres. This would indicate, that the higher pullout forces of the hook-end fibres were acceptable for the stronger matrix DM, compared to the matrix L, where the same fibre type and volume performed worse. Unlike the dissipated energy values, the peak loads were similar between the samples of mixture DM containing the hook-end fibres and 2 % of straight fibres. The mixture R showed an increasing concave trend peaking somewhere around the 4 % fibre volume for the dissipated energy, but for the peak load, the trend was almost linear.

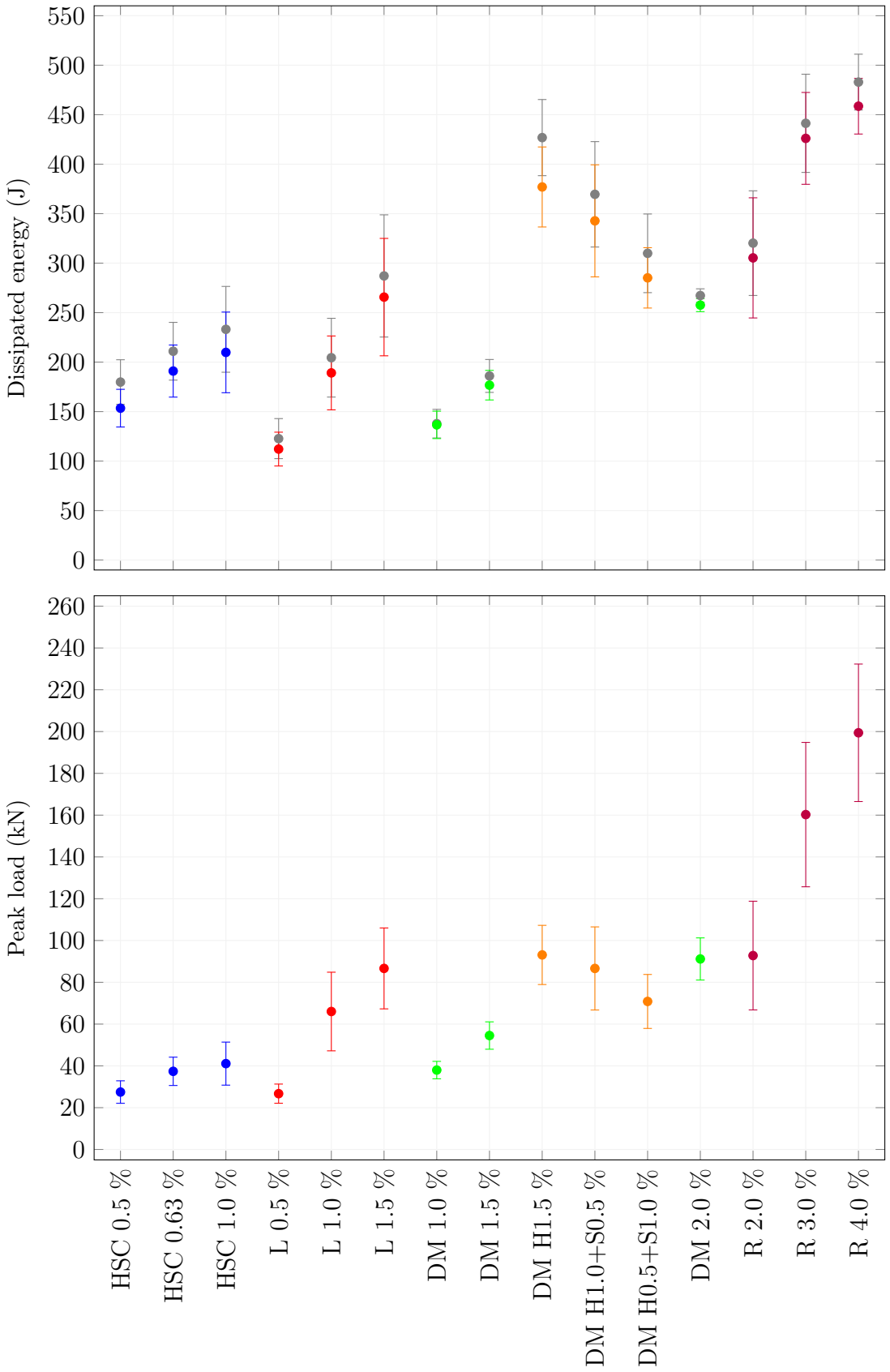

Figure 69: The dissipated energies (up to 20 mm CMOD + total in grey) and peak loads for the impact loading experiments.

Table 8: Dissipated energies and peak loads for the impact loading experiments. Numbers in brackets are the standard deviations.

Mixture	Fibres (%)	Dissipated energy (J) failure		Dissipated energy (J) 20 mm CMOD		Peak load (kN)	
HSC	H 0.5	**179.8**	(22.5)	**153.5**	(19.0)	**27.5**	(5.4)
	H 0.63	**211.0**	(29.2)	**191.0**	(26.3)	**37.4**	(6.8)
	H 1.0	**233.1**	(43.3)	**210.0**	(40.7)	**41.1**	(10.3)
L	H 0.5	**122.7**	(20.2)	**112.1**	(17.1)	**26.7**	(4.6)
	H 1.0	**204.5**	(39.8)	**189.1**	(37.3)	**66.0**	(18.8)
	H 1.5	**287.1**	(61.7)	**265.7**	(59.3)	**86.6**	(19.4)
DM	S 1.0	**137.8**	(14.4)	**136.6**	(13.8)	**38.0**	(4.2)
	S 1.5	**186.0**	(16.6)	**176.7**	(14.9)	**54.5**	(6.5)
	H 1.5	**426.8**	(38.5)	**378.0**	(40.4)	**93.1**	(14.2)
	H 1.0 + S 0.5	**369.5**	(53.3)	**342.7**	(54.3)	**86.6**	(19.9)
	H 0.5 + S 1.0	**309.9**	(39.7)	**285.1**	(56.6)	**70.8**	(12.1)
	S 2.0	**267.3**	(6.8)	**257.6**	(6.6)	**91.1**	(10.1)
R	S 2.0	**320.2**	(52.9)	**305.3**	(60.7)	**92.8**	(26.0)
	S 3.0	**441.3**	(49.6)	**426.1**	(46.4)	**160.3**	(34.6)
	S 4.0	**482.9**	(28.2)	**458.6**	(28.1)	**199.4**	(32.9)

6.3 Non-destructive testing

6.3.1 Electromagnetic coil measurement

The summary of measuring the Q-factor for all samples is in Figure 70. Only averages are drawn, the standard deviations are very small compared to the scale of the chart. The differences between samples are clear. When comparing different materials but the same fibre geometries and volumes, the Q-factors were almost the same. It can be seen, however, that a direct comparison between the different types of fibres is not possible. Not only were there differences between the fibre geometries, but also the manufacturers could have used steel performing differently in a magnetic field.

Care must be taken when examining Figure 70. The markers representing the 100 kHz and 300 kHz have switched vertical positions between the samples with hook-end and straight fibres. If an entire frequency spectrum was analysed, the Q-factor would have peaked at a certain frequency. This frequency would be dependent on the fibre material and its geometry. From the conducted experiments it was clear, that for the given fibres and coil parameters, the hook-end fibres would show Q-factor peak at higher than 300 kHz frequency while the straight fibres at lower than 100 kHz. The 1.0 % straight fibre content in mixture DM shows similar average values for 100 kHz and 200 kHz, indicating that this percentage would show Q-factor peak closely below the 100 kHz value.

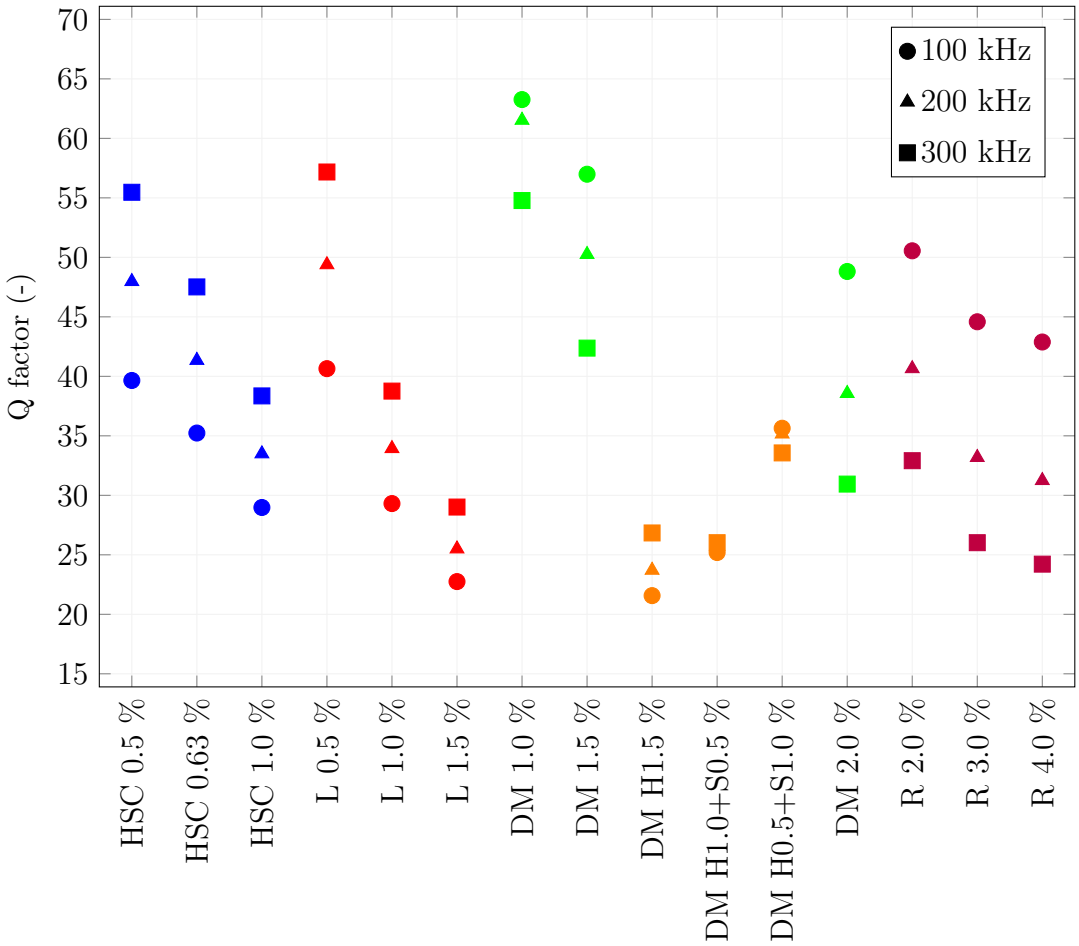

Figure 70: Measurements of the Q-factor.

This frequency dependency means, that combining the different fibre geometries in one specimen renders this measuring method useless. As the contribution to the Q-factor by the fibre dispersion and orientation of the different fibres cannot be distinguished. This was apparent from the two hybrid samples of the mixture DM. The slight differences between mixtures and the same fibre types and volumes could be attributed to overall better fibre dispersion thanks to the mixture qualities. Mixture DM showed the best workability and flowability and, as the Q-factor measurements showed, it achieved lower values for the same 1.5 % hook-end fibre volume compared to mixture L and lower values for 2 % straight fibre volume compared to mixture R. Also between the mixture HSC and L, there was a slight difference between 0.5 % fibre content, which was present in the mechanical parameters results.

Identifying the fibre content and even fibre type should be possible using the Q-factor measurements when compared to an already existing data set. Although, predicting the mechanical parameters is only possible with the previous knowledge of the behaviour of the specific mixture containing those specific fibre types. Different mixtures will utilise the same fibres differently. Examining individual specimens is also possible. Figure 71 shows an example of dissipated energy - Q-factor chart for the mixture DM and straight fibres. It can be seen, that even though the rough fibre volume trend is apparent, the measurement is not sensi-

tive enough to predict the individual dissipated energies with reasonable accuracy. The impact loading results have a worse correlation to the Q-factor compared to the quasi-static results. The hook-end fibres generally showed a worse correlation for both experiments. The rest of the individual Q-factor relationships are not shown, as the results were similarly inconclusive. Measuring the Q-factors using broader frequency range and finer frequency steps might have improved the correlation, but the non-destructive measurements were not the main topic of this work.

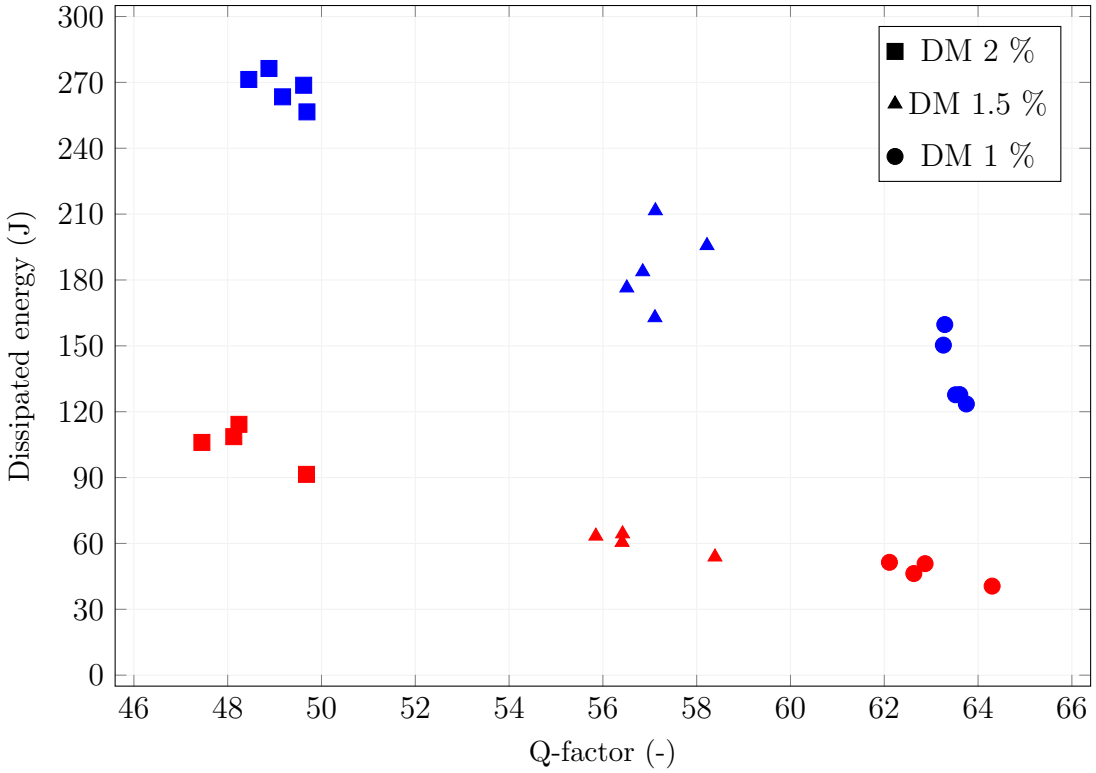

Figure 71: Example of Q-factor measurements paired with the resulting dissipated energy for the quasi-static (red) and impact (blue) experiments. Mixture DM, straight fibres, 100 kHz.

6.3.2 Natural frequency measurement

The measurements of the natural oscillating frequency of the specimens were carried out only on the samples DM with straight fibres. On average, the clearly distinct lowest frequency was approximately 1070 Hz from the acquired signal. There was no significant change of frequency between all the tested specimens. As was pointed out from the literature review, this measurement is only going to reveal the differences between the elastic properties of the materials. The fibres change those characteristics, however, their volume is too low to change them enough for this type of measurement. Mostly the matrix properties and the exact specimen's geometry and weight will affect the natural frequency. But since the goal was to be able to evaluate the fibre reinforcement, this measurement approach was abandoned.

6.4 Damage patterns

After conducting the impact testing, one specimen from each sample was photographed to compare the different damage patterns. All of these photographs are in Appendix C. As mentioned before, the hook-end fibres were more likely to cause higher damage along the crack surfaces, which might have resulted in premature loss of fibre-matrix bond but at the same time could have caused higher energy dissipation. This surface damage was apparent for mixture HSC for all percentages, but especially 1 % fibre volume. For the same volume, mixture L showed slightly less damage, but much more severe for 1.5 %. Also, the fibre bundling, which was noticed during mixing, was present here as well.

For mixture DM with straight fibres, longer cracks are present that would have a tendency to form slices of disconnected material. Comparing the 1.5 % of straight and 1.5 % of hook-end fibres showed a significant difference in the state of the surface. The hook-end fibre specimens formed larger lumps of broken material held together only thanks to the fibres. Interestingly, the damaged surface was similar between the matrix L and DM for the same fibre volume and type, even though much larger aggregate sizes were present in mixture L. This was the result of higher pullout forces for individual hook-end fibres.

The mixture DM with the highest 2 % straight fibre volume also showed significant matrix cracking on the failure surface. This indicated the interactions of an increasing volume of fibres in the matrix. The distances between individual fibres were too small for the matrix to withstand the fibre pullout stresses. The matrix around the contact with one fibre was also loaded by other fibres being pulled out nearby. Also, with increasing fibre content, the main crack's geometry differed more from a straight line from the tip of the notch and the loading point.

In the case of the mixture R, since it started with 2 %, the matrix already exhibited significant cracking on the failure surface. Overall, for the two higher percentages, the matrix seemed very similar without exhibiting more matrix damage. In the example of specimen R 3 % in Figure C.5, the fibres in the centre of the specimen seemed to follow a swirl-like pattern. This was probably tied to the pouring of the fresh mixture into the moulds. As noted earlier, the mixture R, even though able to be mixed with large volumes of fibres, exhibited poor flowability, unlike the mixture DM. The fibres probably remained oriented by the scooping and placement methods.

As can be seen in Figure B.9 for the 4 % sample, one of the specimens exhibited unusually low dissipated energy. This specimen was not included in the average and standard deviation calculations. Figure 72 shows the failure surface of this specimen. It can be seen, that the main crack was initiated partially outside of the notch. Compared to other specimens from the same sample, the amount of visible fibres on the failure surface is unusually low. This could have been caused by the fresh material's placement method or by placing a poorly mixed material volume in this part of the mould. Another specimen from the same sample is shown in Figure 73 with a similar crack formed outside of the notch (right side). This specimen exhibited normal behaviour.

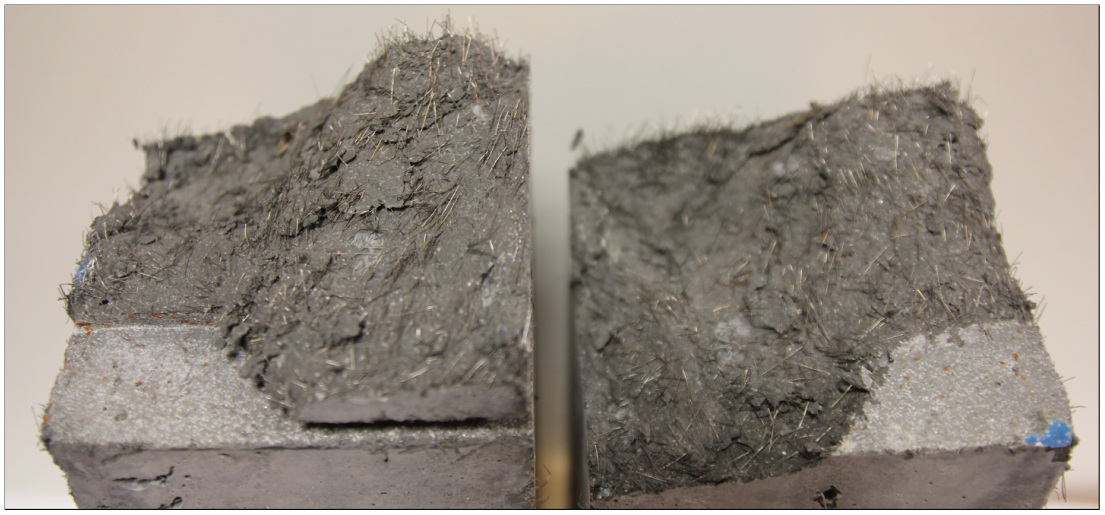

Figure 72: Non-standard damage pattern of one R 4 % specimen.

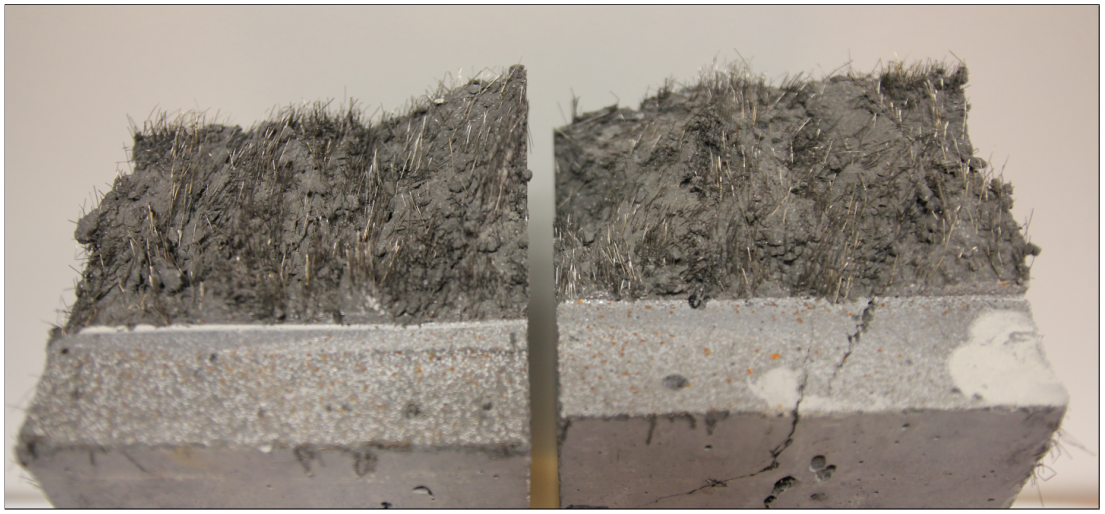

Figure 73: Forming non-standard crack on another R 4 % specimen.

6.5 Results comparison

The ultimate goal of the impact pendulum testing is to tell the difference in material behaviour compared to the quasi-static loading rate. Figure 74 summarises the ratios of averaged dissipated energies and peak loads between the two experiments. The term Dynamic Increase Factor (DIF) is intentionally not used, as it should be emphasised that the experimental configurations are different and direct comparison through the DIF value is misleading. The standard deviations are approximated based on the propagation of uncertainty principle for the division of two uncorrelated variables using the equation

$$\sigma \approx \sqrt{(\frac{\sigma_A}{A})^2 + (\frac{\sigma_B}{B})^2} \tag{19}$$

where σ is the resulting standard deviation, σ_A is the standard deviation of variable A and σ_B is the standard deviation of variable B. This principle logically amplifies the standard deviations (errors) of these resulting ratios of mechanical parameters.

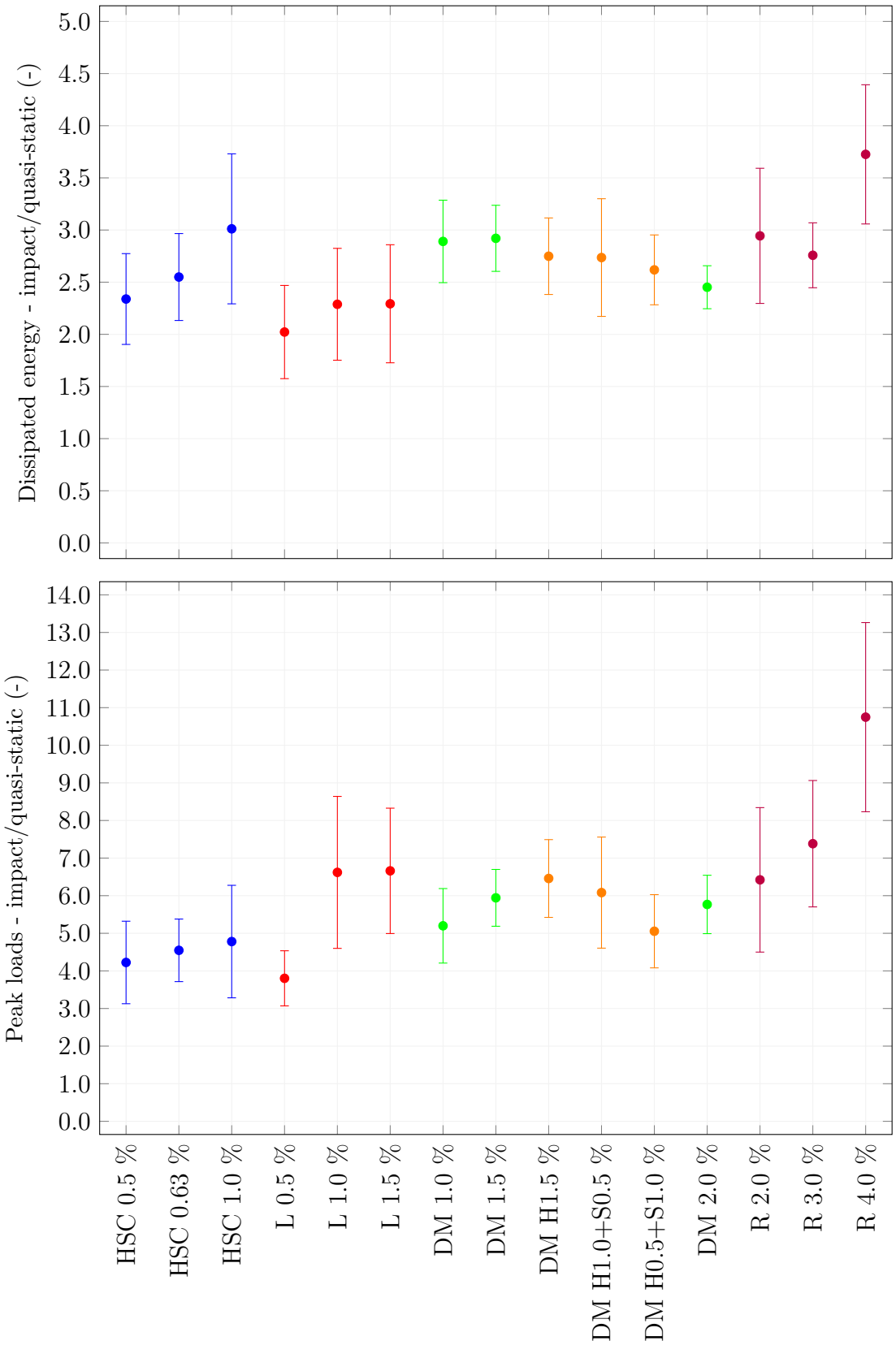

Figure 74: Comparison of the dissipated energies and peak forces between the impact and quasi-static loading.

Regarding the dissipated energies, even though the standard deviations are high, there were still significant differences of the ratios, especially for different mixtures. The mixture DM showed a similar ratio for all of the fibre volumes and types. It also showed the lowest standard deviations for the straight fibres. The lowest ratios were present for mixture L, with a slight increase with increasing fibre volume. Surprisingly, the mixture HSC with 1 % fibre content showed interesting ratio values. The highest ratios were achieved for the mixture R. The 3 % sample achieved the highest dissipated energy values for the quasi-static experiment, while the 4 % sample showed much lower values. For the impact testing, the 4 % sample showed the best performance, which also lead to the highest resulting ratio presented here.

The chart of the peak loads showed slightly different trends. Overall, the peak loads were much higher for the impact loading. But it should be understood, that these are the loads calculated from the coarsely measured dissipated energy curves, so certain inaccuracy is expected. This will be discussed further in the next Chapter. Mixture HSC exhibited similar peak load ratios. Mixture L with the lowest fibre reinforcement had the lowest ratio just like with the dissipated energy, but the higher percentages' averages are much higher, together with the standard deviations. The mixture DM again showed similar ratio values, with only the lowest fibre percentage and the last presented hybrid specimens achieving lower values. The mixture R with the 4 % fibre volume also showed the highest peak load of all the other samples.

Another comparison can be made regarding the shape of the dissipated energy curves. Figure 75 shows three points for all samples, which represent the CMOD values when the 25 %, 50 % and 75 % of total dissipated energies were reached. For the quasi-static experiments, the specimens were clearly divided by the fibre types used. This was a logical result, as the fibres had different lengths and showed different bond characteristics. Slight differences were present between the mixtures HSC and L, when the mixture HSC showed a slightly descending trend with increasing fibre volume.

The impact experiments' chart looks different. The descending trend for the mixture HSC was present here too, but with a higher slope. Mixture L shared this trend as well. Mixture DM with straight fibres and R had very similar 25 % values, but started to differ with 50 % and most notably for 75 %. It is important to note, that higher averages for these two mixtures are accompanied by higher standard deviations, which means that the averages were simply moved because of one or two outlying values. Overall, the specimens seemed to absorb a bigger portion of the total mechanical energy towards the lower values of CMOD. But certain samples, from especially the mixtures HSC and L, showed much higher 75 % point, indicating a slower decay of the strain-softening region in the impact testing.

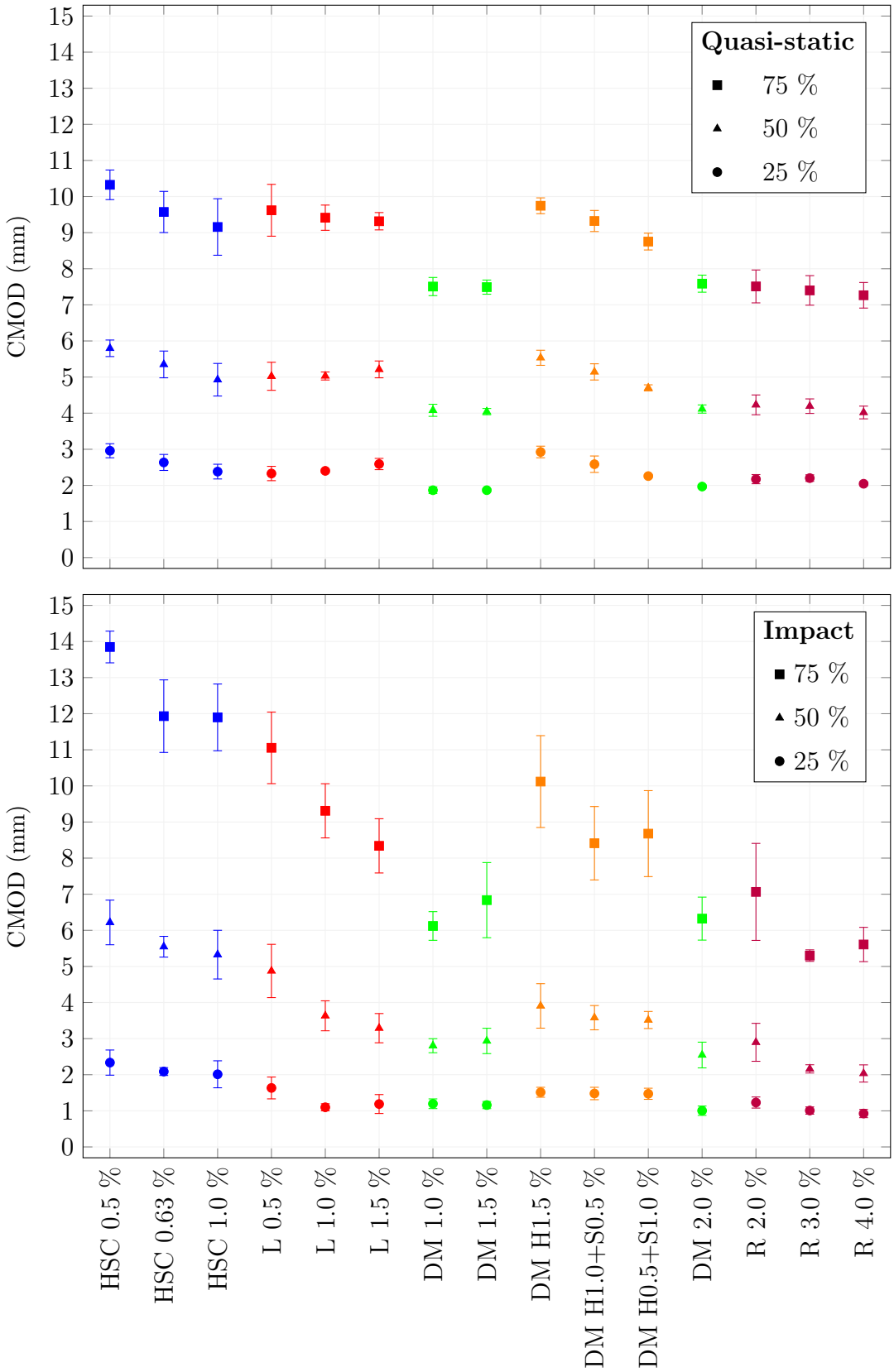

Figure 75: Analysis of the shape of the dissipated energy - CMOD curves. Points represent the CMOD positions of percent of the total dissipated energies.

Chapter 7

Conclusions

7.1 Impact pendulum evaluation

7.1.1 Technical side

One of the main goals of this thesis was to create a mean of high strain-rate testing of fibre-reinforced concrete specimens. This goal was achieved, however, it is still important to present general thoughts and evaluation of the principle and its suitability for material testing. Regarding the ease of conducting the experiments and data analysis, the impact pendulum and the measuring frames performed adequately. During the design process of the measuring frames, several key technical aspects were identified. The rigidity of the entire structure plays a crucial role. Ideally, the impactor should be connected to a separate structure. When the impactor is released from its initial height, the reaction forces from the cable attachments cause a slight deflection of the structure, which can be picked up by the measuring instruments.

Through many improvements of the measuring frames' structure, optical elements positioning and electronics, the data acquisition process became reasonably reliable. The addition of the optical lenses in front of the photodiodes was very important, as it allowed for certain small vibration of the frames that still did not affect the signal quality. Without the lenses, the laser beam could have moved slightly out of the photodiode sensing area which would change the measured voltage. This effect would have been amplified by the number of optical gate pairs on the frame and severely distort the acquired signal. The vibration of the frame is still undesirable even with the lenses, as the beam positions fluctuate during the sample-movement phase. The effect on accuracy, however, was deemed negligible.

The laser beam modules on the lower beams were firmly glued into their positions. The manufacturer of the modules states a certain allowed tolerance for the deflection of the beam from the axis of the module housing. It was discovered, that this tolerance is rather high, and each module needed to be carefully oriented before gluing, to achieve proper aim towards the photodiodes on the upper beams. Ideally, each of the laser modules should have been placed in some mechanism that would allow further alignment and subsequent firm locking. Disassembling of the measuring frames (to make way for a different experiment on the impact

pendulum) and a repeated assembling now requires careful and time-consuming alignment of the whole structure, including precise tightening of the bolted connections, adding washers and shims. All of this while monitoring the photodiodes' circuit signal level, to achieve the lowest possible base voltage on both frames at the same time.

As explained in the description of the measuring frames, first twenty laser beam modules had a spacing of 3 cm, while the rest of the modules had a spacing of 5 cm. This higher density towards the impact point was thought to be necessary for low-energy impacts to obtain a sufficient number of measured points. However, it was discovered, that as the sample starts rotating after the impact, it reaches a certain rotation, when its horizontal projection is close to 12 cm long. This means, that immediately when a laser beam is interrupted, another one is illuminated again. The measured signal then either shows just a small spike or no change at all. Different spacing between the optical gates should have been chosen (between 5 cm and 3 cm) and uniform spacing on the entire frame should have been used.

In terms of the analysis script, it also went thought numerous optimisations and changes to better deal with certain signal occurrences. A simple rule was added to the algorithm which calculated the time intervals between subsequent signal changes. As the specimen slowed down and moved higher on the circular trajectory, these time intervals must have been increasing. If a point was mistakenly identified with significantly incorrect time interval change, it was automatically discarded. But certain manual processes, such as identification of the time interval when the specimen stopped moving, or cutting the acquired data to the moment of impact, were still performed manually. The ideal situation of creating such an analysis process, that would have been automatically performed by the computer right after acquiring the data after the impact, was not achieved. It would most probably require creating a completely custom software for the impact pendulum testing, which was beyond the scope of this work and the author's specialisation. The main goal with the script analysis, however, was to be able to perform the analysis much faster compared to the analysis of the high-speed camera footage, which was done in the previous research. This goal was achieved, as the time needed to analyse one impact for one specimen was approximately one minute with the final version of the script.

7.1.2 Material testing

Let's examine the behaviour of the concrete specimen during the impact pendulum experiments and possible negative effects on the results. First, the effect of repeated loading of one specimen. This approach was chosen to fully deplete, in a controllable way, the energy dissipating (flexural) capacity. If we loaded the specimen by a single high-energy impact, we would somehow have to choose a specific initial height of the impactor to deplete enough energy of the specimen right before failure or to always achieve the same damage criterion. This is not possible. Since this experimental approach needs the specimen to remain in one piece in order to track its position, we need to apply multiple impacts.

Figure 76 shows an example of a quasi-static bending experiment on a notched beam sample that was loaded until approximately 3.5 mm of CMOD and then unloaded and immediately loaded again. The lower chart shows a detail of this unloading event on a dissipated energy - CMOD diagram. The descending part of the dissipated energy curve should be understood as a situation when the sample released a portion of its stored mechanical energy back into the loading mechanism. In the case of the impact loading, this event happens directly after the impact. The main difference, however, is that instead of returning portion of its energy back to the impactor, the specimen starts oscillating. This effect was explained in Chapter 4. Since the CMOD and even the position measurements are conducted well after the contact between the objects, these effects are already automatically accounted for and the unloading has no effect on the absorbed and dissipated energy.

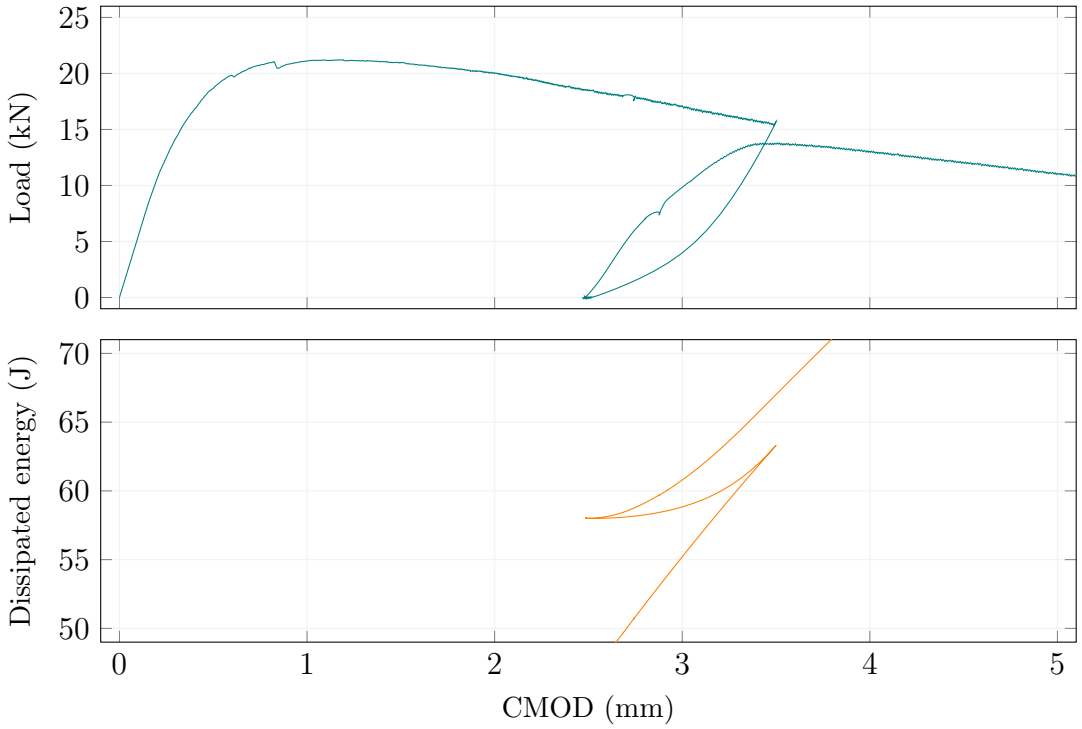

Figure 76: An example of a load - CMOD diagram with unloading event and a detail of the unloading event in dissipated energy - CMOD diagram.

In the quasi-static experiments, the load, as presented in the diagrams throughout this work, is the exact load that pushes on the centre of the specimen. Since the dissipated energy is calculated as an area under the load - deflection curve, it should be interpreted as the work done by the loading piston. However, in the case of the impact loading, interpreting the calculated forces as a force physically applied by the impactor to the specimen is wrong.

In the dynamic loading, the reaction is created by the inertia of the specimen and forms a dynamic equilibrium which rapidly changes in the impact interval. But the dissipated energy curves are made from points of partial dissipated energies measured post-impact, not taking into consideration any force equilibriums or any other events that resulted in the energy dissipation itself. The calculated

loads for the impact experiments should, therefore, be considered as arbitrary forces needed to act on certain lengths represented by the CMOD values. Or even more universally, the calculated diagrams could be simply considered to be just gradients of the dissipated energy curves that describe its shape. Clearly, the unloading is not present in the calculated diagrams, because that information is not conveyed by the dissipated energy curves.

In the previous Chapter, the loads were compared between the quasi-static and impact experiments even through the use of the ratios in Figure 74. However, as noted before, this should not be interpreted as a direct peak load or even a flexural strength ratio. The charts were presented to illustrate the peak force trends for the different mixtures and fibre volumes between the quasi-static and impact loading as they are all tied to the dissipated energies. But the dissipated energies are the main focus of this work. The last remark about the calculated impact experiment load curves is related to their overall accuracy. It should be taken into consideration that they are calculated from an ideally fitted spline curve which is fitted to a relatively small number of points of the experimental data.

The main principle behind the energy approach required the assumption that no other energy loses occur during the impact. The acoustic energy loss is immediately apparent. It is unclear how much energy is consumed for the acoustic effect, which is simply a transfer of certain part of mechanical energy into the surrounding medium. Next, there is the energy lost as heat, primarily in the impactor. Plastic deformation (and energy dissipation) of the impactor's front is none or negligible, thanks to the hardened steel nose. Inside the specimen, a portion of the mechanical energy is dissipated as heat, as the main energy dissipating mechanism is the fibre-matrix friction. Another loss can be attributed to the inevitable compressive deformation and damage of the sample in the contact region with the impactor. However, all of these energy losses related to the specimen can be interpreted as inseparable parts of the material performance, as they would be present even in a real high strain-rate loading situation. The rest of the losses regarding the impactor or the apparatus' structure are considered negligible.

7.2 Strain-rate effects on studied materials

Creation of the impact loading experimental approach is only a tool to achieve the second main goal of this work - to study the effects of elevated strain-rate on the mechanical performance of fibre-reinforced concretes. The main differences between the quasi-static and impact loading experiments were presented in the previous Chapter. The comparison of results showed in Figure 74 presented a clear increase of dissipated energies for the impact loading. However, it is important to take into consideration the different loading methods between the experiments. Certain reference results would be needed to know the exact difference between the impact pendulum and bending experiments without the influence of strain-rate. That is of course not possible, as we cannot load the sample in the impact pendulum using a quasi-static loading rate nor can we load the beam in the bending setup using an impact rate.

The main focus of comparing the results should then be on the trends between the mixtures and the fibre types and volumes since all of the samples were tested the same way in the corresponding experiments. The only difference for the impact pendulum testing was the changing initial height of the impactor. But based on the literature overview, the strain-rate effects in the region of low-velocity impact loading significantly change only between orders of magnitude of the applied strain-rate. The initial heights of the impactor ranged from 0.15 m to 0.60 m depending on the specimen. This translates to approximately 2.0 ($\mathrm{m\,s^{-1}}$) and 8.3 ($\mathrm{m\,s^{-1}}$) impact velocity. For highly damaged specimens in later stages of the experiment, lower initial heights were used as needed.

The mixture HSC offered probably the most surprising results. It achieved high dissipated energy values for the quasi-static testing. But compared to the mixture DM with straight fibres, it saw lower ratios for the two lowest percentages. The highest 1 % fibre content, on the other hand, exhibited a high average ratio of 3. This was caused by relatively poor performance for the quasi-static experiments, but the dissipated energy trend for the impact experiments was almost linear with increasing fibre volume. Interestingly, the mixture L showed the lowest ratio values of all the mixtures. It also presented almost identical ratio values between the 1 % and 1.5 % fibre volumes.

The comparison between the mixtures HSC and L is especially interesting, as both of these mixtures contained the same fibre types and aggregate size, but mixture L contained more cement and admixtures. This made the mixture L perform better than mixture HSC under quasi-static conditions, at least for the 1 % fibre content and up. But the impact loading results between mixtures HSC and L were comparable, therefore mixture HSC ended up with better ratio values. Figure 75 compared the shapes of the dissipated energy curves for the impact loading. Here we can observe much higher values of CMOD for the later stages of the curves for mixture HSC. This means that when the main crack was already significantly opened, the specimens still had relevant amounts of dissipating capacity left. A possible theory behind this behaviour could be, that the fibres were anchored much strongly in the matrix L thanks to the silica fume, but overall, the tensile strength of matrix L wasn't that much higher compared to matrix HSC, so premature fibre-matrix failure occurred in matrix L more often than in matrix HSC. This effect could have been amplified by the higher strain-rate. Strong evidence for this are the final shapes of the fibres. Mixture HSC shows almost all fibres straightened, which indicates a complete pullout, while some fibres on the failure surfaces of specimens L still showed the hook-ends, especially the 1.5 % L specimen in Figure C.2.

The mixture DM exhibited the largest ratio values for the two lowest percentages of straight fibres while diminishing with the addition of hook-end fibres. Interestingly, the lowest ratio is for the highest straight fibre volume. Since the straight fibres are shorter, the faster-plateauing dissipated energy curves are to be expected. The straight fibre specimens all exhibited steeper curves in the impact loading compared to the same samples in quasi-static testing. This is the opposite effect compared to the mixture HSC, but similar to mixture L with the highest fibre content. But compared to mixture L in the impact testing, the mixture DM

performed better, which lead to the higher ratio values. Comparing the 1.5 % hook-end fibres for mixtures L and DM, we can see a significant difference in both the ratios and the shapes of the dissipated energy curves. If we assume the above mentioned theory, this means that the mixture DM was able to withstand the stresses resulting from the impact loading fibre pullout better than mixture L. Looking at the shapes of the fibres on the failure surfaces, there are more straightened fibres for the mixture DM, although significant amount remains hooked, indicating a certain unused potential for even better impact loading performance. The two hybrid samples for mixture DM show almost all fibres straightened and much less overall damage on the failure surfaces.

A similar comparison can be made between the 2 % straight fibre volume for mixtures DM and R. Since the mixture R should be stronger, based on the much higher amount of cement and silica fume, the results support the previous trends. The ratio value for dissipated energy is higher, although with significant standard deviation. This is most probably caused by a problem with homogeneity of the mixture, as mentioned in the previous Chapter. Both samples have an almost identical quasi-static performance. The shape of the dissipated energy curve for the impact loading is less steep for the sample R, once again indicating the effect of stronger matrix which is able to hold the fibres longer. The R 3 % and 4 % samples then show faster plateauing of the curves, as 75 % of energy was dissipated much earlier compared to the 2 % sample. This would indicate, that perhaps the individual fibres were affecting each other too much already and the matrix was not able to hold them, especially towards the later stages of the experiments. On the other hand, the 4 % fibre volume sample showed the highest dissipated energy for impact loading and also the highest ratio value. Once again, this is caused by a vastly different trend compared to the quasi-static loading, where the 4 % did not perform well.

However, with the mixture R, another effect could have been responsible for the better impact loading performance - the formation and branching of multiple cracks. This was already indicated by Figures 72 and 73 in the previous Chapter. It is caused by using very high volumes of reinforcing fibres. It can be considered as part of the strain-hardening effect, although during the impact loading, it plays a more important role. It could be partially explained by rapidly shifting force balances, as the stress waves move through the specimen and inconsistently load different regions.

If a crack is initiated in a low fibre volume specimen, then the crack is already the weakest link of the composite so it keeps growing until failure. In a high fibre volume composite, the formation of a crack doesn't necessarily create the weakest point, as the fibres are able to transfer the tensile stresses through the crack. This means that another crack can easily be initiated elsewhere, or the main crack could start branching, which all leads to higher energy dissipation. This effect is clearly strain-rate sensitive and in a way relates to the strain-rate effects described in Section 2.4.2. Additionally, all of the specimens tested on the impact pendulum were subjected to the effects of strain-rate sensitive matrix damage, mostly in the direct proximity of the reinforcing fibres.

7.3 Final thoughts and summary

Overall, the impact pendulum testing provides a good and reliable way of testing fibre-reinforced concretes for their ability to dissipate mechanical energy when subjected to a high strain-rate load. The energy approach seems more suited as an evaluating quantity, compared to the standard load/strength approach of the quasi-static testing. The absence of fixed supports eliminated possible energy loses due to support vibration or damage.

Even though both the quasi-static and the impact testing methods revealed certain results, the material could still behave differently when subjected to real high strain-rate loads. Good examples are the ballistic experiments presented in study [92], where the HSC material performed worse compared to the (ultra) high-performance fibre-reinforced concretes, even though the results from the impact pendulum would suggest otherwise. The laboratory testing such as this is intended for the preliminary comparative testing when conducting basic material research. But for specific applications, other testing methods, or preferably the full-scale real loading scenarios, should be employed. The whole process of creating a better material is then an iteration using the obtained experience.

In terms of the experimental campaign of this work, the focus was more on the individual mixtures and the performances of different volumes in them. In the end, this campaign should have been altered to also include the same reinforcing fibres (preferably both) in all of the mixtures in the same volumes, as these comparisons would reveal the matrix effects better. Nevertheless, vast amounts of experimental data were acquired, which can serve in future material research. But most importantly, the experiments served as a final test of the impact pendulum testing approach. The main goals and other points of this work can be briefly summarised:

- Successful design and construction of the impact pendulum's data acquisition tools.
- Further optimisation of the impact pendulum testing.
- The creation of a robust software script to analyse the acquired data.
- Execution of an extensive experimental campaign using various mixture compositions.
- Analysis of the results in terms of strain-rate effects.

Based on the experience with this work, several recommendations for future testing can be made. Clearly, the ability to test smaller specimens would be beneficial, as relatively large amounts of raw materials were used and the specimen logistics proved challenging. However, this would pose a problem especially for testing the larger reinforcing fibres. The measuring frame of the impact pendulum would probably need to be altered. The spread of the resulting values of mechanical characteristics is a direct consequence of the nature of fibre-reinforcing. Ideally, the tested specimens need to be more numerous, or better manufacturings method needs to be employed for better homogeneity. Parallel to this work, a research project is under way that explores the possibility of controlled fibre orientation using a magnetic field.

The materials chosen for this study were mostly ordinary materials used in the past or compositions taken after the literature sources. The author believes, that the fibre reinforcement still needs to be researched. New combinations of constituents specifically optimised for creating efficient fibre-reinforced composites should be found. With the help of the new impact pendulum testing, achieving this goal should be possible.

References

[1] Pierre-Claude Aïtcin. *Vysokohodnotný beton*. 1st Czech. Prague: Informační centrum ČKAIT, 2005, p. 320.

[2] Sidney Mindess. *Developments in the Formulation and Reinforcement of Concrete*. 2nd ed. Woodhead Publishing, 2019.

[3] Armen Amirkhanianand and Jeffery Roesle. *Overview of Fiber-Reinforced Concrete Bridge Deck: Final Report*. Tech. rep. Iowa State University, 2019.

[4] Antonio Grimaldi, Alberto Meda, and Zila Rinaldi. "Experimental behaviour of fibre reinforced concrete bridge decks subjected to punching shear". In: *Composites Part B: Engineering* 45.1 (Feb. 2013), pp. 811–820.

[5] Ductal®. *Hydraulic Structures*. URL: `https://www.ductal.com/en/engineering/hydraulic-structures` (visited on 04/05/2020).

[6] V. Marcos-Meson, G. Fischer, C. Edvardsen, T.L. Skovhus, and A. Michel. "Durability of Steel Fibre Reinforced Concrete (SFRC) exposed to acid attack – A literature review". In: *Construction and Building Materials* 200 (Mar. 2019), pp. 490–501.

[7] Hanson UK. *Fibre Reinforced Concrete - Plastic, Steel & Poly*. URL: `https://www.hanson.co.uk/en/ready-mixed-concrete/reinforced-concrete` (visited on 04/13/2020).

[8] Nemkumar Banthia, Vivek Bindiganavile, John Jones, and Jeff Novak. "Fiber-reinforced concrete in precast concrete applications: Research leads to innovative products". In: *PCI Journal* 57.3 (June 2012), pp. 33–46.

[9] Mingke Deng, Fudong Ma, Shifei Song, Hao Lü, and Hongzhe Sun. "Seismic performance of interior precast concrete beam-column connections with highly ductile fiber-reinforced concrete in the critical cast-in-place regions". In: *Engineering Structures* 210 (May 2020), p. 110360.

[10] Arnon Bentur and Sidney Mindess. *Fibre Reinforced Cementitious Composites*. 2nd ed. New York: Taylor & Francis, 2007.

[11] Dong Zhang, Aravind Dasari, and Kang Hai Tan. "On the mechanism of prevention of explosive spalling in ultra-high performance concrete with polymer fibers". In: *Cement and Concrete Research* 113 (Nov. 2018), pp. 169–177.

[12] Kai Lyu, Wei She, Honglei Chang, and Yue Gu. "Effect of fine aggregate size on the overlapping of interfacial transition zone (ITZ) in mortars". In: *Construction and Building Materials* 248 (July 2020), p. 118559.

[13] G.M. Sadiqul Islam, M.H. Rahman, and Nayem Kazi. "Waste glass powder as partial replacement of cement for sustainable concrete practice". In: *International Journal of Sustainable Built Environment* 6.1 (June 2017), pp. 37–44.

[14] Y.S. Tai. "Flat ended projectile penetrating ultra-high strength concrete plate target". In: *Theoretical and Applied Fracture Mechanics* 51.2 (Apr. 2009), pp. 117–128.

[15] Doo-Yeol Yoo, Goangseup Zi, Su-Tae Kang, and Young-Soo Yoon. "Biaxial flexural behavior of ultra-high-performance fiber-reinforced concrete with different fiber lengths and placement methods". In: *Cement and Concrete Composites* 63 (Oct. 2015), pp. 51–66.

[16] A.M.T. Hassan, S.W. Jones, and G.H. Mahmud. "Experimental test methods to determine the uniaxial tensile and compressive behaviour of ultra high performance fibre reinforced concrete (UHPFRC)". In: *Construction and Building Materials* 37 (Dec. 2012), pp. 874–882.

[17] Doo-Yeol Yoo and Nemkumar Banthia. “Mechanical properties of ultra-high-performance fiber-reinforced concrete: A review”. In: *Cement and Concrete Composites* 73 (Oct. 2016), pp. 267–280.

[18] Nancy A. Soliman and Arezki Tagnit-Hamou. “Using glass sand as an alternative for quartz sand in UHPC”. In: *Construction and Building Materials* 145 (Aug. 2017), pp. 243–252.

[19] Zemei Wu, Kamal Henri Khayat, and Caijun Shi. “How do fiber shape and matrix composition affect fiber pullout behavior and flexural properties of UHPC?” In: *Cement and Concrete Composites* 90 (July 2018), pp. 193–201.

[20] Yin-Wen Chan and Shu-Hsien Chu. “Effect of silica fume on steel fiber bond characteristics in reactive powder concrete”. In: *Cement and Concrete Research* 34.7 (July 2004), pp. 1167–1172.

[21] Petr Konrád. “Experimentální vyšetřování mechanické energie absorbované prvky z vysokohodnotného vlákny vyztuženého betonu”. Master Thesis. Czech Technical University in Prague, Faculty of Civil Engineering, 2017.

[22] Ronald F. Zollo. “Fiber-reinforced concrete: an overview after 30 years of development”. In: *Cement and Concrete Composites* 19.2 (Jan. 1997), pp. 107–122.

[23] Sadoon Abdallah, Mizi Fan, and David W. A. Rees. “Bonding Mechanisms and Strength of Steel Fiber–Reinforced Cementitious Composites: Overview”. In: *Journal of Materials in Civil Engineering* 30.3 (Mar. 2018), p. 04018001.

[24] Doo-Yeol Yoo, Booki Chun, and Jae-Jin Kim. “Effect of calcium sulfoaluminate-based expansive agent on rate dependent pullout behavior of straight steel fiber embedded in UHPC”. In: *Cement and Concrete Research* 122 (Aug. 2019), pp. 196–211.

[25] Doo-Yeol Yoo and Soonho Kim. “Comparative pullout behavior of half-hooked and commercial steel fibers embedded in UHPC under static and impact loads”. In: *Cement and Concrete Composites* 97 (Mar. 2019), pp. 89–106.

[26] Hesham Othman and H. Marzouk. “Strain Rate Sensitivity of Fiber-Reinforced Cementitious Composites”. In: *ACI Materials Journal* 113.2 (Apr. 2016).

[27] Malgorzata Pajak. “The influence of the strain rate on the strength of concrete taking into account the experimental techniques”. In: *Architecture Civil Engineering Environment* 4.3 (2011), pp. 77–86.

[28] Fanlu Min, Zhanhu Yao, and Teng Jiang. “Experimental and Numerical Study on Tensile Strength of Concrete under Different Strain Rates”. In: *The Scientific World Journal* 2014 (2014), pp. 1–11.

[29] Joško Ožbolt, Akanshu Sharma, Barış İrhan, and Emiliano Sola. “Tensile behavior of concrete under high loading rates”. In: *International Journal of Impact Engineering* 69 (July 2014), pp. 55–68.

[30] Joško Ožbolt, Akanshu Sharma, and Hans-Wolf Reinhardt. “Dynamic fracture of concrete – compact tension specimen”. In: *International Journal of Solids and Structures* 48.10 (May 2011), pp. 1534–1543.

[31] Natalija Bede, Joško Ožbolt, Akanshu Sharma, and Bariş İrhan. “Dynamic fracture of notched plain concrete beams: 3D finite element study”. In: *International Journal of Impact Engineering* 77 (Mar. 2015), pp. 176–188.

[32] Ilse Vegt and Jaap Weerheijm. “Influence of moisture on the fracture behaviour of concrete loaded in dynamic tension”. In: *Proceedings of the 9th International Conference on Fracture Mechanics of Concrete and Concrete Structures*. IA-FraMCoS, May 2016.

[33] Y.Y.Y. Cao, Q.L. Yu, H.J.H. Brouwers, and W. Chen. “Predicting the rate effects on hooked-end fiber pullout performance from Ultra-High Performance Concrete (UHPC)”. In: *Cement and Concrete Research* 120 (June 2019), pp. 164–175.

[34] Jun Kil Park, Seung Hun Park, and Dong Joo Kim. “Effect of matrix shrinkage on rate sensitivity of the pullout response of smooth steel fibers in ultra-high-performance concrete”. In: *Cement and Concrete Composites* 94 (Nov. 2018), pp. 226–237.

[35] Yuh-Shiou Tai, Sherif El-Tawil, and Ta-Hsiang Chung. “Performance of deformed steel fibers embedded in ultra-high performance concrete subjected to various pullout rates”. In: *Cement and Concrete Research* 89 (Nov. 2016), pp. 1–13.

[36] Man Xu, Bryan Hallinan, and Kay Wille. “Effect of loading rates on pullout behavior of high strength steel fibers embedded in ultra-high performance concrete”. In: *Cement and Concrete Composites* 70 (July 2016), pp. 98–109.

[37] Taher Abu-Lebdeh, Sameer Hamoush, and Brian Zornig. “Rate Effect on Pullout Behavior of Steel Fibers Embedded in Very-High Strength Concrete”. In: *American Journal of Engineering and Applied Sciences* 3.2 (Feb. 2010), pp. 454–463.

[38] Dong Joo Kim, Sherif El-Tawil, and Antoine E. Naaman. “Loading rate effect on pullout behavior of deformed steel fibers”. In: *ACI Materials Journal* 105 (2008), pp. 576–584.

[39] Petr Konrád and Radoslav Sovják. “Experimental procedure for determination of the energy dissipation capacity of ultra-high-performance fibre-reinforced concrete under localized impact loading”. In: *International Journal of Protective Structures* 10.2 (June 2019), pp. 251–265.

[40] Bo Zhou and Yuichi Uchida. “Relationship between fiber orientation/distribution and post-cracking behaviour in ultra-high-performance fiber-reinforced concrete (UHPFRC)”. In: *Cement and Concrete Composites* 83 (Oct. 2017), pp. 66–75.

[41] Bensaid Boulekbache, Mostefa Hamrat, Mohamed Chemrouk, and Sofiane Amziane. “Flowability of fibre-reinforced concrete and its effect on the mechanical properties of the material”. In: *Construction and Building Materials* 24.9 (Sept. 2010), pp. 1664–1671.

[42] European Committee for Standardization. “EN 14889-1:2006 Fibres for concrete - Part 1: Steel fibres - Definitions, specifications and conformity”. In: (2006).

[43] European Committee for Standardization. “EN 14845-1:2007 Test methods for fibres in concrete - Part 1: Reference concretes”. In: (2007).

[44] Czech office for standards metrology and testing. “ČSN P 73 2451 Fibre-reinforced concrete – Testing of fresh fibre-reinforced concrete”. In: (2015).

[45] European Committee for Standardization. “EN 14721:2005+A1:2007 Test method for metallic fibre concrete - Measuring the fibre content in fresh and hardened concrete”. In: (2007).

[46] VicRoads. “RC 377.01 Determination of the Fibre Content of Fresh Concrete (Wash-out Method)”. In: (2019).

[47] Japan Society of Civil Engineers. “JSCE-F 554 Test method for content of steel fiber in steel fiber reinforced concrete”. In: (1999).

[48] Czech office for standards metrology and testing. “ČSN P 73 2452 Fibre-reinforced concrete - Testing of hardened fibre-reinforced concrete”. In: (2015).

[49] European Committee for Standardization. “EN 14488-3:2006 Testing sprayed concrete - Part 3: Flexural strengths (first peak, ultimate and residual) of fibre reinforced beam specimens”. In: (2006).

[50] Japan Society of Civil Engineers. “JSCE-G 552 Test method for bending strength and bending toughness of steel fiber reinforced concrete”. In: (2010).

[51] American Society for Testing and Materials. “ASTM C1609 / C1609M - 19a Standard Test Method for Flexural Performance of Fiber-Reinforced Concrete (Using Beam With Third-Point Loading)”. In: (2019).

[52] European Committee for Standardization. “EN 14651:2005+A1:2007 Test method for metallic fibre concrete - Measuring the flexural tensile strength (limit of proportionality (LOP), residual)”. In: (2007).

[53] American Concrete Institue. “ACI 544.2R-89 Measurement of Properties of Fiber Reinforced Concrete”. In: (1999).

[54] Sallal R. Abid, Munther L. Abdul-Hussein, Nadheer S. Ayoob, Sajjad H. Ali, and Ahmed L. Kadhum. "Repeated drop-weight impact tests on self-compacting concrete reinforced with micro-steel fiber". In: *Heliyon* 6.1 (Jan. 2020), e03198.

[55] Japan Society of Civil Engineers. "JSCE-SF7 Method of Tests for Fiber Content of Steel Fiber Concrete". In: *Concrete Library International* 3 (1984), pp. 71–74.

[56] Josep M. Torrents, Ana Blanco, Pablo Pujadas, Antonio Aguado, Pablo Juan-García, and Miguel Ángel Sánchez-Moragues. "Inductive method for assessing the amount and orientation of steel fibers in concrete". In: *Materials and Structures* 45.10 (Oct. 2012), pp. 1577–1592.

[57] Doo-Yeol Yoo, Nemkumar Banthia, Su-Tae Kang, and Young-Soo Yoon. "Effect of fiber orientation on the rate-dependent flexural behavior of ultra-high-performance fiber-reinforced concrete". In: *Composite Structures* 157 (Dec. 2016), pp. 62–70.

[58] Miguel A. Vicente, Gonzalo Ruiz, Dorys C. González, Jesús Mínguez, Manuel Tarifa, and Xiaoxin Zhang. "Effects of fiber orientation and content on the static and fatigue behavior of SFRC by using CT-Scan technology". In: *International Journal of Fatigue* 128 (Nov. 2019), p. 105178.

[59] Dorys C. González, Jesús Mínguez, Miguel A. Vicente, Francisco Cambronero, and Guillermo Aragón. "Study of the effect of the fibers' orientation on the post-cracking behavior of steel fiber reinforced concrete from wedge-splitting tests and computed tomography scanning". In: *Construction and Building Materials* 192 (Dec. 2018), pp. 110–122.

[60] Hau Y. Leung and Ramapillai V. Balendran. "Resonant Frequency in Polypropylene Fibre Reinforced Concrete (PFRC) with Pozzolanic Materials". In: *Journal of Civil Engineering and Management* 8.3 (2002), pp. 169–176.

[61] Mingxin Wu, Zhenfu Chen, and Chuhan Zhang. "Determining the impact behavior of concrete beams through experimental testing and meso-scale simulation: I. Drop-weight tests". In: *Engineering Fracture Mechanics* 135 (Feb. 2015), pp. 94–112.

[62] J.C. Vivas, R. Zerbino, M.C. Torrijos, and G. Giaccio. "Effect of the fibre type on concrete impact resistance". In: *Construction and Building Materials* 264 (Dec. 2020), p. 120200.

[63] Hamid Sadraie, Alireza Khaloo, and Hesam Soltani. "Dynamic performance of concrete slabs reinforced with steel and GFRP bars under impact loading". In: *Engineering Structures* 191 (July 2019), pp. 62–81.

[64] Vimal Kumar, M.A. Iqbal, and A.K. Mittal. "Experimental investigation of prestressed and reinforced concrete plates under falling weight impactor". In: *Thin-Walled Structures* 126 (May 2018), pp. 106–116.

[65] Y.Y.Y. Cao, G. Liu, H.J.H. Brouwers, and Qingliang Yu. "Enhancing the low-velocity impact resistance of ultra-high performance concrete by an optimized layered-structure concept". In: *Composites Part B: Engineering* 200 (Nov. 2020), p. 108221.

[66] J.C. Vivas, R. Zerbino, M.C. Torrijos, and G. Giaccio. "Effect of the fibre type on concrete impact resistance". In: *Construction and Building Materials* 264 (Dec. 2020), p. 120200.

[67] Thong M. Pham, Wensu Chen, Mohamed Elchalakani, Ali Karrech, and Hong Hao. "Experimental investigation on lightweight rubberized concrete beams strengthened with BFRP sheets subjected to impact loads". In: *Engineering Structures* 205 (Feb. 2020), p. 110095.

[68] Thuy-Tien Nguyen, A P Pearce, D Carpanen, D Sory, G Grigoriadis, N Newell, J Clasper, A Bull, W G Proud, and S D Masouros. "Experimental platforms to study blast injury". In: *Journal of the Royal Army Medical Corps* 165.1 (Feb. 2019), pp. 33–37.

[69] C.T. SUN. "Testing methods for dynamic interlaminar fracture toughness of polymeric composites". In: *Delamination Behaviour of Composites*. Elsevier, 2008, pp. 87–116.

[70] C. Sun, X. Chen, H. Li, Y. Zhen, and J. Zhang. "Dynamic and quasi-static compressive properties of modified double-base propellant at low temperature". In: *Recent Advances in Structural Integrity Analysis - Proceedings of the International Congress (APCF/SIF-2014)*. Elsevier, 2014, pp. 417–421.

[71] Matthias Quast and Manfred Curbach. “Concrete under biaxial dynamic compressive loading”. In: *Procedia Engineering* 210 (2017), pp. 24–31.

[72] Robert Panowicz and Jacek Janiszewski. “Tensile Split Hopkinson Bar Technique: Numerical Analysis of the Problem of Wave Disturbance and Specimen Geometry Selection”. In: *Metrology and Measurement Systems* 23.3 (Sept. 2016), pp. 425–436.

[73] Robert Gerlach, Christian Kettenbeil, and Nik Petrinic. “A new split Hopkinson tensile bar design”. In: *International Journal of Impact Engineering* 50 (Dec. 2012), pp. 63–67.

[74] Ali A. Heravi, Iurie Curosu, and Viktor Mechtcherine. “A gravity-driven split Hopkinson tension bar for investigating quasi-ductile and strain-hardening cement-based composites under tensile impact loading”. In: *Cement and Concrete Composites* 105 (Jan. 2020), p. 103430.

[75] Mohammad Reza Khosravani and Kerstin Weinberg. “A review on split Hopkinson bar experiments on the dynamic characterisation of concrete”. In: *Construction and Building Materials* 190 (Nov. 2018), pp. 1264–1283.

[76] X. J. Wu and D. A. Gorham. “Stress Equilibrium in the Split Hopkinson Pressure Bar Test”. In: *Le Journal de Physique IV* 07.C3 (Aug. 1997), pp. C3–91–C3–96.

[77] Alexis Rusinek. “Laboratory testing of ductile and brittle materials under high strain rates”. In: *5th International Conference on Protective Structures*. Poznan, Poland, 2018.

[78] Radoslav Sovják, Tomáš Vavřiník, Jan Zatloukal, Petr Máca, Tomáš Mičunek, and Michal Frydrýn. “Resistance of slim UHPFRC targets to projectile impact using in-service bullets”. In: *International Journal of Impact Engineering* 76 (Feb. 2015), pp. 166–177.

[79] Heng Dong, Zihao Liu, Haijun Wu, Xudong Gao, Aiguo Pi, and Fenglei Huang. “Study on penetration characteristics of high-speed elliptical cross-sectional projectiles into concrete”. In: *International Journal of Impact Engineering* 132 (Oct. 2019), p. 103311.

[80] Chuang Liu, Xianfeng Zhang, Haihua Chen, Jipeng Wang, Haiyang Wei, and Wei Xiong. “Experimental and theoretical study on steel long-rod projectile penetration into concrete targets with elevated impact velocities”. In: *International Journal of Impact Engineering* 138 (Apr. 2020), p. 103482.

[81] Xiangzhao Xu, Tianbao Ma, and Jianguo Ning. “Failure mechanism of reinforced concrete subjected to projectile impact loading”. In: *Engineering Failure Analysis* 96 (Feb. 2019), pp. 468–483.

[82] Xueyan Zhang, Haijun Wu, Shuang Zhang, and FengLei Huang. “Projectile penetration of reinforced concrete considering the effect of steel reinforcement: Experimental study and theoretical analysis”. In: *International Journal of Impact Engineering* 144 (Oct. 2020), p. 103653.

[83] Sebastjan Kravanja, Radoslav Sovják, Petr Konrád, and Jan Zatloukal. “Penetration Resistance of Semi-infinite UHPFRC Targets with various Fiber Volume Fractions against Projectile Impact”. In: *Procedia Engineering* 193 (2017), pp. 112–119.

[84] T. Sugano, H. Tsubota, Y. Kasai, N. Koshika, S. Orui, W.A. von Riesemann, D.C. Bickel, and M.B. Parks. “Full-scale aircraft impact test for evaluation of impact force”. In: *Nuclear Engineering and Design* 140.3 (June 1993), pp. 373–385.

[85] Mario Mongiardini, Ronald K. Faller, John D. Reid, Dave Meggers, Moni G. El-Aasar, and Jerry D. Plunkett. “Design and Testing of a Concrete Safety Barrier for Use on a Temporary FRP Composite Bridge Deck”. In: *Journal of Bridge Engineering* 18.11 (Nov. 2013), pp. 1198–1208.

[86] Marek Foglar, Radek Hajek, Josef Fladr, Jiri Pachman, and Jiri Stoller. “Full-scale experimental testing of the blast resistance of HPFRC and UHPFRC bridge decks”. In: *Construction and Building Materials* 145 (Aug. 2017), pp. 588–601.

[87] Michal Mára, Petr Konrád, Jindřich Fornůsek, Jan Zatloukal, Michal Frydrýn, Luboš Nouzovský, Tomáš Mičunek, and Radoslav Sovják. “Development of mobile road barrier made of ultra-high-performance fibre-reinforced concrete”. In: *Materials Today: Proceedings* (Apr. 2020).

[88] Tuan Kiet Tran and Dong Joo Kim. “Strain Energy Frame Impact Machine (SEFIM)”. In: *Journal of Advanced Concrete Technology* 10.3 (2012), pp. 126–136.

[89] R. Yu, L. van Beers, P. Spiesz, and H.J.H. Brouwers. “Impact resistance of a sustainable Ultra-High Performance Fibre Reinforced Concrete (UHPFRC) under pendulum impact loadings”. In: *Construction and Building Materials* 107 (Mar. 2016), pp. 203–215.

[90] Tomáš Janda, Alena Zemanová, Petr Hála, Petr Konrád, and Jaroslav Schmidt. “Reduced order model of glass plate loaded by low-velocity impact”. In: *International Journal of Computational Methods and Experimental Measurements* 8.1 (Jan. 2020), pp. 36–46.

[91] Radoslav Sovják, Tomáš Vavřiník, Jan Zatloukal, Petr Máca, Tomáš Mičunek, and Michal Frydrýn. “Resistance of slim UHPFRC targets to projectile impact using in-service bullets”. In: *International Journal of Impact Engineering* 76 (Feb. 2015), pp. 166–177.

[92] Radoslav Sovják, Tomáš Vavřiník, Petr Máca, Jan Zatloukal, Petr Konvalinka, and Yupu Song. “Experimental Investigation of Ultra-high Performance Fiber Reinforced Concrete Slabs Subjected to Deformable Projectile Impact”. In: *Procedia Engineering* 65 (2013), pp. 120–125.

[93] Karel Kolář, Zdeňka Bažantová, and Petr Konvalinka. *Suchá prefabrikovaná směs multifunkčního silikátového kompozitu*. 2015.

[94] B. Luccioni, F. Isla, R. Codina, D. Ambrosini, R. Zerbino, G. Giaccio, and M.C. Torrijos. “Effect of steel fibers on static and blast response of high strength concrete”. In: *International Journal of Impact Engineering* 107 (Sept. 2017), pp. 23–37.

[95] Ravi Ranade, Victor C. Li, and William F. Heard. “Tensile Rate Effects in High Strength-High Ductility Concrete”. In: *Cement and Concrete Research* 68 (Feb. 2015), pp. 94–104.

[96] Japan Concrete Institute. “JCI-S-001-2003: Method of test for fracture energy of concrete by use of notched beam”. In: (2003).

Appendix A Quasi-static loading

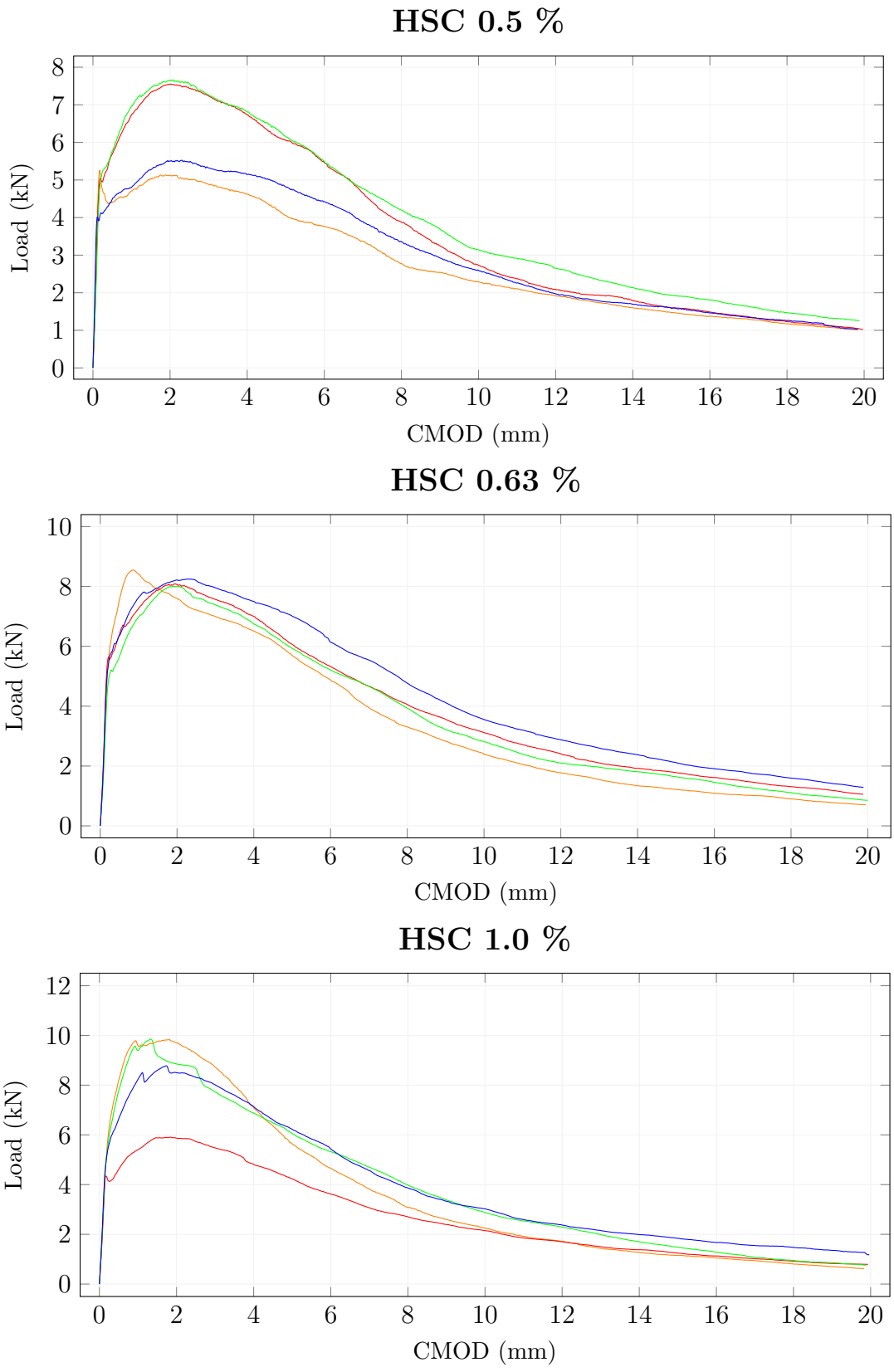

Figure A.1: Quasi-static loading, load - CMOD diagrams. Material HSC.

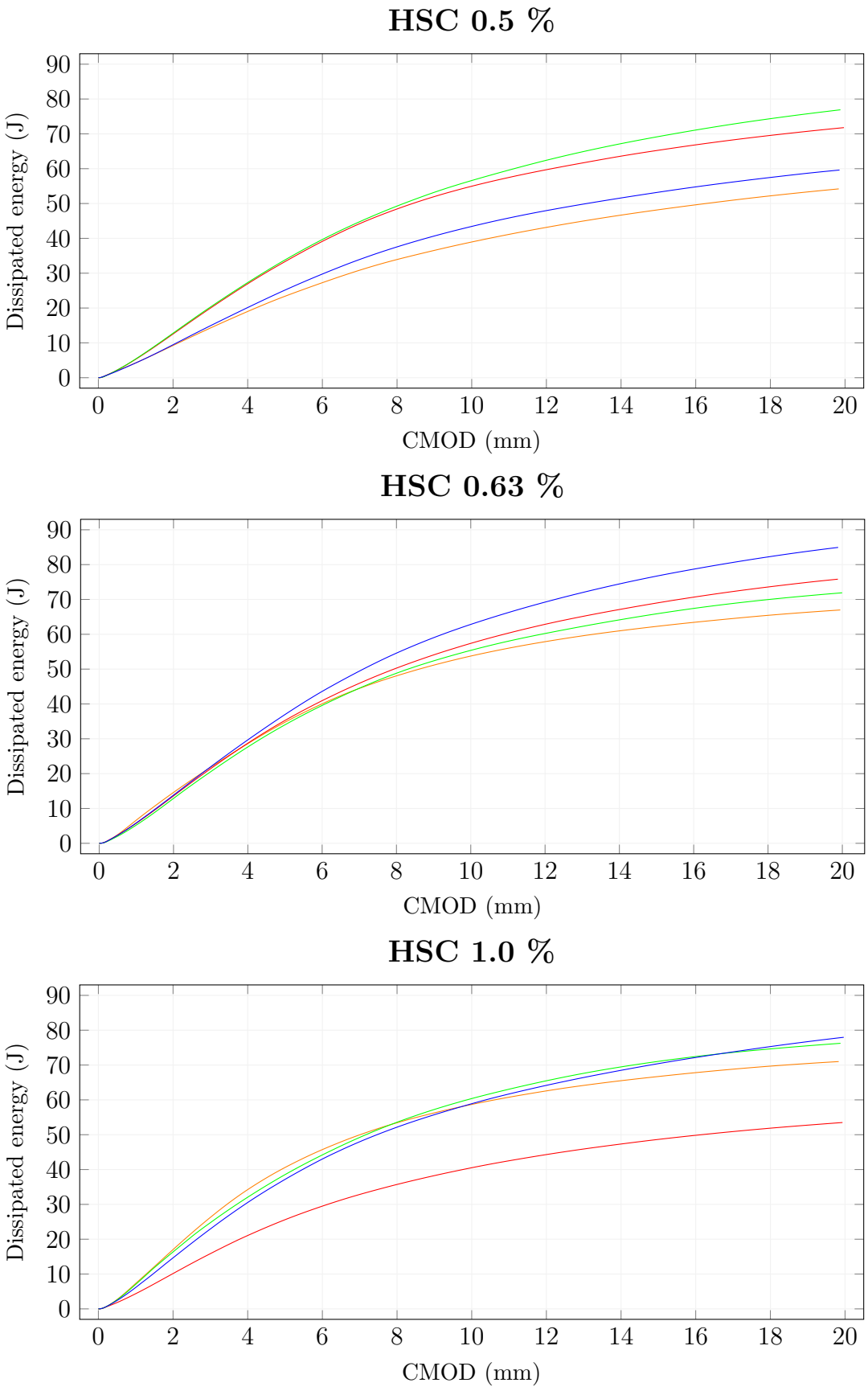

Figure A.2: Quasi-static loading, dis. energy - CMOD diagrams. Material HSC.

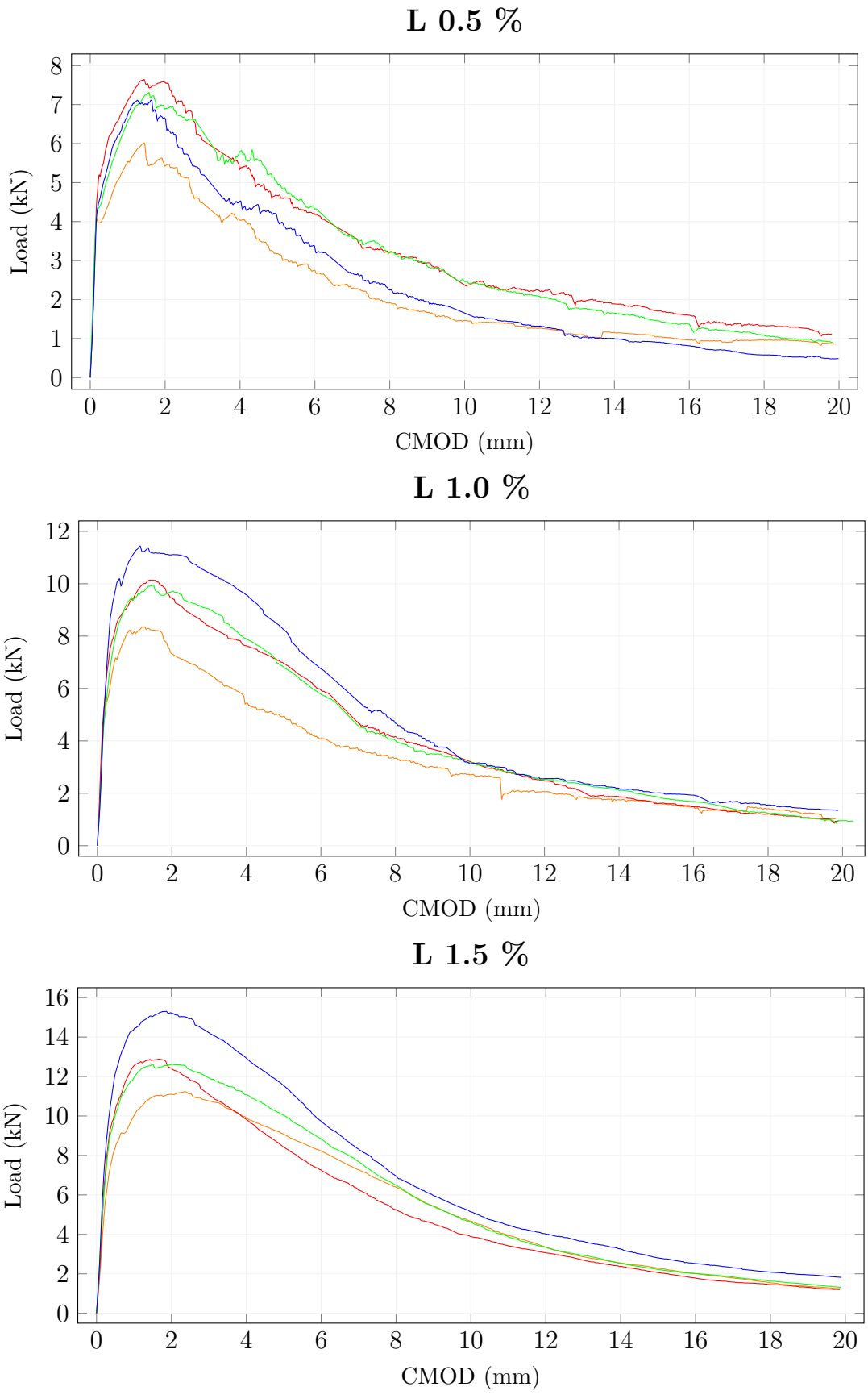

Figure A.3: Quasi-static loading, load - CMOD diagrams. Material L.

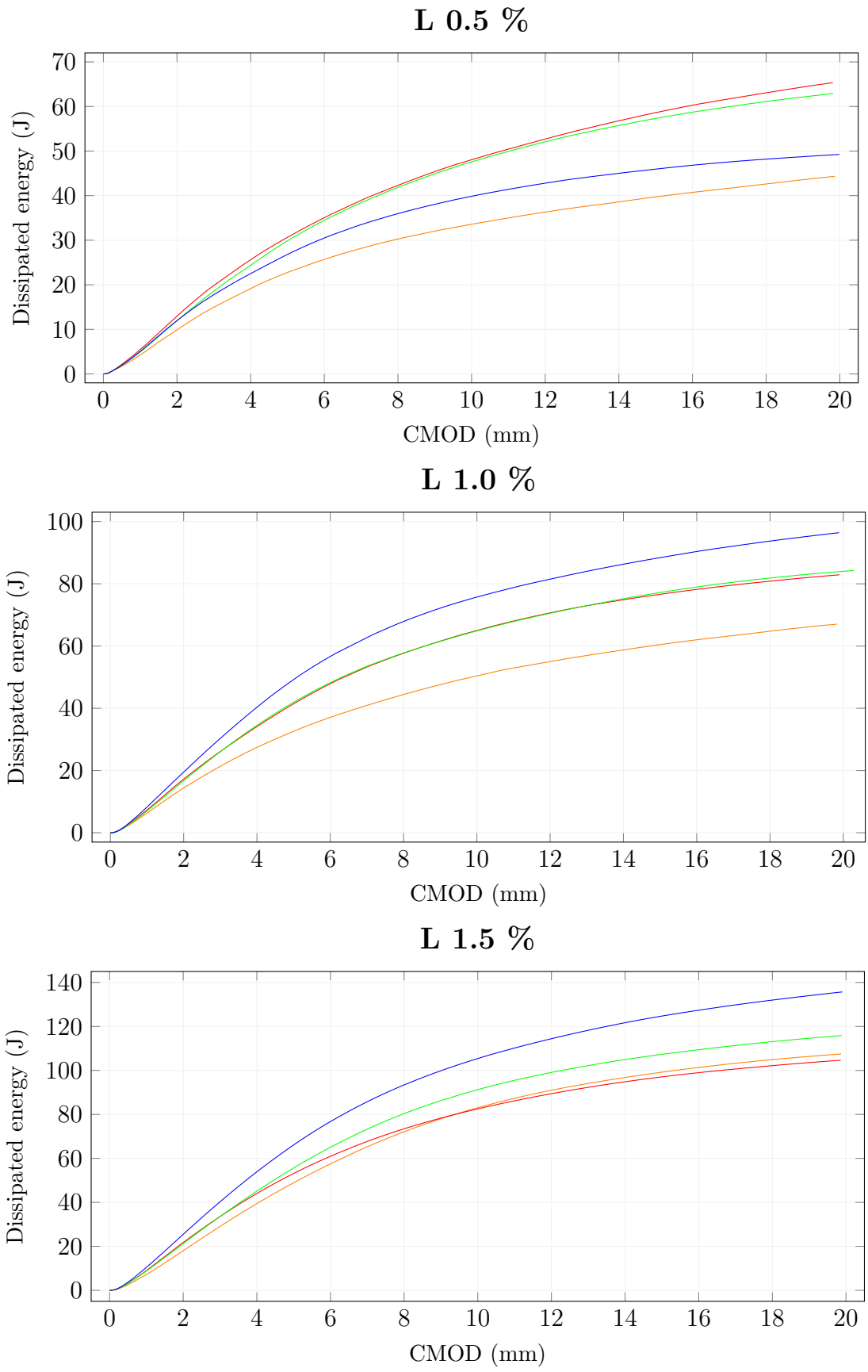

Figure A.4: Quasi-static loading, dis. energy - CMOD diagrams. Material L.

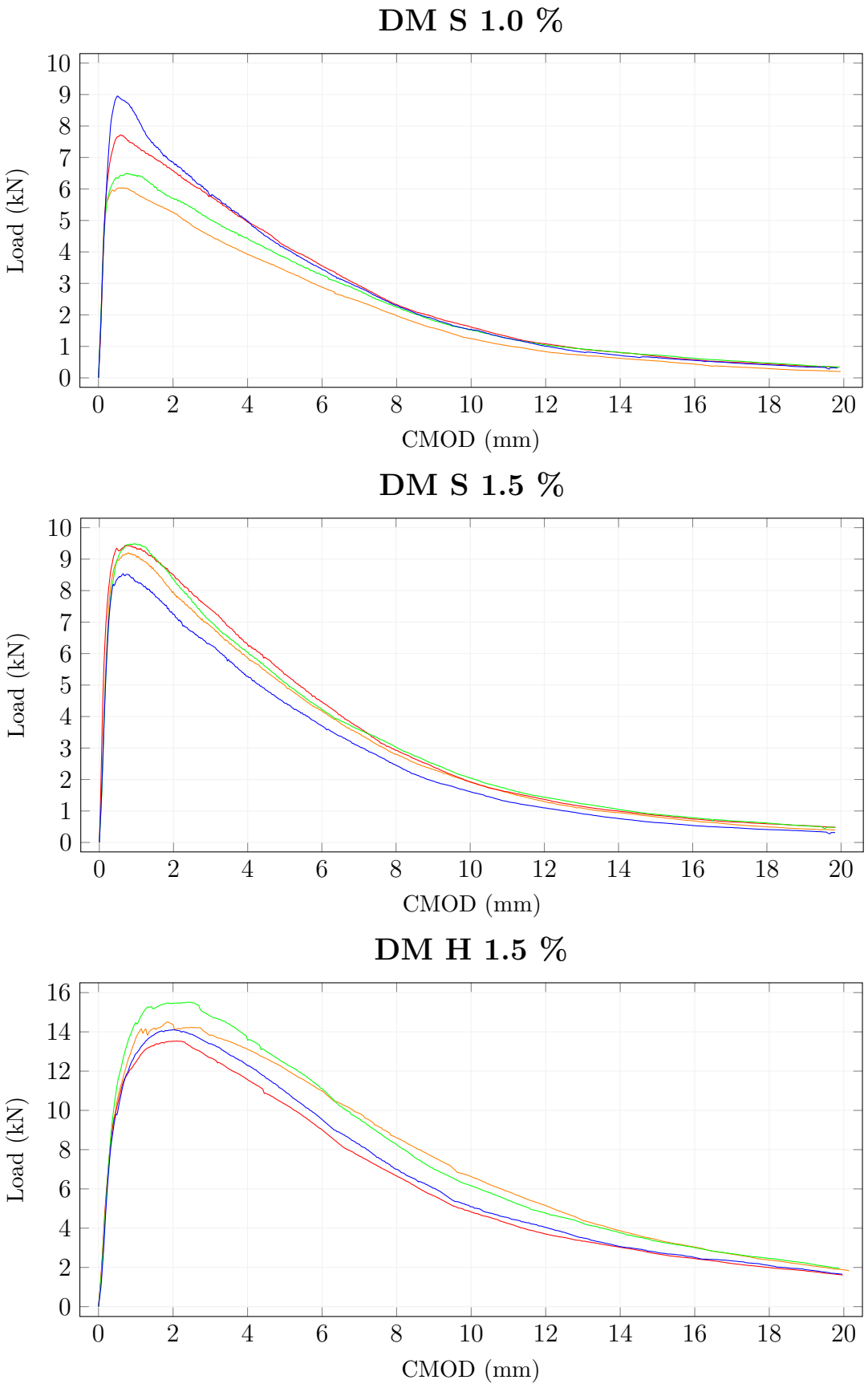

Figure A.5: Quasi-static loading, load - CMOD diagrams. Material DM.

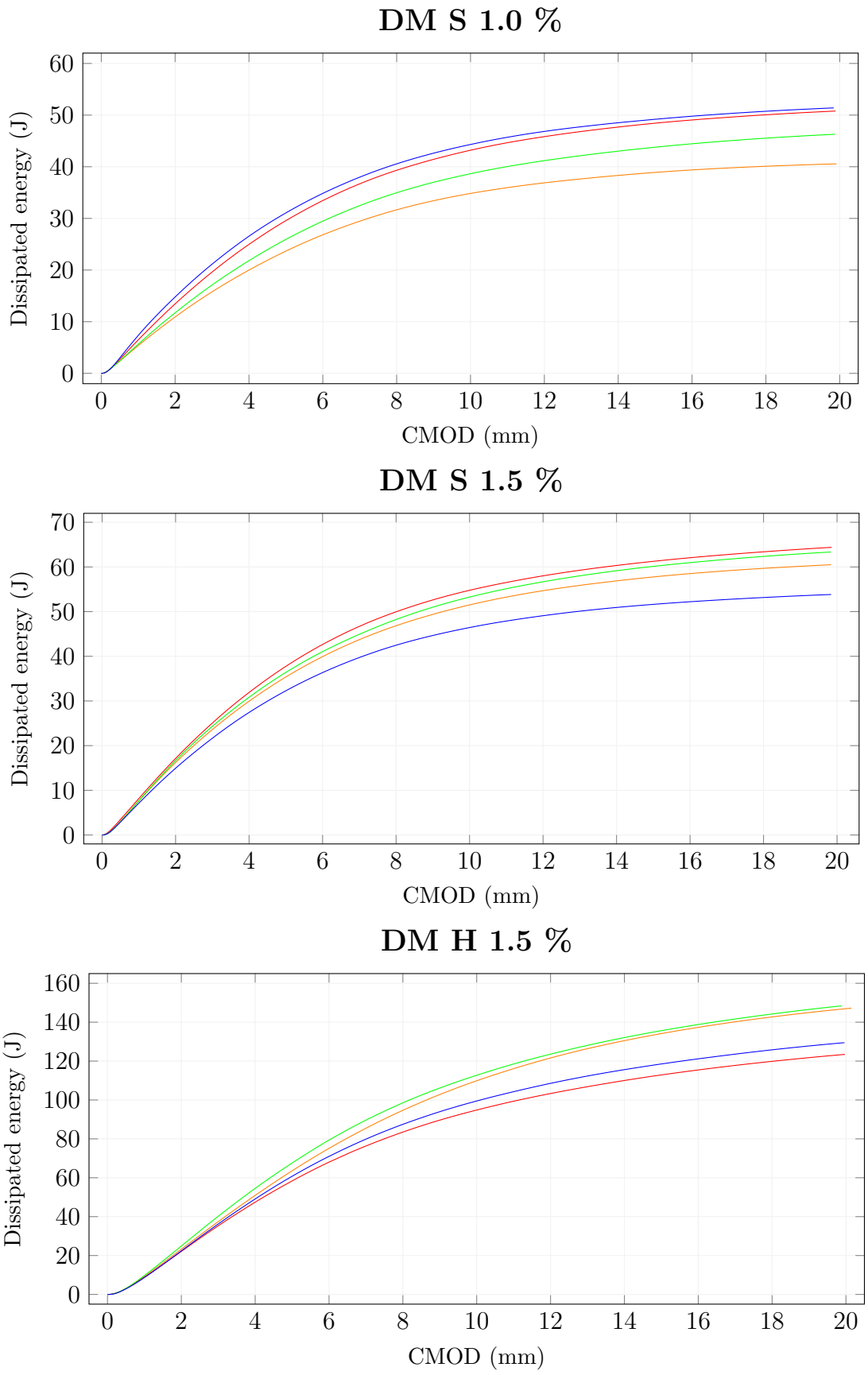

Figure A.6: Quasi-static loading, dis. energy - CMOD diagrams. Material DM.

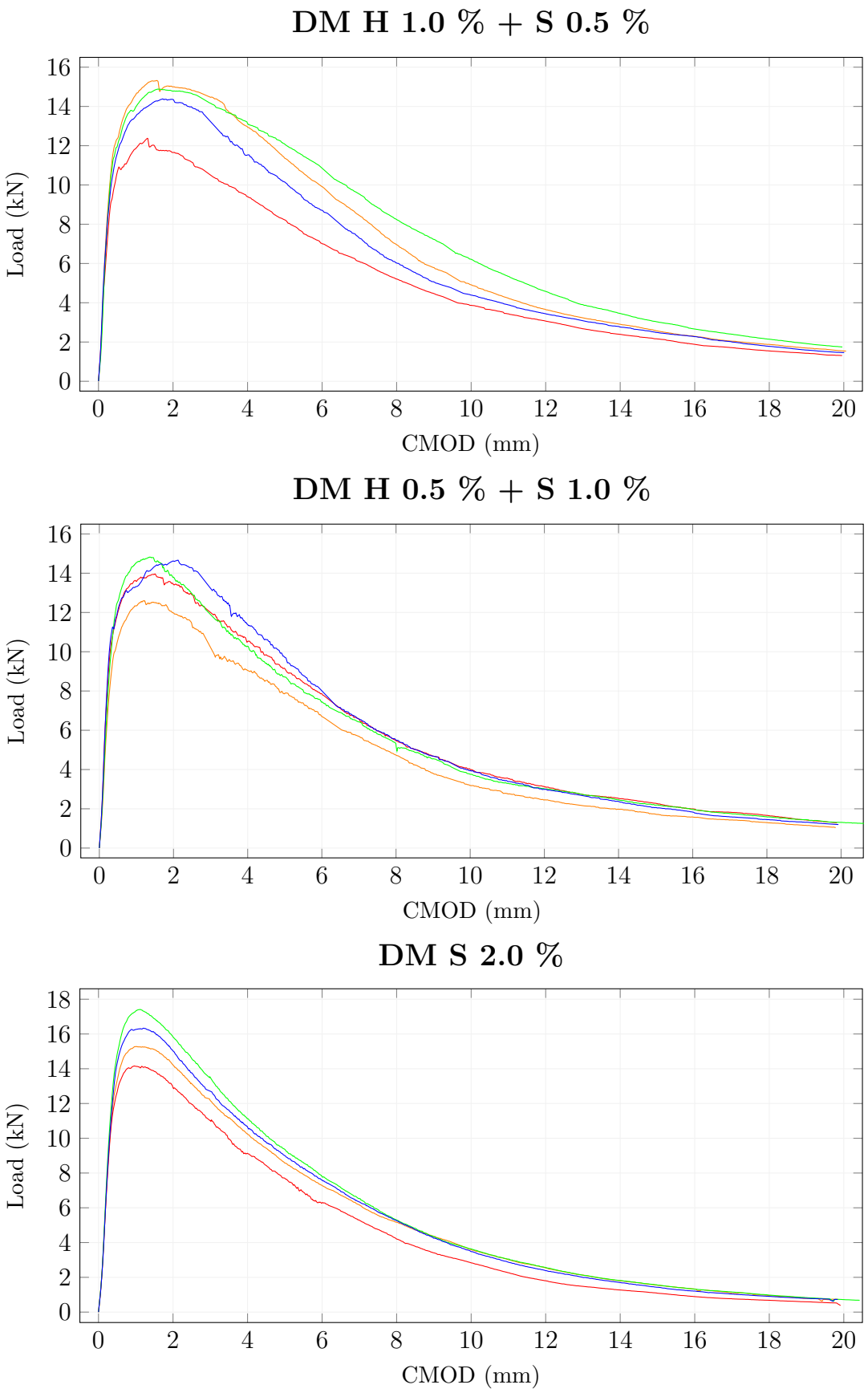

Figure A.7: Quasi-static loading, load - CMOD diagrams. Material DM.

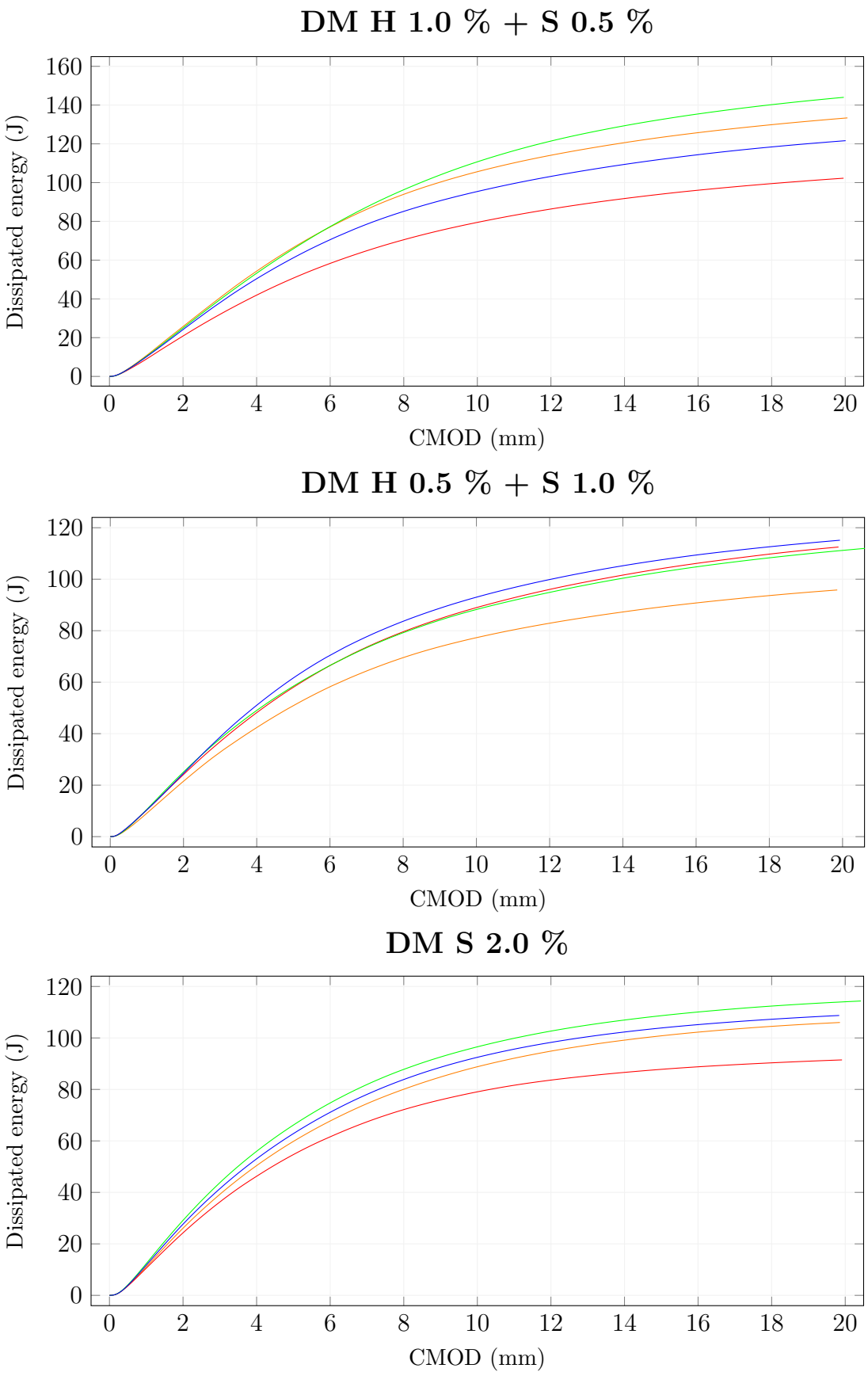

Figure A.8: Quasi-static loading, dis. energy - CMOD diagrams. Material DM.

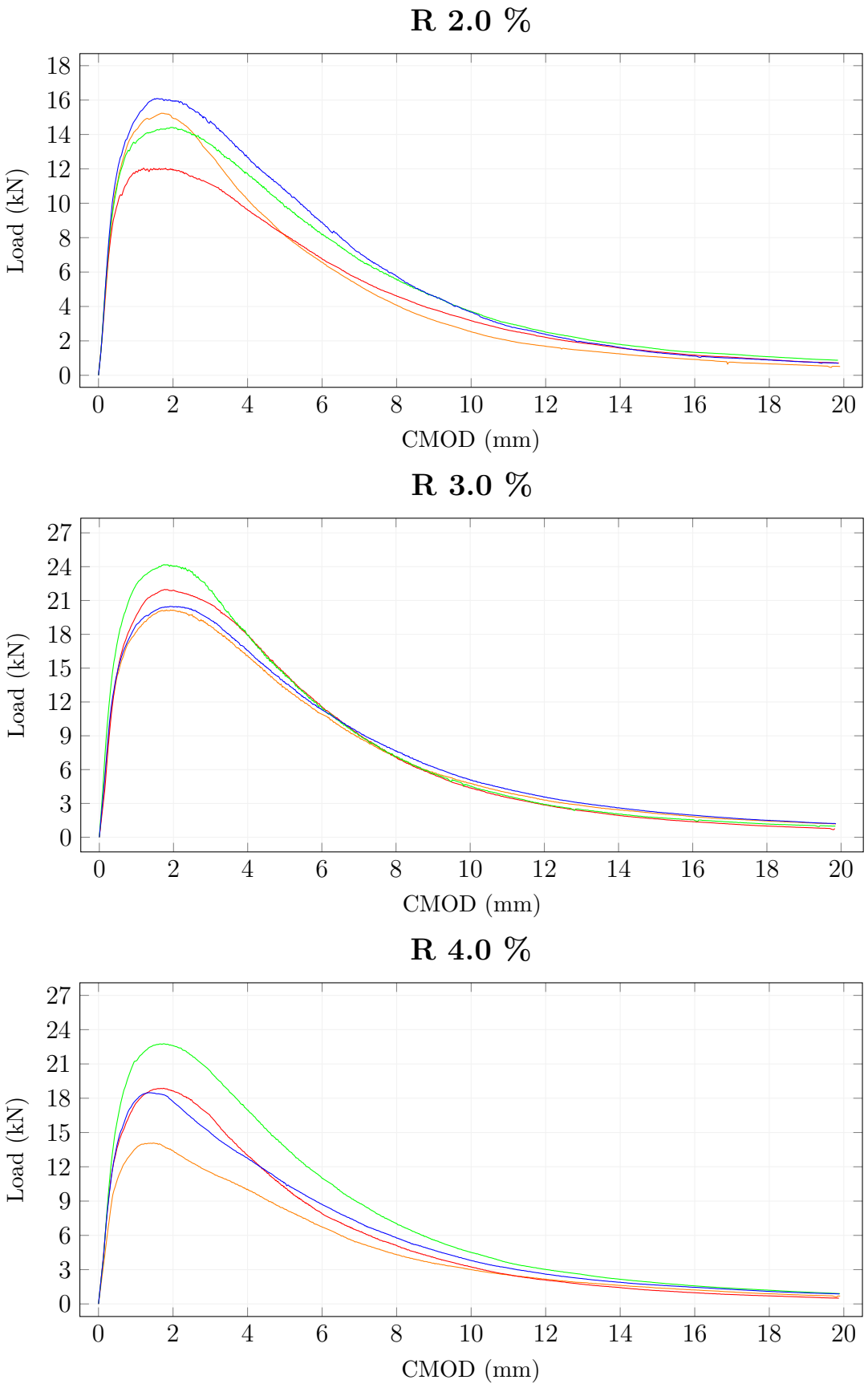

Figure A.9: Quasi-static loading, load - CMOD diagrams. Material R.

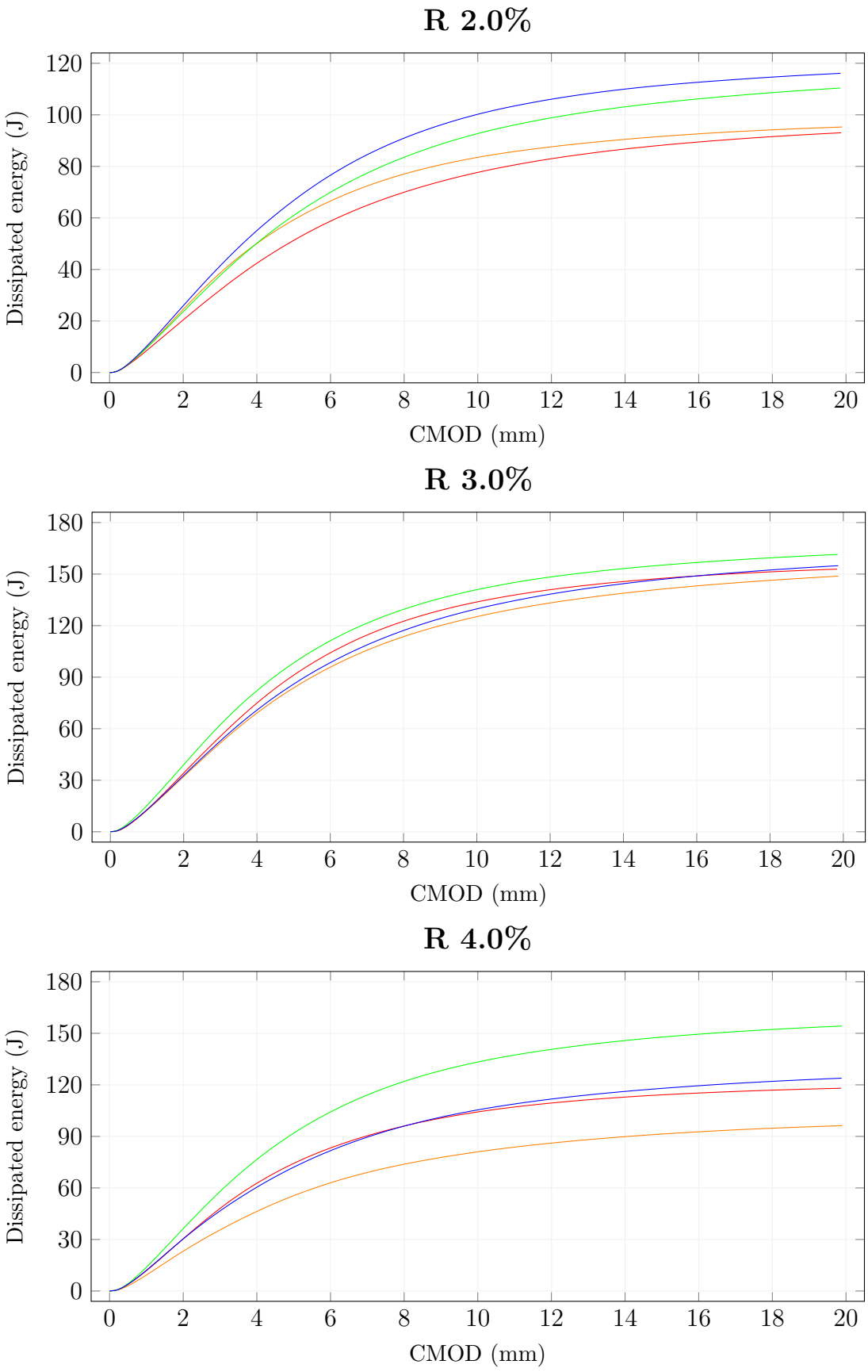

Figure A.10: Quasi-static loading, dis. energy - CMOD diagrams. Material R.

Appendix B

Impact loading

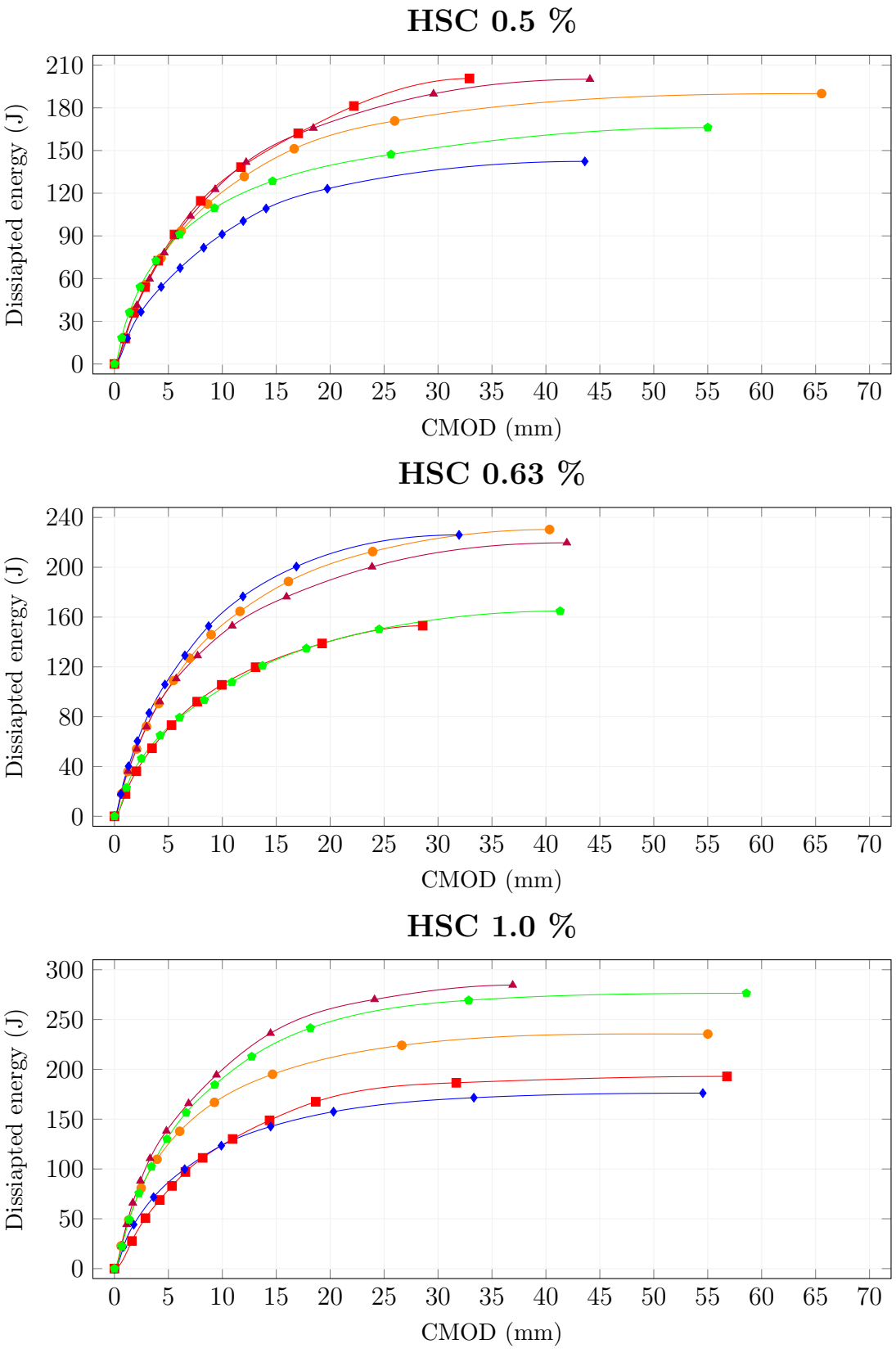

Figure B.1: Impact loading, dissipated energy - CMOD diagram. Material HSC.

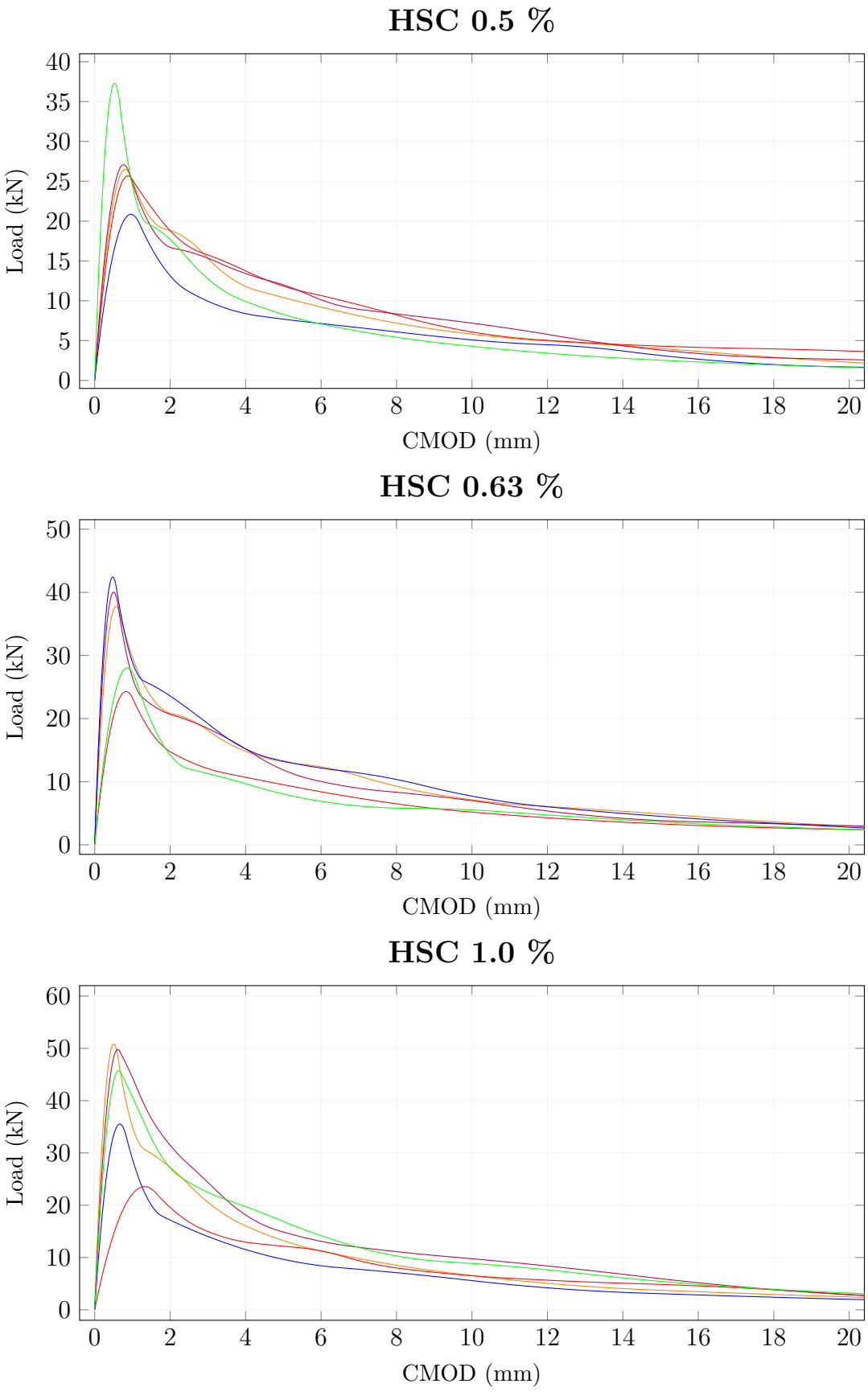

Figure B.2: Impact loading, calculated load - CMOD diagrams. Material HSC.

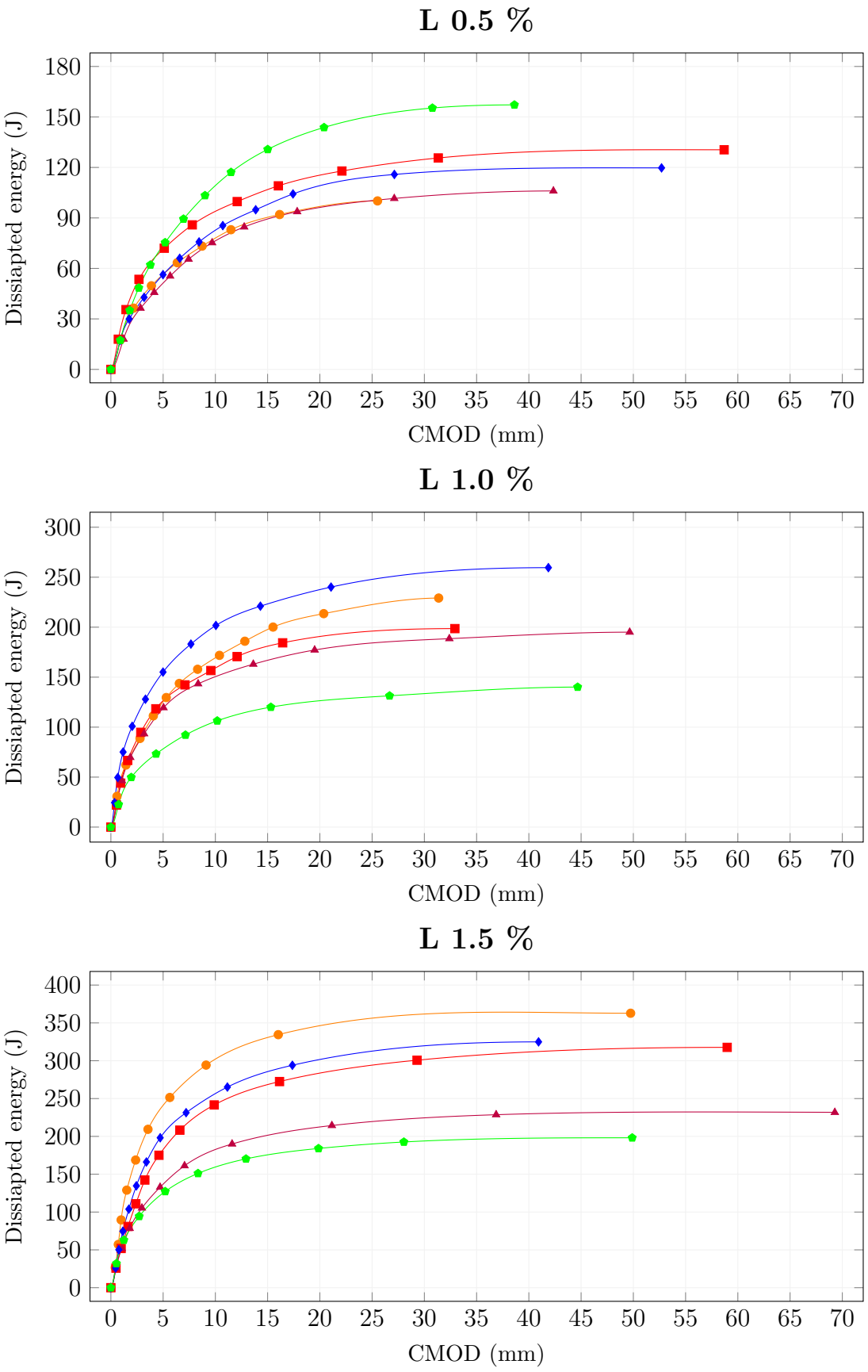

Figure B.3: Impact loading, dissipated energy - CMOD diagram. Material L.

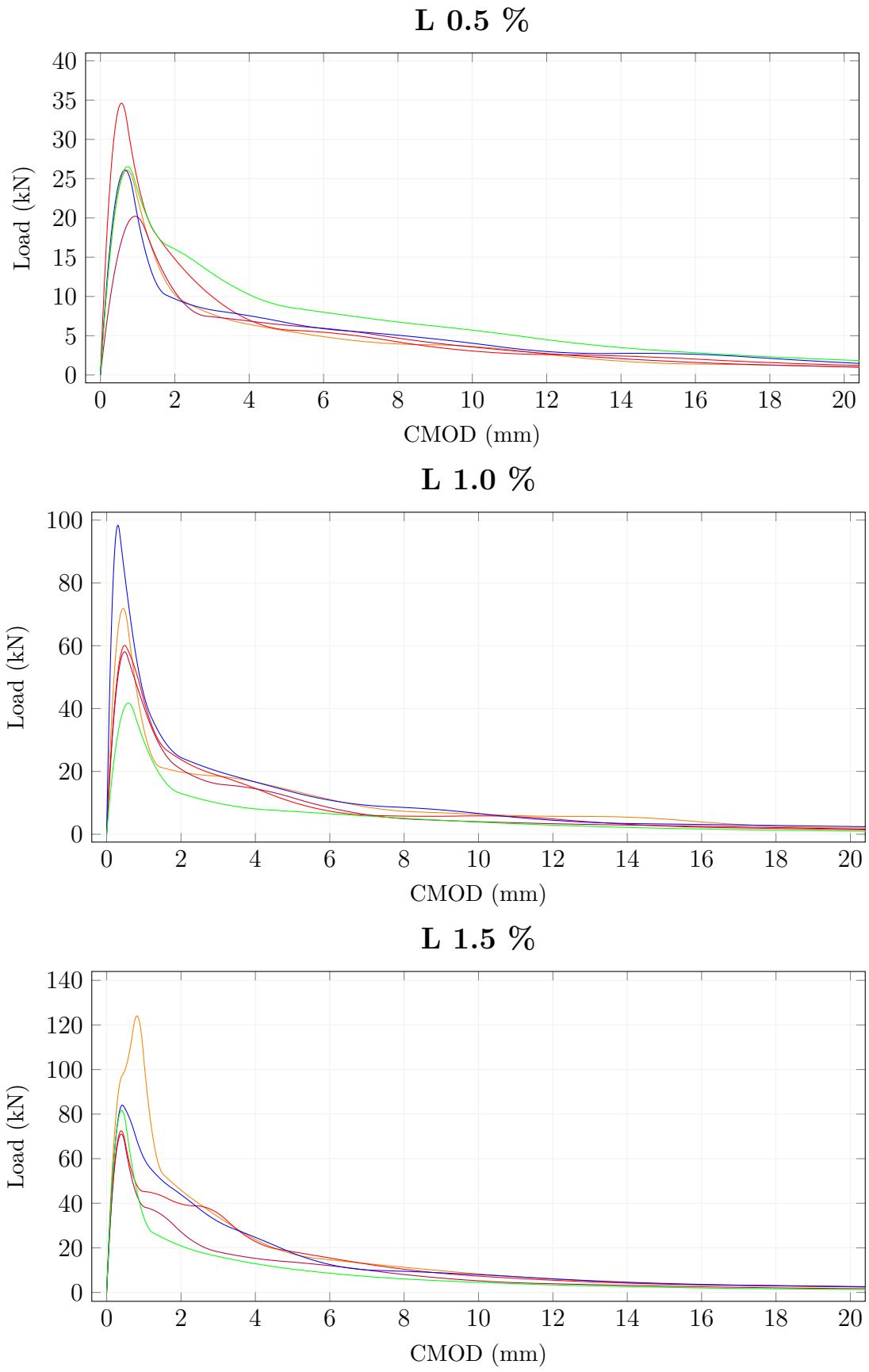

Figure B.4: Impact loading, calculated load - CMOD diagrams. Material L.

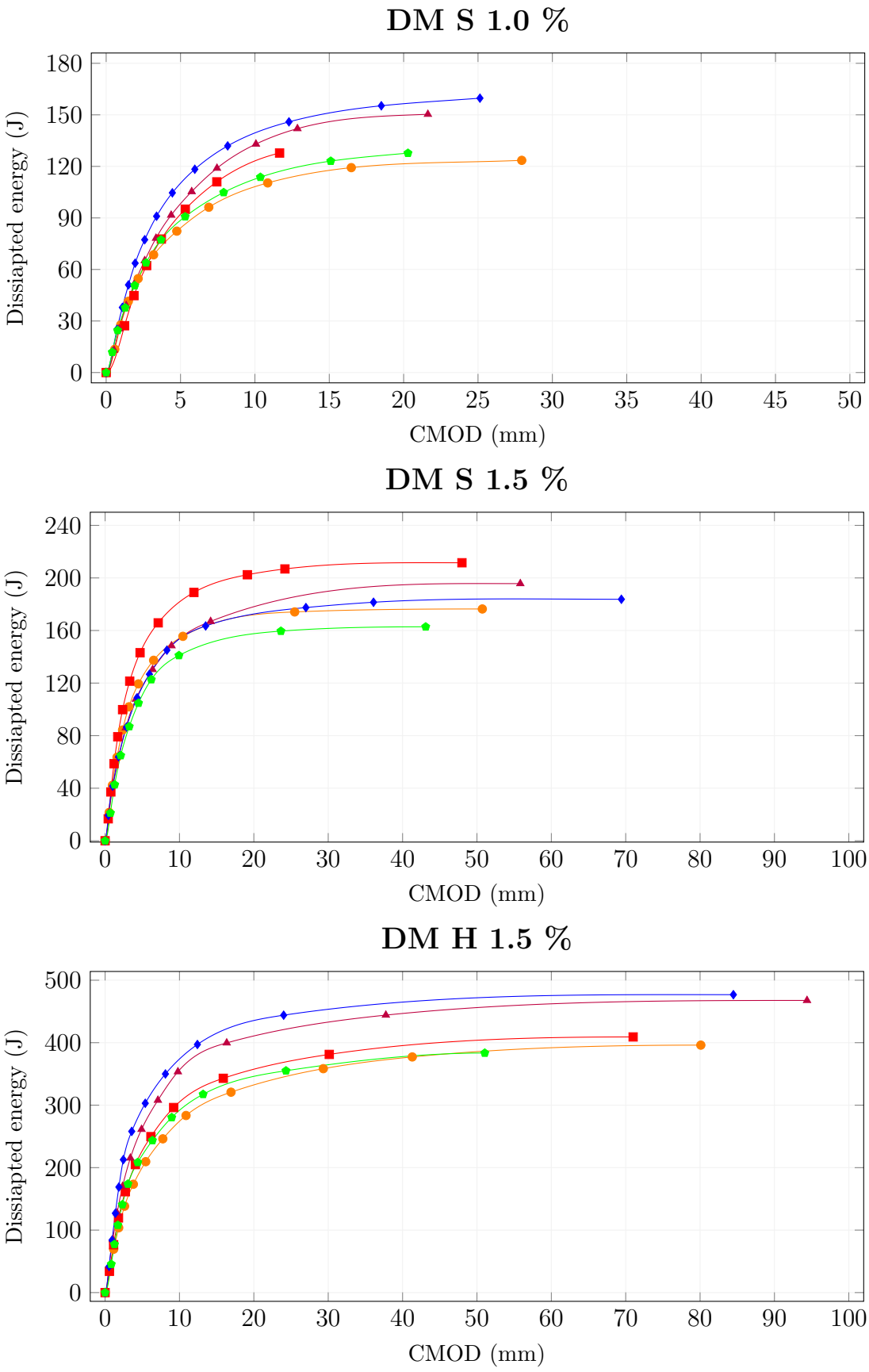

Figure B.5: Impact loading, dissipated energy - CMOD diagram. Material DM.

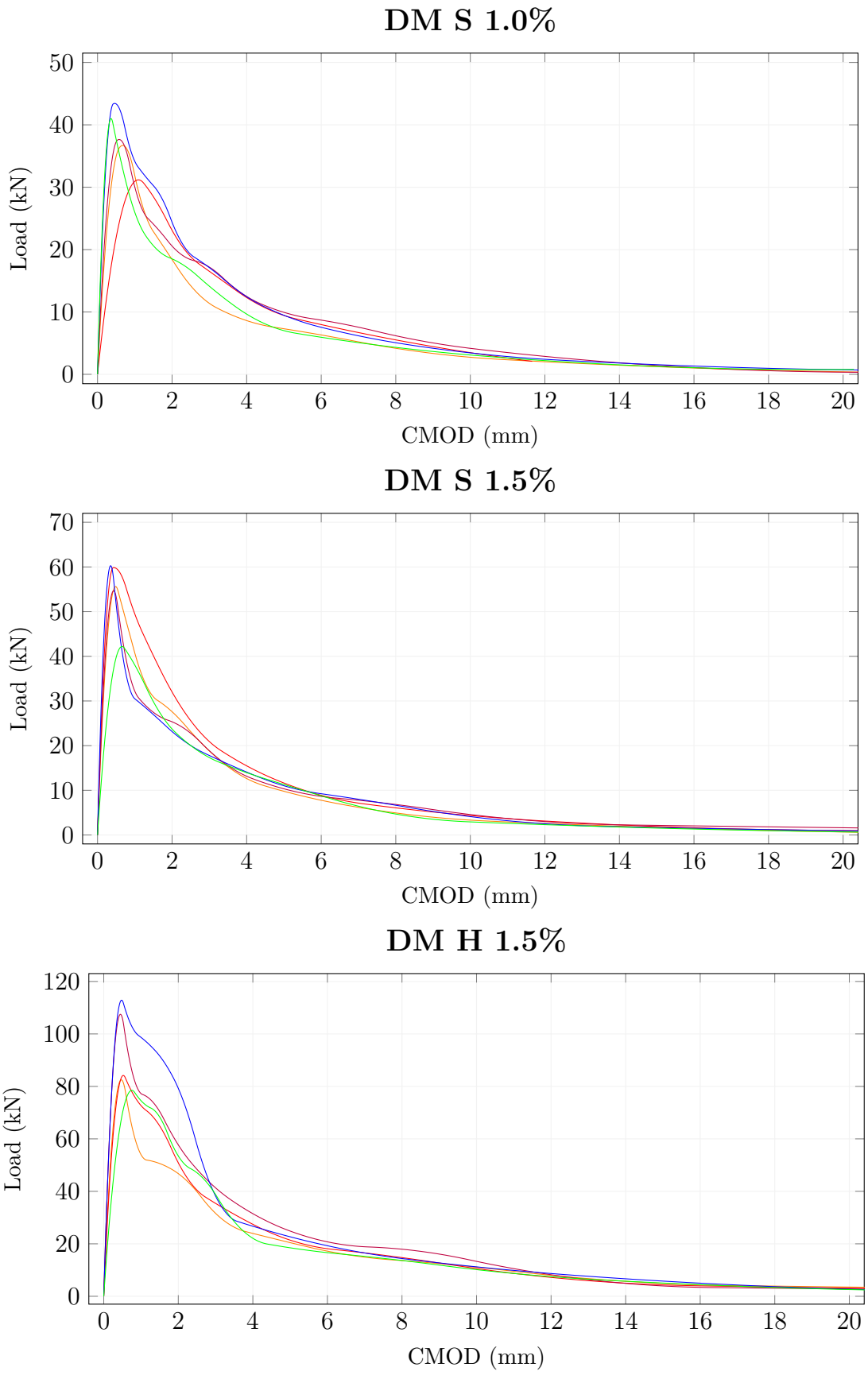

Figure B.6: Impact loading, calculated load - CMOD diagrams. Material DM.

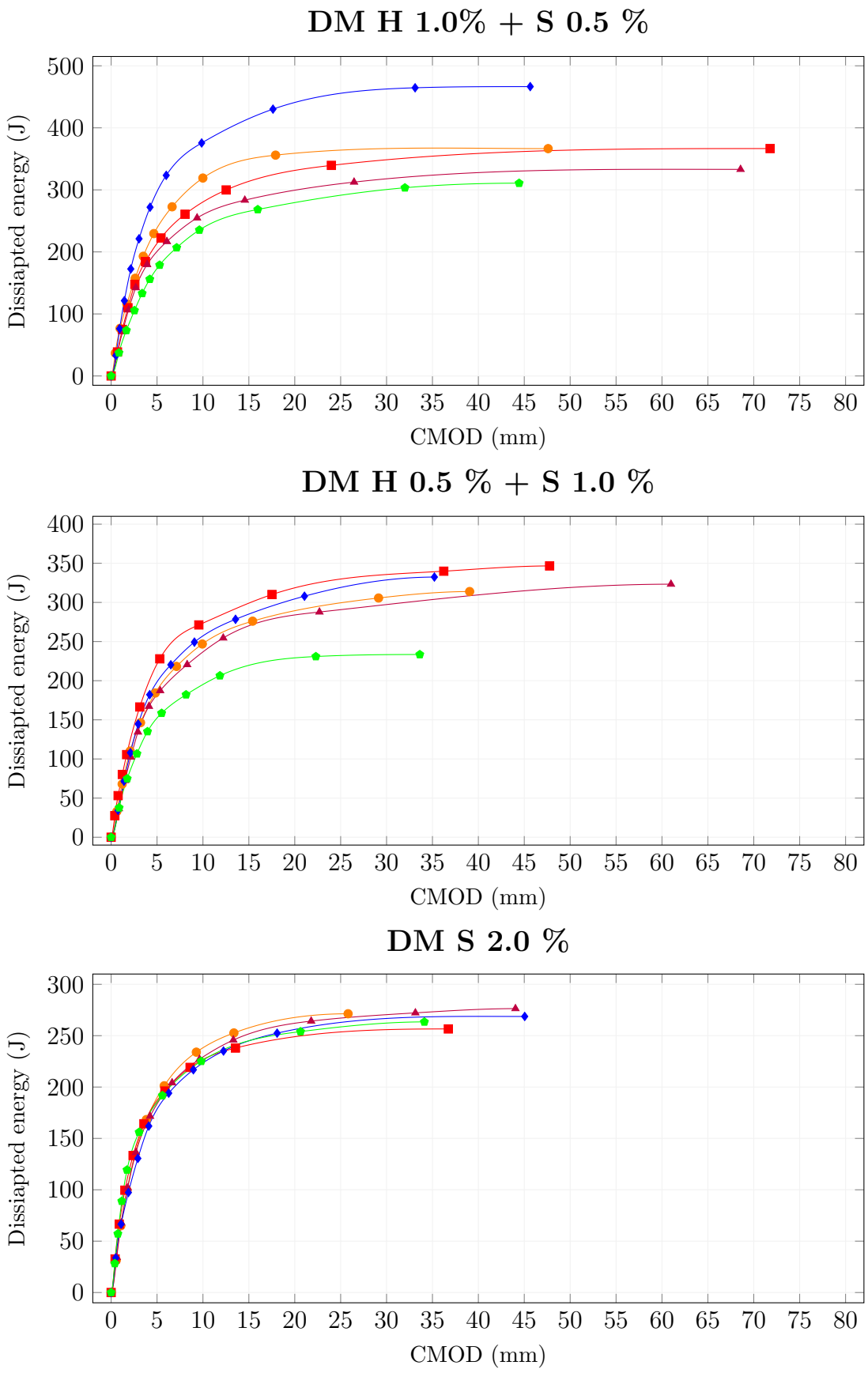

Figure B.7: Impact loading, dissipated energy - CMOD diagram. Material DM.

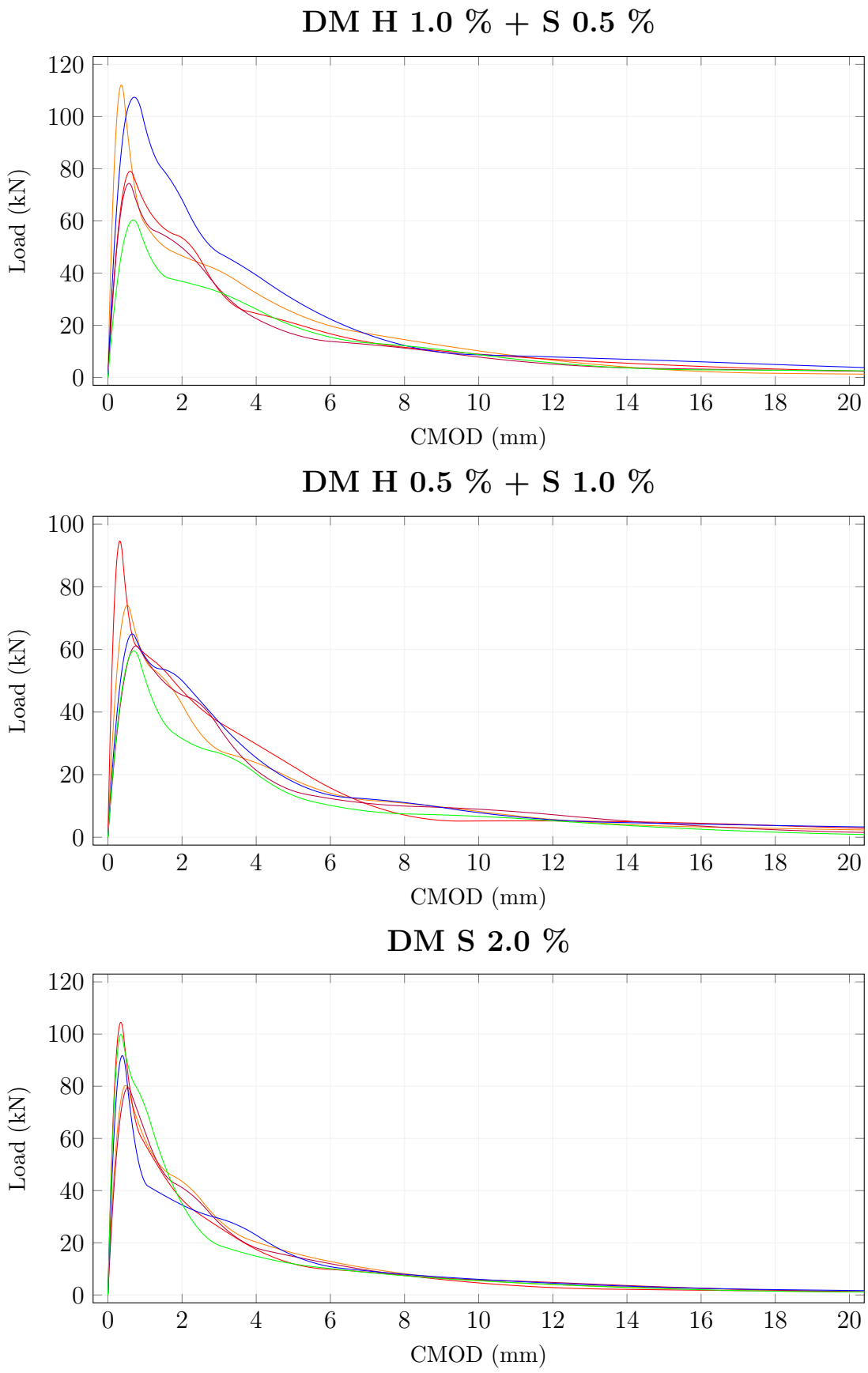

Figure B.8: Impact loading, calculated load - CMOD diagrams. Material DM.

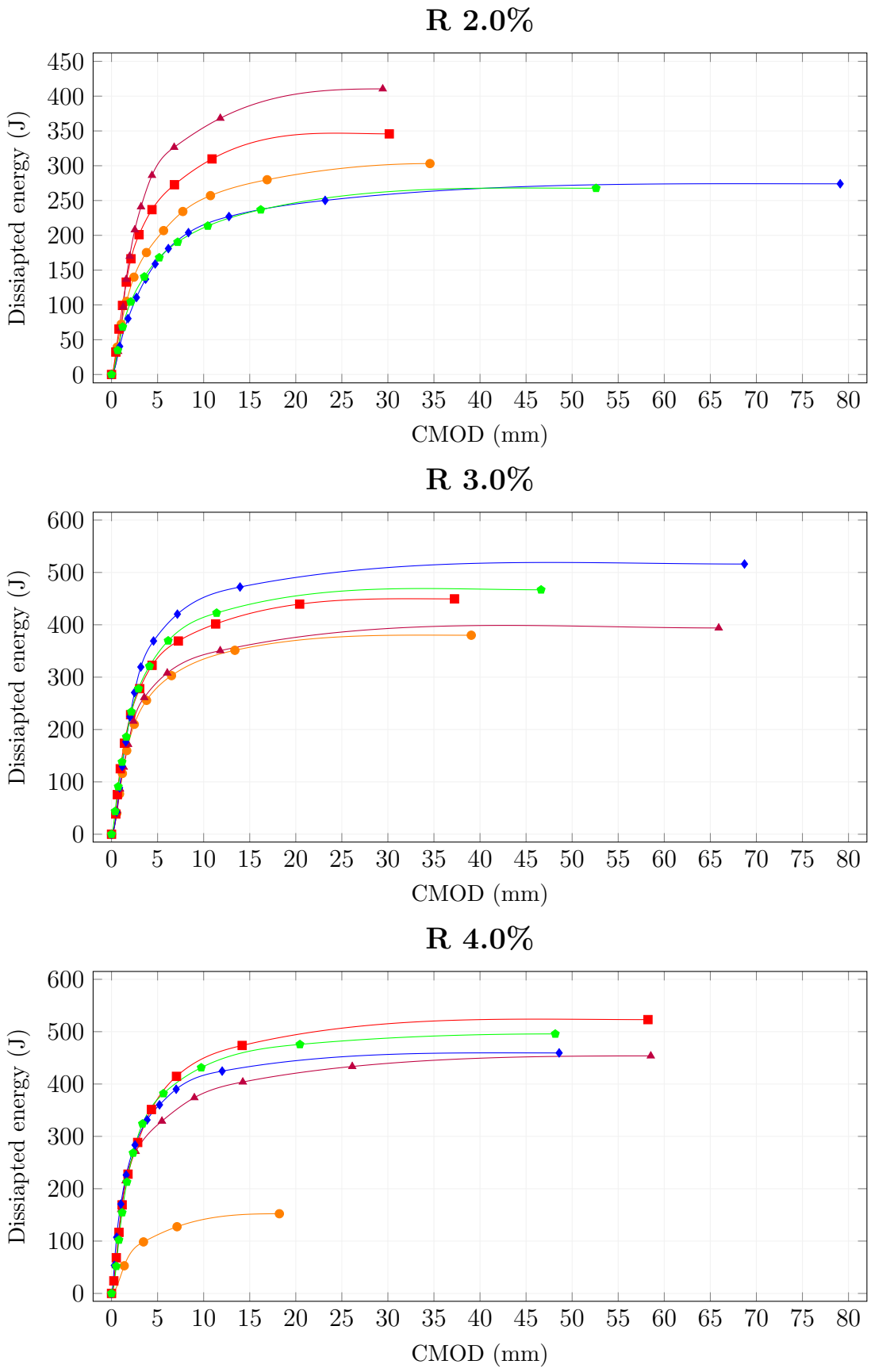

Figure B.9: Impact loading, dissipated energy - CMOD diagram. Material R.

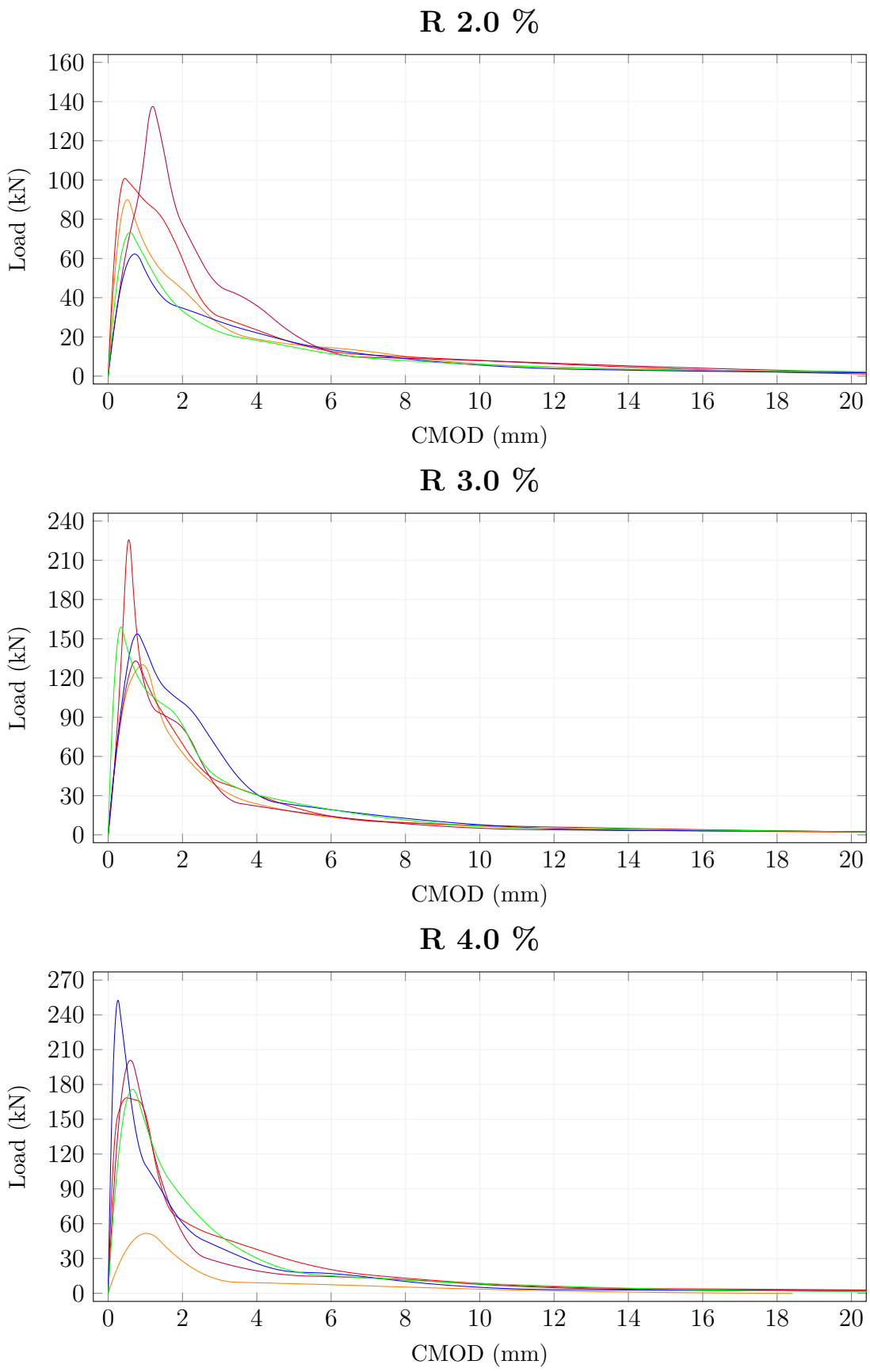

Figure B.10: Impact loading, calculated load - CMOD diagrams. Material R.

Appendix C Damage patterns

HSC 0.5 %

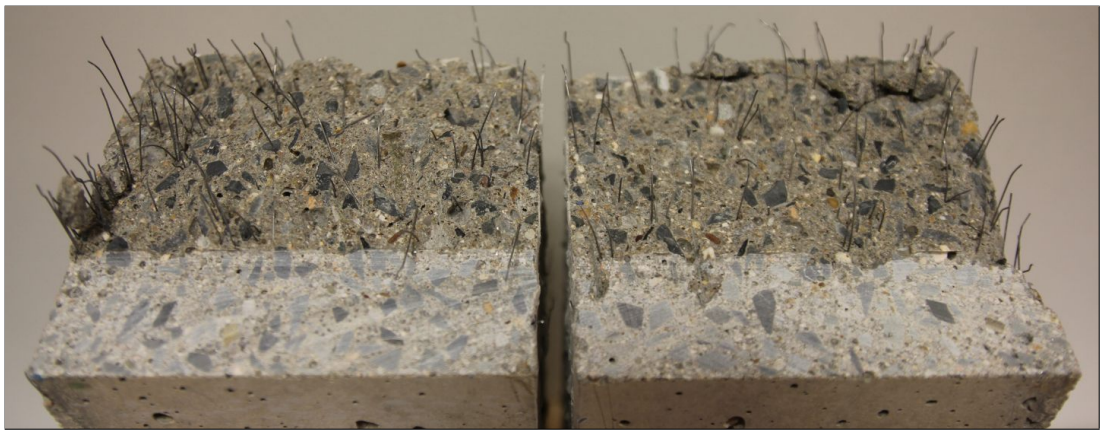

HSC 0.63 %

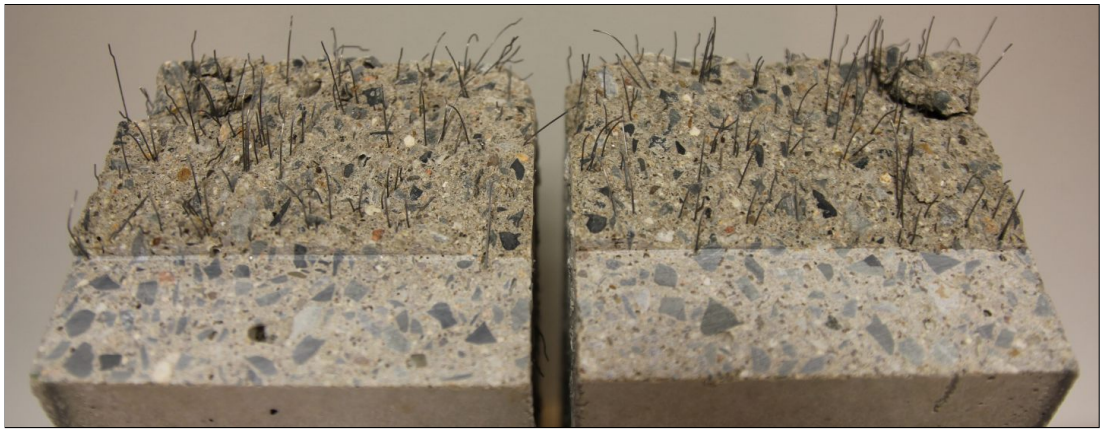

HSC 1 %

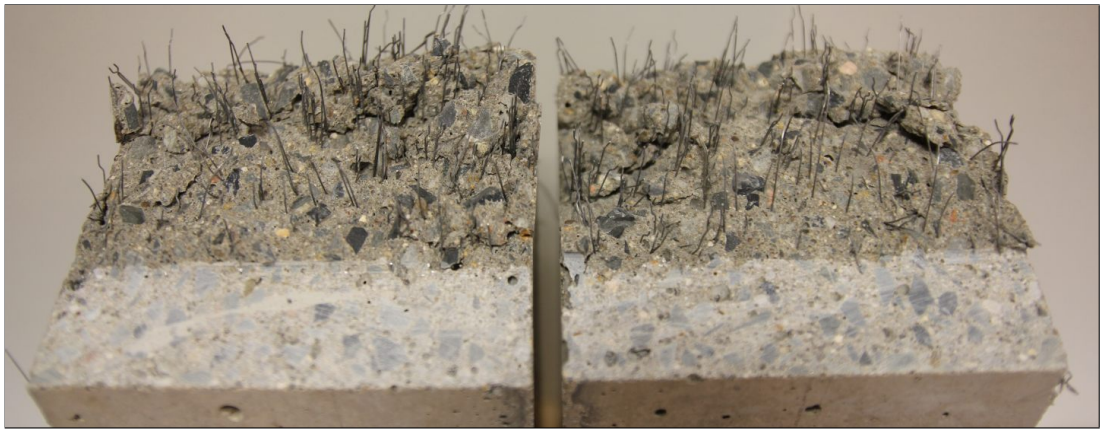

Figure C.1: Damage patterns after impact loading. Mixture HSC.

L 0.5 %

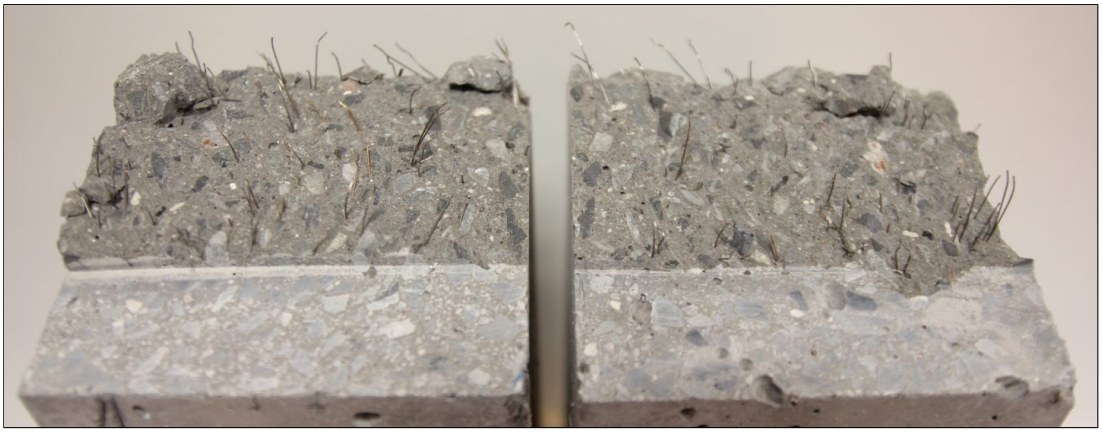

L 1 %

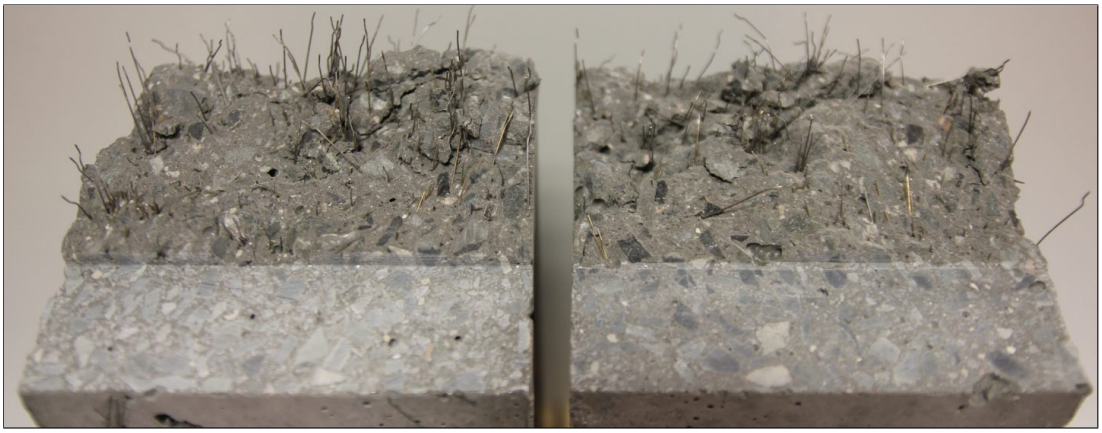

L 1.5 %

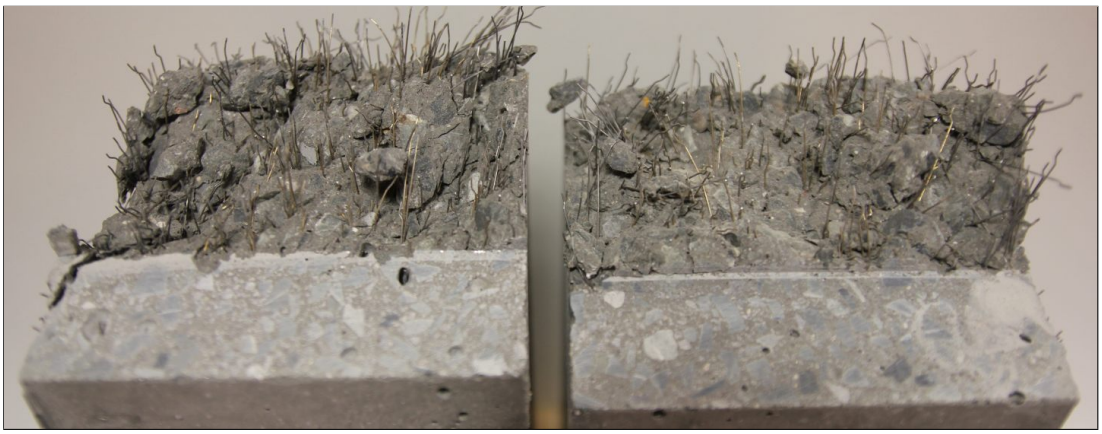

Figure C.2: Damage patterns after impact loading. Mixture L.

DM S 1.0 %

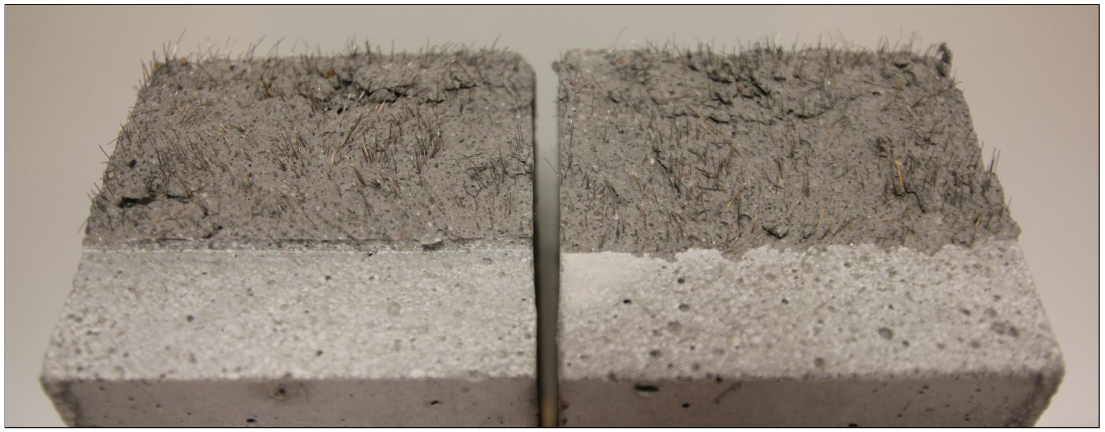

DM S 1.5 %

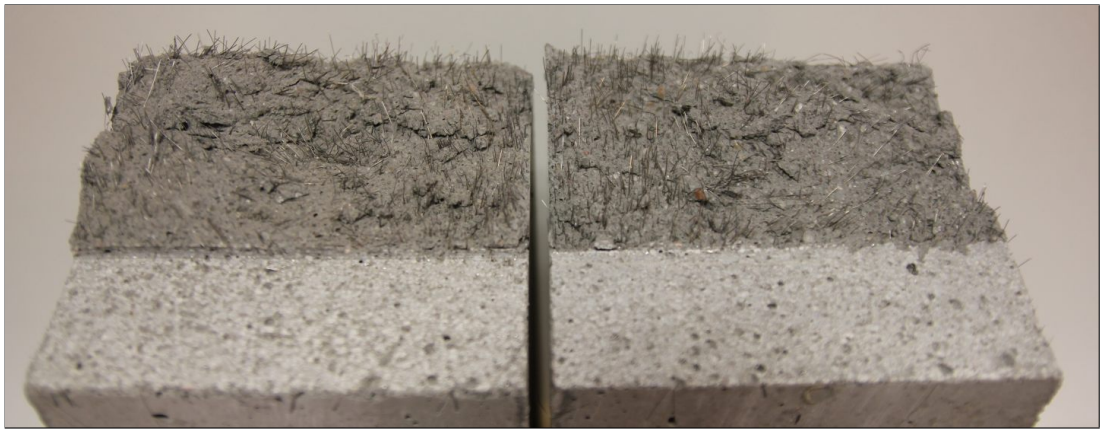

DM H 1.5 %

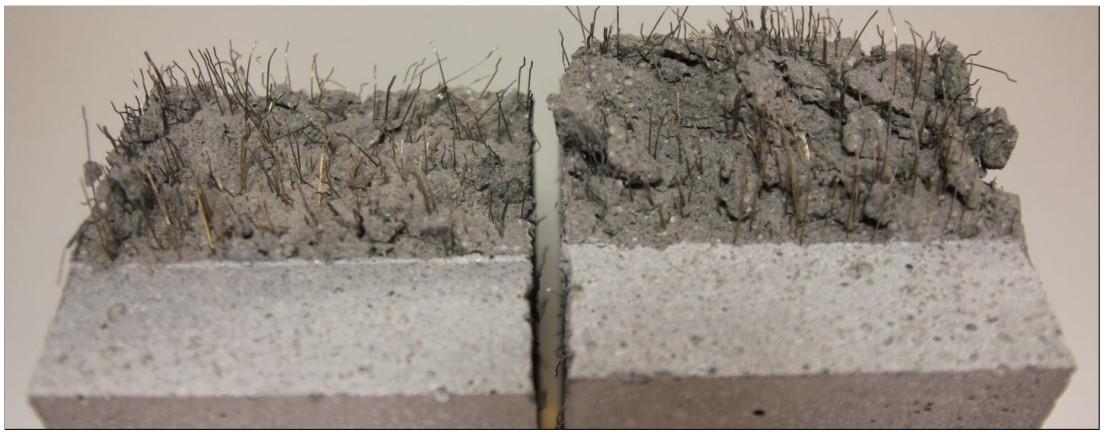

Figure C.3: Damage patterns after impact loading. Mixture DM.

DM H 1.0 % + S 0.5 %

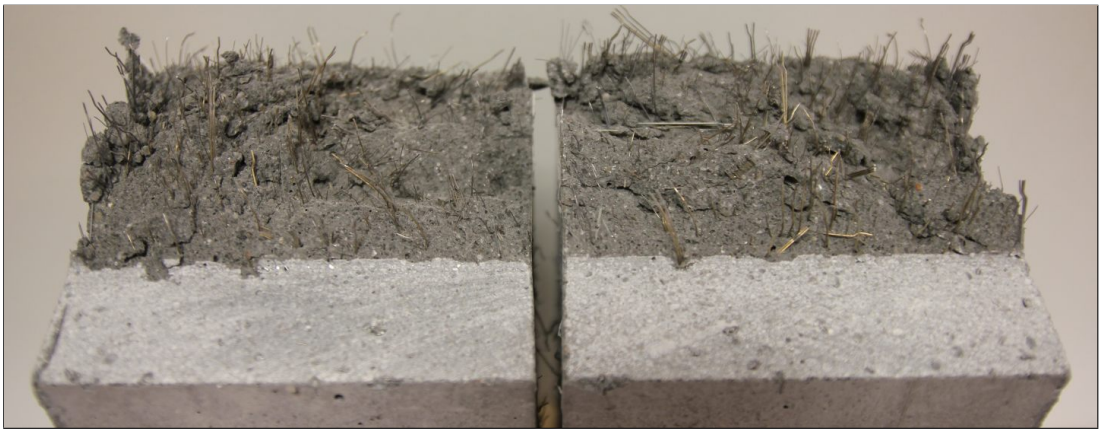

DM H 0.5 % + H 1.0 %

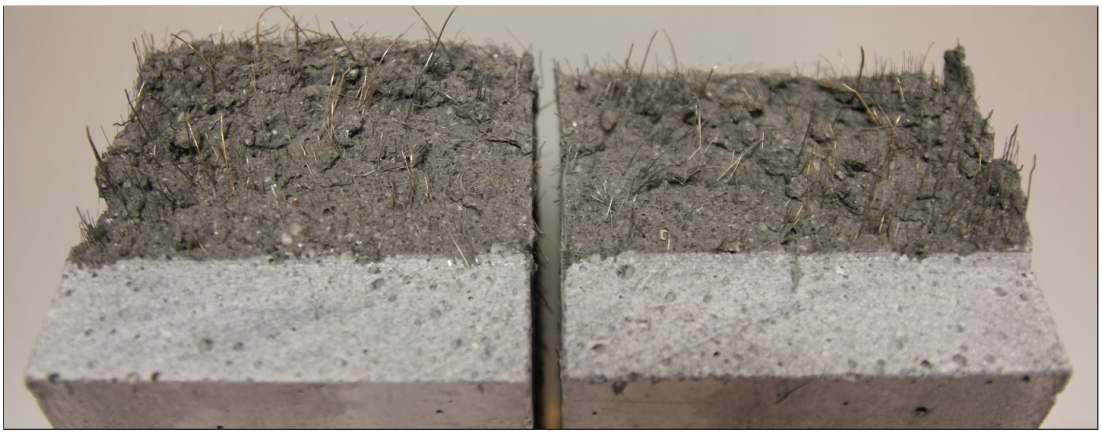

DM S 2.0 %

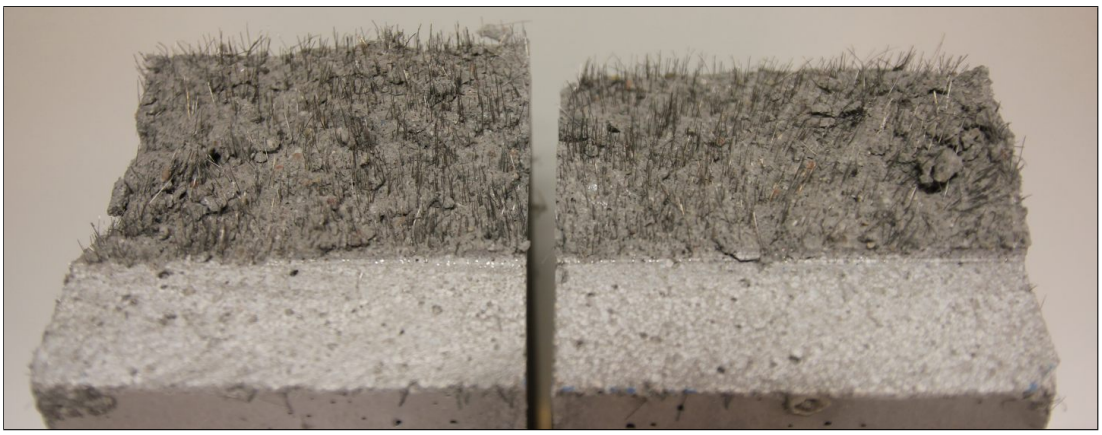

Figure C.4: Damage patterns after impact loading. Mixture DM.

R 2 %

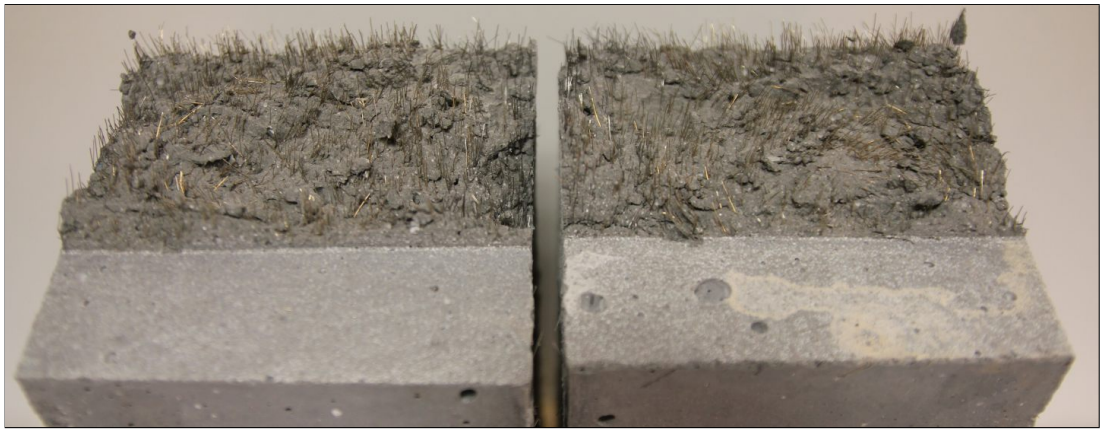

R 3 %

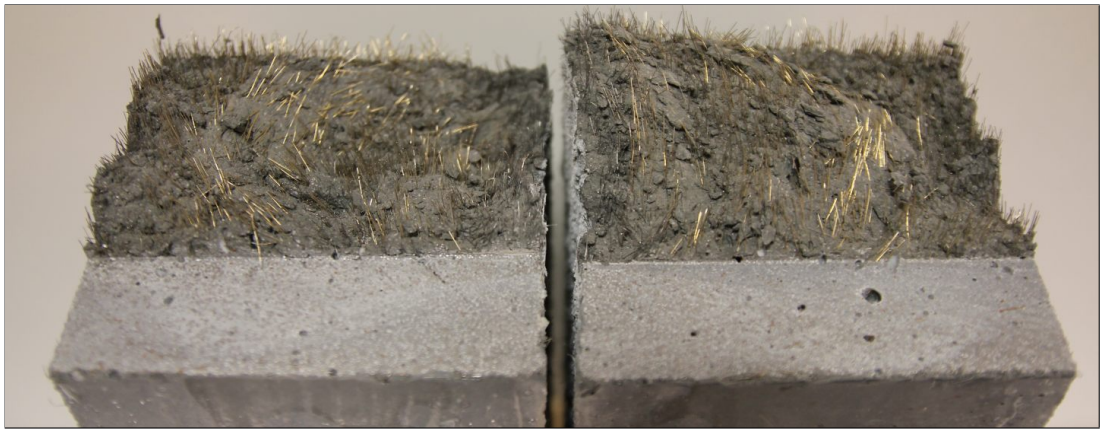

R 4 %

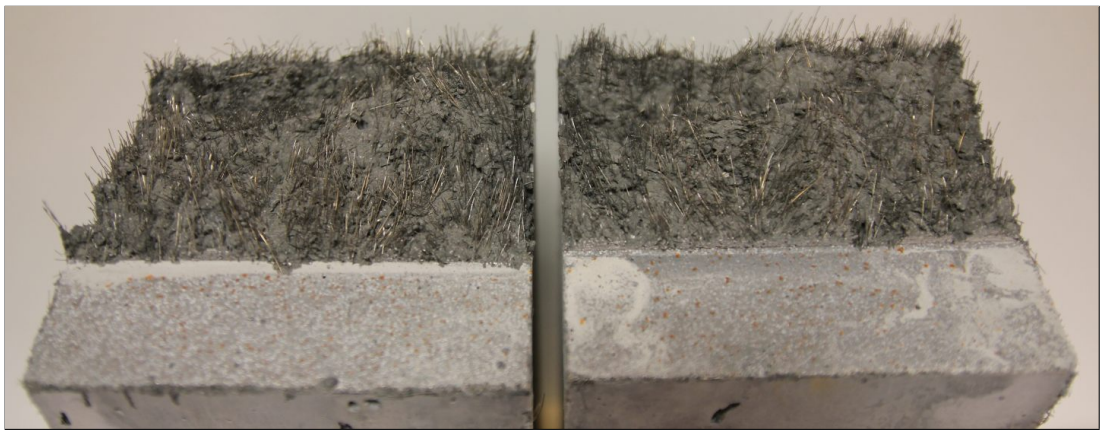

Figure C.5: Damage patterns after impact loading. Mixture R.